Search for the Sources of the Astrophysical High-Energy Muon-Neutrino Flux with the IceCube Neutrino Observatory

Von der Fakultät für Mathematik, Informatik und
Naturwissenschaften der RWTH Aachen University zur Erlangung
des akademischen Grades eines Doktors der Naturwissenschaften
genehmigte Dissertation

vorgelegt von

René Reimann, M. Sc.

aus

Neuss.

Berichter:
Universitätsprofessor Dr. Christopher Wiebusch
Universitätsprofessor Dr. Philipp Mertsch

Tag der mündlichen Prüfung: 19.11.2019

Abstract

Cosmic rays have been measured for more than a century, however, their sources and their acceleration process are still a major open questions in astroparticle physics. Ideal messenger particles and a smoking gun signal for this hadronic acceleration are neutrinos. With the observation of an high-energy astrophysical neutrino flux in 2013 and the confirmation in the independent detection channel of high-energy through-going muon-neutrinos, the IceCube Neutrino Observatory opened a new window to the non-thermal universe.

In this thesis we search for point-like sources of the observed astrophysical high-energy muon-neutrino flux. The search is based on a high statistic and high purity data sample taken by the IceCube Neutrino Observatory and contains data from eight years of livetime. The event selection focus on well-reconstructed, up- and through-going muon neutrino events, which are reconstructed with a median angular resolution of $\sim 1^\circ$ at $1\,\mathrm{TeV}$ energy and $\sim 0.3^\circ$ at $1\,\mathrm{PeV}$ energy. An unbinned likelihood method is used to test celestial positions for the existence of a point-like source. The likelihood method is optimized to sources showing similar characteristics as the observed astrophysical high-energy muon-neutrino flux. The sensitivity on the muon-neutrino flux of a point-like source with an E^{-2} spectrum is of the order of $E^2\,\mathrm{d}N/\mathrm{d}E = 3 \cdot 10^{-13}\,\mathrm{TeV\,cm^{-2}s^{-1}}$ and improves by about $\sim 35\%$ compared to previous published analyses.

We perform a scan of the full Northern Hemisphere to search for a point-like source any where in the sky. As this test suffers from the large number of tested positions, in addition, sky positions from a pre-defined source list, motivated by gamma-ray observations, are tested to reduce the number of trials. Both test results are non significant and compatible with only background. We also test for neutrino emission from the source position of the blazar TXS 0506+056 for which a gamma-ray flare has been found in spatial and temporal coincidence with a extreme-high-energy neutrino alert by IceCube. This test results in a p-value of 2.93% and thus is still compatible with only background.

As no test for a single point-like source shows a significant deviation from background only, we also test for the existence of a population of sub-threshold sources, both using the results from the northern sky scan and the source list. Therefore, we set up a population analysis, which tests for an excess of small but non significant p-values. Also these tests for populations of sources show no significant excess above only background. Thus, exclusion limits are calculated on the flux normalisation for sources following a baseline E^{-2} spectrum and source spectra found in the literature. In addition, also exclusion limits are calculated on populations of neutrino sources in dependence of their effective neutrino luminosity and effective source density. We conclude that rare but strong sources, such as BL Lacs and FSRQs, are challenged by the non observation as a significant excess in the population analysis.

Zusammenfassung

Die kosmische Strahlung wird seit mehr als einem Jahrhundert vermessen, allerdings sind ihre Quellen und die zugrunde liegenden Beschleunigungsmechanismen weiterhin eine offene Frage. Ein ideales Botenteilchen um diese Frage zu beantworten ist das Neutrino. Mit der Messung eines hochenergetischen astrophysikalischen Neutrinoflusses in 2013 und einer Bestätigung durch den unabhängigen Detektionskanal von hochenergetischen durchlaufenden Muonneutrinos, hat das IceCube Neutrino Observatorium ein neues Fenster zum nicht thermischen Universum geöffnet.

In dieser Arbeit suchen wir nach Punktquellen des beobachteten astrophysikalischen hochenergie Muonneutrinofluss. Die Suche basiert auf einem hoch-statistik und hoch-reinen Datensatz, der Daten von 8 Jahren, gemessen mit dem IceCube Neutrino Observatorium, umfasst. Die Ereignisselektion ist auf gut rekonstruierte, aufwärtslaufende und den Detektor durchquerende Muonneutrinoereignisse ausgelegt. Diese Ereignisse werden mit einer mittleren Winkelauflösung von $\sim 1^\circ$ und $\sim 0.3^\circ$ bei Energien von 1 TeV und 1 PeV rekonstruiert. Um eine Himmelsposition auf die Existenz einer Punktquelle zu testen, wird ein ungebinnter Likelihood verwendet. Die Likelihoodmethode ist optimiert auf Quellen, die eine ähnlicher Charakteristik zum astrophysikalischen hochenergie Muonneutrinofluss zeigen. Die Sensitivität auf den Muonneutrinofluss einer Punktquelle mit einem E^{-2} Spektrum is in der Größenordnung von $E^2\,\mathrm{d}N/\mathrm{d}E = 3 \cdot 10^{-13}\,\mathrm{TeV\,cm^{-2}s^{-1}}$ und stellt eine Verbesserung von $\sim 35\%$ gegenüber vorherigen publizierten Analysen dar.

Wir führen einen Scan des gesamten Nordhimmels durch, um nach Punktquellen irgendwo am Himmel zu suchen. Diese Suche verliert allerdings durch die große Anzahl an getesteten Positionen ihre Sensitivität. Um die Anzahl an getesteten Positionen zu reduzieren wird eine vordefinierte Liste, die durch Messungen von Gammastrahlung motiviert wurde, separat getestet. Beide Resultate sind nicht Signifikant und somit kompatible mit dem Untergrund. Zusätzlich testen wir die Himmelsposition des Blasars TXS 0506+056, für den ein Flare in zeitlicher und räumlicher Koinzidenz mit einem extrem hochenergetischen Neutrino gefunden wurde. Dieser Test liefert eine Wahrscheinlichkeit von 2.93% für die Kompatibilität mit reinem Untergrund.

Da keine signifikante Neutrinopunktquelle gefunden wurde, verwenden wir die Resultate des Himmelsscans und der Quellkanidatenliste, um nach einer Population von schwachen Quellen zu suchen. Hierzu erstellen wir eine Analyse die nach einem Überschuss an kleinen Wahrscheinlichkeiten sucht. Auch die Resultate dieser Suchen nach Populationen von schwachen Quellen ist nicht signifikant. Daher berechnen wir Ausschlussgrenzen auf die Flussnormalisierung von Referenzspektren und Neutrinoflussspektren für individuelle Quellen, die in der Literatur gefunden werden können. Weiterhin berechnen wir Ausschlussgrenzen für Populationen von Neutrinoquellen in Abhängigkeit ihrer effektiven Neutrinoluminosität und effektiven Quelldichte. Durch die nicht Beobachtung eines signifikanten Überschusses in der Populationsanalyse werden seltene aber starke Quellen, so wie BL Lacs oder FSRQs, als Quellen des gesamten Neutrinoflusses infrage gestellt.

Contents

List of Figures

List of Tables

Chapter 1

Motivation

Charged cosmic-rays - electron, protons and heavy nuclei - are known for over 100 years and their energy spectrum has been measured up to energies of $10^{20}\,\mathrm{eV}$. The energy spectrum follows a falling power-law and thus is clearly of non-thermal origin. Identifying the sources and the acceleration mechanisms within these sources of cosmic-rays are outstanding questions in astro-particle physics. However, it is difficult to identify sources of cosmic-rays using their arrival direction on Earth since they are deflected in magnetic fields during their propagation from the source to the observer.

However, it is possible to study sources of cosmic-rays by other messenger particles that are produced by interactions of cosmic-rays in the vicinity of the source with surrounding matter as depicted in Figure 1.1. These messenger particles are gamma-rays and neutrinos.

High-energy gamma-rays are neutral particles and thus are not deflected, however they can be absorbed by interactions with matter within the vicinity of the source or during their propagation. Especially at the highest energies, the range of gamma-rays is limited by interactions with background photons, e.g. from the cosmic microwave background (CMB) [2].

High-energy neutrinos on the other hand are also not charged and thus are not deflected in magnetic fields. As they only interact weakly, they are rarely absorbed during their propagation. However, this advantage comes with the cost of a very small interaction probability within neutrino detectors. Thus, for neutrino detection huge volumes are needed.

In 2013, the IceCube collaboration reported the first observation of a diffuse, astrophysical, high-energy, all-flavor neutrino flux using neutrino signatures fully contained within the detector volume [3]. This observation marks the beginning of neutrino astronomy which is a new window to understand high-energy processes within our universe.

This observation was confirmed by the measurement of a diffuse, astrophysical, high-energy muon-neutrino flux using the complementary detection channel of through-going muon-neutrinos, i.e. neutrino events with interaction vertex in the vicinity of the detector [4, 5, 6]. These analyses are restricted to the Northern Hemisphere to suppress the background of atmospheric muons that arises from cosmic-ray air showers. The diffuse, astrophysical, high-energy muon-neutrino flux is best described by a single power-law with a spectral index of 2.19 ± 0.10 and a flux normalization of $(1.01^{+0.26}_{-0.23}) \times 10^{-18}\,\mathrm{GeV^{-1}\,cm^{-2}\,s^{-1}\,sr^{-1}}$ at $100\,\mathrm{TeV}$ neutrino energy with a significance of $6.7\,\sigma$ above background only [6].

The detection of astrophysical neutrino sources is a smoking gun for hardronic acceleration within these sources and may contribute to answer one of the outstanding questions of astro-particle physics: *What are the sources of high-energy cosmic-rays?*

Searches to identify these sources are commonly based on spatial clustering of astrophysical neutrino events within the background of atmospheric muons and neutrinos which are

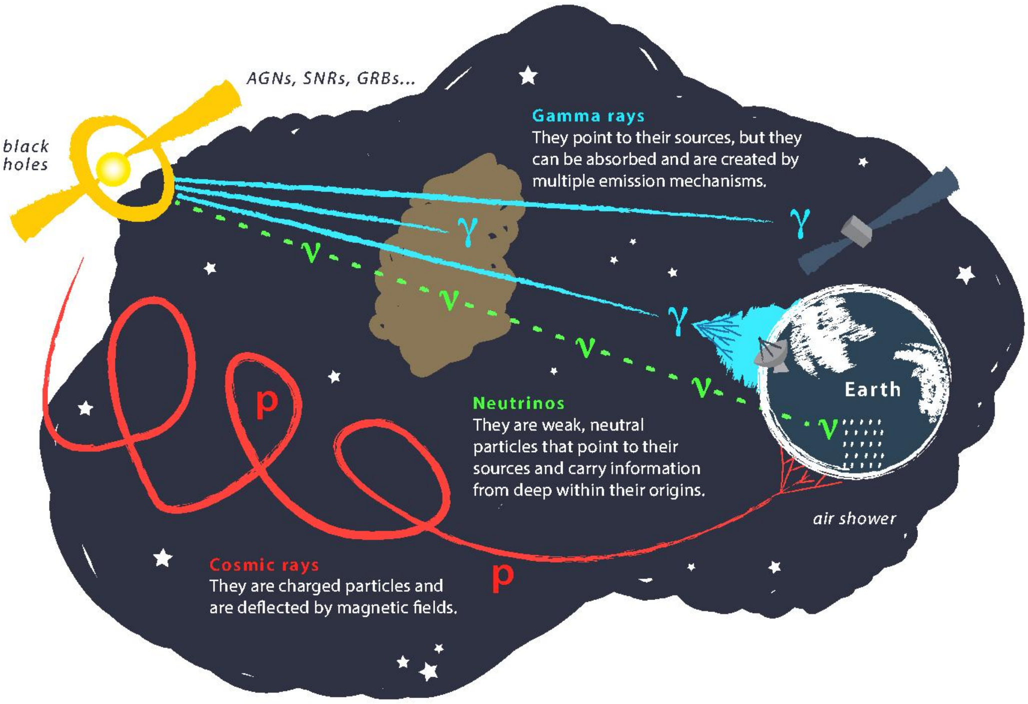

Figure 1.1: Illustration of the multi-messenger approach to search for high-energy astrophysical sources. Charged cosmic-rays, mainly protons p, shown in red are deflected by magnetic fields, gamma-rays γ shown in blue travel at geodesic lines but can be absorbed especially at high energies due to interactions with background photons of the cosmic microwave background. Neutrinos ν shown in yellow also propagate on geodesic lines but due to there low interaction probability are not absorbed. From [1].

uniformly distributed.

There are several search strategies to search for sources of astrophysical neutrinos including time-integrated and time-dependent searches, triggered and un-triggered searches, searches for point-like, extended and large-scale structure emission which are based on self-correlation or cross-correlation with multi-wavelength data. Despite huge effort, no unambiguous source or source class of these high-energy neutrinos could be identified yet [7, 8, 9, 10, 11, 12, 13, 14, 15, 16, 17, 18]. However, recently the IceCube collaboration reported evidence for neutrino emission emitted by a blazar [19, 20].

The goal of this thesis is to push the sensitivity for time-integrated neutrino emission from point-like sources by several improvements in the analysis technique and using more a competitive data sample compared to the previous published steady-point source analysis by IceCube [13]. This analysis is specialized for sources with the same characteristics as the measured diffuse, astrophysical, muon-neutrino flux. Moreover, the analysis relies on the same sample, used to measure the diffuse, astrophysical, muon-neutrino flux in Ref. [6], allowing to use the atmospheric and astrophysical flux parametrization of the same sample within the analysis. In total 8 years of IceCube data from the Northern Hemisphere are analyzed. The tested hypotheses comprise a scan for point-like neutrino emission from sources on the Northern hemisphere as well as a test of sources within a pre-defined source list that is motivated by gamma-ray observations. Since no significant source is found, exclusion limits are calculated.

Beside testing for individual point-sources, also populations of sub-threshold sources are tested. In particular, one test focuses on a point-like emission from the direction of TXS 0506+056, for which evidence of a neutrino emission has been reported recently [20].

In Chapter 2 and 3, messenger particles and their advantages and disadvantages, possible sources of cosmic-rays and astrophysical neutrinos and hadronic acceleration mechanisms are discussed. Neutrino interactions, and detection techniques as well as the IceCube Neutrino Observatory and the used data sample are discussed in Chapter 4 and 5. The unbinned maximum likelihood used in this thesis is described in Chapter 6 and the performance of this method is studied in Chapter 7. The results are presented in Chapter 8 and astrophysical implications are given in Chapter 10. Tests for populations of sub-threshold sources are discussed in Chapter 9 and their astrophysical implications are given in Chapter 10. The thesis closes with a Summary and Outlook in Chapter 11. Further supplemental material can be found in the Appendices A, B, C, D, E, F and G.

Chapter 2

High-Energy Messenger Particles

Supernova explosions, super-massive black holes in active galactic nuclei, neutron stars and gamma-ray bursts are some of the most violent environments in the high-energy, non-thermal universe. Understanding these astrophysical sites can give insights into the fundamental laws of physics and reveal new phenomena. As these environments can not be tested on Earth, one has to rely on information about these distant sources via messenger particles.

In this chapter, requirements on messenger particles that carry information about their sources are introduced in Section 2.1. The spectrum and properties of cosmic-rays are discussed in Section 2.2 and basic properties of gamma-rays are described in Section 2.3. Section 2.4 gives a summary about high-energy astrophysical neutrinos. The chapter closes with a short discussion of recently discovered gravitational waves in Section 2.5 and a summary of advantages and disadvantages of the different messenger particles in Section 2.6.

2.1 Requirements for Messenger Particles

Astrophysical messenger particles travel a long way from there origin to the observer and thus have to be stable on astrophysical time scales[1]. The range, that a relativistic particle with mass m and energy E can travel, is $r = c\tau\gamma = \frac{\tau E}{mc}$ where τ is the lifetime of the particle in its rest frame, γ is the Lorenz factor and c is the speed of light in vacuum. In the standard model of particle there are three types of particles that are stable on astrophysical scales. These are cosmic rays (including electrons, protons and other charged nuclei), photons and neutrinos. In addition, the recently discovered gravitational waves [23] may provide further information about astrophysical sources[2]. In the following sections, these messenger particles are introduced. All these particles carry complementary information and a comparison of their advantages and disadvantages is given in Section 2.6.

---

[1] The galactic center is about 8 kpc away from the Sun [21] which corresponds to $\sim$ 26000 ly and thus a particle that travels with nearly speed of light takes 26000 yr to reach the Earth on a straight line. This is a typical galactic scale. The nearest major galaxy is the Andromeda Galaxy at a distance of 0.77 Mpc [22] giving a lower bound on extra-galactic scales that are ranging up to several Gpc.

[2] Gravitational waves are not included in the standard model of particle physics because of the lack of a unified theory. However in the context of multi-messenger astronomy gravitational waves can be seen as another messenger *particle*.

2.2 Cosmic Rays

Cosmic rays are ionized nuclei, mainly protons (about 90%) and helium (about 9%), as well as electrons and heavier elements that hit the Earth's atmosphere at a rate of $\sim 1000\,\mathrm{m}^{-2}\,\mathrm{s}^{-1}$ [24].

Cosmic rays were first discovered by Victor Hess in 1912 in a balloon-flight measuring the discharge of electroscopes by ionizing radiation, for which he received the Nobel price in 1936. He found that above $\sim 3000\,\mathrm{m}$ the ionizing radiation rapidly increases leading to the conclusion that the ionizing radiation has to come from outer space [25]. This discovery marks the beginning of modern astro-particle physics. About 50 years later the first ultra-high energy cosmic-ray (UHECR) event with an energy of above $10^{20}\,\mathrm{eV}$ was measured with the Volcano Ranch experiment [26].

Within the last century, many experiments were performed to measure the flux of cosmic-rays. Today the spectrum of cosmic-rays is known in the energy range from $\sim 10^{8}\,\mathrm{eV}$ to $\sim 10^{20}\,\mathrm{eV}$. The measured flux ranges from $\sim 10^{4}\,\mathrm{m}^{-2}\mathrm{sr}^{-1}\mathrm{GeV}^{-1}\mathrm{s}^{-1}$ at 100 MeV to a flux of $10^{-28}\,\mathrm{m}^{-2}\mathrm{sr}^{-1}\mathrm{GeV}^{-1}\mathrm{s}^{-1}$ at 100 EeV.

Remarkably, the spectrum can be nearly described by a falling power-law with spectral index γ and flux normalization Φ_0

$$F(E) \quad = \quad \Phi_0 \cdot E^{-\gamma} \tag{2.1}$$

over a wide energy range. As the spectrum does not follow a Planck-spectrum, it is obvious that the cosmic-ray spectrum is not of thermal origin and thus coming from non-thermal sources. The lowest energy of few GeV and below, cosmic rays are effected by the magnetic field of the sun and show an anti-correlation with the solar activity [27]. Between few GeV to $10^{15}\,\mathrm{eV}$ the spectral index is $\gamma \approx 2.7$. At high energies the spectrum has three prominent features: the *knee* at $10^{15}\,\mathrm{eV}$ to $10^{16}\,\mathrm{eV}$ where the spectral index softens to $\gamma \approx 3.0$, the *ankle* at about $10^{18.5}\,\mathrm{eV}$, where the spectral index hardens again towards $\gamma \approx 2.7$ and a *cut-off* at the highest energies of about $10^{19.5}\,\mathrm{eV}$ [27]. Between the knee and the ankle another kink at about $10^{17}\,\mathrm{eV}$ shows up that is called *second knee*. In Figure 2.1, the all-particle spectrum above $10^{13}\,\mathrm{eV}$ is shown as a function of energy-per-nucleus E. The all-particle flux $F(E)$ has been multiplied by $E^{2.6}$ to visualize the structures in the spectrum.

The shape of the energy spectrum is related to the acceleration and propagation mechanism. As cosmic rays are charged particles they are deflected within magnetic fields with a gyro radius of

$$\frac{r_{\mathrm{gyro}}}{\mathrm{m}} = 3.3 \frac{p_{\perp}/\mathrm{GeV}}{z \cdot B/\mathrm{T}}, \tag{2.2}$$

where $p_{\perp}$ is the momentum of the particle perpendicular to the magnetic field, z is its charge in units of the elementary charge e and B is the magnetic field strength. Using the size and the magnetic field strength of our galaxy, cosmic rays below the knee have to be of galactic origin due to the size of the corresponding gyro radius, while cosmic rays above the ankle have to be of extra-galactic origin. There are two models to explain the cosmic-ray spectrum above the *knee*: the mixed composition model and the dip model.

The mixed composition model bases on a change of composition within the spectrum as described in Ref. [28]. In this model, the total flux is given by the summed flux from several

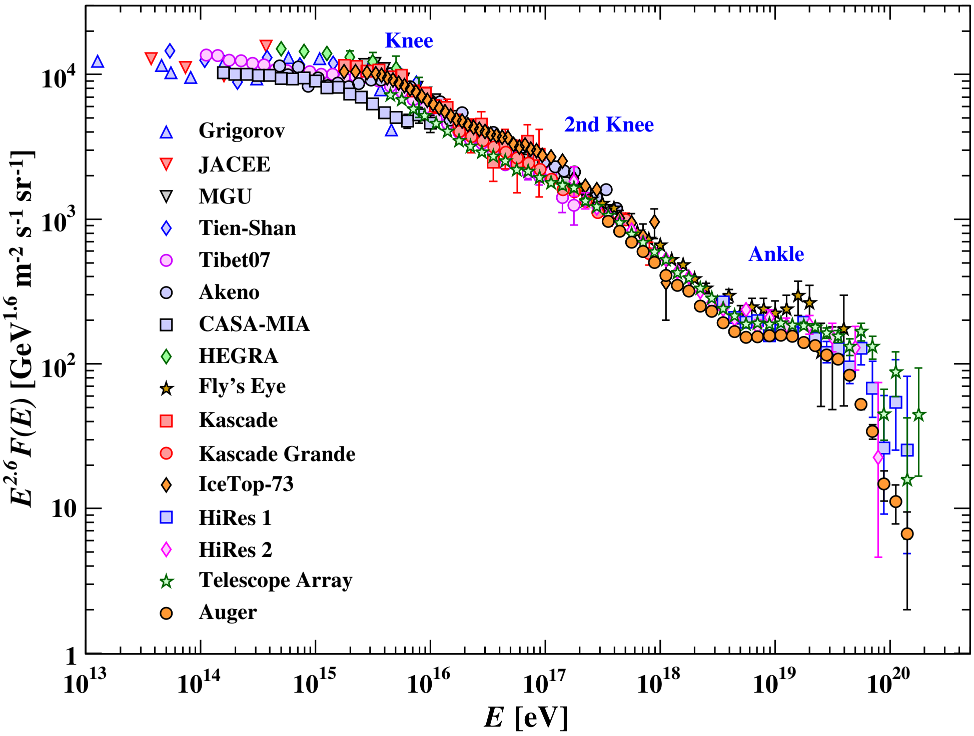

Figure 2.1: The all-particle flux $F(E)$ as a function of E (energy-per-nucleus) from air shower measurements. The spectrum has been multiplied by $E^{2.6}$ to make features of the energy spectrum more apparent. The plotted spectrum consist of measurements from air shower detectors. These measure the high-energy component of the cosmic ray flux as lower energy cosmic rays produce air showers that are not observable with this technique. Measurements from space based experiments are not shown. From Ref. [27] and references [91-106] in there.

different populations of source environments, each having characteristic power-laws and cut-offs. The model assumes that the spectrum for particles of type i follows a power-law with spectral index $\gamma_{i,j}$ with a cut-off at the characteristic regidity $R_{c,j}$ of an accelerating source population j. The maximal particle energy that can be achieved within an accelerator with a characteristic rigidity R_c is $E_{\max} = ZeR_c$. At least three different source populations contributing to the cosmic ray flux are needed to describe the cosmic-ray spectrum, where each population consists of a mixed composition with five groups of elements: hydrogen (H), helium (He), carbon, nitrogen and oxygen (CNO), magnesium, aluminium and silicon (MgAlSi), and iron (Fe) [28, 29, 30, 31, 32]. The all particle spectrum is given by:

$$\phi(E) = \sum_{j}^{3} \sum_{i \in A} n_{i,j} \left(\frac{E}{Z_i e R_{c,j}} \right)^{-\gamma_{i,j}} \times \exp\left(-\frac{E}{Z_i e R_{c,j}} \right) , \tag{2.3}$$

where $n_{i,j}$ are the normalization of the individual particle fluxes of source population j and $A = \{\, \mathrm{H, He, CNO, MgAlSi, Fe} \,\}$.

Within the mixed composition model the first population is assumed to consist of galactic supernova remnants using about 10% of their kinetic energy to accelerate galactic cosmic-rays [31]. The knee is described by the proton cut-off of the first population and the steepening of the spectrum above the knee is a result from less abundant heavier nuclei components in this population. The ankle is described by the change from galactic to extra-galactic cosmic-rays. The cut-off at the highest energies is explained by the maximal acceleration power of the third component. There are two versions of this model: the H4a model where the third population has just a proton component and the H3a model where the third population has a mixed composition [31].

The dip model assumes there is just one galactic and one extra-galactic component. Both the ankle and the cut-off at highest energies are described by propagation effects of the extra-galactic component. In this model, the ankle is caused by the pair-production of protons and photons from the cosmic microwave background (CMB) during propagation:

$$p + \gamma_{\mathrm{CMB}} \to e^+ e^- \, . \tag{2.4}$$

The extra-galactic component continues below $\sim 1\,\mathrm{EeV}$ where the galactic to extra-galactic transition occurs. In this model, there is no need for a second galactic component [33]. In contrast to the mixed composition model, the cut-off at the highest energies is described by pion production in collisions of CMB photons and high energy cosmic rays. This effect is dominated by resonant production of Δ^+-baryons [34, 35]:

$$\begin{aligned} \gamma_{\mathrm{CMB}} + \mathrm{p} \; &\to \Delta^+ \to \; \mathrm{n} + \pi^+ \, , && (2.5) \\ \gamma_{\mathrm{CMB}} + \mathrm{p} \; &\to \Delta^+ \to \; \mathrm{p} + \pi^0 \to \mathrm{p} + \gamma + \gamma \, , && (2.6) \\ \gamma_{\mathrm{CMB}} + \mathrm{p} \; &\to \Delta^+ \to \; \mathrm{p} + m\pi \, , \; m \in \mathbb{N}. && (2.7) \end{aligned}$$

This effect is known as the Greisen-Kuzmin-Zatsepin cut-off, which sets in at about 6×10^{19} eV due to its enhanced cross-section at the Δ^+-resonance[3].

In principle, the dip model and the mixed component model can be distinguished by measuring the composition of UHECR, however until now the measurements are not conclusive [37, 38]. A second way to distinguish between these models is to measure neutrinos or photons that are produced by the GZK-effect, called GZK-neutrinos and GZK-photons, which would favour the dip-model.

---

[3] Nucleon-pion interactions set in at slightly lower energies with an energy threshold of $E_{\mathrm{th}} = \frac{m_N m_\pi + m_\pi^2/2}{\epsilon}$ [36]. Here m_N, m_π are the mass of the nucleon and pion and ϵ is the energy of the CMB-photon. However due to the strong increase in cross-section due to the Δ^+ resonance slightly above that threshold, the energy loss is dominated by the Δ^+-resonance.

Even though the spectrum of cosmic-rays is well known for over 100 years, the sources are not yet identified. As cosmic rays are charged, they can be accelerated in magnetic and electric fields within astrophysical sites and thus are the primary messenger particle for hadronic acceleration. In addition, cosmic ray particles can be produced by interactions of other cosmic ray particles during propagation in which case they are called secondary particles. This leads to a diffuse emission which changes the energy spectrum and composition of cosmic rays.

Due to magnetic fields in the interstellar medium (ISM), charged cosmic-rays are deflected and thus they do not point back to there origin as depicted in Figure 1.1. For the very highest energies where the bending radius becomes small compared to the propagation distance the isotropization reduces to a smear out of the source position.

However, at highest energies the range of cosmic rays is limited due to the GZK-effect described above [34, 35]. These interactions lead to an attenuation length of about 10 Mpc making the universe opaque for highest energy cosmic rays and thus just the local universe can be observed with cosmic rays [36]. Also neutron decay $n \to p + e^- + \bar{\nu_e}$, electron-positron pair production $p + \gamma \to p + e^+ + e^-$ and photo-pion production $N + \gamma \to N + (m\pi)$, $m \in \mathbb{N}$, $N \in \{n, p\}$ interactions with the photon fields of extra-galactic background light and radio sources limit the mean free path-length for high energy cosmic rays. The energy dependent energy attenuation length for protons are shown in Figure 2.2 [36]. The electron component which makes up about 1-2% of the cosmic-rays number density at a GeV [30] is limited to lower energies due to synchrotron radiation in the extra-galactic and inter-galactic magnetic field [36]. Synchrotron radiation is negligible for protons and heavier nuclei since the energy loss per path length scales with m^{-4}.

Thus, the limited range and the deflection of cosmic rays make it hard to identify the sources of cosmic-rays.

The primary spectrum of charged cosmic-rays gives information about the acceleration process in the astrophysical sites, but is altered by propagation effects like interaction and decay (see [24] Chapter 9). In addition, the chemical composition of cosmic-rays can give further information about the type and processes in the production site. However the chemical composition is also affected by the production of secondary cosmic-rays during propagation.

2.2.1 Secondary Production of Messenger Particles

In interactions of cosmic-rays with matter or photon-fields in the vicinity of their sources, secondary particles are produced. Within these hadro-nuclear and photo-hadronic interactions charged and neutral pions and heavier mesons are produced. The dominant processes are:

$$
\begin{aligned}
p + p &\to X + \pi^0\,, && (2.8)\\
p + p &\to X + \pi^\pm\,, && (2.9)\\
p + \gamma &\to p + \pi^0\,, && (2.10)\\
p + \gamma &\to n + \pi^+\,. && (2.11)
\end{aligned}
$$

Pions $\pi^0, \pi^\pm$ are short living particles with lifetimes of $\tau_{\pi^0} \approx 8.5 \times 10^{-17}\,\mathrm{s}$ and $\tau_{\pi^\pm} \approx 2.6 \times 10^{-8}\,\mathrm{s}$ [27]. Due to this short live-time, their decay probability is much larger compared to

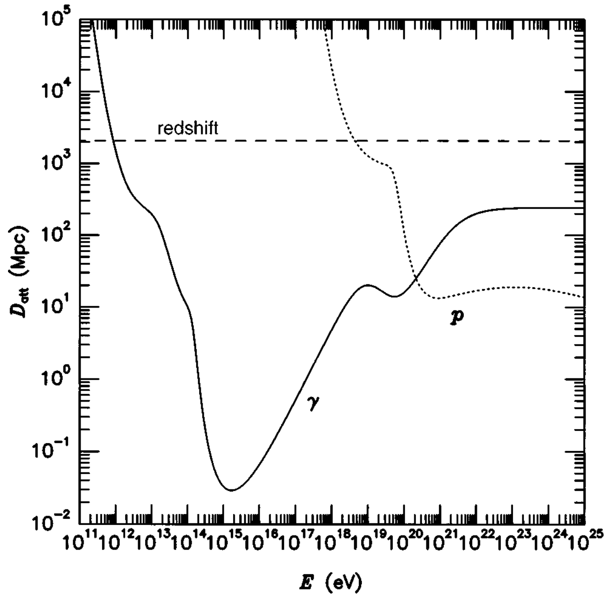

Figure 2.2: Energy attenuation length for "cascade photons" (solid, see Section 2.3 for definition) and protons (dotted) as a function of energy. Curves assume radiation background from CMB, radio and infrared-optical photons and are calculated in a continues energy loss approximation [36].

their interaction probability. Thus, these pions decay with the dominant channels and their branching fractions being:

$$\pi^0 \quad \rightarrow \gamma + \gamma \qquad (98.823 \pm 0.034)\% \tag{2.12}$$

$$\pi^+ \quad \rightarrow \mu^+ \nu_\mu \rightarrow e^+ \nu_e \bar{\nu}_\mu + \nu_\mu \qquad (99.98770 \pm 0.00004)\% \tag{2.13}$$

$$\pi^- \quad \rightarrow \mu^- \bar{\nu}_\mu \rightarrow e^- \bar{\nu}_e \nu_\mu + \bar{\nu}_\mu \qquad (99.98770 \pm 0.00004)\%\,. \tag{2.14}$$

As the pions produced by cosmic ray interactions carry ~20% of the initial cosmic ray nucleon energy and neutrinos receive on average ~25% of the pion energy, the resulting neutrinos have a typical energy of $E_\nu \approx E_{\mathrm{CR}}/20$ [39]. The π^0-decay to photons is a two body decay, such that each photon gets 50% of the pion energy, resulting in a photon energy of about $E_\gamma \approx E_{\mathrm{CR}}/10$ and thus $E_\gamma \approx 2E_\nu$ for protons and neutrinos from cosmic rays with the same primary energy.

Similar to the production of pions ($\pi^\pm$ and π^0) also kaons ($K^\pm$ and K^0) can be produced at high energies. Due to their higher mass of $m_{K^\pm} = 493.677 \pm 0.013\,\mathrm{MeV}$ ($m_{K^0} = 497.614 \pm 0.022\,\mathrm{MeV}$) compared to the mass of pions $m_{\pi^\pm} = 139.57018 \pm 0.00035\,\mathrm{MeV}$ ($m_{\pi^0} = 134.9766 \pm 0.0006\,\mathrm{MeV}$), the threshold for production is increased [40]. Charged kaons have a mean livetime of $\tau_{K^\pm} = (1.2380 \pm 0.0021) \cdot 10^{-8}\,\mathrm{s}$ and decay within $(63.55 \pm 0.11)\%$ of all cases into a (anti-)muon and (anti-)muon neutrino and in $(20.66 \pm 0.08\%)$ of all cases into a charged and a neutral pion [40]. The neutral kaon is a mixture of the eigenstates K^0_S and K^0_L, which have livetimes of $\tau_{K^0_S} = (0.8954 \pm 0.0004) \cdot 10^{-10}\,\mathrm{s}$ and $\tau_{K^0_S} = (5.116 \pm 0.021) \cdot 10^{-8}\,\mathrm{s}$ [40]. The K^0_S decays mainly into charged and neutral pions, while the K^0_L decays mainly in charged and neutral pions, electrons, muons and neutrinos [40].

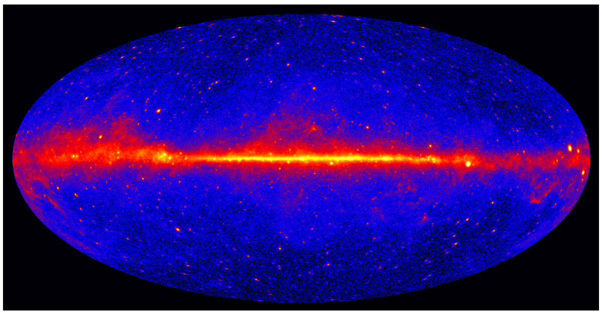

Figure 2.3: Gamma-ray sky at energies >1 GeV based on five years of data from the LAT instrument on NASA's Fermi Gamma-ray Space Telescope. Brighter colors indicate larger gamma-ray fluxes [42].

The neutrons produced in $p\gamma$-interactions are not stable and decays with a live-time of $880.2 \pm 1.0\,\mathrm{s}$ [27], according to

$$n \rightarrow p + e^- + \bar{\nu}_e\,. \tag{2.15}$$

The cross-section for hadro-nuclear interactions is about 100 times larger than the photo-hadronic interactions, however the dominant production process depends on the source properties, especially on the density of matter and photons.

As the radiation and particle fields around sources are much denser than in the ISM, neutrinos and gamma rays are generated within or in the vicinity of the sources. Thus, sources of cosmic-rays are expected to also be sources of gamma-rays and neutrinos. In addition, to secondary production in the surrounding of the source, cosmic rays can also interact during their propagation, that leads to a diffuse flux of neutrinos and gamma-rays.

2.3 High-Energy Gamma-Rays

Gamma-rays are photons with energies above 100 keV. They are produced by interactions of cosmic rays during their propagation or within the vicinity of cosmic ray sources and provide another detection channel for astrophysical accelerators (see Section 2.2.1). As gamma-rays are electrically neutral, they are not deflected within galactic and extra-galactic magnetic fields. They were first measured in the early 1960s [41] and today detailed gamma-ray maps of the sky at different energies are produced. These maps feature identifiable sources up to TeV energies. In Fig. 2.3, the sky-map of gamma-rays with energies $> 1\,\mathrm{GeV}$ is shown as measured within 5 years of data by the Fermi Large Area Telescope (LAT) [42].

To observe a source, the source environment has to be optically thin to allow the gamma-rays to escape the source region. Beside being produced by hadronic cosmic-ray interactions, gamma-rays can also be produced by leptonic processes like bremsstrahlung, inverse-Compton scattering (IC) and synchrotron-self-Compton scattering (SSC). Thus, a gamma-ray source is no direct evidence for hadronic acceleration.

Gamma-rays with energies $E_\gamma \geq \frac{m_e^2}{E_{\mathrm{bgd}}}$ undergo pair-production of electron positron pairs ($\gamma + \gamma_b \rightarrow e^+ + e^-$) with background photons of the cosmic microwave background (CMB) at

PeV energies and extra-galactic background light at TeV energies[4]. The resulting high energy electrons and positrons undergo inverse Compton scattering ($e^{\pm}+\gamma_b \to e^{\pm}+\gamma$), with inelasticity of about 90% at these high energies, leading to photons with reduced energy compared to the initial high-energy gamma-rays. These processes drive a electromagnetic cascade that can effectively be described by energy losses of *cascade photons*. While photons can not lose energy, a cascade photon relates the secondary photon produced by the inverse Compton scattering of pair-produced electrons or positrons to the primary photon. Beside pair-production of electron-positron pairs and inverse Compton scattering also double pair-production ($\gamma + \gamma_b \to e^+ + e^+ + e^- + e^-$), triple pair-production, pair-production of heavier particles, Bethe-Heitler pair-production (that includes atoms or ions in the process), pair-production with additional photons in the final state and pair-production on magnetic fields contribute to the energy loss processes [36]. The energy attenuation length for these *cascade photons* are shown in Fig. 2.2. It can be seen that gamma-rays suffer from stronger energy losses than cosmic-ray particles with the same energies. Thus, only the local universe can be observed with high energy gamma-rays with a horizon of about $z \approx 0.1$ for energies of 1 TeV [2]. This corresponds to $\sim 460\,\mathrm{Mpc}$ assuming a flat universe with $\Omega_M = 0.3$, $\Omega_H = 0.7$ and $H_0 = 70$.

Due to the precise identification of point sources the spectral energy distribution (SED) of individual gamma-ray sources can be measured. In principle, leptonic and hadronic acceleration within the source can be distinguished by the SED, but propagation effects alter the observable SED and the distinction is difficult in practice. Most gamma-ray sources are best described by leptonic production. However in [43, 44, 45] the measurement of the spectrum of galactic supernova remnants W44 and IC443 have been distinguished from leptonic gamma-ray emission by characteristic signatures of pion decay in the SED, leading to the first direct evidence for hadronic acceleration in supernova remnants.

2.4 Astrophysical Neutrinos

Neutrinos are leptons that can interact in three different flavors: electron-neutrinos ν_e, muon-neutrinos ν_μ and tau-neutrinos ν_τ. As they are neutral they are not deflected by galactic or extra-galactic magnetic field and thus their arrival direction points back to their sources. Neutrinos interact only via the weak force by exchange of $W^{\pm}$ and Z^0-bosons. Their interaction cross-section is orders of magnitude smaller than for gamma-rays or cosmic-rays such that neutrinos are typically not absorbed during their propagation to Earth and are capable to leave even optically thick environments. Moreover they lose energy only due to their redshift since they do not interact with the interstellar medium and thus the direct source spectrum can be observed at Earth and thus provide an unobstructed view on the universe. However, due to the small cross-section neutrinos are hard to detect and only small rates are measured. Neutrino interactions are discussed in detail in Section 4.

Neutrinos are produced by cosmic-ray interactions during their propagation and within the vicinity of cosmic ray sources via pion or heavy meson decay (see Section 2.2.1). Thus, the detection of neutrino sources would be direct evidence for hadronic acceleration. At these sites

---

[4] $E_{\mathrm{bgd}} \sim 10^{-3}\,\mathrm{eV}$ for CMB photons and $E_{\mathrm{bgd}} \sim 10^{-8}\,\mathrm{eV}$ for radio photons.

also gamma-rays are produced via hadronic interactions. However, gamma-rays can only leave optically thin environments, while neutrinos can also leave optical thick regions and thus give insights into the interior of these sources.

Neutrinos are produced in pion-decays, subsequent muon-decays and neutron decays. Magnetic fields within the sources can lead to synchrotron radiation from charged particles like muons, pions and other heavy mesons. This reduces the energy of these charged particles, which is also called cooling. Depending on the source properties the dominant production mechanism can change the energy dependent flavor ratios $(\nu_e : \nu_\mu : \nu_\tau)$ at the source [46]. The sources can be characterized as:

Pion beam source Pion and muon decay contribute equally to the produced neutrino-flux. The flavor ratio is given by $(\nu_e : \nu_\mu : \nu_\tau) = (1 : 2 : 0)$.

Muon damped sources Magnetic fields lead to strong muon cooling and the neutrino-flux is dominated by pion-decay. The flavor ratio is given by $(\nu_e : \nu_\mu : \nu_\tau) = (0 : 1 : 0)$.

Muon beam source Muons that have been cooled down by synchrotron radiation pile-up at lower-energy. In this energy range the neutrino-flux is dominate by muon-decay. The flavor ratio is given by $(\nu_e : \nu_\mu : \nu_\tau) = (1 : 1 : 0)$.

Neutron beam source Very strong magnetic fields lead to strong cooling of both pions and muons. In this energy-range neutrino production is dominated by neutron-decay. The flavor ratio is given by $(\nu_e : \nu_\mu : \nu_\tau) = (1 : 0 : 0)$.

Due to neutrino oscillation, the flavors are mixed during neutrino propagation, resulting in an almost uniform distribution of flavors after traveling astrophysical distances as can be seen in Fig. 2.4.

2.4.1 Neutrino Oscillations on Astrophysical Scales

The production and interaction states of neutrinos ν_e, ν_μ, ν_τ are flavor eigenstates, while time evolution of flavor state is trivially described by the time evolution of the mass-eigenstates ν_1, ν_2, ν_3. The observation of neutrino oscillations indicates that these eigenstates are not the same and that at least two neutrino mass-eigenstates have a non-zero mass. The rotation of the eigenstates is described by the unitary *Pontecorvo-Maki-Nakagawa-Sakata*-matrix (PMNS) U_{PMNS} [47].

$$\begin{pmatrix} \nu_1 \\ \nu_2 \\ \nu_3 \end{pmatrix} = U_{\text{PMNS}} \cdot \begin{pmatrix} \nu_e \\ \nu_\mu \\ \nu_\tau \end{pmatrix} \tag{2.16}$$

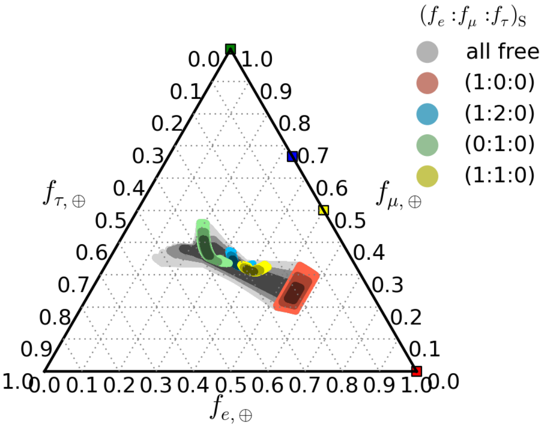

Figure 2.4: Allowed flavor-ratio at Earth for different flavor-ratios at the source according to Eq. 2.19. The different shaded regions are allowed by assuming oscillation parameters within their 1σ, 2σ and 3σ uncertainty range. Uncertainties are conservatively assumed to be uncorrelated. The gray region shows the flavor-ratio at Earth marginalized over an arbitrary flavor-ratio at the source. The different colored regions assume a source flavor ratio as indicated in the legend. Colored markers indicate the flavor-ratio at the source.

The PMNS-matrix can be characterized by 3 mixing angles θ_{12}, θ_{13}, θ_{23} and a complex CP violating phase δ_{CP}. In this parametrization the PMNS-matrix is given as:

$$\begin{aligned} U_{\mathrm{PMNS}} &= \begin{pmatrix} 1 & 0 & 0 \\ 0 & c_{23} & s_{23} \\ 0 & -s_{23} & c_{23} \end{pmatrix} \begin{pmatrix} c_{13} & 0 & s_{13}\mathrm{e}^{-i\delta_{\mathrm{CP}}} \\ 0 & 1 & 0 \\ -s_{13}\mathrm{e}^{i\delta_{\mathrm{CP}}} & 0 & c_{13} \end{pmatrix} \begin{pmatrix} c_{12} & s_{12} & 0 \\ -s_{12} & c_{12} & 0 \\ 0 & 0 & 1 \end{pmatrix} \begin{pmatrix} 1 & 0 & 0 \\ 0 & e^{i\frac{\alpha_{21}}{2}} & 0 \\ 0 & 0 & e^{i\frac{\alpha_{31}}{2}} \end{pmatrix} \\ &\equiv \begin{pmatrix} U_{e1} & U_{e2} & U_{e3} \\ U_{\mu 1} & U_{\mu 2} & U_{\mu 3} \\ U_{\tau 1} & U_{\tau 2} & U_{\tau 3} \end{pmatrix} \end{aligned} \tag{2.17}$$

where $s_{ij} = \sin\theta_{ij}$, $c_{ij} = \cos\theta_{ij}$ and θ_{ij} are the mixing angles [27]. α_{21} and α_{31} are two additional CP violating Majorana phases that exist, if neutrinos are their own anti-particles [48].

Since interaction states and propagation states are different, neutrinos created with flavor α can be detected in a different flavor eigenstate β. The probability to detect a neutrino, created in flavor state α with energy E_ν, that propagated a distance L, in flavor eigenstate β, is given by:

$$\begin{aligned} P_{\nu_\alpha \to \nu_\beta}(L, E_\nu) = \delta_{\alpha\beta} &- 4\sum_{i=1}^{3}\sum_{j=i}^{3} \mathrm{Re}\left(U^*_{\alpha,j} U_{\beta,j} U_{\alpha,i} U^*_{\beta,i}\right) \sin^2\left(\frac{\Delta m^2_{ij} L}{4E_\nu}\right) \\ &+ 2\sum_{i=1}^{3}\sum_{j=i}^{3} \mathrm{Im}\left(U^*_{\alpha,j} U_{\beta,j} U_{\alpha,i} U^*_{\beta,i}\right) \sin\left(\frac{\Delta m^2_{ij} L}{2E_\nu}\right) \end{aligned} \tag{2.18}$$

where $\Delta m^2_{ij} = m^2_i - m^2_j$ are the squared mass difference between mass eigenstates i and j. The

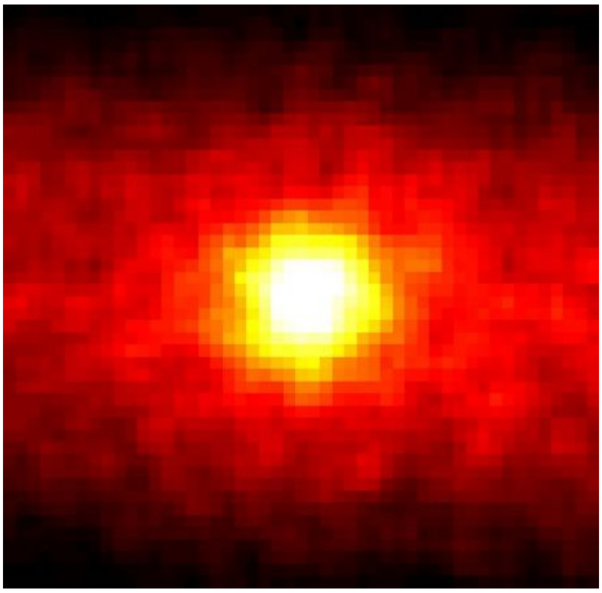

Figure 2.5: "Neutrino image" of the Sun, using 500 days of Super-Kamiokande data. Centered on the Sun's position, the picture covers a significant fraction of the sky (90×90 degrees in R.A. and Dec.). Brighter colors represent a larger flux of neutrinos [52].

typical scale of the oscillation length is $L_{\text{osc}} = 2\pi\frac{2E_\nu}{|\Delta m^2_{ij}|}$.

In case of an extended production region, with typical size ΔL, and a detector with energy resolution ΔE it is not possible to observe the exact oscillation pattern. The probability $P_{\nu_\alpha \to \nu_\beta}$ has to be folded with the spatial production distribution of the source and the energy resolution of the detector to obtain the detectable oscillation pattern. For $2\pi(L/L_{\text{osc}})(\Delta E/E) \gg 1$ and/or $2\pi\Delta L/L_{\text{osc}} \gg 1$, which is usually the case for astrophysical distances, the oscillation pattern is averaged over many oscillation lengths [27]. In this case the sine term vanishes, $\langle \sin x \rangle \to 0$, and $\langle \sin^2 x \rangle \to \frac{1}{2}$ and thus:

$$P_{\nu_\alpha \to \nu_\beta} = \sum_{j=1}^{3} |U_{\alpha,j}|^2 |U_{\beta,j}|^2 \, . \tag{2.19}$$

Using Eq. 2.19 the neutrino flavor-ratio at Earth $(\nu_e : \nu_\mu : \nu_\tau)_\oplus$ can be calculated from the neutrino flavor-ratio at the source $(\nu_e : \nu_\mu : \nu_\tau)_{\text{S}}$. In Figure 2.4 the allowed flavor-fraction at Earth is shown for different flavor ratios at the source using oscillation parameters from Ref. [49, 50]. The effect of current uncertainties on oscillation parameters, conservatively assuming they are uncorrelated, are shown by the different shaded regions [51]. For any source ratio at the source the flavor-ratio results in an nearly equal partition of flavors at the Earth (gray region). Thus, independent of the flavor-ratio at the source about 1/3 of the source neutrino-flux can be observed as muon-neutrino flux.

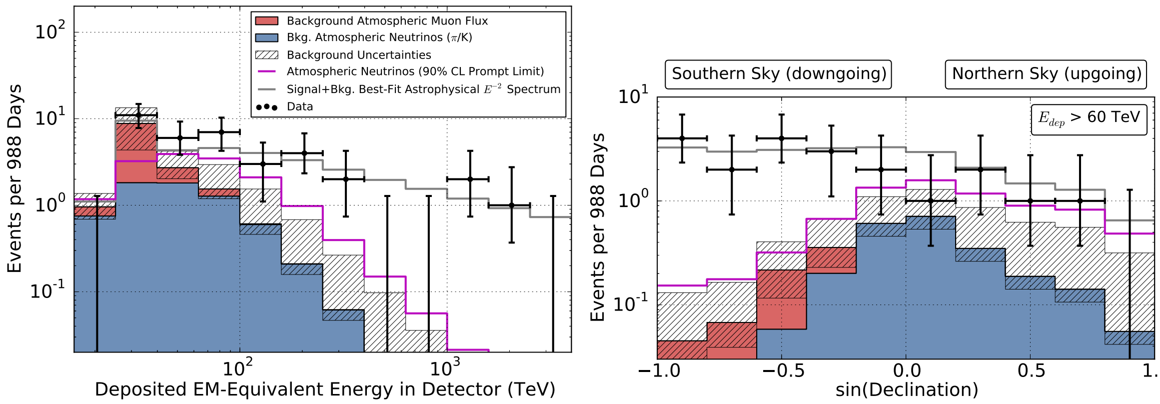

Figure 2.6: Histogram of deposited electromagnetic-equivalent energy in the detector (left) and sine of declination (right) for high-energy starting events in three years of IceCube data. Data points are marked as round markers with error-bars. Best fit atmospheric neutrino background from π and K decay (blue) and atmospheric muons (red) are shown as histograms. The magenter line gives a 90% CL upper limit on the contribution of a flux of atmospheric neutrinos from charm and heavier meson decay. The best fit astrophysical spectrum is shown in gray [59].

2.4.2 Observation of Astrophysical Neutrinos

Extra-terrestrial neutrinos have first been measured from the Sun, where neutrinos are produces in nuclear fusion in the solar interior. They were discovered by the Homestake Chlorine Detector [53]. In Figure 2.5, the Sun is shown in *neutrino light* as measured with the Super-Kamiokande detector [54]. The second resolved source of extra-terrestrial neutrinos has been observed in 1987 where several underground observatories – originally designed to measure the proton decay – measured several neutrinos in coincidence from supernova SN1987a [55, 56, 57, 58]. Both the Sun and SN1987a produce neutrinos with energies of a few MeVs. However, in the following, this thesis will focus on high-energy neutrinos with energies $> 100\,\mathrm{GeV}$.

A diffuse high-energy astrophysical neutrinos-flux has first been observed by IceCube in 2013 [3, 59]. As the flux of these astrophysical neutrinos is small and due to the small cross-section of neutrino interaction (see Section 4), huge detection volumes are needed. The IceCube detector consists of $1\,\mathrm{km}^3$ of ice at the South Pole with light sensors measuring the Cherenkov light of charged secondary particles from neutrino interactions (see Section 5). There are two main strategies to search for diffuse high-energy astrophysical neutrinos and distinguish it from atmospheric muons and neutrinos, which are a challenging background.

The first method that lead to the first observation of high-energy astrophysical neutrinos-fluxes is based on a separation of the detection volume into two separate regions: a veto-region and a fiducial volume. The veto-region makes up the outer part of the detector. Events that start within the detector and can not be seen within the veto region have to be induced by neutrinos as atmospheric muons would have deposited light also in the veto-region. The veto has the advantage that also atmospheric neutrinos starting inside the detector can be vetoed by coincident muons from the same air shower, which is called a self-veto. To make the veto-region work efficient a threshold on the deposited light is required. Astrophysical neutrinos can be distinguished from remaining atmospheric neutrinos on a statistical basis using their energy distribution and arrival direction. In Figure 2.6 the histogram of deposited electromagnetic-equivalent energy in the detector is shown for three years of IceCube data [59]. At high energies a clear excess can be seen above the background expectation. In the right panel of Fig. 2.6 the sine of declination distribution is shown for the same events as in the left panel. Also in this distribution a clear deviation from background only can be seen. This analysis rejects the atmospheric only hypothesis at the $5.7\,\sigma$ level [3] using 37 events. The latest update of this analysis reported 103 events with a deposited energy above 60 TeV [60]. A sky-map in galactic coordinates of these events is shown in Fig. 2.7 (top panel) where event positions are marked by "x" if the event topology was track like and "+" otherwise. The color-scale shows the test statistic value of a point source search similar to the technique used in this thesis (see Section 6).

The second strategy to separate astrophysical neutrinos uses the Earth to shield atmospheric muons. For this the sample is restricted to events from the opposite hemisphere, which is the Northern hemisphere in case of the IceCube detector. In addition, quality cuts on the reconstructions have to be applied to reduce background from mis-reconstructed events. These samples provide larger statistic of muon-neutrino events as the fiducial volume is much larger compared to starting events. The astrophysical diffuse flux has been also measured in this detection channel at the $5.6\,\sigma$ level [5]. A sky-map of events with a reconstructed energy larger than 200 TeV is shown in Figure 2.7 (bottom panel). This sample will be discussed in more detail in Section 5.5 and is used within this thesis.

Despite the existence of astrophysical neutrinos is confirmed, no unambiguous source or source class has been discovered yet [7, 8, 9, 10, 11, 12, 13, 14, 15, 16, 17, 18]. However, the IceCube collaboration recently reported evidence for time-dependent neutrino emission from the blazar TXS 0506+056 [20]. This blazar showed a flare in coincidence with a high energy neutrino event detected by IceCube [19]. This blazar and the evidence for neutrino emission are discussed in Section 8.3

Using multi-wavelength data, it is possible to predict neutrino fluxes for individual sources. In Ref. [61], neutrino fluxes have been predicted based on gamma ray spectra using the relations introduced in Section 2.2.1. Based on these model the amount of hadronic interactions within the sources can be tested. In Ref. [62], a multi-wavelength model including photons, electrons and protons in lepton hadronic interactions has been proposed, from which neutrino fluxes are predicted. With these models the proton luminosity of a source can be tested.

Beside astrophysical accelerators it is proposed that neutrinos can also be produced in self-annihilations or decay of heavy dark matter particles. This is noted here for completeness but is not further investigated in this thesis.

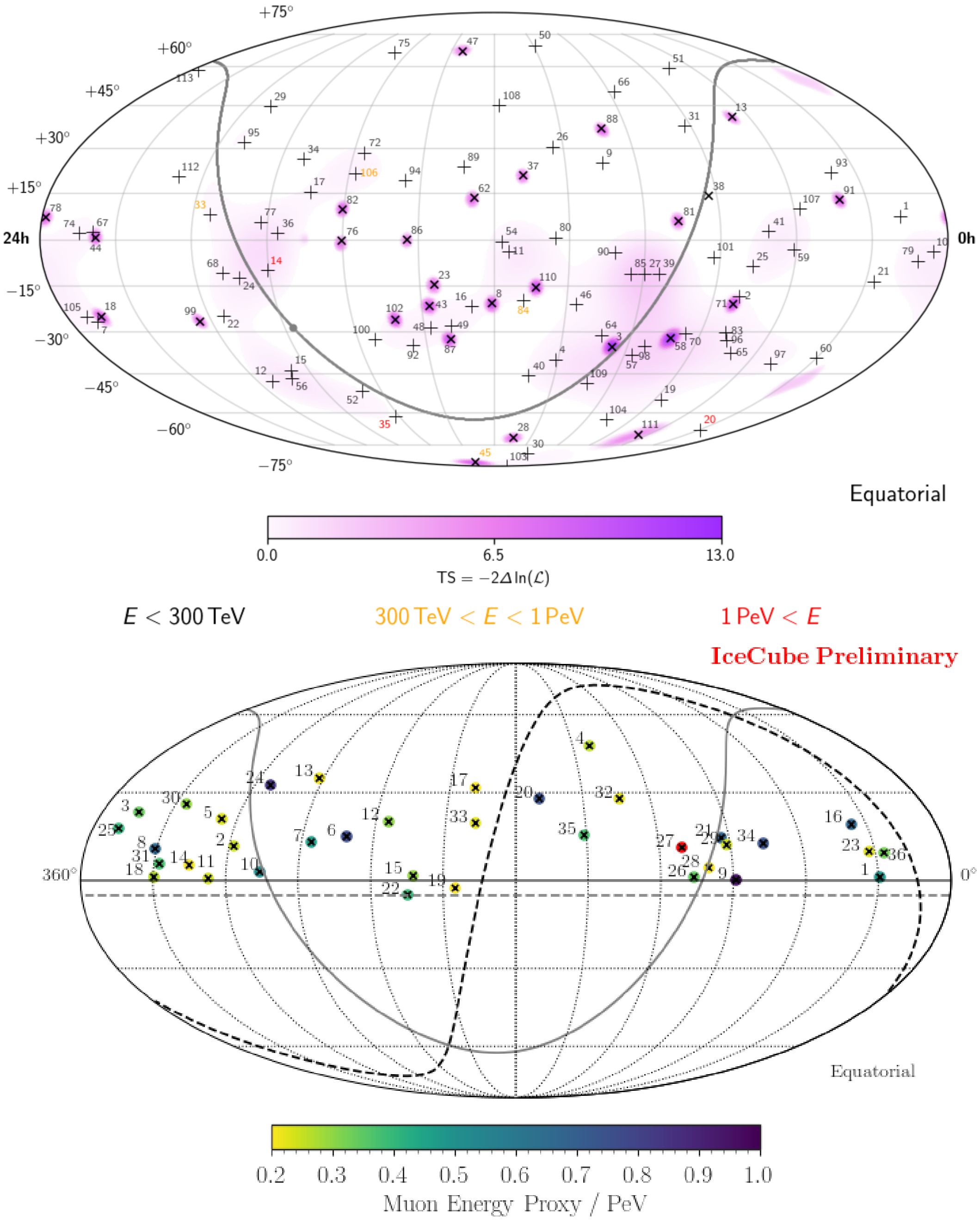

Figure 2.7: Top: Skymap of high-energy starting events in galactic coordinates from 7.5 years of IceCube data. Events with track-like signature are marked with ”x” others are marked with ”+”. The color in the background gives the test statistic value of a search for point sources using the shown events [60]. Bottom: Skymap of muon-neutrinos events with reconstructed energy > 200 TeV from 8 years of IceCube data in equatorial coordinates. The color of the markers gives the reconstructed energy of these events [6].

2.5 Gravitational Waves

Gravitational waves were predicted by Albert Einstein in 1916 [63, 64]. They are generated by the acceleration of large masses and thus are not directly linked to cosmic-ray acceleration in the first place. They carry information complementary to other multi-messenger particles about different physical processes from the same sources. Gravitational waves are almost not affected by any kind of interaction (except gravity) and thus propagate unperturbed from their origin to Earth, giving unique information from the very center of the source. Within the measurements properties of the astrophysical events like the distance from Earth, the amount of participating masses and the type of merged objects can be determined.

In 2016 the LIGO and Virgo collaborations reported the first direct observation of gravitational waves from a binary black hole merger [23] proving the existence of gravitational waves in general and thus opening a new window for multi-messenger observations. In 2017, the LIGO and Virgo collaboration together with Fermi Gamma-ray Burst Monitor and the International Gamma-Ray Astrophysics Laboratory (INTEGRAL) reported the detection of a binary neutron star inspiral [65] with a gamma-ray burst measured in coincidence [66]. This is the first observation of gravitational waves with an associated optical counterpart. The event was followed up with different multi-messenger observations [67].

2.6 Summary of Messenger Properties

In this chapter, four different astrophysical messenger particles have been introduced: charged cosmic-rays, gamma-rays, neutrinos and gravitational waves. Gravitational waves originate from different physical processes as the other messenger particles and give complementary information. Cosmic-rays, gamma-rays and neutrinos are linked to each other by the processes discussed in Section 2.2.1. Due to their particle physical properties, they have different properties regarding their production and propagation and thus their observation gives complementary information.

In Table 2.1 the basic properties for cosmic-rays, gamma-rays and neutrinos are summarized. The properties are split up into two sub-groups describing basic particle physics quantities and production and propagation properties.

	Cosmic-Rays	**Gamma-Rays**	**Neutrinos**
		Particle Physics Properties	
EM Charge	positive / negative	neutral	neutral
Dominant Interactions	strong, EM	EM	weak
Decay	stable	stable	stable
		Production & Propagation Properties	
Acceleration Mechanism	hadronic	indirect hadronic indirect EM	indirect hadronic
Production Site	within accelerator	vicinity of accelerator cosmogenic	vicinity of accelerator cosmogenic
Trajectory	deflected / curved	undeflected / straight	undeflected / straight
Dominant Energy Loss, *Absorption &* *Propergation Effects*	radiation in EGMF GZK-effect Bethe-Heitler Giant Dipol Resonance nuclear fragmentation	red shift pair production Photopion production	red shift neutrino-oscillation
Composition	chemical composition	–	flavor composition

Table 2.1: Summary of multi-messenger properties. Listed are properties of cosmic-rays, gamma-rays and neutrino. The properties are divided into sub-sections: the first section gives particle physics properties like charge and interactions. The second section gives properties of production and propagation. Abbreviations: electromagnetic (EM), Greisen-Kuzmin-Zatsepin effect (GZK), extra-galactic magnetic field (EGMF).

Chapter 3

Sources of High-Energy Neutrinos

In Chapter 2, different messenger particles have been described that can be used to study the high-energy universe. In this chapter, the possible sources of these high-energy messengers are discussed. In top-down models high-energy neutrinos arise from the decay of super-massive elementary particles on the energy scale of the grand unified theories (GUT), e.g. topological defects. These models assume beyond standard model physics and require the existence of these super-massive elementary particles. These models are not discussed further within this thesis. Instead, this thesis focus on bottom-up models where charged particles are accelerated within astrophysical environments. In Section 3.1, criteria for acceleration and possible acceleration mechanism are discussed. In Section 3.2, possible source candidates for Cosmic Rays and thus neutrinos are introduced. The current status of searches for high energy neutrino sources is described in Section 3.3.

3.1 Acceleration of Cosmic Rays

The acceleration process of cosmic rays is not yet known and is one of the most interesting questions in astro-particle physics. An accelerator model has to explain the power-law structure of the cosmic ray spectrum with a spectral index between two and three. The acceleration process should allow to accelerate charged particles up 10^{20} eV. In addition, it should explain the abundance of the different elements in the universe.

In general, the acceleration of a charged particle is given by the equation of motion

$$\frac{\mathrm{d}}{\mathrm{d}t}(\gamma m\vec{v}) = q\left(\vec{E} + \frac{\vec{v}\times\vec{B}}{c}\right) \tag{3.1}$$

where $\gamma = (1-|\vec{v}|/c)^{-1/2}$, $\vec{v}$ is the velocity of the particle, m its rest mass, c the speed of light in vacuum and $\vec{E}$ and $\vec{B}$ the electric and magnetic field, respectively. Acceleration can be divided in two mechanisms, an inductive or *one-shot acceleration* and a stochastic *diffuse* acceleration. In inductive acceleration models, particles are accelerated in a strong, ordered electric field within the acceleration environment [29]. However, in the nearly empty interstellar medium (ISM) electric fields are hard to establish as they lead to a flow of plasma, dissipating the electric field. However, there are scenarios, e.g. rapidly rotating black holes or pulsar, which can lead to a large potential difference between the surface of the object and infinity. A general model of accelerators generating a power-law spectrum by stochastic, diffuse acceleration in magnetic fields was proposed by Fermi [68] and is commonly known as Fermi-acceleration.

Another possible acceleration mechanism are e.g. acceleration by magnetic reconnection [69] or shear acceleration [70].

Fermi-Acceleration

The Fermi-mechanism explains how charged particles can be accelerated to produce a power-law spectrum, assuming three requirements on the acceleration process [71]:

1. particles are accelerated in small steps by many iterations,
2. the energy gain is proportional to the particles energy,
3. the probability to escape the acceleration region is constant.

After n iterations a particle with initial energy E_0 has an energy E_n of

$$E_n = E_0 \, (1+\zeta)^n \tag{3.2}$$

where ζ is the relative energy gain per iteration. Thus, it needs $n = \frac{\ln(E_n/E_0)}{\ln(1+\zeta)}$ iterations to accelerate the particle to E_n. The probability that a particle has not yet escaped from the region after these n interaction is $P_n = (1 - P_{\text{esc}})^n$ and thus the number of particles above an energy E is given by [71]:

$$N(>E) \propto \sum_{m=n}^{\infty} (1-P_{\text{esc}})^m = \frac{1}{P_{\text{esc}}} \left(\frac{E}{E_0}\right)^{-\frac{\ln\left(\frac{1}{1-P_{\text{esc}}}\right)}{\ln(1+\zeta)}} = \frac{1}{P_{\text{esc}}} \left(\frac{E}{E_0}\right)^{-\alpha} \tag{3.3}$$

with

$$\alpha = \frac{\ln\left(\frac{1}{1-P_{\text{esc}}}\right)}{\ln(1+\zeta)}. \tag{3.4}$$

In case of small ζ and P_{esc}, this α reduces to $\alpha \approx \frac{P_{\text{esc}}}{\zeta}$. In this case, the differential energy spectrum has the form of equation 2.1 with $\gamma = 1+\alpha$. Assumption 1 and 3 above are motivated by a diffuse walk in the acceleration region and a stochastic probability to leave that region. In the following, it is discussed how a relative energy gain per interaction can be achieved.

Energy gain

Charged particles can gain energy by interactions with moving, magnetically turbulent regions. Assuming a highly relativistic particle traveling with speed $v \approx c$ and energy E_1 as well as a magnetic turbulent region that moves with velocity v_{mag} (see Fig. 3.1), the energy of the particle in the rest frame of the magnetic turbulent region E'_1 can be calculated to [71]:

$$E'_1 = \gamma E_1 (1 - \beta \cos\theta_1). \tag{3.5}$$

Here, $\gamma = 1/\sqrt{1-\beta^2}$ and $\beta = \frac{v}{c}$ are the Lorentz factor and the velocity of the magnetic region relative to the speed of light in vacuum c respectively. θ_1 is the angle between the in-coming

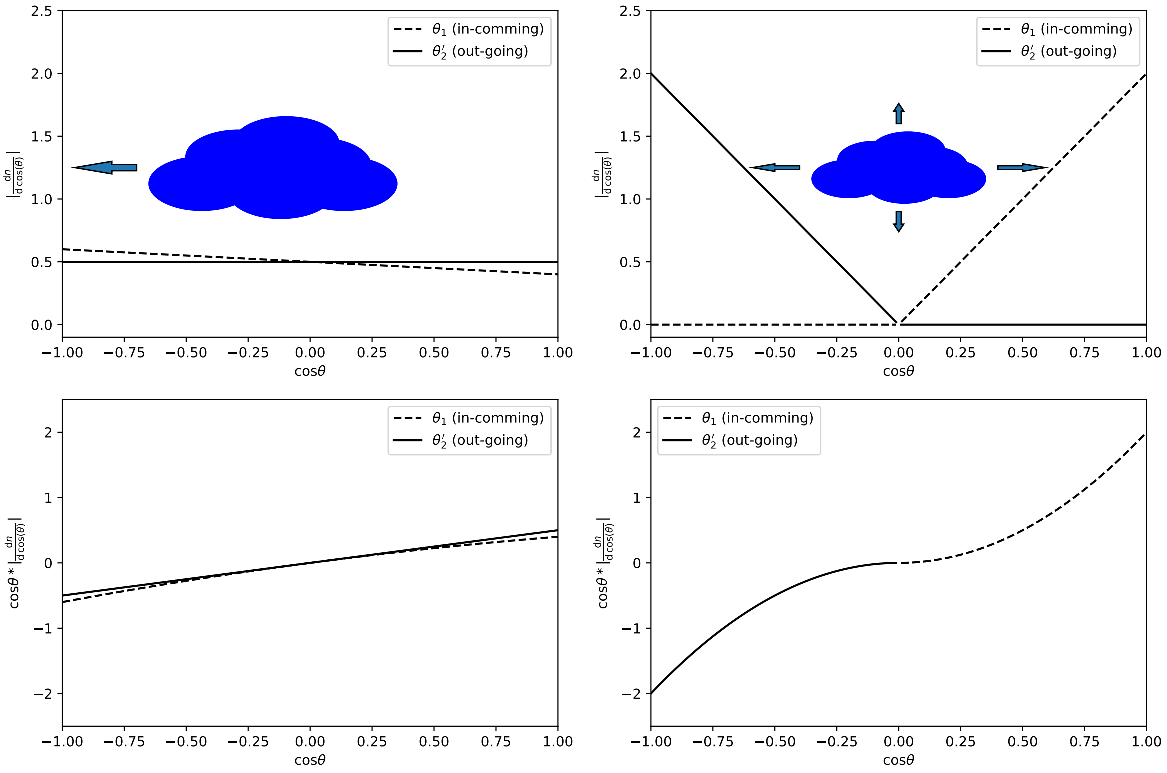

Figure 3.1: Phase space distribution (top panels) of particles entering (dashed) and leaving (solid) the magnetized region at angle θ_1 and θ_2', respectively. The lower panels shows the phase space distribution multiplied by the angle. The absolute value of this quantitiy is proportional to the energy gain. The left panels are made for the magnetic cloud scenario, where the magnetic cloud moves randomly at non or mildly relativistic speed. The right panels are made for the shock front scenario where the shock front is going outwards.

direction of the particle and the velocity of the magnetically turbulent region v_{mag}. Within the magnetically turbulent region, the particle is deflected by the magnetic field. This process is assumed to be energy-conserving and thus *elastic* meaning that $E_2' = E_1'$. *After several interactions*, the direction of particles are diffuse and will follow the clouds motion on average. Once the particle leaves the cloud again with energy E_2' the energy in the original rest frame is [71]:

$$E_2 \quad = \quad \gamma E_2'(1 + \beta\cos\theta_2') \,. \tag{3.6}$$

Here θ_2' is the angle between the out-going direction of the particle and the velocity of the magnetically turbulent region. Thus, the energy difference after one encounter compared to the original energy E_1 is

$$\Delta E \quad = \quad E_1 \left(\gamma^2(1 - \beta\cos\theta_1 + \beta\cos\theta_2' - \beta^2\cos\theta_1\cos\theta_2') - 1\right) . \tag{3.7}$$

As a result, the net energy gain in one encounter depends on the angles θ_1 and θ_2'. On a statistical basis, the energy gain can be calculated using $\langle\cos\theta_1\rangle = \int \cos\theta_1 \frac{\mathrm{d}n}{\mathrm{d}\cos\theta_1}\,\mathrm{d}\cos\theta_1$ and

$\langle\cos\theta_2'\rangle = \int \cos\theta_2' \frac{\mathrm{d}n}{\mathrm{d}\cos\theta_2'}\,\mathrm{d}\cos\theta_2'$. The form of $\frac{\mathrm{d}n}{\mathrm{d}\cos\theta_1}$ and $\frac{\mathrm{d}n}{\mathrm{d}\cos\theta_2'}$ and thus the energy gain depends on the specific assumptions on the interactions discussed below.

Magnetic clouds In case of a moving magnetic clouds at speed $\vec{v}_{\mathrm{cloud}}$, the distribution of in-coming particles is [71]:

$$\frac{\mathrm{d}n}{\mathrm{d}\cos\theta_1} = \frac{1}{2}(1-\beta_{\mathrm{cloud}}\cos\theta_1). \tag{3.8}$$

with $-1 \leq \cos\theta_1 \leq 1$. This is shown in Fig. 3.1 (left panels). Inside the cloud, the particles diffuse through the field, leaving the cloud isotropically as depicted in Fig. 3.1 (left panels). This corresponds to a uniform distribution of out-going directions $\cos(\theta_2')$, such that

$$\frac{\mathrm{d}n}{\mathrm{d}\cos\theta_2'} = \mathrm{const}\,, \tag{3.9}$$

with $-1 \leq \cos\theta_2' \leq 1$. Thus, on average $\langle\cos\theta_1\rangle = -\frac{\beta_{\mathrm{cloud}}}{3}$ and $\langle\cos\theta_2'\rangle = 0$, while the energy gain is

$$\Delta E = E_1\left(\gamma^2\left(1+\frac{\beta^2_{\mathrm{cloud}}}{3}\right)-1\right) \approx E_1\left(\frac{4\beta^2_{\mathrm{cloud}}}{3}\right), \tag{3.10}$$

where $\beta_{\mathrm{cloud}} \ll 1$ has been assumed in the last step.

For such processes the escape probability can be expressed as $P_{\mathrm{esc}} = \frac{T_{\mathrm{cycle}}}{T_{\mathrm{esc}}}$, where the cycle time T_{cycle} for one encounter is estimated by the rate of "*collisions*" between a relativistic particle at speed $\sim c$ and magnetic clouds at a density of ρ_{cloud} and the effective "*cross-section*" of the interactions σ_{cloud} [71]. Thus, the escape probability is $P_{\mathrm{esc}} = \frac{1}{c\rho_{\mathrm{cloud}}\sigma_{\mathrm{cloud}}T_{\mathrm{esc}}}$.

Using the calculated energy gain and escape probability, the spectral index is [71]:

$$\gamma \;\approx\; \frac{1}{\frac{4}{3}\beta^2_{\mathrm{cloud}}c\rho_{\mathrm{cloud}}\sigma_{\mathrm{cloud}}T_{\mathrm{esc}}}. \tag{3.11}$$

In this scenario the spectral index depends on the specific properties of the magnetic clouds. In particular, the spectral index can become very soft. The acceleration process is relatively inefficient as it scales with $\beta^2_{\mathrm{cloud}} \ll 1$. However, this process can post-accelerate particles during propagation and thus compensate energy losses during propagation. This mechanism is often called second order Fermi-acceleration because of the β^2_{cloud} scaling.

Supersonic shock front A shock front is the border between two regions of the medium that moves with a velocity v_{shock} above the speed of sound c_{s} of the ISM. At the shock-front there is a drastic change in pressure, dividing the medium in a unshocked upstream region and a shocked downstream region.

In case of a shock-front, the velocity vector of the shock is always pointing outwards. Thus, by crossing the shock front, θ_1 is restricted to the range $[-\pi/2, \pi/2]$ and the angular distribution with respect to the direction of the shock-front is given by $\frac{\mathrm{d}n}{\mathrm{d}\cos\theta_1} = 2\cos\theta_1$ (compare Fig. 3.1, right panels) [71]. By crossing back from the shocked to the unshocked region θ_2' is restricted to $[-\pi, -\pi/2] \cup [\pi/2, \pi]$. This results in $\langle\cos\theta_1\rangle = -\frac{2}{3}$ and $\langle\cos\theta_2'\rangle = \frac{2}{3}$. Following equation 3.7 yields an energy gain that is [71]:

$$\zeta = \frac{1+\frac{4}{3}\beta+\frac{4}{9}\beta^2}{1-\beta^2} - 1 \approx \frac{4}{3}\beta\,, \tag{3.12}$$

where $\beta = \frac{v_{\text{shock}}}{c}$ and v_{shock} is the velocity difference before and after the shock-front.

The probability to escape from the shock front region is given by the ratio of the loss rate of particles due to convection downstream $\rho_{\text{CR}} v_2$ and rate of particles crossing the shock front $\frac{c\rho_{\text{CR}}}{4}$. Thus, the escape probability is $P_{\text{esc}} = \frac{4v_2}{c}$ and from Eq. 3.4 follows $\alpha = \frac{3}{\frac{v_1}{v_2}-1}$ which just depends on the ratio of velocities upstream and downstream [71].

Based on the conservation of mass, energy-flux and momentum-flux at the shock front and assuming an ideal gas, the ratio of v_1 and v_2 can be calculated. Using the Mach-number M which is the ratio of the speed of the shock front and speed of sound in the medium the spectral index is [71]:

$$\alpha = \frac{3}{\frac{v_1}{v_2} - 1} = \frac{\frac{3}{2}(\kappa - 1) + 3/M^2}{1 - 1/M^2} \frac{3}{2}(\kappa - 1) + \frac{(3 + \frac{3}{2}(\kappa - 1))}{M^2}\,, \tag{3.13}$$

assuming large M, $\alpha \approx 1 + \frac{4}{M^2}$ for a mono-atomic, ideal gas with $\kappa = \frac{5}{3}$ and thus $\gamma \approx 2 + \epsilon$ in Equation 2.1.

This mechanism gives an environment independent spectral index of the source energy spectrum. It only assumes the existence of strong shocks. As the acceleration mechanism is proportional to β it is often called first order Fermi-acceleration.

In the discussion above, the escape probability P_{esc} has been assumed to be constant. However, it is likely that the escape time is rigidity and thus energy dependent. Allowing for an energy dependent escape probability softens the spectral index. The energy dependence of the escape time is supported by observations of the energy dependent secondary element to primary element ratio, e.g. the boron to carbon ratio. The ratio shows an energy dependence, indicating a change of the spectral index by $\delta \approx 0.6$. Thus, the spectral index of the energy spectrum at Earth is about $\gamma \approx 2.6 + \epsilon$ which is well in agreement with the observation (cf. Section 2.2).

The acceleration mechanism discussed here results in a power-law spectrum with spectral index of $\gamma \approx 2.6 + \epsilon$. However, particles can not be accelerated to arbitrary high energies.

Acceleration by Magnetic Reconnection

Another proposed acceleration mechanism is acceleration by reconnection of magnetic field lines. Magnetic reconnection has been observed in solar flare, e.g. [72], and in large plasma machines, e.g. in tokamaks [73]. However, the micro-physics is not yet understood [71]. This leak of understanding is mainly caused by a large difference in predicted and observed reconnection rate. While in solar flares the reconnection rate is of the order of hours, the typical magnetic field diffusion time scale predicted by magnetic hydro dynamic (MHD) is of the order $\tau_C = \sigma\mu_0 L^2$ [71]. Here $\sigma \propto T^{3/2}$ is the electrical conductivity, T is the temperature of the plasma, μ_0 is the permeability of free space and L is the size of the reconnection region. For typical values of solar flares $\tau_C = 10^7\,\text{yr}$ which is many orders of magnitudes away from the observed time scale [71].

A model predicted by Sweet and Parker can significantly reduce the predicted time scale for magnetic reconnection [74, 75]. Sweet and Parker assumed the geometry illustrated in

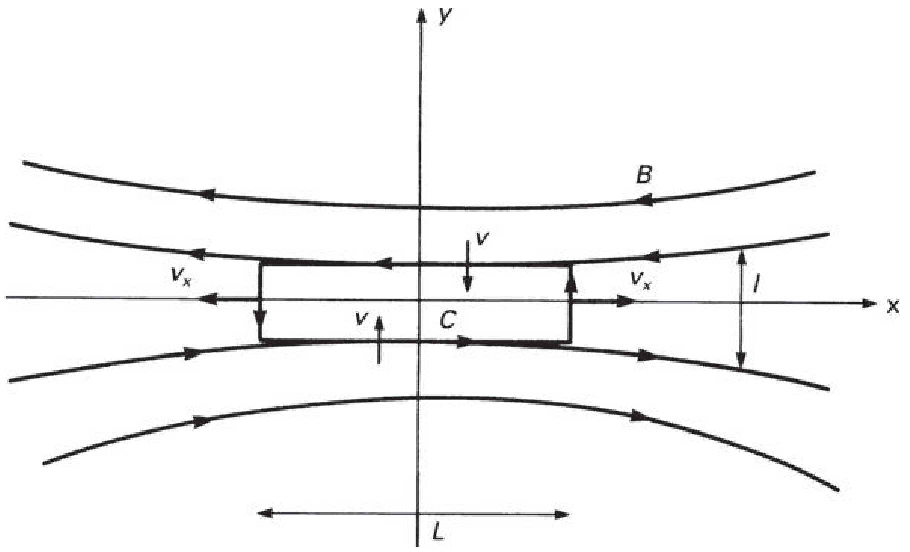

Figure 3.2: Magnetic field reconnection according to the Sweet-Parker model. The magnetic field reverses at the x-axis leading to a large current density in the z-direction. While magnetic field lines are convected into the neutral sheet along the y-axis, matter flows out along the x-axis. The length of the current sheet is L while the width is l. From Ref. [71].

Fig. 3.2, where the magnetic field line direction changes at the x-axis forming a neutral sheet. Magnetic field lines are convected with velocity v along the y-direction towards the x-axis. This causes a strong current in z-direction. In this 2D model, the picture extends infinitly into the z-direction. Due to conservation of matter, matter has to flow outwards along the x-axis. Within this model, the current in z-direction has a strength of $J \approx 2B/(\mu_0 l)$ which depends on the magnetic field strength B and the width of the neutral sheet l. For sufficient narrow sheets, ohmic energy losses can become significant despite of the large electrical conductivity of the plasma. The dissipation rate per unit volume can be calculated to $J^2/\sigma = 4B^2/(\sigma\mu_0^2 l^2)$. Due to pressure balance in the region, the outflow along the x-axis has to be at a speed $v_x = B/\sqrt{\mu_0\rho} = v_A$, where ρ is the mass density, and v_A is called the Alfvén speed. Because of matter conservation, matter is convected into the neutral sheet with a velocity of $v = (l/L)v_A$. The reconnection velocity can be calculated to $v_r = \sqrt{4v_A/(\sigma\mu_0 L)}$ which has typical values in the order of years which is significantly shorter than the time-scale from magnetic diffusion but still to large compared to the observed rates [71].

Several extensions of the Sweet and Parker mechanism can predict event faster reconnection rates, e.g. the model by Petschek which includes a standing shock wave [76] or the model by Forbes and Priest which can become as fast as the Alfvén speed [77]. In addition, several effects have to be taken into account like turbulences, instabilities and especially that the model described above is a 2D model.

A model to accelerate particles within the reconnection region is e.g. summarized in [69]. Here a particle spirals along a reconnected magnetic field line and bounces back and forth between two points within the reconnection region caused by of streaming instabilities induced by energetic particles or by magnetic turbulence in the reconnection region. As the recon-

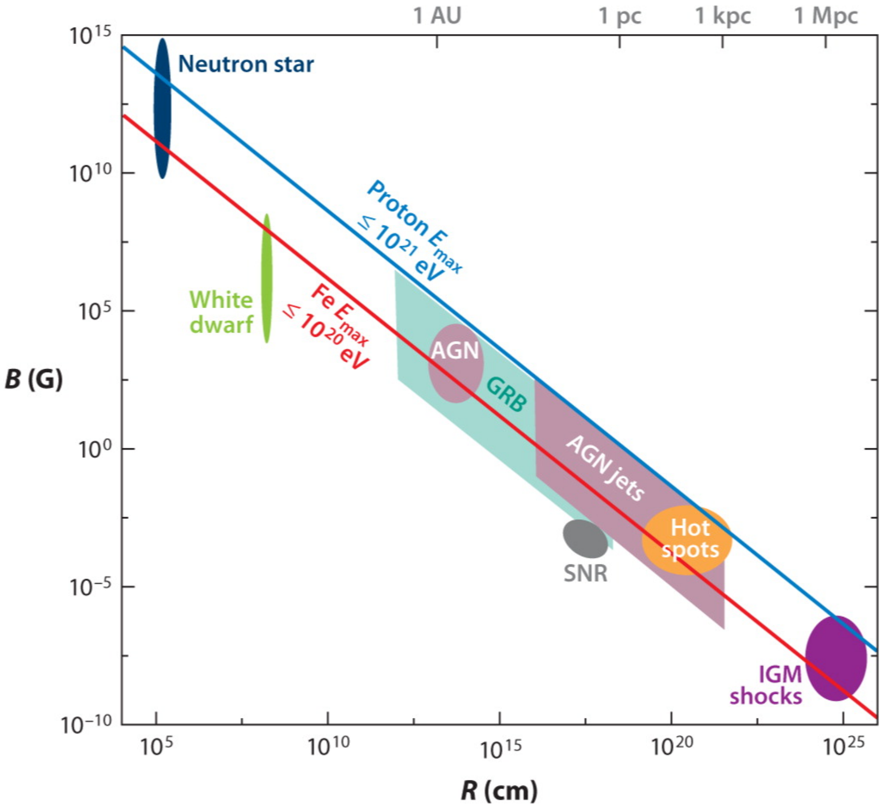

Figure 3.3: Updated Hillas diagram [29]; Size and magnetic field strength for possible source candidates. Above the dark blue lines, protons can be confined to energies above $E_{\max} = 10^{21}$ eV. Above the red line, iron nuclei can be confined to energies above $E_{\max} = 10^{20}$ eV. The most powerful candidate sources are shown with the uncertainties in their parameters. Abbreviations: AGN, active galactic nuclei; GRB gamma-ray bursts; IGM intergalactic medium SNR supernova remnant. From Ref. [78].

nection region moves towards the neutral sheet with velocity v_R the particle can gain energy interactions with the magnetic irregularities within the converging fluxes [69]. This process is very similar to first-order Fermi acceleration in shock fronts. The energy gain per encounter can be calculated to be $\Delta E = \frac{8}{3}\frac{v_R}{c}E_0$ and the probability to remain within the reconnection region is $P = 1 - 4\frac{v_R}{c}$ [69]. From this the probability to find a particle with energy E or larger can be computed to be $N(E) \propto E^{-5/2}$ which gives a similar power law as the Fermi acceleration in shock fronts [69]. For a more in depth review also of numerical simulation we refer to [69].

Maximal acceleration energy

To confine a charged particle in the acceleration region the particle must be bended by magnetic fields. The Larmor-radius r_L, also called gyro-radius, for ultra relativistic charged particles is given by

$$r_L = \frac{E}{ZeB_\perp} \tag{3.14}$$

where E is the energy and Z the charge in units of the elementary charge of the particle, e is the elementary charge and $B_\perp$ is the magnetic field strength perpendicular to the movement of the particle in the acceleration region [27]. Thus, to accelerate particles up to an energy of $E_{\max}$ the radius of the acceleration site has to be $R \leq r_L$ or

$$E_{\max} \sim ZeBR = 1\,\mathrm{EeV} \cdot Z \cdot \left(\frac{B}{1\,\mu\mathrm{G}}\right) \cdot \left(\frac{R}{1\,\mathrm{kpc}}\right) \tag{3.15}$$

This necessary condition is called the *Hillas criterion* which was proposed by [29]. In relativistic outflows acceleration takes place just within R/Γ where Γ is the Lorentz factor of the outflow which has to be taken into account within the Hillas criterion [79].

A common way to illustrate the maximal energy of the acceleration is the Hillas diagram as shown in Figure 3.3. Different potential source classes are plotted depending on their typical size and magnetic field strength. Levels of constant acceleration energy for a specific element class are lines with a slope of -1. For illustration, lines are shown for a proton energy of $E_{\max} = 10^{21}\,\mathrm{eV}$ (dark blue) and iron energy of $E_{\max} = 10^{20}\,\mathrm{eV}$. All sources above these lines are capable to accelerate particles of these energies.

Beside this necessary condition, more stringent requirements come from the relation between the time, which is needed to accelerate a particle to the maximal energy t_{acc} (acceleration time), its escape time t_{esc}, the age of the source or dynamical timescale T_{age} and the time scale of the particles' energy loss t_{loss} during the acceleration process [80].

$$t_{\mathrm{acc}} \leq \min(t_{\mathrm{esc}}, T_{\mathrm{age}}, t_{\mathrm{loss}}) \tag{3.16}$$

These requirements have to be discussed for each source class separately and are take into account for specific source modeling.

3.2 Astrophysical Source Candidates of High-Energy Neutrinos

Neutrinos can be produced in interactions of charged cosmic rays in regions of higher density, e.g. the galactic plain or the Fermi bubbles. Further neutrinos may also be produced in processes involving beyond standard model physics.

Source candidates can be divide into galactic and extra galactic sources. They differ by the maximal acceleration energy. In the following, several candidates are discussed, starting with galactic sources and followed by extra-galactic sources.

3.2.1 Galactic

Supernova Remnants

At the end of a stars lifetime with a mass $M > 8M_\odot$ the star collapses, which is called supernova, releasing a large fraction of the star's mass in an explosion. In this explosion, most energy is released by thermal MeV neutrinos, as measured from SN1987a. In addition, a lot of matter is ejected into the circumstellar medium producing a shell that expands with about $v = 0.01c$ into the interstellar medium and leads to a supersonic shock-front. The shock front collects matter from the surrounding medium and continues until it is decelerated to speeds that are no longer sufficient to accelerate protons. The, typical timescale for deceleration is about 1000 years. In this time, the shock-front is an ideal place for diffuse shock acceleration.

The average power output per galaxy from supernova remnants can be estimated using the ejected material of a supernova of $\sim 10M_\odot$, the velocity of the shell of about 10^7 m/s and the typical rate of supernova of about 2 ± 1 per century. This gives a power output per galaxy of about $W_\mathrm{SN} = 10^{43}$ J/yr. Compared to the average energy density of cosmic rays[1] $W_\mathrm{CR} = 3 \cdot 10^{41}$ J/yr, a few percent of the total Supernova power output are sufficient to provide energy for the acceleration of cosmic-rays.

Based on the ~ 1000 yrs of lifetime of the supernova shock-front, the maximal energy is limited to $E_\mathrm{max} \leq Z \times 300\,\mathrm{TeV}$. This is shown in Figure 3.3. Fermi data indicates that a large fraction of cosmic-rays come from supernovae [43].

At lower energies close-by SNR may dominate the local cosmic-ray flux causing an anisotropy of cosmic-rays seen at Earth. Moreover, unresolved sources lead to a diffuse SN background. In Ref. [81], the diffuse SN background and individual source spectra have been calculated using a non-linear diffusive shock acceleration model.

Pulsars and Pulsar Wind Nebulae

Star-collapse Supernova can result in fast rotating neutron stars, called pulsars. The fast rotation is a result of angular momentum conservation during the Supernova explosion. Due to the small radius of $10 - 20$ km of the resulting neutron star, the rotation frequency is of the order of ~ 1000 Hz. Due to magnetic flux conservation during the collapse, also the magnetic fields in pulsars become very strong and are of the order 10^8 T up to $\sim 10^{12}$ T. In case the rotation and magnetic field axis are not aligned, electrons in the vicinity of the neutron star move on a spiral path along magnetic field lines and emit synchrotron radiation. This radiation results in two radio-beams along the magnetic poles. Due to the fast rotation of the neutron star the beam can be seen as short pulsed radio signal.

Due to the fast rotation of the Pulsar, the magnetic field has to co-rotate with the pulsar to remain closed. In a certain distance the magnetic field would have to move with velocity larger than the speed of light and thus results in magnetic dipole radiation. The fast rotating magnetic fields can be interpreted as large electrical fields, accelerating charged particles in a single iteration. The electrical field strength is in the order of $\sim 10^{16}$ V/m. This scenario has two drawbacks: Firstly, electric fields of this strength may not exist, as charged particles would cause a short circuit. Secondly, this is a one-shot acceleration instead of a stochastic process and does not naturally result in a power-law energy spectrum.

---

[1] The energy density of cosmic rays within our galaxy is given by $W_\mathrm{CR} = \frac{\rho_\mathrm{E} \pi R^2 D}{\tau}$, where $\rho_\mathrm{E} = 1\,\mathrm{eV/cm^3}$ is the energy density of cosmic rays, $D \sim 0.3$ kpc and $R \sim 15$ kpc are the thickness and radius of the galaxy disc $\tau \sim 3 \cdot 10^6$ yr is the averaged age of a cosmic ray before leaving the galaxy.

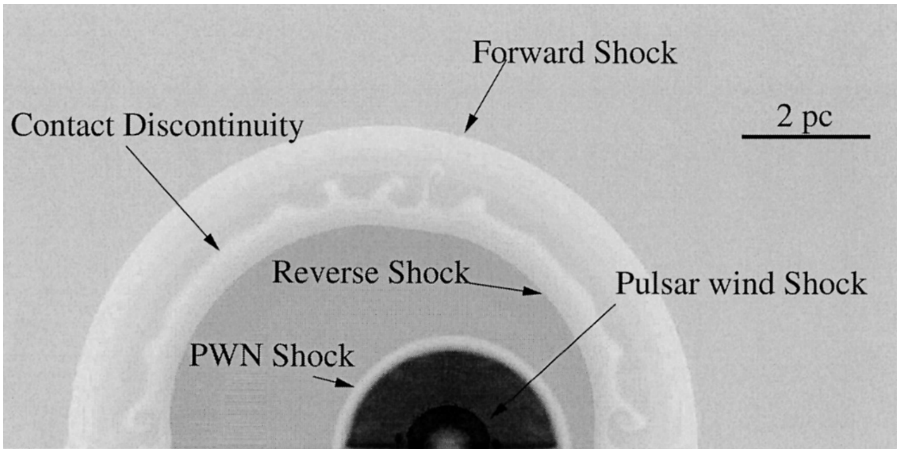

Figure 3.4: Hydrodynamic numerical simulation of the interaction of a Pulsar Wind Nebular and a Supernova Remnant. Logarithmic gray-scale plot of the matter density distribution at an age $t_{\mathrm{snr}} = 1000\,\mathrm{yr}$. The outer region corresponds to interstellar medium. From Ref. [83].

Together with the creation of a pulsar, the supernova leads to a supernova remnant. It is often observed that the pulsar gets a kick velocity relative to the SNR of $\sim 500\,\mathrm{km/s}$ due to initial asymmetries in the supernova explosion [82]. The interaction of the pulsar magnetized wind and the ambient gas leads to a Pulsar Wind Nebulae.

The interaction of the magnetized relativistic wind of pulsars and the surrounding ambient gas leads to a termination shock, a discontinuity in the magnetic field, which is presumably the place where particle acceleration occurs. Hydrodynamic numeric simulations show that there are four different stages in the evolution of a pulsar wind nebular: the supersonic expansion stage, the reverse shock interaction stage, the subsonic expansion stage and the bow shock stage [83]. In Figure 3.4, the density profile from a numerical simulation in the supersonic expansion stage is shown. There are models for specific sources that predict high-energy neutrino-fluxes from these sources [84].

The strongest steady source in TeV gamma-rays is the Crab Nebular which is a PWN from SN 1054 at a distance of 6500 ly, which is also a promising source candidate for cosmic rays acceleration.

Binaries/Microquasars

Galactic X-ray binaries (GXB) with resolvable radio jet are called microquasar. It is assumed that a microquasar consists of a compact object, e.g. neutron star or a black hole, and a giant massive companion star. In the binary system, the compact object accretes matter from the companion star forming an accretion disc. Microquasars exhibit relativistic jets visible in radio and sometimes also in the IR. The ejection can be time dependent and / or periodic, e.g. LSI +61° 303, or steady, e.g. SS433. The observed radiation from microquasars is consistent with non-thermal synchrotron emission of shock-accelerated electrons. The internal shock model for microquasars by Ref. [85] assumes that inhomogeneities in the jets lead to internal shocks which accelerate protons and electrons according to a power-law. The neutrino production in jets can occur by photo-meson interaction. In [86] neutrino fluxes were predicted for sources where sufficient information is available. Also X-ray binaries with unresolved jets may have the same underlying properties.

Diffuse Galactic Emission

A guaranteed flux of astrophysical neutrinos comes from the galactic disc. The flux either originates from the acceleration of cosmic rays or from the interaction of cosmic-rays with the interstellar matter within the galactic plane as described in Section 2.2.1. The detailed models depend on the matter density as well as the cosmic-ray density within the galactic plane and have to reproduce the diffuse gamma-ray emission as measured e.g. by the High Energy Stereoscopic System HESS [87] or Fermi-Large Area Telescope (LAT) [88]. One such model is Ref. [89]. In contrast to previously discussed sources, the diffuse galactic emission is a large-scale structure and can not be detected by as search for point-like sources. The current limit on a diffuse galactic flux by the IceCube collaboration is at the level of the Model from Ref. [89].

The Fermi-LAT telescope identified a pair of highly extended double-lobed gamma-ray bubbles extending $\sim 50^\circ$ above and below the Galactic plane in the energy range of $1-100\,\mathrm{GeV}$, called Fermi Bubbles [90]. There are models that describe the bubbles by pure leptonic or pure hadronic gamma-ray emission. In case of hadronic gamma-ray emission also neutrinos are expected up to energies of $\sim 20\,\mathrm{PeV}$ from these regions.

Dark Matter

About 23% of the energy content of the universe is made up of dark matter [91]. In beyond standard model scenarios there are models in which dark matter particles can self-annihilate or decay into standard model particles [92]. In this dark matter self-annihilation / decay also neutrinos are produced, either directly or via the decay of other heavy standard model particles. A candidate for PeV neutrinos is the decay of super-heavy dark matter [93]. In such a scenario the observation of a neutrino flux and the non observation of a source can be explained. In regions with enhanced dark matter content, the neutrino production is higher such that the neutrino flux features anisotropies that are correlated with the dark matter distributions. Commonly discussed regions of enhanced dark matter are the galactic center, the galactic halo, dwarf galaxies or the center of the sun and the Earth.

3.2.2 Extra-Galactic

Extra galactic sources are assumed to dominate the cosmic ray flux above the ankle. Based on the energy production rate of cosmic rays, Waxman and Bahcall predicted a model independent upper limit on the cumulative neutrino flux from $p\gamma$ dominated sources [94]. In optical thin sources neutrinos are produced by $p\gamma$-interactions of accelerated protons and the radiation field of the source. In these interactions, cosmic rays lose some fraction ϵ of their energy in $p\gamma$-interactions. The muon neutrino (ν_μ and $\bar{\nu}_\mu$ combined) flux $\frac{\mathrm{d}N}{\mathrm{d}E_\nu}$ is related to the cosmic-ray energy production rate by

$$E_\nu^2 \frac{\mathrm{d}N}{\mathrm{d}E_\nu} \approx \frac{1}{4}\epsilon \xi_\mathrm{Z} t_\mathrm{H} \frac{c}{4\pi} E_\mathrm{CR}^2 \frac{\mathrm{d}\dot{N}_\mathrm{CR}}{\mathrm{d}E_\mathrm{CR}} \tag{3.17}$$

Here, t_H is the Hubble-time and ξ_Z is a dimensionless constant that corrects for unresolved high-redshift sources and redshift in neutrino energy. The factor 1/4 comes from the fact that in about half of the interactions neutral pions are produced which do not contribute to the neutrino flux and that half of the energy in the pion decay is transferred to the neutrino. The factor $c/4\pi$ converts from energy density to flux. $E_\mathrm{CR}^2 \frac{\mathrm{d}\dot{N}_\mathrm{CR}}{\mathrm{d}E_\mathrm{CR}} = \dot{\epsilon}_\mathrm{CR}^{[10^{19},10^{20}]}/\ln(10^{21}/10^{19})$ is the energy production rate where $\dot{\epsilon}_\mathrm{CR}^{[10^{19},10^{20}]} \sim 5 \cdot 10^{14}\,\mathrm{erg/Mpc^3/yr}$. The upper bound is reached if $\epsilon = 1$ thus $E_\nu^2 \frac{\mathrm{d}N}{\mathrm{d}E_\nu} \approx 1.5 \times 10^{-8} \xi_\mathrm{z}\,\mathrm{GeV cm^{-2} s^{-1} sr^{-1}}$.

Active Galactic Nuclei

Active Galactic Nuclei (AGN) are very luminous galaxies with a super massive black hole within there center. The super massive black hole accretes surrounding matter and an relativistic, rotating, accretion disc is formed. Due to friction the accretion disc becomes very hot. The gravitational energy from matter accreted by the super massive black hole powers two relativistic jets that are formed perpendicular to the accretion disc. Within the jet a relativistic plasma outflow is formed. Around the accretion disc a dust torus provides even more matter and often obscures the view into the central part of an AGN. In addition, hot and cold gas exist within and outside the dust torus, that can be observed by a continuum radiation with brought and narrow absorption lines and thus is called broad emission line region and narrow emission line region, respectively.

The luminosity of an AGN is given in term of the Eddington-luminosity, which is the maximum isotropic luminosity at which the gravitational force on protons equals the radiation pressure on the electrons:

$$L_\mathrm{Edd} = 1.3 \times 10^{46} \left(\frac{M}{10^8 M_\odot} \right) \frac{\mathrm{erg}}{\mathrm{s}}\,, \tag{3.18}$$

where $M_\odot$ is one solar mass [95]. AGN often outshine their host galaxy and thus appear as quasi-stellar object, in which case they are called Quasars. Beside the luminosity also the host galaxy, the structure of the dust torus and the existence and structure of the jets are characteristic quantities of an AGN. It is assumed that there is a tight connection of the formation of jets and the spin of the super massive black hole.

AGNs are divided in several categories, which are based on historical observational classification. In a unified AGN model most of these classifications can be explained by the orientation of the AGN and its jets to the line of sight to the observer [96]. The different classifications can be seen in Figure 3.5. In case the AGN is seen from the side the central core is obscured by the dust torus and the prominent features are the extended jets, in which case it is called a Radio Galaxy or Seyfert 2 Galaxy. AGNs seen under an angle, so that the broad emission region can be seen, which is within the dust torus, is called a Seyfert 1 Galaxy. In case a Seyfert 1 Galaxy outshines its host galaxy it is called a quaser. In case the line of sight is close to one of the jet axis the AGN is called a blazar. Blazars are some of the most powerful objects and are the dominant component in the high-energy gamma-ray sky. They show very strong time variability even below one day, which puts constrains on the size of the emission region. Blazars are further subdivided into Flat Spectrum Radio Quasars and BL Lac objects which depends on the existence of broad emission lines.

Jets of AGN are ideal acceleration environments for shock acceleration: the relativistic jets contain strong radiation fields and the matter density within the jet is low. Thus, protons interaction with internal or external radiation fields by $p\gamma$ interaction produce secondary particles including high-energy neutrinos. In case a dense cloud traverses the jet neutrinos are also produced by pp interaction, however at lower energies. Within the central region protons also loss energy by photo-hadronic interaction, however photons produced in these processes are absorbed, protons are captured and thus only neutrinos may leave the central region [97]. In these astrophysical beam dump physical processes like synchrotron radiation, synchrotron self absorption, inverse-Compton scattering, pion production and pair production have to be taken into account. There are many models predicting neutrino fluxes available, e.g. [62, 98, 99].

Blazars can be observed in multiple wavelength from radio up to very high-energy gamma rays. The spectral energy distribution (SED) of photons is dominated by two peaked distributions that are assigned to synchrotron radiation at lower energies and inverse-Compton scattering or π^0 decay at higher energies.

Tidal disruption events

A tidal disruption event (TDE) happens when a star comes closer to a super massive black hole than the Roche radius. In this case the tidal force exceeds the gravitational force of the star and matter from the star is accreted by the super massive black hole. Thus, the star is disrupted. The TDEs themselves can be bright for over a year, they brighten for about 50 days then follow a $t^{-5/3}$ power law [101]. The accretion disk often emits X-rays by which they are identified. It is assumed that CR are accelerated in jets from the super massive black hole that may interact via $p\gamma$ [102]. For few TDE candidates, that are typically found with a redshift of 0.02 or more, the Lorentz-factor of jets has been measured to be in the range of $\Gamma \sim 10$ [101]. It is assumed that TDEs happen in the center of galaxies with super massive black holes. It is assumed that TDEs cause galactic nuclei to become active [101]. They can basically be described as transient blazars.

Gamma ray bursts

Gamma ray bursts (GRB) are the most energetic transient gamma-ray events within the universe with a duration of 0.1 to 100 seconds. Within that time range GRBs are so bright that they exceed the total gamma-ray luminosity of the visible universe. GRBs are found to be isotropically distributed in the sky and from optical afterglow the redshift of the host galaxies could be measured. The majority of GRBs has large redshift and thus they are of extra-galactic origin. The short emission duration restricts the size of the emission region to $< 10^{16}$ cm [103]. As a very small emission region would have very high photon densities and

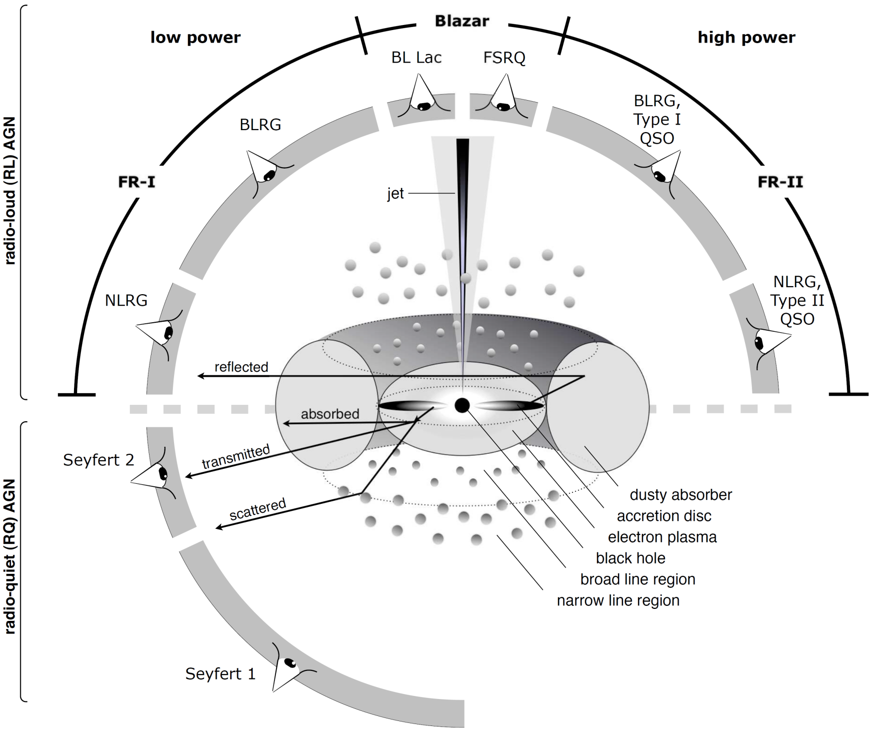

Figure 3.5: Schematic representation of our understanding of the AGN phenomenon in the unified scheme [100]. The type of object we see depends on the viewing angle, whether or not the AGN produces a significant jet emission, and how powerful the central engine is. Note that radio loud objects are generally thought to display symmetric jet emission.

the region would be optical thick, the emission has to be beamed and thus comes from a jet. Typical Lorentz factors are of the order of 100-1000 and thus much larger than for AGNs. The energy emission of a GRB is typically of the order of $\sim 10^{51}$ erg/s, which reduces to $\sim 10^{49}$ erg/s assuming beamed emission. Due to the extreme conditions that are needed to generate the beamed emission, GRBs are promising sources for CR acceleration. Due to the extremely large gamma-ray emission huge photon densities can be assumed and thus $p\gamma$-interactions can produce neutrinos [103].

The distribution of gamma ray burst duration show two distinct distributions, one with duration $<$ 2 seconds and one with longer duration, which are called short and long GRBs, respectively. It is assumed that short GRB are the result of the merger of either two neutron stars or of a neutron star and a black hole. The gravitational energy is converted in two jets similar to AGN but on a very different scale. Long GRBs are assumed to be produced by the collapse of fast-rotating central core of stars with masses exceeding 28 solar masses. The resulting jet breaks through the stars shell.

One prominent model is the fireball model that features the collision of internal shock fronts in the jets. These shocks can both explain the short time variability of GRBs, as well as the spectral shape of the observed gamma-rays. However several models are already constrained by searches for GRBs by IceCube [14, 104].

Starburst Galaxies

Starburst galaxies are galaxies with an unusual high amount of star formation rate. It is assumed that for example merger of galaxies can cause a large amount of star formation and thus a starburst galaxies. Within a starburst galaxy high amount of SN and GRB are expected due to high density gas in the ISM. Due to the high amount of SN and GRB a high production rate of high-energy cosmic-rays is expected. In fact, synchrotron radio emission is routinely observed, confirming the presence of at least relativistic electrons within starburst galaxies. Starburst galaxies are ideal environments for neutrino production due to the enhanced amount of interstellar matter where cosmic rays interact with the interstellar matter producing charged and neutral pions which in turn produce high-energy neutrinos. Due to there high density in interstellar matter they are basically astrophysical calorimeter, also called beam-dumps, for cosmic rays. This calorimetric behavior holds up to $E/Z \leq 10\,\mathrm{PeV}$ for typical starburst galaxies [105]. The energy distribution of cosmic rays within a starburst galaxy may not be compatible with the energy distribution of CR observed on Earth. As starburst galaxies show stronger magnetic fields, it is expected that the position of the knee is shifted to higher energy as both confinement and acceleration depend on the magnetic field strength.

Most starburst galaxies are found with a redshift of ~ 2 with about 10^8 starburst galaxies within the observable universe. This corresponds to about 30 starburst galaxies per square degree. With current pointing of neutrino telescopes, these sources are indistinguishable and the neutrino flux of starburst galaxies shows up as a diffuse component. It was proposed that a lower bound on the cumulative neutrino background from starburst galaxies in the energy range of GeV exists which may be extrapolated to higher energies [105]. However this lower bound is in tension with the observed extra galactic background light in gamma-ray data above 50 GeV which can be described by unresolved blazar contribution leaving only small room for an additional flux from starburst galaxy [106].

Galaxy Clusters

Clusters of galaxies have an enhanced matter content and photonic background than the extra-cluster medium, giving a good target for secondary particle production like neutrinos. Galaxy clusters also have strong magnetic fields, which are the only extra-galactic magnetic fields that can be observed. They are measured by Faraday rotation of linearly polarized emission [107]. The magnetic field strength ranges from few μG on 10 kpc scales up to 10-40 μG on 3-5 kpc scales for cool core clusters [107]. Thus, cosmic rays with energies of $E \leq 5 \times 10^{17}\,\mathrm{eV} \times Z$ can be confined for more than 10^8 years, where Z is the electrical charge number.

Galaxy clusters are the largest gravitationally bound objects in the universe that further grow through accretion of matter and merging with other clusters. By this, they can generate powerful shock waves on Mpc scales, called cosmological shocks or intergalactic magnetic shocks [108]. These shocks may accelerate cosmic rays to highest energies. In addition, galaxy clusters contain many sources which can accelerate cosmic rays to ultra high energies like active galactic nuclei, compact stellar remnants or gamma ray burst.

Cosmogenic Neutrinos

Cosmogenic neutrinos are neutrinos produced within the GZK-process where ultra high energy cosmic rays interact with photons of the CMB or the extra-galactic background light. This process is discussed in Section 2.2. The expected neutrino spectrum shows a two-peaked structure where the low-energy peak at about 10 PeV corresponds to interactions of cosmic rays with the extra-galactic background light and the high energy peak at 1 EeV corresponds to interactions of cosmic rays with the cosmic microwave background [109]. First models are constrained by the non observation of neutrino events with energies above 10 PeV by IceCube [110].

3.2.3 Summary

In this section several neutrino source candidates have been introduced and discussed. A summary of these sources is given in Table 3.1, where acceleration processes, cosmic ray interactions and typical values characterizing the sources are shown. Note, that values and processes given in this table are benchmark values and can vary for specific models.

This thesis focuses on the search for steady, point-like neutrino sources. Therefore, typical values for source extension and time-scale of source variability are given. Sources that emit neutrinos for more than a year can be classified as steady in view of this analysis. Even optimized for point-like neutrino sources the analysis developed within this thesis can also be sensitive to extended sources with an extension slightly larger than the angular resolution.

Source Class	**origin**	**interaction**	**accel. proc.**	**jet (Γ)**	$E_{\mathrm{p,max}}$	**size**	**extension**	**time-scale**
SNR	gal.	pp	shock accel.	—	$10^{15} - 10^{16}$ eV	10-100 pc	$<$ few 0.1 deg	1000 years
Pulsar	gal.	pp	one-shot accel.	—	10^{21}	10 km	point-like	100-1000 years
PWN	gal.	pp	shock accel.	—	10^{15}	10 pc	$<$ few deg	100-1000 years
X-Ray binary Microquasar	gal.	$p\gamma$	shock accel.	10	10^{16} eV	1000 km (accretion disc) ~ 1 pc (jets)	point-like	periodic time-dependent continuous
AGN	ext. gal.	$p\gamma$ (pp)	shock accel.	$10 - 100$	10^{18} eV	$10^{-3} - 10^{-2}$pc (accretion disc) $10 - 10^{2}$ pc (torus) 100 kpc (jets)	point-like	10^{5} years variable
GRB	ext. gal.	$p\gamma$	shock accel.	$100 - 1000$	10^{20} eV	$< 10^{-3}$ pc	point-like	0.1-100 seconds
Starburst Galaxies	ext. gal.	pp	SN / GRB	—	10^{16} eV	10^{2} pc	point-like	10^{6} years
Galaxy Clusters	ext. gal.	pp	AGN	—	10^{21} eV	10^{6} pc	$<$ few deg	10^{9} years
TDE	ext. gal.	$p\gamma$	shock accel.	2-10	10^{20} eV	10^{-6} pc	point-like	1 year
Diffuse Galactic Emission	gal.	pp	—	—	10^{14} eV	10^{3} pc	large scale structure	continuous
GZK	ext. gal.	$p\gamma_{\mathrm{CMB}} \rightarrow \Delta^{+}$	—	—	10^{20} eV	—	diffuse	continuous
Waxman / Bahcal	ext. gal.	$p\gamma$	—	—	—	—	diffuse	continuous
Dark Matter	gal. / ext. gal.	$\chi\chi$-annihilation χ-decay	top-down	—	—	—	point-like large scale structure diffuse	continuous

Table 3.1: Summary of source candidates for high-energy neutrino production. Note that values and processes given in this table are benchmark values and can vary for specific models. The table is divided in two sections: in the first half specific source classes are summarized; the second half give a summary of processes that are not directly linked to a specific source class. References can be found in the text.

3.3 Searches for Neutrino Sources - Current Status

The search for point-like sources of high-energy neutrinos is running for more than 10 years now and many searches have been performed. Basically the analyses can be sub-divided in three main categories: searches for auto-correlations of neutrinos clustering either spatially and / or in time, off-line cross-correlation with other multi-messenger particles and correlations due to real-time and follow-up programs.

3.3.1 Auto-Correlation

In auto-correlation searches for astrophysical neutrinos one searches for spatial clustering of high-energy neutrinos [111]. Beside the spatial information one can also use energy information of the events to suppress the background of atmospheric neutrinos which are much more abundant at lower energies. Using auto-correlation searches, the result is model independent especially it does not depend on any information of other messenger particles. The most generic search is to scan the entire sky, also called all-sky scan, for the existence of a point-like source. These searches are usually performed on samples with a very good pointing and large statistic. These kind of analysis have a long history in ANTARES and IceCube and its predecessor AMANDA [112, 113, 114, 115, 116, 117, 118, 119, 120, 121, 122], however even the latest IceCube search in [13] did not find any significant source.

In addition, special searches e.g. to lower the energy threshold for neutrino sources searches are performed but did also result in a non significant result [10, 123]. Also searches for neutrino source are performed on cascade like neutrino samples that have a worse angular resolution but have less atmospheric background contamination at the same time [17]. Other searches are done for extended sources up to several degree have been tested [112, 121]. In the Southern Hemisphere where IceCube's sensitivity to point-like neutrino sources is reduced due to atmospheric background, the ANTARES detector gives complementary data and also first combined analysis by ANTARES and IceCube for neutrino sources are performed [9]. All these sources are non significant so far. Even if considering only the highest energy events, which show a clear astrophysical component and have a probability to be of astrophysical origin $> 50\%$, do not show significant clustering [5, 59, 124].

Beside the spatial and energy information also time information can be used to suppress the background of atmospheric neutrinos. If in addition to spatial clustering, a clustering in time is searched for, the background of atmospheric neutrinos can largely be reduced. Such short time neutrino clustering signals are e.g. expected from Gamma-Ray Bursts [14, 104] and Fast Radio Bursts [125]. The most general search is an untriggered search for time dependent sources or periodic sources in an all-sky scan but also here no significant excess has been identified[8, 126, 127]. Based on the non-observations, constrains on minute scale transient astrophysical sources could be set [128].

All auto-correlation searches before search for individual point-like or extended sources, however also populations of weak sources could potentially be identified by auto-correlation searches. Two-point auto-correlation analysis and multipole expansion of the neutrino samples have been performed to find hints for sub-threshold sources [129, 130]. Beside these specialized searches for weak sources, also the occurrence of many small p-values in the all-sky scan can point at the existence of many weak sources, which are non significant on their own [13]. Also these searches looking for populations of neutrino sources did not show a positive result so far.

3.3.2 Offline Cross-Correlation using Multi-Messenger Astronomy

The auto-correlation searches suffer from the large number of trials that are made when testing the whole sky. Even a local significant p-value gets non-significant if corrected for the number of individual spots tested. These trials can be reduced by physically-motivated pre-selection of spots for neutrino candidate sources. These pre-selected neutrino candidate, often motivated by high-energy gamma ray measurements, largely enhance the discovery potential. Searches for sources from these pre-selected catalogs however are non significant [13].

Also one can search for large scale structures using template fits, e.g. for the galactic plane [18]. Even a combined analysis of IceCube and ANTARES is not yet significant but seeing a mild excess limiting the galactic plane contribution to the total astrophysical flux to $< 10\%$ [131].

Another way to search for multiple sources from the same class of sources is a stacking analysis. In these analysis the potential signal accumulates while background fluctuations cancel each others and thus increasing the sensitivity. A variety of source classes have been tested so far: galactic PWN, galactic SNR, blazar catalogs, TeV gamma-ray sources observed by Milagro, local starburst galaxies, clusters of galaxies, SNRs and galaxies with super massive black holes [112]; Fermi 2LAC blazars [11], WHSP blazas, 2FHL HBLs, 3LAC FSRQs [132] and Obscured Flat Spectrum Radio AGN [133]. All these sources did not show a positive excess limiting the contribution of these sources to the total astrophysical flux, e.g. for the Fermi 2LAC blazars to 27% assuming an $E^{-2.5}$ spectrum.

In addition, direct correlation analysis with other multi-messengers are performed, e.g. for correlation of high-energy neutrinos and ultra-high-energy cosmic rays (UHECR) [134] and neutrinos with gravitational waves [16, 135, 136]. While the high-energy neutrino and UHECR correlation shows a mild excess, the correlation of neutrinos with gravitational waves is non-significant.

For offline cross-correlation analysis also time information can be taken into account. Thus, searches for neutrino flares in coincidence with blazar flares are performed [137] and analysis for special sources e.g. for the BL Lac object 1ES 1959+650 which exhibited an "orphan flare" in 2002 [138] or for a flare of the Crab Nebular in 2010 [139]. Note that also these searches are non-significant.

3.3.3 Real-Time Programs

Many sources show strong time variability in the electro-magnetic spectrum. Thus, for these sources coincident or timely follow-up observations are crucial, to find neutrinos resulting from short time variable processes. While IceCube has the possibility to look back in archival data this is in general not the case for other instruments, e.g. Imaging Air Cherenkov Telescopes

(IACTs) which have a typical field of view of a few degrees. Thus, prompt follow up observations are only possible if the observatories are notified in time.

IceCube detected a multi-PeV muon-neutrino event with good pointing in 2014, which was the highest observed lepton at that time. Unfortunately, follow-up observation were started only about a year later, because the data processing and selection was done on a yearly basis and a notification was send out about a year after its detection [140]. To avoid this unnecessary latency, the IceCube Collaboration set up an realtime system, checking for spectacular events live at the South Pole [141, 142]. If a spectacular neutrino event is detected a notice is send to the Gamma-ray Coordinated Network (GCN) [143] via the Astrophysical Multi-Messenger Observatory Network (AMON) [144] with a typical delay of about 33 seconds for an initial alert [141]. Beside checking only for single spectacular events, the realtime system also looks for spatial and temporal clustering of neutrino events around known gamma-ray sources with time scales of up to a few weeks [12].

For one of the alerts from the extreme-high energy steam a flaring counter part was found in spatial and temporal coincidence. This alert event called IceCube-170922A and its counter part the blazar TXS 0506+056 are discussed in detail in Sec. 8.3.

In addition, to sending alerts, IceCube has developed a fast response analysis to quickly follow-up sources of interest that exhibits e.g. unusual strong flares in other multi-messengers [145]. The results of the fast response analysis are communicated to the community by an Astronomer's Telegram [146] to extend the overall picture of the source of interest and thus potentially motivate further follow-up observations.

Note that beside the alert event IceCube-170922A and its counter part, the blazar TXS 0506+056, no source shows a significant excess.

Chapter 4

High-Energy Neutrino Detection

Neutrinos are neutral particles and thus they can not be observed directly. Thus, neutrino detection has to rely on the measurement of secondary particles produced in neutrino interactions. In this Chapter the detection principle for current high-energy neutrino detectors is explained. Therefore, neutrino interactions with matter are discussed in Section 4.1 and energy loss of the resulting secondary particles is discussed in Section 4.2. A typical detection principle is the detection of Cherenkov light emitted by secondary particles during propagation through optical transparent media, which is described in Section 4.3. The Chapter closes with a short overview over current high-energy neutrino detectors and other detection principles in Section 4.4 and a discussion of atmospheric neutrinos which are the dominant background for astrophysical neutrino detection in Section 4.5.

4.1 Neutrino Interactions

Neutrino interaction with Standard-Model particles is completely described by the electroweak theory in the Standard Model of particle physics [147], which is given by the general gauge theory of $SU(2)_L \otimes U(1)_Y$. Due to only this weak interactions the cross-section of neutrinos at 100 GeV energy is of the order of $0.1\,\mathrm{pb} = 10^{-41}\,\mathrm{m}^2$ [148], which makes neutrinos an ideal astrophysical messenger particles.

The total and differential cross-section of neutrinos with fermions can be calculated within the framework of the standard model. The cross-section is general given by [149]:

$$\frac{\mathrm{d}\sigma}{\mathrm{d}q^2} = \frac{1}{16\pi} \frac{|\mathcal{M}^2|}{(s-(m_f+m_\nu)^2)(s-(m_f-m_\nu)^2)} \approx \frac{1}{16\pi} \frac{|\mathcal{M}^2|}{(s-m_f^2)^2}\,, \tag{4.1}$$

where $s = (p_\nu + p_f)^2$ is the center of mass energy for a neutrino with momentum p_ν and mass m_ν interacting with a fermion with momentum p_f and mass m_f. $-q^2 = (p_\nu - k_l)$ is the momentum transfer to the outgoing lepton. The approximation in Eq. 4.1 neglects the masses of neutrinos, which are much smaller than the masses of all other fermions [40]. The interaction is fully described by the matrix element $\mathcal{M}$ associated with the interaction.

Interactions of neutrinos can be divided in three types within the $SU(2)_L \otimes U(1)_Y$ gauge theory: interactions mediated by the exchange of a charged W boson, called charged current (CC) interaction, interactions mediated by the exchange of a neutral Z^0 boson, called neutral current (NC) interaction and an interference between the charged current and neutral current amplitudes for $\nu_e + e \rightarrow \nu_e + e$ interactions [149].

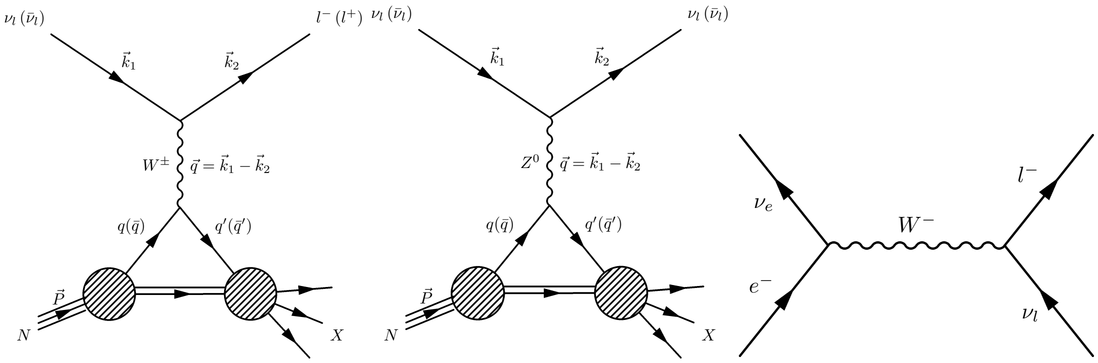

Figure 4.1: Feynman diagram representing (anti-)neutrino interactions mediated by the exchange of a $W^\pm$ boson (left) and a Z^0 boson (middle). The scattering occurs on a quark (q) or anti-quark ($\bar{q}$) from the target nucleon N. The remaining part of the nucleon fragments into a hadronic shower (X). The Feynman diagram on the right shows the resonant production of a W^- boson by neutrino electron interaction in an s-channel diagram.

The Lagrangian of the CC and NC interaction are [149]:

$$\mathcal{L}_{CC} = -\frac{g}{2\sqrt{2}}\left(j^\mu_W W_\mu + j^{\mu,\dagger}_W W^\dagger_\mu\right), \tag{4.2}$$

$$\mathcal{L}_{NC} = -\frac{g}{2\cos\theta_W} j^\mu_Z Z_\mu\,, \tag{4.3}$$

where W_μ and Z_μ are the heavy gauge fields, θ_W is the weak mixing angle and g is the coupling constant. The charged current j^μ_W and neutral current j^μ_Z are given by [149]:

$$j^\mu_W = 2\sum_{\alpha=e,\mu,\tau} \bar{\nu}_{\alpha,L}\gamma^\mu l_{\alpha,L} \tag{4.4}$$

$$j^\mu_Z = 2\sum_{\alpha=e,\mu,\tau} g^\nu_L \bar{\nu}_{\alpha,L}\gamma^\mu \nu_{\alpha,L} + g^f_L \bar{l}_{\alpha,L}\gamma^\mu l_{\alpha,L} + g^f_R \bar{l}_{\alpha,R}\gamma^\mu l_{\alpha,R}\,, \tag{4.5}$$

where $\nu_{\alpha,L(R)}$ is the neutral left-/right-handed leptonic field, $l_{\alpha,L(R)}$ is the charged left-/right-handed leptonic field and g^ν_L, g^f_L, g^f_R are the fermion left- and right-handed couplings.

The interactions can be represented by the Feynman diagrams as shown in Fig. 4.1 (left and middle).

While in principle the interaction is fully described by the electroweak Lagrangian, in practice cross-section calculations have to handle unclear initial state contributions, final state interactions, subtle nuclear corrections and other effects. Thus, a discussion of the cross-section for the relevant energy range is needed.

In Fig. 4.2 measurements of the total neutrino and anti-neutrino per nucleon CC cross section are shown as a function of energy. The predictions of different contributing processes are shown as well. Processes where the neutrino scatters of a nucleon elastically and freeing a nucleon from the target are called quasi-elastic scattering in case of CC interaction and elastic scattering in case of NC [149]. If the neutrino excited a nucleon in the target into a baryonic resonance state which further decays is called resonance production. At high energies, the

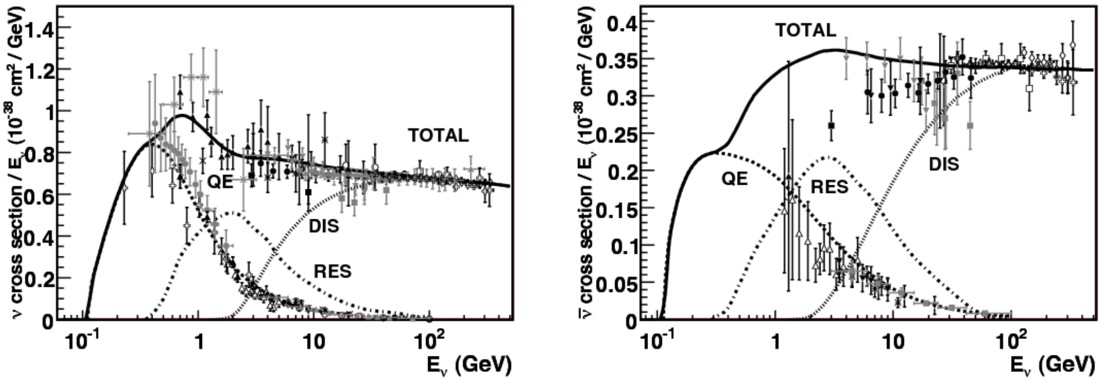

Figure 4.2: Total neutrino (left) and anti-neutrino (right) per nucleon CC cross section divided by neutrino energy as a function of energy. The predictions for the contributing processes of "quasi-elastic scattering" (dashed), "resonance production" (dot-dash) and "deep inelastic scattering" (dotted) are shown. Measurements from several experiments are shown by markers. Plots from [149].

neutrino resolved the inner structure of the nucleon and scatters on individual quarks. In this process called deep inelastic scattering (DIS) a hadronic shower is always induced due to the break up of the nucleon. In this thesis we will cover the energy range from ∼ 100 GeV and above. From Fig. 4.2 one can see that for this energy range only deep inelastic scattering is of practical relevance.

The process of deep inelastic scattering can be described by three dimensionless kinematic variables [149]:

$$Q^2 = (p_\nu - k_\mu)^2 \,, \tag{4.6}$$

$$y = \frac{p_e \cdot q}{p_e \cdot p_\nu} \,, \tag{4.7}$$

$$x = \frac{Q^2}{2 p_e \cdot q} \,, \tag{4.8}$$

which are the 4-momentum transfer Q, the inelasticity y and the Bjorken scaling variable x at leading order. The Bjorken x gives the fraction of energy-momentum of the nucleus that is carried by the interacting fermion. In deep inelastic scattering both CC and NC interactions are possible, described by [149]:

$$\nu_l N \to l^- X \qquad \bar{\nu}_l N \to l^+ X \tag{4.9}$$

$$\nu_l N \to \nu_l X \qquad \bar{\nu}_l N \to \bar{\nu}_l X \tag{4.10}$$

where N is the nucleus, ν_l ($\bar{\nu}_l$) are the (anti-)neutrino of flavor l and l^- and l^+ are the corresponding charged lepton and anti-lepton. The hadronic fragments are labeled as X.

The neutrino and anti-neutrino cross section for DIS can be written as [149]:

$$\frac{\mathrm{d}^2\sigma^{\nu,\bar{\nu}}}{\mathrm{d}x\,\mathrm{d}y} = \frac{G_F^2 M E_\nu}{\pi(1+Q^2/M_{W,Z}^2)^2} \begin{array}{c} \left[\frac{y^2}{2} 2xF_1(x,Q^2) + \left(1 - y - \frac{Mxy}{2E}\right) F_2(x,Q^2)\right. \\ \left. \pm y\left(1 - \frac{y}{2}\right) xF_3(x,Q^2)\right] \end{array} \tag{4.11}$$

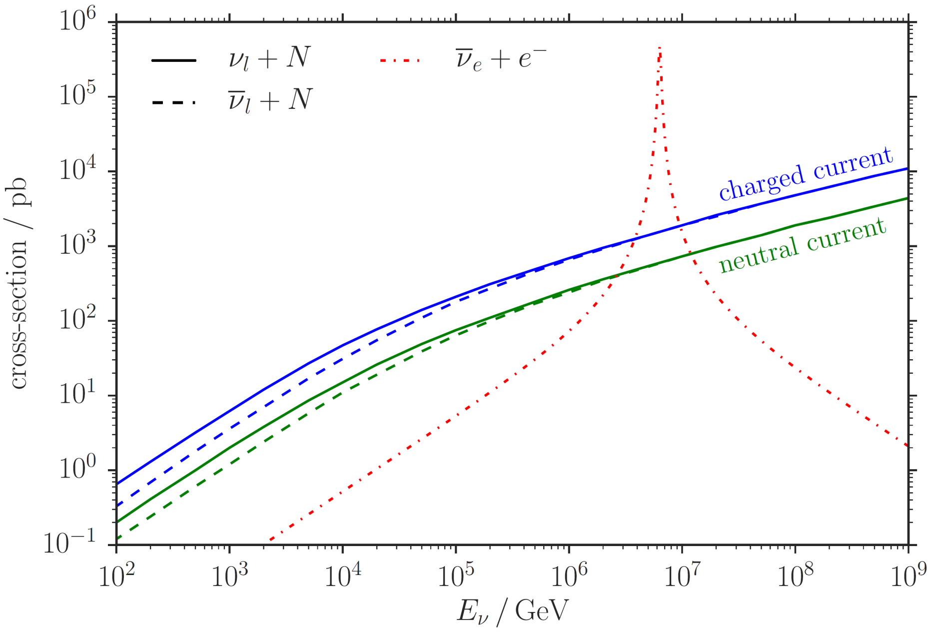

Figure 4.3: Neutrino (solid) and anti-neutrino (dashed) charged current (blue) and neutral current (green) cross section as functions of neutrino energy (data from [148]). The Glashow resonance cross-section (red) is shown in addition. Plot from [150].

where G_F is the Fermi weak coupling constant, $M_{W,Z}$ is the mass of the $W^\pm$ and Z^0 boson, respectively, M is the nucleon mass and the ± sign corresponds to neutrino and anti-neutrino interaction. The functions $F_1(x, Q^2)$, $F_2(x, Q^2)$ and $F_3(x, Q^2)$ are the dimensionless nucleon structure functions that encode the underlying structure of the target [149]. Here we use the neutrino and anti-neutrino charged and neutral current cross-sections from [148] that are calculated in next to leading order perturbative QCD taking modern parton density function fits into account.

Note that cross-sections measurement, especially for small Bjorken-x have to rely on extrapolations because no direct measurements are available. Due to the extrapolation, the uncertainties of neutrino and anti-neutrino cross sections for small Bjorken-x have to be studied carefully [148, 149]. The uncertainties on the neutrino cross-sections at 10^4 GeV center of mass energy are of the order of $\pm 4\%$ and increase to $\pm 14\%$ for center of mass energies of 10^6 GeV [149].

In Fig 4.3, the neutrino and anti-neutrino cross sections are shown for energies from 100 GeV to 1 EeV. The charged current cross section is about a factor 2.4 larger than the neutral current cross section [149]. For energies $< 10^4$ GeV the cross-section increases linearly with neutrino energy, however above the propagator term is no longer dominated by the heavy gauge boson mass and the cross-section is suppressed [149]. In addition, the cross-sections for neutrinos and anti-neutrinos become equal for energies $> 10^6$ GeV as the relevance of sea-quarks and gluons becomes dominant [151]. At the highest energies, the cross-section scales like $\propto E_\nu^{0.363}$ [151].

Neutrino electron interaction is usually sub-dominant due to the small mass of the target electron, however at PeV energies electron anti-neutrinos produce intermediate W-boson in interactions with electrons which is resonant enhanced. The corresponding Feynman diagram is shown in Fig. 4.1 (right). The resonance energy is given by $E_{\text{res}} = M_W^2/2m_e = 6.3\,\text{PeV}$. At the resonance energy the anti-neutrino-electron cross section is about two orders of magnitude larger than neutrino-nucleon cross section as can be seen in Fig. 4.3. The mechanism was already suggested in 1960 by Glashow and is called the Glashow resonance [152].

Due to their low cross-section it is possible to observe neutrinos that went through the Earth. However, this is not true for all energies, because the neutrino cross-section increases with increasing neutrino energy. Thus, the Earth gets intransparent for neutrinos with energies larger than $\sim 100\,\text{TeV}$. The strength of the absorption depends on the Earth density profile, the path length through the Earth, the neutrino flavor and the neutrino energy. The propagation of neutrinos can be simulated using the All Neutrino Interaction Simulation (ANIS) program [153] which uses the Preliminary Reference Earth Model (PREM) as Earth density parametrization. The effect of Earth absorption is illustrated for different neutrino flavor, zenith angles (corresponding to path length through the Earth) as a function of neutrino energy in [154].

For tau neutrinos, the Earth is completely transparent due to the short life time of the tau lepton of $(290.3 \pm 0.5) \cdot 10^{-15}\,\text{s}$ [40, 155]. If a tau neutrino interacts it produces a τ lepton which again decays producing another tau neutrino at lower energies, due to the energy loss in the interactions [155], this process is called tau neutrino regeneration. In addition, tau neutrinos lose energy due to NC interactions. Thus, tau neutrinos are not absorbed by the Earth but their spectrum is shifted to lower energies [155].

The 4-momentum transfer, the inelasticity and the Bjorken-x are not directly accessible by experiments. However, e.g. for interactions with an outgoing muon, theses quantities can be related to experimental observables like the energy E_μ, momentum p_μ and scattering angle θ_μ by:

$$
\begin{aligned}
Q^2 &= -m_\mu^2 + 2E_\nu(E_\mu - p_\mu \cos\theta_\mu)\,, && (4.12)\\
y &= E_{\text{had}}/E_\nu\,, && (4.13)\\
x &= Q^2/(2ME_\nu y)\,. && (4.14)
\end{aligned}
$$

The scattering angle between neutrino and outgoing muon is given by [153],

$$
\cos\theta_\mu = 1 - \frac{xy}{1-y}\frac{m_{\text{N}}}{E_\nu}\,, \qquad (4.15)
$$

where m_N is the mass of the target nucleon. Note that the median scattering angle between a high-energy neutrino and an outgoing muon from a CC interaction scales approximately like $0.7°(E_\nu/\text{TeV})^{-0.7}$ [156, 157]. In Fig. 4.4, the distribution of scattering angles between the initial neutrino direction and the outgoing muon direction from a CC interaction is shown for different neutrino energies (upper left panel). The median and central 90% quantile of the scattering angles are shown as a function of neutrino energy in the upper right panel of Fig. 4.4. At energies of $\sim 10\,\text{TeV}$ the median opening angle is about $0.1°$ and further decreases with higher energies.

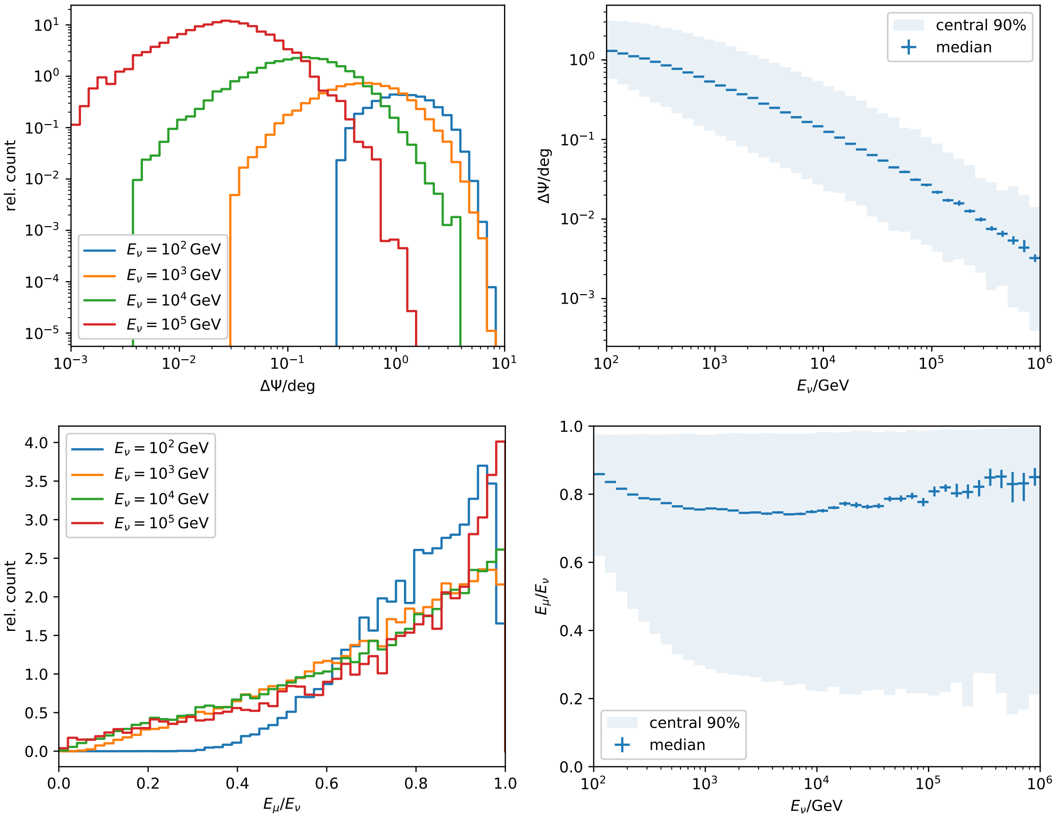

Figure 4.4: Opening angle (upper panels) and energy transfer (lower panels) from a muon neutrino to an outgoing muon in a CC interaction. The left panels show the distribution of the variable for four different neutrino energies while the right panel shows the central 90% quantile and the median as a function of neutrino energy. The distributions are based on the final sample selection as described in Sec. 5.5. Interactions are simulated using the NuGen package based on the ANIS event generator [153].

The distribution of the energy transfer from a muon neutrino to the muon in a CC interaction, $E_\mu/E_\nu = 1 - y$, is shown in Fig. 4.4 (lower left) for different neutrino energies. The central 90% and the median energy transfer as a function of neutrino energy is shown in the lower right panel of Fig. 4.4. Note that in median the muon gets about 80% of the neutrinos energy, however the distribution shows non negligible tails to low energy transfers. Therefore, the muon energy can not be directly related to the neutrino energy and the interpretation always takes into account the neutrino spectrum.

4.2 Energy Loss of Secondary Particles

In the following we are mainly interested in neutrinos with energies > 100 GeV and as discussed in Sec. 4.1, for these interaction deep inelastic scattering is of practical relevance. In these interactions a hadronic cascade is initiated. For CC interactions a charged lepton of the same flavor as the interacting neutrino is produced in addition. The neutrino produced in NC interactions does not leave a signature and escapes unseen. Therefore we discuss the energy loss of electrons, muons and taus as well as of hadronic cascades. Note that in this thesis we focus on muons from CC muon neutrino interaction. Electrons, taus and hadronic cascades are only discussed shortly at the end of this section.

The energy loss of muons can be described by electronic losses and radiative losses. The mean stopping power $\langle -\frac{\mathrm{d}E}{\mathrm{d}X} \rangle$ can be described by [158]:

$$\left\langle -\frac{\mathrm{d}E}{\mathrm{d}X} \right\rangle = a(E) + b(E) \cdot E\,, \tag{4.16}$$

where $a(E)$ describes the electronic energy loss and $b(E) \cdot E$ describes the radiative energy loss.

At low initial energy, charged leptons lose energy by ionization while passing through matter. The energy loss due to ionization and excitation is described by the Bethe-Bloch formula [159, 160] to which several corrections at low energies, a correction due to the polarization of the medium at high energies and a correction for heavy spin 1/2 particles are added [158]. This Bethe-Bloch formula is the contribution $a(E)$ in Eq. 4.16 and is nearly constant at high energies [158].

The radiative energy loss can be split in multiple components resulting from bremsstrahlung, where a photon is radiated by the lepton in the field of a nucleus, pair-production of e^+e^- pairs produced by muon interactions with atomic nucleons (note that muon pair production is about $m_\mu^2/m_e^2 \approx 2 \cdot 10^4$ times smaller and neglected here [161]) and photonuclear interactions by inelastic interactions with atomic nuclei [158]:

$$b \equiv b_{\mathrm{brems}} + b_{\mathrm{pair}} + b_{\mathrm{nucl}}\,. \tag{4.17}$$

The bremsstrahlung and pair-production cross-sections are suppressed at highest energies by the Landau-Pomeranchuk-Migdal and the Ter-Mikaelian effects which describe the multiple scattering of the incident muon and the disturbance of the photon wave function as the photon Compton-scatters off an electron in the medium [40, 161]. The uncertainties on the muon energy loss due to ionization, bremsstrahlung and pair production are at the order of $2-3\%$, while the uncertainties on the photonuclear interactions are about $10-20\%$ [161].

The mean stopping power of a muon traversing ice is shown in Fig. 4.5 as a function of the kinetic energy of the muon. The components from bremsstrahlung, pair-production and photonuclear interactions are shown separately as dotted lines. The components due to ionization and radiative processes are shown separately as dashed lines. The total cross section is shown as a solid line. The energy for which energy loss due to ionization and radiation are equal, is called critical energy which is $E_\mu^{\mathrm{crit}} = 1031\,\mathrm{GeV}$ in ice [162].

Note that before only the mean energy loss is discussed. However, the differential cross-section with respect to energy transfer to the nucleus ν in bremsstrahlung and photonuclear processes scales roughly as $1/\nu$ while for pair-production is scales as ν^{-3} to ν^{-2} [158]. Therefore, "hard" losses by bremsstrahlung and photonuclear interaction are more probable. These processes where a substantial fraction of the energy is transferred to the nucleus, lead to the stochastic nature of the radiative processes. While bremsstrahlung and pair production initiate an electromagnetic cascade along the muon track itself, photonuclear processes initiate

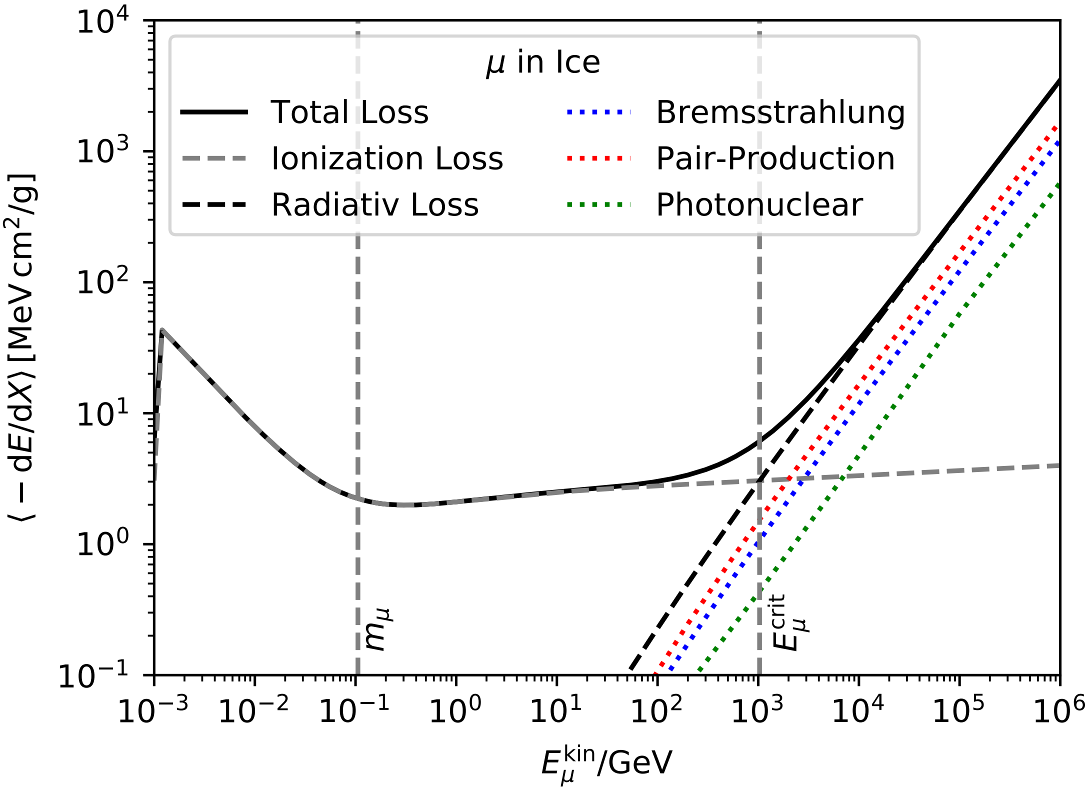

Figure 4.5: Mean energy loss of muons traversing ice as a function of kinetic energy of the muon. The dotted lines show the individual contributions from bremsstrahlung, pair-production and photonuclear processes. The contribution from ionization and radiative processes are shown separately as shaded lines. The total energy loss is shown as solid black line. The vertical dashed lines give the muon rest mass energy and the critical energy for which energy losses of ionization and radiation are equal. Data taken from [158, 162].

a hadronic cascade. At TeV energies and above, the range of a muon is several km of water equivalent (see e.g. Fig. 3 in [163]).

Beside the energy loss due to interactions, the muon can also decay due to its mean lifetime of $\tau_\mu = (2.1969811 \pm 0.0000022) \cdot 10^{-6}\,\mathrm{s}$ [40] into an electron, and two neutrinos with nearly 100% branching fraction [40]. However at high energies the mean decay length is several hundreds of kilometers.

For electrons bremsstrahlung dominates above an energy of about few tens of MeV [40] producing bremsstrahlungs photons. These high-energy photons produce e^+e^- pairs. These electrons and positrons again produce bremsstrahlung as long as they have energies above the critical energy and an electromagnetic cascade evolves. The shower of the electromagnetic cascade has a maximum range of $x = X_0 \cdot (\ln(E/E_C) \pm 0.5)$ where X_0 is the radiation length of the material, E_C is the critical energy and the ± corresponds to an initial photon or electron [40]. The critical energy and radiation length of an electron (positron) and in ice are $E_e^{\text{crit}} = 78.60\,MeV$ (76.50 MeV) and $X_0 = 36.08\,\text{g}\,\text{cm}^{-2}$ [162]. With a specific gravity of $0.9180\,\text{g}\,\text{cm}^{-3}$ [162] the range of an electromagnetic cascade ranges from about 1 m at 1 GeV initial energy to about 7 m at 1 PeV.

In hadronic interactions a cascade similar to electromagnetic cascades are induced. However, in hadronic cascaded mainly pions are produced. While charged pions interact with the medium which keeps the hadronic cascade alive, neutral pions decay into two photons initiating electromagnetic cascades. Thus, a hadronic cascade is always accompanied by a bunch of electromagnetic cascades. Similar to the electromagnetic case a nuclear interaction length can be defined, which is $\lambda_{\text{int}} = 90.77\,\text{cm}$ in ice [162]. Due to its hadronic nature the development of the cascade is much more effected by stochastics.

The mean decay length of a tau lepton with a lifetime of $\tau_\tau = (290.3 \pm 0.5) \cdot 10^{-15}\,\text{s}$ [40] is typically $50\,\text{m}\frac{E_\tau}{\text{PeV}}$. The tau decays with a probability of $(17.39 \pm 0.04)\%$ into a muon and a neutrino and in $(17.82 \pm 0.04)\%$ of all cases into an electron and neutrinos. All other decay channels are semi-leptonic or hadronic and will initiate a hadronic cascade. Due to the short path length of a tau lepton, the secondary electromagnetic/hadronic cascade may coincide with the first hadronic cascade started by the initial neutrino interaction. Only at PeV energies a clear distinction of the two cascades is possible. Muons produced by taus that result from tau neutrino interactions make up a non-vanishing fraction of observable muon.

Energy loss of secondary leptons in IceCube is simulated by the software package PROPOSAL which includes several parametrization for the processes described above [161, 164].

The event topology of neutrino interactions discussed in this section and the previous section is summarized and illustrated in Fig. 4.6. In NC interactions a neutrino along with a hadronic cascade is initiated. Because the neutrino leaves unobserved, due to its low interaction probability, the signature of a NC interaction is a hadronic cascade with a size of a few meters.

For CC interactions the topology of the event depends on the resulting charged lepton. For electron neutrinos, the signature is a hadronic cascade resulting from the DIS interaction and an electromagnetic cascade from the high-energy electron which overlap and have a typical size of a few meters.

The event signature of a muon neutrino consists of an initial hadronic cascade and energy losses along the muon track. The muon track can range over several km for muon energies in the TeV range. When the muon stops or decays, an electro-magnetic cascade is initiated.

The signature of a tau neutrino is in principle similar to a the signature of a muon neutrino however due to the short livetime of the tau lepton the hadronic cascade from the DIS interaction of the neutrino and the electromagnetic or hadronic cascade of the tau decay overlap. Only above energies of PeV the cascades are separated by several tens of meters and can be observed separately.

For a low resolution detector with sensors separated by several tens of meters like IceCube (see Sec. 5.1), the event signatures can be classified in either track-like (CC muon interaction) and cascade-like (NC and CC electron and tau interaction for tau energies lower than PeV).

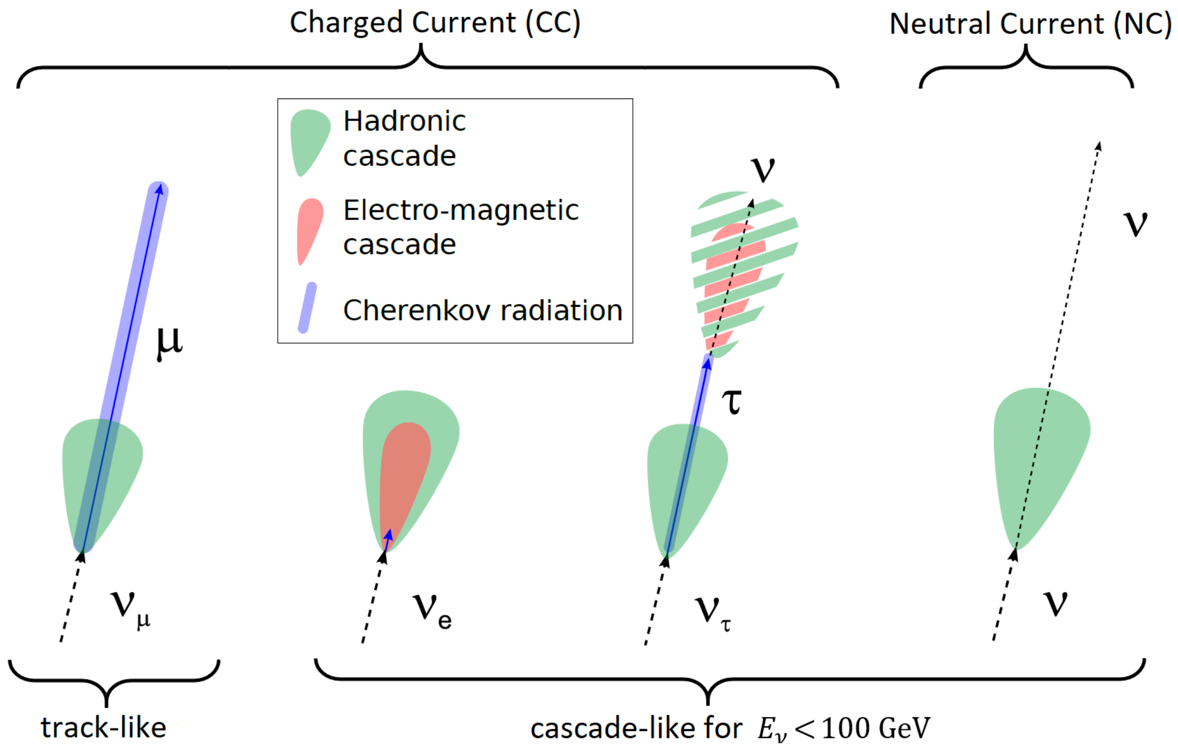

Figure 4.6: Event signature of high energy NC and CC neutrino interactions. The signature is decomposed in hadronic and electromagnetic cascades and Cherenkov radiation from a single long ranging particle. The type of cascade from the tau decay depends on the decay channel of the tau. For energies below a PeV the two cascades of the tau signature overlap and can not be distinguished. For a sparse instrumented detector like IceCube, the events can be classified in track-like and cascade-like. Plot modified from [165] based on [166, 167].

4.3 Cherenkov Effect

Charged particles that propagate at a velocity larger than the local phase velocity of light v_{ph} emit Cherenkov radiation. This radiation is not important for the energy loss of the particles, however in transparent media this light can be used to detect particles going through the medium [40].

The threshold velocity for Cherenkov radiation is $\beta_{th} = 1/n$, where n is the refractive index of the medium [40]. The Cherenkov radiation is emitted at an angle of $\cos\theta_C = \frac{1}{n\beta}$ towards the propagation direction of the particle and thus produces a small conical shell. Note that the Cherenkov cone propagates with the group velocity instead of the phase velocity [168], however for the purpose of IceCube this effect is negligible [169].

The number of photons emitted per unit path length dx by a particle with charge ze and per unit wavelength dλ is given by the Frank-Tamm formula [40, 170]:

$$\frac{\mathrm{d}^2N}{\mathrm{d}\lambda\mathrm{d}x} = \frac{2\pi\alpha z^2}{\lambda^2}\left(1 - \frac{1}{\beta^2 n^2(\lambda)}\right) , \tag{4.18}$$

which scales with λ^{-2}, with wavelength λ. This means, the dominant fraction of photons is emitted at small wavelengths. Note that the index of refraction n can be a function of the photon wavelength λ. To find out the actual number of emitted neutrinos in a wavelength band Eq. 4.18 has to be integrated.

The refractive index of ice is $n \approx 1.33$ at 300 nm [169]. Thus, particles with a velocity larger than $\beta_{\mathrm{th}} = 0.76$ emit Cherenkov radiation and the Cherenkov angle is $\theta_C \approx 41°$. The number of photons emitted by a particle with $z = 1$ and $\beta \approx 1$ in the wavelength range $[300\,\mathrm{nm}, 500\,\mathrm{nm}]$ is $\sim 265.7/\mathrm{cm}$.

Note that a dominant fraction of Cherenkov light is not emitted by the leading muon of a CC muon neutrino interaction but by particles of the secondary cascades. Thus, also the Cherenkov cone is washed out as the particles of secondary cascades are not pointing exactly in the same direction. The photon light yield of electromagnetic cascades is proportional to the initial energy. In contrast, the photon light yield of hadronic cascades is suppressed as e.g. due to neutrinos produced in charged pions decay, which carry away energy unseen [171].

4.4 High-Energy Neutrino Detectors

High-energy neutrino detectors mainly rely on the detection of secondary charged particles by Cherenkov radiation. These detectors are called Cherenkov Neutrino detectors. One of these detectors is the Super-Kamiokande detector which is deployed in an underground cavern consisting of a cylindrical stainless steel tank filled with pure water and photo sensors installed on the detector wall [172]. To increase the rate of high energy neutrinos one has to go to even larger detectors making human made tanks inapplicable. Therefore, natural transparent media have to be used as target material and have to be equipped with light sensors. Detectors of the first generation using the Cherenkov technique in natural media i.e. water and ice were e.g. DUMAND near Hawaii, NT200 in Lake Baikal and AMANDA at the South Pole [173].

The current generation of Cherenkov neutrino telescopes are the ANTARES (Astronomy with a Neutrino Telescope and Abyss environmental RESearch) detector [174] located in the Mediterranean Sea and the IceCube Neutrino Observatory located at the geographic South Pole [175]. The IceCube Neutrino Observatory instrumented about $1\,\mathrm{km}^3$ of clear antarctic ice as detection medium while ANTARES is about 10 times smaller but can observe neutrinos from the Southern Hemisphere through the Earth.

Next generation detectors are either under construction e.g. Baikal-GVD [176] and KM3Net [177] or in preparation e.g. IceCube-Gen2 [178].

Beside the *classical* Cherenkov technique, alternative methods are tested for neutrino detection. One of these methods uses radio signals to detect UHE neutrinos. The radio signal is generated by the Askaryan effect [179], where electromagnetic radiation in the radio range is generated by charged particles propagating through a dielectric medium. This effect is used e.g. by the ARA [180] and the ARIANNA [181] detectors. Another approach uses acoustic detectors to measure acoustical signals generated by UHE neutrino interactions which deposit a large amount of energy in a small region of the detection medium and thus lead to a fast temperature increase accompanied by increased pressure. This technique is tested by the SPATS [182] detector in ice and by the AMADEUS [183] detectors in sea water. At UHE neutrino interaction can also produce cosmic ray air showers. They can be distinguished from normal cosmic ray air showers if the shower direction comes from Earth skimming neutrinos or neutrinos passing through massive mountains. Air shower detectors like the Pierre Auger Observatory [184] and the ANITA [185] balloon experiment search for such UHE neutrinos.

Within this thesis we will use data taken by the IceCube Neutrino Observatory which will be discussed in more depth in Chapter 5. Before, however, we will discuss the dominant background for astrophysical neutrino searches, which are atmospheric muons and neutrinos produced in cosmic ray air showers.

4.5 Atmospheric Muons and Neutrinos from Cosmic Ray Air Showers

The observation of high-energy muon neutrinos in a Cherenkov detector relies on the observed light emitted by the secondary muon track or other secondary particles. However, from the observation of a traversing muons in the detection volume we can not conclude about the primary source of the muon directly. Therefore, all processes that lead to muons in the ice make up a background for searches of point-like sources of astrophysical neutrinos.

High-energy muons or muon neutrinos are produced in cosmic ray induced air showers. Cosmic ray particles constantly bombard the Earth's atmosphere from outer-space inducing interactions with the air's molecules [24]. By this first hadronic interaction of a cosmic ray particle and molecules in the atmosphere a hadronic shower is initiated. Depending on the cosmic ray particle's energy, an extended air shower evolves [24] (see Fig. 4.7).

The particle shower can be decomposed in three main components, a hadronic cascade, an electromagnetic cascade and a muonic component. Within the hadronic interactions multiple hadronic particles are created. The probability and multiplicity of a hadronic interaction

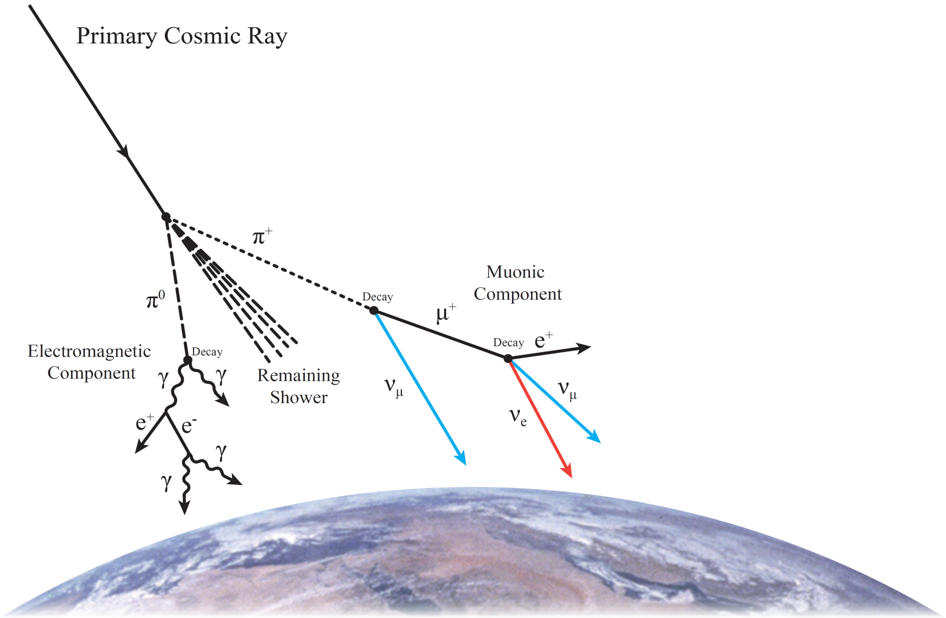

Figure 4.7: Illustration of a cosmic ray air shower. The primary cosmic ray initiates a particle shower including hadrons e.g. charged and neutral pions, electrons and photons which make up the electromagnetic component and muons and neutrinos (blue and red lines) which can lead to a particle flux underground. Plot from [154].

depends on the energy of the particles and on the density of the atmosphere. Thus, the interaction probability is depth and temperature dependent [24, 186]. Interactions inside the upper atmosphere also produce charged and neutral mesons at lower energies than the initial particle. At high energies, interaction is more likely because the hadronic interaction length is smaller than the decay length. However at lower energies, decay becomes more probable. Depending on the density of the traversed atmosphere these particles interact again or they decay due to their short lifetime. Neutral pions decay into two photons in nearly 100% of all cases [40], and they are the seed of an electromagnetic shower similar to the shower discussed in Sec. 4.2. These photons which undergo e^+e^- pair-production and the resulting electrons and positrons emitting bremsstrahlung, drive the electromagnetic component of the shower. Additionally in the upper atmosphere, where the density is quite low, the charged pions and kaons decay. Charged pions decay in $(99.98770 \pm 0.00004)\%$ of all cases and kaons in $(63.55 \pm 0.11)\%$ of all cases into (anti-)muons and (anti-)muon neutrinos [40]. This component is called muonic component.

The particle production yield depends on the traversed amount of matter, which is measured in atmospheric depth. The vertical flux of cosmic rays in the Earth atmosphere is shown in Fig. 4.8 (left) for different components of the shower as a function of atmospheric depth (and altitude). It can be seen that hadrons like protons and neutrons, as well as pions are most abundant in the top of the atmosphere. While the amount of electrons and hadrons quickly decreases with atmospheric depth, the number of muons and muon neutrinos are nearly constant after their production. Muons and muon-neutrinos are typically produced in a height of

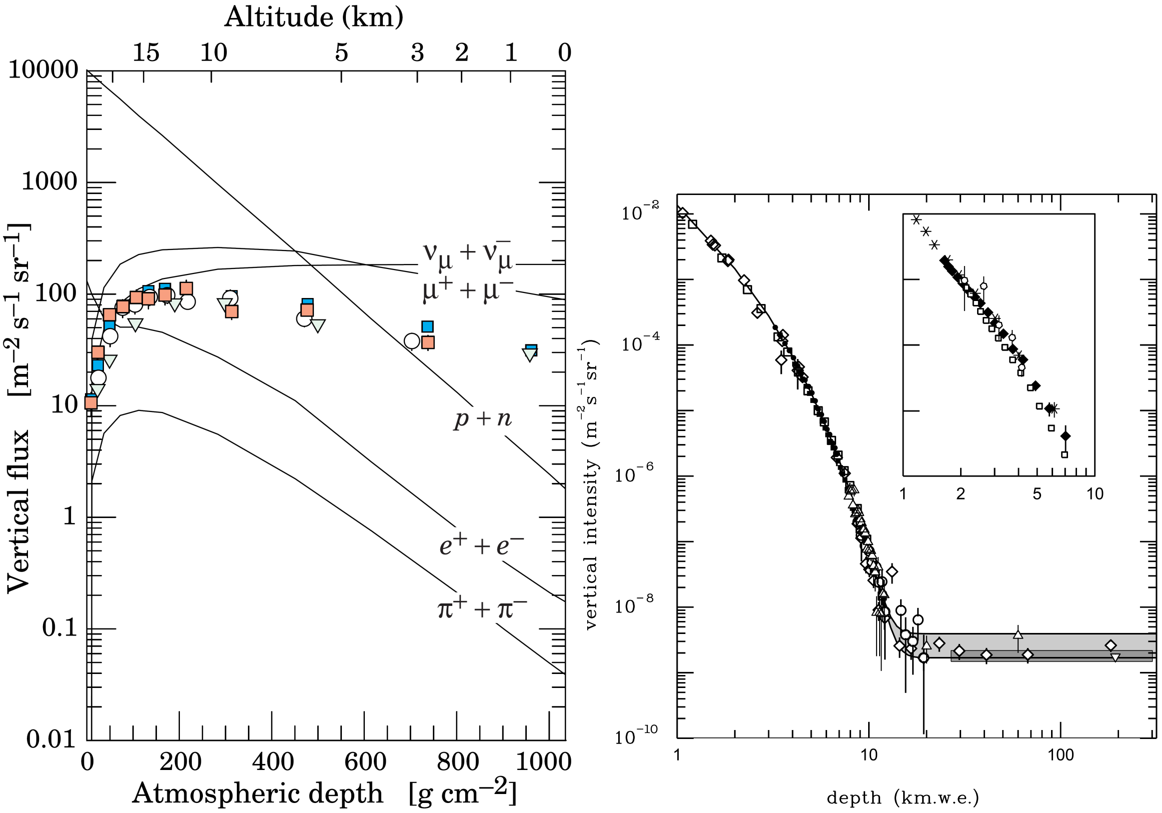

Figure 4.8: Left: Vertical flux of cosmic ray induced particles in the Earth atmosphere with energies above 1 GeV as a function of atmospheric depth and altitude. The contribution from different components is marked as solid lines. Measurements of negative muons with energies above 1 GeV are shown as markers. Right: Vertical muon intensity as a function of depth in km water equivalent (km w.e.). Markers show experimental measurements from different experiments, the gray shaded areas at large depths represent neutrino-induced muons of energy above 2 GeV. The insert shows the data for water and ice. Plots from [40].

$\sim$ 15 km [40] and are the most abundant particles at see level [40]. Due to their long range, muons can also be measured underground. In Fig. 4.8 (right) the vertical muon intensity is shown as a function of depth. The flux is decreasing exponentially and reaches a plateau at a depth of about 10 km w.e.. This plateau is caused by muons from muon-neutrino interactions in the Earth. One can see that at depth of 2 km, the muon flux is on the order of $2 \cdot 10^{-3}\,\mathrm{m^{-2}s^{-1}sr^{-1}}$. At energies much larger than 1 TeV, the energy spectrum of atmospheric muons is about one power steeper than the primary cosmic ray spectrum due to energy losses in interactions [40].

The atmospheric neutrino flux is modeled e.g. by Honda *et al.* taking into account neutrinos from pion and kaon decay [187]. This so called *conventional* atmospheric component assumes an power-law cosmic ray spectrum neglecting the knee [187]. Using more realistic CR spectra and composition from the H3p cosmic ray model by Gaisser [188] the conventional atmospheric neutrino model can be improved [189, 190]. The conventional atmospheric neutrino flux increases towards the horizon because interaction of vertical mesons is less likely.

The atmospheric neutrino flux prediction assumes all neutrinos to be produced in pion and kaon decays, however atmospheric neutrinos from heavy meson decay (charm and bottom quarks) production in CR air showers is expected [191]. Due to their short live time of order 10^{-13} s [40], the mesons decay instantaneously without any interaction. Thus, their energy spectrum has approximately the same shape as the primary CR spectrum with a power law of $\sim E^{-2.7}$. This component is called *prompt* atmospheric neutrino contribution and is expected to start at about 10 TeV and would become dominant at 1 PeV. In contrast to neutrinos from pions and kaons (conventional atmospheric neutrinos) the flux of prompt atmospheric neutrinos is expected to be isotropic up to 10 PeV. A model based on the Gaisser H3p cosmic ray model [188] is given by Enberg *et al.* [191], however this component has not been observed so far and exclusion limits reach down to 0.5 times the model prediction at a 90% CL [5].

Both atmospheric muons and atmospheric neutrinos are the dominant background for searches of sources of the astrophysical neutrino flux. Note that even if the flux from muons and atmospheric neutrinos is much higher than the astrophysical neutrino flux (see Sec. 5.8), atmospheric muons and neutrinos do not lead to a clustering in space. A selection to reduce the contamination of background and a precise parametrization is discussed in Sec. 5.5 and Sec. 5.8.

Chapter 5

IceCube Neutrino Observatory and Experimental Data

Declaration of Pre-released Publications The event selection presented in this chapter have been previously published by the IceCube Collaboration in M. G. Aartsen *et al.* (IceCube Collaboration), "Search for steady point-like sources in the astrophysical muon neutrino flux with 8 years of IceCube data" The European Physical Journal C 79, 234 (2019) and is based on the IceCube Collaboration in M. G. Aartsen et al. (IceCube Collaboration), "Observation and characterization of a cosmic muon neutrino flux from the northern hemisphere using six years of IceCube data," The Astrophysical Journal 833, 3 (2016). The author of this thesis has written the publication "Search for steady point-like sources in the astrophysical muon neutrino flux with 8 years of IceCube data" as a corresponding author. The author contributed to the final reconstruction of the event direction and the estimation of event individual uncertainties. The livetime calculation has been performed by the author of this thesis.

In this Chapter the detector and data sample are introduced. In Sec. 5.1, the detector layout, the detection medium and the light sensors are introduced. The triggering and online filtering is discussed in Sec. 5.2. For modern particle detectors the simulation of the detector response is essential. Therefore, the Monte Carlo Simulation of the detector response is introduced in Sec. 5.3. The event reconstruction and event selection for the final data sample are presented in Sec. 5.4 and Sec. 5.5. The Chapter ends with a characterisation of the sample with respect to key quantities relevant for a point source analysis and a parametrization of the different flux components in Sec. 5.7 and Sec. 5.8.

5.1 Experimental Setup

5.1.1 Detector Layout

The IceCube Neutrino Observatory is a neutrino detector located close to the geographic South Pole and the Amundsen-Scott South Pole Station [175]. The observatory consists of three subdetectors called InIce, DeepCore and IceTop [175, 192]. An illustration of the observatory with its components is shown in Fig. 5.1.

The InIce detector utilizes the deep, clear Antarctic ice as detection medium for high-energy neutrinos. Neutrino detection relies on the optical detection of Cherenkov radiation emitted by secondary particles produced in the neutrino interaction in the surrounding ice or the nearby bedrock. Therefore, 5160 light sensors, called digital optical modules (DOMs), are arranged on 86 strings with 60 DOMs each. For the primary InIce detector, consisting of 78 strings, the DOM-to-DOM distance is 17 m and the strings are arranged in a hexagonal pattern with

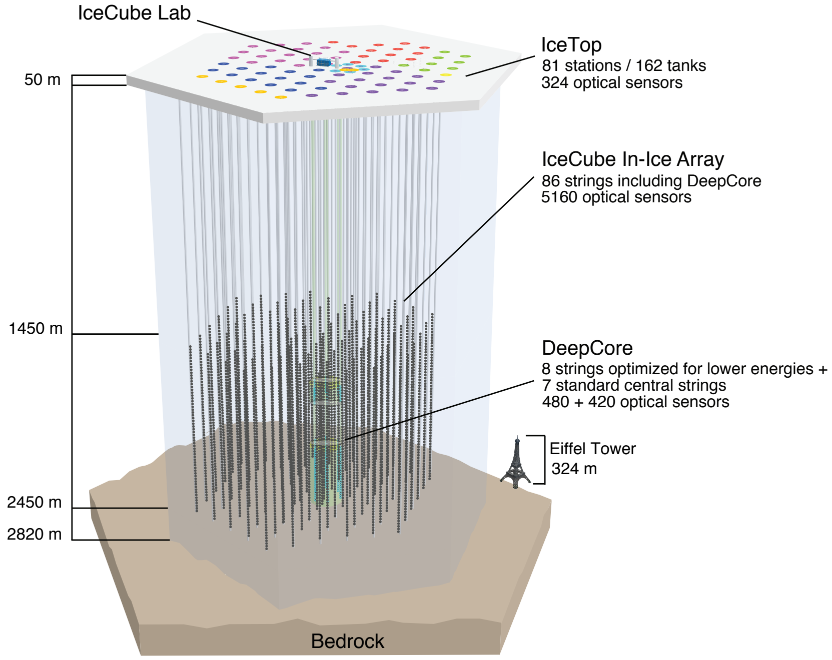

Figure 5.1: The IceCube Neutrino Observatory with the InIce array, its sub-array DeepCore, and the cosmic ray air shower array IceTop. The different string/station colors represent different deployment seasons. The size of the Eiffel Tower is shown for comparison. Plot taken from [192].

a string-to-string spacing of about 125 m [175, 192]. The DOMs are installed at a depth of 1450 m to 2450 m below the surface and the instrumented volume is about 1 km^3 [175, 192]. The geometry was designed to detect neutrinos in the energy range of $\mathcal{O}(TeV)$ to $\mathcal{O}(PeV)$ [175, 192].

The DeepCore detector is a low energy extension of the InIce detector consisting of eight specialized strings equipped with high quantum efficiency DOMs and the central seven strings of the InIce detector. The strings are located in the center of the InIce detector with a average spacing of 72 m [175]. The lower 50 DOMs are arrange with a DOM-to-DOM spacing of 7 m in a depth between 2100 m and 2450 m [175]. The upper 10 DOMs have a DOM-to-DOM spacing of 10 m and are located between 1900 m and 2000 m [175]. The DeepCore detector was designed to lower the energy threshold for neutrino detection to about 10 GeV [175, 193].

The IceCube Neutrino Observatory is completed by the IceTop array which is a surface detector consisting of 81 stations [175, 194]. Each station consists of two ice-filled tanks equipped with two DOMs each. The DOMs detect Cherenkov light emitted by particles traversing the ice within the tank [175, 194]. The IceTop stations are located above the InIce strings and allow to detect the surface footprint of cosmic ray air shower.

The IceCube Laboratory (ICL) located at the surface in the center of the array is the operational building of the experiment, housing a server room [175]. Cables from the subdetectors are routed into the building by two cable towers on either side of the building [175].

The detector construction was finished in 2010, however the detector was operating in partial configuration already during construction. Data taking seasons are labeled by the number of operational strings, e.g. IC59 where 59 strings were operating in the season 2009/2010 and IC79 where 79 strings were operating in the season 2010/2011. The fully operational detector is therefore often labeled as IC86 followed by the year where the data taking started [175].

5.1.2 Properties of the Antarctic Ice at the Geographic South Pole

Crucial for the detection of the Cherenkov light from secondary particles of neutrino interactions is the detection medium and especially its optical properties. Because a cubic kilometer size of the detection volume and high matter density is required, one has to rely on a natural medium, which in the case of IceCube is the clear antarctic ice.

Even though the three kilometer thick ice sheet at the South Pole is among the clearest natural media on Earth, the properties of the ice are location depended and are not perfectly uniform. Due to the environmental influences during the growth of the ice sheet over thousands of years, impurities are enclosed in the compressed snow e.g. dust in the air. Therefore, the ice layers can be associated with different epochs and the impurities depend on the weather conditions in the atmospheres at these epochs. Thus, the properties of the ice are expected to show an age and thus depth dependence [195].

The most relevant parameters are the scattering and absorption lengths $\lambda_{\mathrm{abs/scat}}$ or coefficients $k_{\mathrm{abs/scat}} = \lambda^{-1}_{\mathrm{abs/scat}}$ [196]. Fig. 5.2 shows the effective absorption and scattering coefficients of the bulk-ice as a function of depth. It can be seen that with increased depth, absorption and scattering become weaker. At shallow depth air bubbles in the ice resume an additional target for scattering, however at deeper depth these air bubbles vanish due to the increased pressure [197]. In the depth of about 2000 m to 2100 m a layer with increased

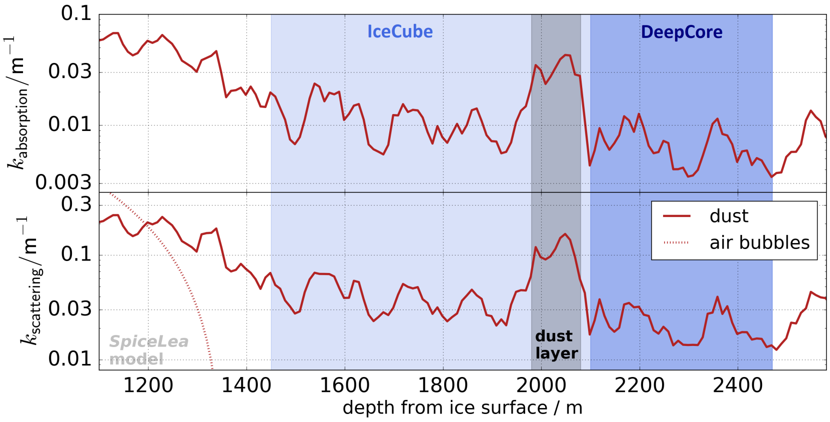

Figure 5.2: Effective absorption (upper panel) and scattering coefficient (lower panel) as a function of depth from the ice surface at a wavelength of 400 nm using the SpiceLea bulk-ice model. The contribution from dust and air bubbles are shown separately. The depth of the IceCube and DeepCore detector are shaded in gray and blue. The *dust layer*, which shows an increased absorption and scattering coefficient is marked in dark gray. Plot from [165].

absorption and scattering is found, called dust-layer.

While the depth dependence is the most prominent effect, more subtle effects influence the ice properties. Due to the landscape of the underlying bedrock, the ice of an ice layers from the same epoch corresponds to different depth in the very deep ice. This effect gets washed-out with increasing height above the bedrock but is still relevant at the depth of the IceCube detector. This effect called *tilt* results in different depth dependence of the ice at different string positions [196].

In addition, the ice is effected by glacial movements, where the ice sheet at the South Pole is moving by about 10 m per year. This flow of ice leads to an anisotropic attenuation of the ice. While the underlying effect for the anisotropy of absorption and scattering properties is not yet fully understood, it is under investigation [196, 198].

The ice properties discussed so far are related to the natural grown ice, called bulk-ice. However, due to the deployment of the IceCube strings, by melting a hole in the ice and letting it refreeze again, the ice within the drill holes is of different nature. This hole ice leads to further complications in the description of optical light detection [198].

For the scope of this thesis we will use the *SPICE LEA* ice model [198], which incorporates depth dependent effective absorption and scattering parameters, the tilt and the anisotropic attenuation effect, if not stated otherwise.

5.1.3 Digital Optical Modules and On-Board DAQ

The fundamental light sensor and data acquisition system is the *digital optical module* (DOM, see Fig. 5.3). The main component is a 10 inch down-ward looking photomultiplier tube (PMT) [199] along with on-board read-out electronics. A mu-metal grid shields the PMT from the ambient South Pole magnetic field [175]. The PMT is surrounded by a spherical

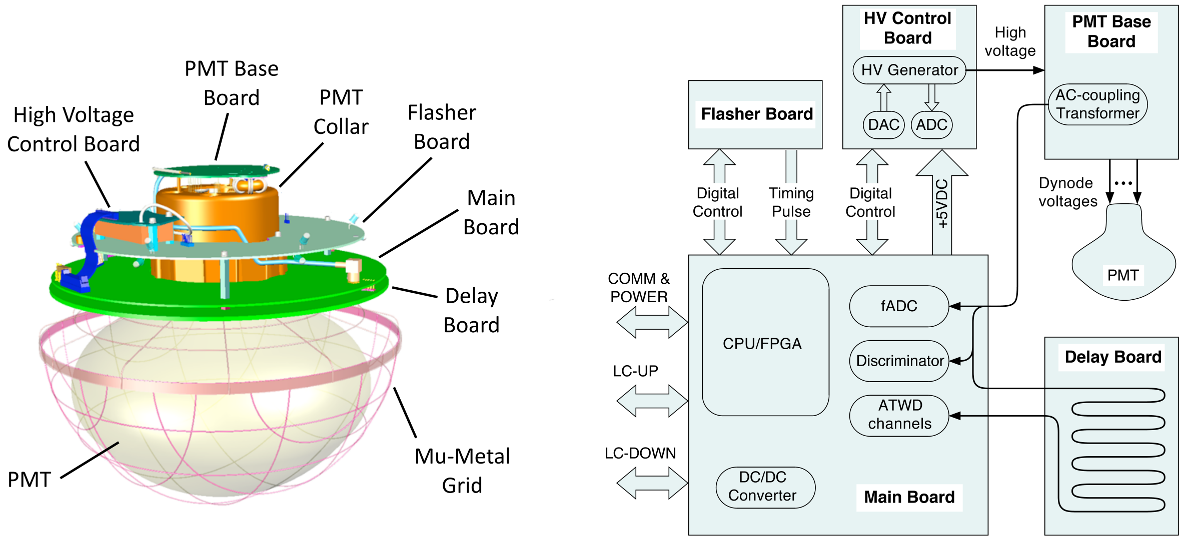

Figure 5.3: Components of the DOM, showing mechanical layout (left) and functional connections (right). Plot from [175].

glass pressure vessel to protect the inside against the high pressure of 2.6 km-equivalent water column [175]. A penetrator assembly allows to connect the DOM with cables needed for power supply and data communication. The PMT is coupled to the glass housing using optical gel.

The PMT is sensitive in the wavelength range from 300 nm to 650 nm with an optical quantum efficiency of 25% at 390 nm [199]. The dark rate at a temperature of $-40°$C is about 500 Hz. The width of a waveform convolved with the transit-time spread is about 3.2 ns [199]. At a gain of 10^7, the response is linear to 10% up to 50 mA corresponding to 31 PE/ns [199]. The signal saturates at about 150 mA [175, 199].

The on-board electronic consist of a main-board, a high voltage control board to power the PMT, a PMT base, a delay board used to delay the analog signal until a trigger decision is made and a flasher board equipped with LEDs for calibration purpose [175, 200].

The PMT voltage is compared to a discriminator threshold corresponding the voltage amplitude of 0.25 photon electrons pulse (PE) [175]. We define a *photon electron* (PE) as the voltage amplitude of the peak in a single photon pulse distribution. To digitize the full waveform of an event, the signal is routed through the delay board, which delays the signal by about 75 ns [175], to wait until the trigger decission is made. The PMT waveform can be digitized by two *analog transient waveform digitizer* (ATWD) [200] chips, each with three channel connected to three different amplifiers with different gains to cover the full dynamic range of the PMT and a continuously sampling fast-ADC (fADC) with 40 Msps (Mega samples per second) [175]. The ATWD can sample the first 427 ns of a waveform with a resolution of 300 Msps [175]. Two ATWD chips are implemented such that one ATWD can digitize the waveform while the other one can be read out, which reduced the dead-time of the DOM. The digitized waveform is transferred to SDRAM lookback memory resulting in a hit record and can be send to the surface on request. The main board can communicate with the nearest and next-to-nearest neighboring DOMs to check if they also launched within a $\pm 1\mu$s leading to a local coincidence [175]. A launch is defined as a trigger threshold crossing. In case of a local coincidence, the full ATWD sampled waveform is send to the surface to ICL, otherwise only a time stamp and a charge summary are send. Once sent to the surface the trigger criteria of the detector are applied, as described in Sec. 5.2.

The flasher board of the DOM is equipped with 12 405 nm LEDs which are pointing into different directions into the surrounding ice [175]. The LED can produce light pulses for calibration purpose of up to 70 ns pulse-length and up to 10^{10} photons [175].

Each DOM has the capability to perform calibration routines, called DOMCal, which provide calibration constants to translate the DOM waveform into physical units [175]. Due to the time stability of these calibration constants, this routine is run once a year [175]. In addition, a global time calibration of the full array is achieved by the RAPCal procedure which runs during data-taking [175]. The absolute optical efficiency of the DOMs has been measured in the laboratory prior to deployment [175, 199]. In addition, in-situ measurements using Cherenkov light from low-energy muons in the ice are used to determine effects such as the cable shadowing the DOM and the refrozen hole ice [175].

5.2 Triggering and Filtering

The data acquisition system of the full detector is located in the ICL, where the data of the individual DOMs are received. The first step of the data acquisition however is performed on the DOMs itself using the local coincidence decision described in Sec. 5.1.3. The hits are classified as hard local coincidences (HLC hits) in case the local coincidence criteria are met and otherwise are classified as soft local coincidences (SLC hits) [175].

The hits are read out by special computers of the data acquisition system located in the ICL. Global trigger conditions are checked on the full array based on the HLC hits. Most of the triggers are *Simple Multiplicity Triggers* (SMT) requiring a certain number of HLC hits within a given time window, e.g. the SMT-8 trigger requires 8 HLC hits within the in-ice array within $5\,\mu$s [175]. In addition, volume triggers checking for four HLC hits within a cylinder and single string triggers locking for multiple HLC hits along a single string are applied [175]. Moreover specialized triggers for slow moving particles and fixed rate triggers are implemented [175].

All SLC and HLC hits within a time window starting $-4\,\mu$s before and ending $6\,\mu$s after the fulfilled trigger condition are combined into an *event*. If multiple trigger are satisfied the read out is combined to a single event. The seasonal varying event rate of 2.5 kHz to 2.9 kHz leads to a data rate of about 1TB/day [175].

To reduce the event rate initial reconstructions and filtering are run at a server farm in the ICL, called Processing and Filtering (PnF) [175]. The processing and filtering step includes calibration of the raw DOM response, extraction of monitoring quantities and generation of data files and meta information [175]. In addition, a separate realtime system is running, looking for spectacular events of probable astrophysical origin and generating realtime alerts [141]. The digitized waveforms are deconvoluted using the best knowledge of the detector response to extract photon induced pulses [201]. The photon response of an event is saved as a pulse map.

The experimental data are compressed into the Super Data Storage and Transfer format (SuperDST) to reduce the data size [202]. About 25 different filters including initial reconstructions of energy and direction are running to select events that are transferred over satellite to the data center in Madison, Wisconsin, USA using a dedicated system for data movement called JADE [175]. The filters are motivated to select events useful for physics analysis. Due to the limited computational power and processing time at the South Pole, only fast reconstructions are performed online [175, 203, 204].

The data taking is organized in runs which have a typical length of 8 h. The trigger and filter conditions are reviewed each year by the IceCube Collaboration however only small changes are typically applied [205].

The events used in this thesis have to fulfill the SMT-8 trigger and are based on the muon and extremely-high-energy filters [154, 205]. Due to the yearly updated trigger and filter requirements, the filters slightly changed from year to year [154, 205, 206, 207, 208, 209, 210, 211, 212, 213].

The extreme-high-energy (EHE) filter for the complete detector IC86, requires a total charge Q_{tot} of more than 1000 photo-electrons (PE). The muon filter requires the following criteria

$$\begin{aligned} \tfrac{\log \mathcal{L}}{n_{\text{DOMs}}-3} &\leq 8.9 \quad \text{if} \quad -1.0 \leq \cos\theta < +0.2\,, \\ Q_{\text{tot}} &> 3.9\cos\theta + 0.65 \quad \text{if} \quad +0.2 \leq \cos\theta < +0.5\,, \\ Q_{\text{tot}} &> 0.6\cos\theta + 2.30 \quad \text{if} \quad +0.5 \leq \cos\theta < +1.0\,. \end{aligned} \tag{5.1}$$

Here n_{DOMs} is the number of hit DOMs and Q_{tot} is the total charge of the event. $\mathcal{L}$ is the likelihood and θ is the reconstructed zenith angle of the angular reconstruction. Due to the filter selection the data rate is reduced substantially.

5.3 Monte-Carlo Simulation of Detector Response

Simulations of the expected detector response are essential for physics analyses of particle detectors and are essential for the interpretation of the experimental data. The required statistics of simulated data should substantially exceed the experimental data statistics to minimize statistical uncertainties and should cover the full parameter space of systematic uncertainties. Therefore, the response of the IceCube detector is simulated.

The simulation consists of four main steps:

- **Generation** of the primary particle. Depending on the type of signal, events are generated with different programs. To generate high energy events a program called `NuGen` is used which is based on the "All Neutrino Interaction Simulation" ANIS [153]. The neutrinos events are generated at the Earth's surface and propagated through the Earth taking into account neutrino absorption in the Earth, neutral-current regeneration and tau regeneration. The Earth density is modeled by the Preliminary Earth Model (PREM) [214]. Neutrino oscillations are not simulated and the event is forced to interact near the detector which can be accounted for by weighting the events. The program `Genie` [215] is used to generate low energy events. Background events of atmospheric muons and neutrinos can be generated by the software package "Cosmic Ray Simulation for KAscade", `CORSIKA` [216] where typically the five elements Hydrogen, Helium, Nitrogen, Aluminium and Iron are simulated as representatives for the groups of nuclei H, He, CNO, Mg-Si and Mn-Fe [31]. Special datasets for systematic studies could generate events with `muongun` [217] where special properties of the primary particle could be specified.

- **Lepton Propagation** The primary particle causes a shower with many secondary charged particles. These particles are propagated through the detector while energy losses and sub cascades are simulated. The propagation is done with the software package `PROPOSAL` [161, 164] which is based on `MMC` [218]. High-energy cascades can be simulated using the CMC tool [219] including the LPM effect [220, 221] and muon production in hadronic cascades.

- **Photon Propagation** of the emitted Cherenkov light. Charged particles radiate light in transparent dielectric material [222, 223]. The emitted light is propagated as individual photons. The simulation of the propagation of these photons through the antarctic ice takes into account the local ice properties, like absorption and scattering [196]. For direct propagation "Photon Propagation Code" `PPC` [196, 224] or `CLSIM` [225] are used. These programs are able to take advantage of GPUs to speed up the simulation. The light propagation depends on the local ice properties given by an ice model. Over the years the modeling of the ice improved thus for different detector configurations always the best ice model known at that time was used. Beside direct propagation lookup tables of direct light propagation for very high energy cascades are needed [226, 227].

- **Detector Simulation** After photons have been propagated through the ice their detection by optical modules is simulated by a series of IceCube specific simulation codes. These include conversion of the photons in the light detectors by `PMTResponseSimulator` and `DomLauncher`, simulation of noise due to radioactivity and afterpulses by `TopSimulator`, `PolyPlopia` and `Vuvuzela`, the use of `CoincidenceAfterProcessing` to simulate coincident events and the simulation of electronic trigger conditions with `TriggerSim`.

The external programs and collaboration internal detector simulations are implemented into a software framework called `IceTray` [228] that is written in `C++` and has wrapper functions for `python`.

Using these programs datasets are generated for all kind of neutrino interactions as well as for atmospheric muons from cosmic ray air showers. The events are generated distributed over the full sky in the energy range from 10 GeV to 10^9 GeV. Special datasets with varied parameters corresponding to systematic uncertainties are also generated.

5.4 Event Reconstruction

The search for sources of astrophysical high-energy neutrinos is based on the events direction and energy. Therefore, the direction and energy have to be reconstructed based on the detected light, represented by a pulse map of the events.

Several reconstruction algorithms exists aiming to reconstruct the direction, energy and angular resolution. These algorithms differ in accuracy, complexity and computing time. It is computationally not possible to apply the best performing reconstruction to all events and several algorithms need a good seed to be successful. Therefore, fast algorithms have to be applied first to all events and a pre-selection has to be applied before the best performing reconstruction can be applied. In the following we will discuss reconstruction algorithms for the event's direction (Sec. 5.4.1), the event's angular resolution (Sec. 5.4.2) and the event's energy (Sec. 5.4.3). We focus on the reconstruction of track-like events as these events are used within this thesis.

5.4.1 Event Direction

LineFit - A First-Guess Direction

A first guess direction can be calculated using the LineFit algorithm [204, 229]. Assuming a particle traversing the detector with speed $\vec{v}$ and neglecting the emission profile of the Cherenkov cone, the hypothesis can be described by a plane wave. The algorithm calculates the least squared distance of all hits to the track hypothesis which is given by:

$$\min_{\vec{x_0},\vec{v}} \sum_{i=1}^{N} \phi(\|\vec{x_i} - (\vec{x_0} + \vec{v}t_i)\|_2) \tag{5.2}$$

with $\|\vec{x_i} - (\vec{x_0} + \vec{v}t_i)\|_2$ being the distance between the photon hit at time t_i at DOM position $\vec{x_i}$ to the track hypothesis and N is the number of hits. $\phi(\rho) = \rho^2$ gives the squared distance. The result for $\vec{v}$ and $\vec{x_0}$ can be calculated analytically.

This LineFit algorithm suffers from hits from scatted photons, which arrive delayed compared to the hypothesis expectation, and from noise hits which have strong influence if they are far away from the track hypothesis, due to the least square method. To overcome this drawbacks an improved LineFit algorithm is defined, including a cleaning to remove scattered hits can be introduced by cutting out hits that have neighbouring hits within a radius r that arrived early than a time difference t [203]. The cleaning parameters have been optimized for muon neutrinos and are $r = 156\,\mathrm{m}$, $t = 778\,\mathrm{ns}$ [203]. To reduce the influence of noise hits a Huber penalty factor can be introduced, thus that ϕ in Eq. 5.2 becomes [203]:

$$\phi(\rho) \equiv \begin{cases} \rho^2 & \text{if } \rho < \mu \\ \mu(2\rho - \mu) & \text{if } \rho \leq \mu \end{cases} . \tag{5.3}$$

Here hits further away from the track than $\mu = 153\,\mathrm{m}$, which has been calibrated to muon simulation, are accounted for linearly instead of quadratic and thus the influence of noise hits is reduced [203]. The improved LineFit improved the median angular resolution by 57.6% compared to the default LineFit, however it has to be minimized numerically [203].

SPE and MPE - Directional Likelihood Reconstruction

Using the likelihood formulation it is possible to reconstruct the event parameters $\vec{a}$ for a given set of observed experimental data $\vec{x}$. For the track reconstruction the experimentally observed

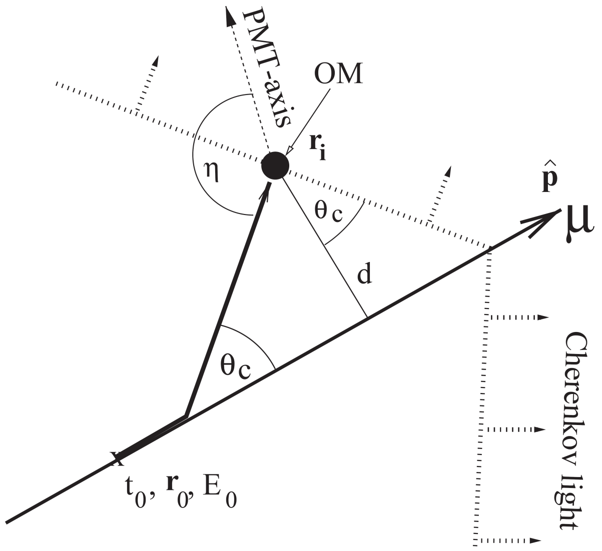

Figure 5.4: Definition of quantities of the geometrically expected arrival time t_{geo} (see Eq. 5.4) from a Cherenkov light front emitted by a relativistic muon. Plot from [204].

data are the arrival times of hits t_i and the observed charge q_i at DOM position $\vec{r}_i$. The parameters particle propagating at speed $\beta = 1$ on a straight infinite track are the direction $\hat{\vec{p}}(\theta, \phi)$ and the position $\vec{r}_0$ at which the particle has been at time t_0. The geometrical expected arrival time assuming Cherenkov photons are emitted and form a cone is given by (see Fig. 5.4 for definition and illustration) [204]:

$$t_{\text{geo}} = t_0 + \frac{\vec{p} \cdot (\vec{r}_i - \vec{r}_0) + d \tan \theta_{\text{C}}}{c_{\text{vac}}} , \tag{5.4}$$

where c_{vac} is the vacuum speed of light. We can write down the likelihood to observe the residual time $t_{\text{res},i} \equiv t_i - t_{\text{geo}}(\vec{r}_i)$ [204]:

$$\mathcal{L}(\vec{r}_0, t_0, \hat{\vec{p}}) = \prod_{i=0}^{N_{\text{hits}}} p_1(t_{\text{res},i} | \vec{r}_0, t_0, \hat{\vec{p}}) . \tag{5.5}$$

Here p_1 is the probability density function of a *single* photon to produce a hit with a residual time $t_{\text{res},i}$. In an ideal world, the $p_1(t_{\text{res}})$ would be a delta function but multiple effects lead to a broadened and distorted distribution, e.g. the PMT jitter, noise and scattering in the ice [204]. The product in Eq. 5.5 runs over all hits, thus that DOMs can contribute multiple times to the likelihood. This likelihood is called *single photon electron* (SPE) likelihood [204]. Because the first photon is typically less scattered than other photons its time residual is expected to be closer to zero and be much more constraining than others. If one only uses the first photon one has to take into account that it is the first out of N photons. This can be achieved by [204]:

$$p_N(t_{\text{res}}) = N p_1(t_{\text{res}})(1 - P_1(t_{\text{res}}))^{(N-1)} \tag{5.6}$$

where P_1 is the cumulative distribution corresponding to the single photon PDF. This PDF is called the *multi-photon-electron* (MPE) probability density function.

The single photon PDF p_1 is determined by Monte Carlo simulations of light propagating through the ice. Therefore, light sources with different orientations and positions are simulated and the number and timing of the Cherenkov photons is saved in multi dimensional histograms. To reduce statistical fluctuations caused by the high number of bins, a smoothing spline representation of these histograms is saved. These spline representations of lookup tables are produced for infinite muon tracks continuously emitting Cherenkov light (without stochastic losses) [230], for averaged energy loss of high energy muons excluding continuous emission [230] and for electromagnetic cascades [231].

A simplified analytic form of the PDF was motivated by Pandel [232] which is given by [204]:

$$p(t_{\mathrm{res}}, d) = \frac{1}{N(d_{\mathrm{eff}})} \frac{\tau^{-d_{\mathrm{eff}}/\lambda} \times t_{\mathrm{res}}^{d_{\mathrm{eff}}/\lambda - 1}}{\Gamma(d_{\mathrm{eff}}/\lambda)} \exp\left(-t_{\mathrm{res}}\left(\frac{1}{\tau} + \frac{c_{\mathrm{vac}}/n}{\lambda_a}\right) - \frac{d_{\mathrm{eff}}}{\lambda_a}\right) \tag{5.7}$$

where λ_a is the absorption length, d_{eff} is the effective distance between track and receiver, c_{vac}/n is the speed of light in ice, N is a normalization factor and τ and λ are phenomenological parameters. This parametrization allows a faster computation, however results in a slightly reduced angular resolution.

It was empirically found that using only the arrival time of the first photon performs better especially at high energies than using the information of all photons [230, 233]. The quality of the reconstruction can be improved by several modifications: Hit-cleaning, accurate noise modelling, convolution of the MPE likelihood with a Gaussian and an energy dependent variation of the Gaussian convolution width and an energy dependent blend between the SPE and MPE likelihood [230, 233]. The reconstruction using the MPE likelihood, the PDF constructed from the smoothing spline representation and the before mentioned modifications is called *SplineMPE-Max* where it is called *SplineMPE* without the additional modifications.

The point spread function which gives the opening angle between the true direction and the reconstructed direction is a measure of the precision of the reconstruction algorithm. The point spread function and median angular resolution is discussed in Sec. 5.7.

MuEX Angular

In the MuEX algorithm, the MPE likelihood using the Pandel parametrization of the single photon PDF with additional depth-dependent ice properties is applied to bootstrapped pulses. Bootstrapping is a re-sampling technique, where pulses are sampled according to a charge weighted multinomial distribution and thus pulses with high charges have a high chance to be selected. Due to the random nature of the re-sampling technique, an intrinsic variation is introduced. Using typically four iterations of bootstrapping, where the direction is reconstructed for each iteration and the final direction is given by the averaged result, are used. This reconstruction is less prone to converge to a local minimum and is often used to seed other algorithms.

5.4.2 Event-Based Angular Resolution

Beside the best fit direction of a reconstruction also an estimate of the angular resolution is of interest. The angular resolution can be estimated on an event by event bases, based on the

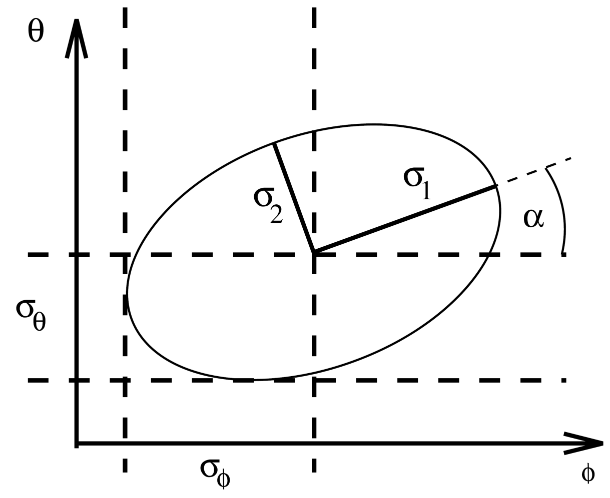

Figure 5.5: Definition of quantities of the paraboloid error ellipse. Plot from [234].

reconstruction likelihood landscape $\mathcal{L}(\hat{\hat{\vec{r}}}_0, \theta, \phi)$ and the best fit likelihood $\mathcal{L}(\hat{\vec{r}}_0, \hat{\theta}, \hat{\phi})$.

Paraboloid

The dimension of the problem to find the angular resolution is reduced by marginalizing over the parameter $\vec{r}_0$ for a given direction (θ, ϕ), which leaves us with a 2D reconstruction landscape $\mathcal{L}(\theta, \phi)$ [234, 235]. The uncertainty contour on the reconstruction parameters, especially on the direction (θ, ϕ), is given by the contour defined by [234, 235]:

$$\Delta(-\log \mathcal{L}) = (-\log \mathcal{L}_{\text{ellipse}}) - (-\log \mathcal{L}_{\text{best}}) \overset{!}{=} \frac{1}{2} \,. \tag{5.8}$$

This assumes that Wilks' theorem [236] is valid and the likelihood can be described by a 2D-Gaussian in the region around the best fit direction the $1\,\sigma$ contour is given by an ellipse with major axis σ_1, semi-major axis σ_2 and rotation α [234, 235]. For a definition see Fig. 5.5.

To determine the parameters of the $1\,\sigma$ ellipses the likelihood difference $\Delta(-\log \mathcal{L})$ is calculated at 24 grid points. The grid points are located on three rings with different radii and centered at the best fit direction, each having 8 scan point equally distributed on the ring. Before this grid points are determined, a coordinate transformation is applied so that the landscape is orthogonal in θ, ϕ close to the best fit direction [234, 235].

Using the scan point around the best fit direction a paraboloid can be fitted using a χ^2 minimization, that can be performed analytically [234, 235]. The free parameters of the paraboloid can be expressed the major and semi-major axis $\sigma_{1/2}$ and the rotation angle α (see Fig. 5.5) [234, 235] or $\sigma_a = \sqrt{\sigma_1 \cdot \sigma_2}$ which is connected to the area of the ellipsis, the eccentricity $\epsilon = \frac{\sigma_1}{\sigma_2}$ and the rotation angle α.

In previous studies it has been shown, that there is no sensitivity gain in searches for point like sources if the $1\,\sigma$ is used or if a symmetric $1\,\sigma$ circle is used [237, 238, 239]. Therefore, we introduce the radius of a circle based on a squared mean of $\sigma_{1/2}$ which we call *Sigma-Paraboloid*

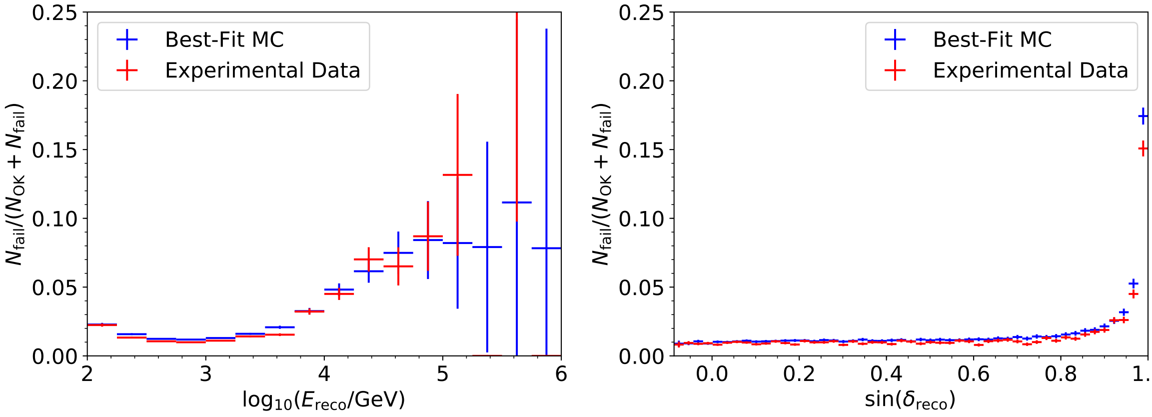

Figure 5.6: Fraction of failed paraboloid fits as a function of reconstructed energy (left) and sine of declination (right) for the season IC86-2012/16. Plots for other sub-samples can be found in Appendix A.

in the following:

$$\sigma = \sqrt{\frac{\sigma_1^2 + \sigma_2^2}{2}} = \sigma_2 \sqrt{\frac{1+\epsilon^2}{2}} \,. \tag{5.9}$$

The determination of the paraboloid can fail due to multiple reasons. The fraction of failed Sigma-Paraboloid fits is shown in Fig 5.6 in dependence of reconstructed energy and sine of declination for the event selection used in this thesis (see Sec. 5.5). It can be seen that for high reconstructed energies and close to the celestial pole ($\sin\delta \sim 1$) the fraction of failed Sigma-Paraboloid fits is increased. This shows that there is a preferred class and topology of events for which the algorithm fails. The median space angle between the reconstructed and true neutrino direction of events with failed paraboloid fits for the season IC86-2012/16 is $\tilde{\Delta\Psi}_{\mathrm{failed}} = 1.048°$ assuming a power law spectrum with $\gamma = -2.19$. For event where the Sigma-Paraboloid fit fails, we thus assign $\sigma = \tilde{\Delta\Psi}_{\mathrm{failed}}$.

Pull Correction

The Paraboloid sigma should on average describe the point spread function (see Sec. 5.7). This works if the assumptions above, which are that Wilks' theorem holds and that the landscape follows a symmetric 2D Gaussian, are valid. However, these are simplifications that do not hold perfect. We therefore calculate the *pull* which is $\Delta\Psi/\sigma$ where $\Delta\Psi$ is the space angle between the true neutrino direction and the reconstructed direction. The pull can be calculated for a data sample consisting of Monte Carlo events, where the true direction is known.

In Fig. 5.7 (left) the cumulative distribution of the $\log_{10}$ pull using the Sigma-Paraboloid is shown for different slices in reconstructed energy E_{prox}. In an ideal case one expects that the 39% quantile of the pull distribution is at 1 and thus the $\log_{10}(\Delta\Psi/\sigma)$ is expected to be at zero, because $\Delta\Psi$ is expected to follow a Rayleigh distribution with the same σ as the 2D Gaussian. The median of $\Delta\Psi$ is expected to be at $\sqrt{2\ln 2}\sigma \approx 1.177\sigma$ for a 2D Gaussian distributed random direction. From Fig. 5.7 (left) it can be seen that this is not. The $\log_{10}$

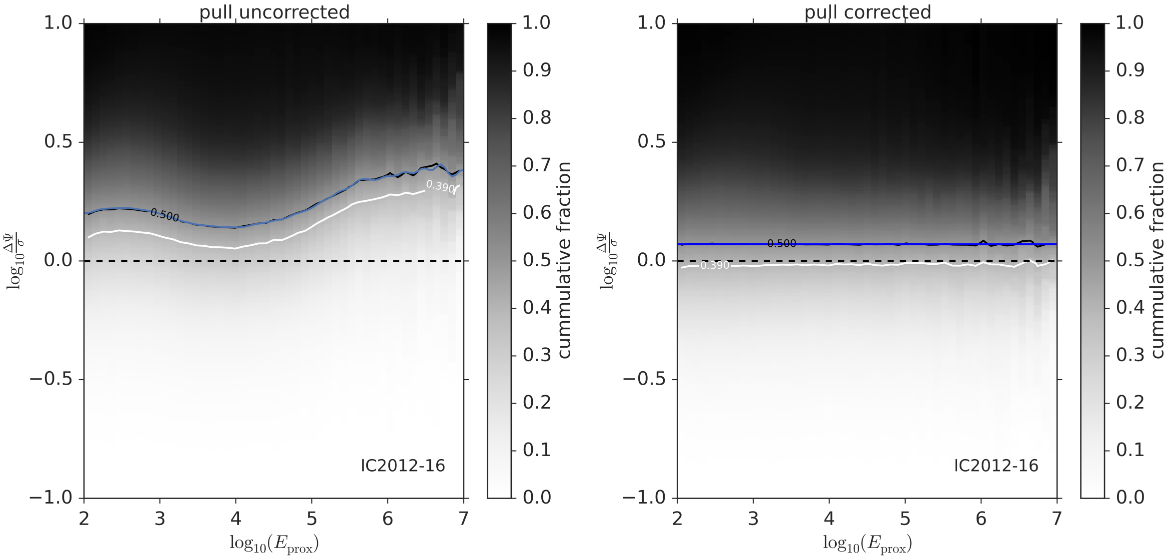

Figure 5.7: Cumulative distribution of the decadic logarithm of the pull for different slices in reconstructed energy. The pull is the space angle $\Delta\Psi$ between the reconstructed and true neutrino direction divided by the angular uncertainty estimate σ. For the left and right panel the uncorrected and corrected σ is used, respectively. The 39% ($1\,\sigma$ of a Rayleigh distribution) and 50% (median) quantiles are indicated by a black and a while contour line. The median quantile is splined by a cubic interpolating spline shown in blue. The final sample selection of the season IC86-2012/16 is used.

pull is always above zero indicating an underestimation of σ. Moreover the median $\log_{10}$ pull is energy dependent and the underestimation of σ is stronger at high reconstructed energies. This can be explained by a wrong tested hypothesis of Cherenkov light front an infinite muon track neglecting stochastic energy losses. The full reasoning however is not yet full understood and is currently under investigation [239].

To correct for the underestimation of σ, a correction factor is calculated. Therefore, the median $\log_{10}(\Delta\Psi/\sigma)$ is splined by a cubic non-smoothing interpolation spline f_{corr} as a function of $\log_{10} E_{\mathrm{prox}}$ (blue line in Fig. 5.7 left). A corrected Sigma-Paraboloid is calculated following:

$$\sigma_{\mathrm{corr}} = \sigma \cdot \frac{f_{\mathrm{corr}}(\log_{10} E_{\mathrm{proxy}})}{\sqrt{2\ln 2}} \,. \tag{5.10}$$

The calculation of the correction factor is done separately for successful and failed Sigma-Paraboloid fits. As the failed Sigma-Paraboloid fits are prior set to $\tilde{\Delta\Psi}_{\mathrm{failed}}$, the σ_{corr} is the energy dependent median $\Delta\Psi$ of failed Sigma-Paraboloid fits.

For verification, the cumulative distribution of the $\log_{10}$ of the pull using the corrected Sigma-Paraboloid σ_{corr} is shown in Fig. 5.7 (right). It can be seen that now the 39% quantile of the $\log_{10}$ pull is very close to zero and the median is a constant over all reconstructed energies.

Note that the pull distribution also has dependencies on other variables like the zenith and azimuth angle, however the energy dependence of the pull is by far the most dominant one [239]. Therefore, we only apply the pull correction as a function of reconstructed energy.

In the following we always will refer to σ_{corr} as the $Sigma-Paraboloid$ and use the symbol σ. The pull correction is always applied if not stated explicitly.

5.4.3 Energy

The energy reconstruction of the high-energy muon is challenging. First the muon is often not fully contained and only a segment of its track is covered by the detector and a calorimetric measurement is only possible for low-energy muons that are fully contained. Thus, we have to rely on the measurement of $\mathrm{d}E/\mathrm{d}x$ and inverting Eq. 4.16 to measure the muon energy. Second, for energies above 1 TeV stochastic processes are dominant leading to a large variance in the energy loss for a given muon energy, which also leads to a large variance in muon energy for a given energy loss.

Truncated Energy

Here we use the *truncated energy* algorithm to estimate the muon energy [240]. In this algorithm a truncated mean is used to reduce the variance at high-energies. Therefore, for each DOM with a local coincidence and within a cylinder of 60 m radius around the track hypothesis, the ratio of expected and measured charge is calculated. The expected charge is calculated for a particle track with an energy loss of 1 GeV/m using the tabulated results of detector simulation using the Photonics [226] simulation. This method is called "DOMs"-method in Ref. [240]. The best correlation of truncated mean and muon energy is obtained for a truncation of the 50% of the DOMs that have the largest energy loss [240].

The energy resolution of this method is about 0.22 in $\log_{10}(E_\mu)$. Note that one can not directly conclude about the neutrino energy from the muon energy.

5.5 Event Selection

For the search of astrophysical neutrino point-source we aim for a high purity neutrino sample. However after triggering and filtering (see Sec. 5.2), which we call now Level-2, the sample is dominated by atmospheric muons followed by atmospheric neutrinos. The event selection follows this strategy: To reduce the number of muons we use the Earth as a shield and only select events coming from the Northern hemisphere. Even if only considering events from the Northern hemisphere, the event rate is dominated by atmospheric muons with failed reconstructions. Therefore, we apply a selection of well reconstructed tracks. This leaves us with an atmospheric neutrino dominated sample which is an irreducible background for the search of astrophysical neutrino sources and can only be distinguished on a statistical basis based on the energy spectrum.

This outlined strategy reconstructions have to be performed on the events, however if is computationally hardly possible to reconstruct all events that pass the triggering and filtering (Level-2, see Sec. 5.2) with a all-sky rate of about 34 Hz [241]. Therefore, a pre-selection is applied selecting muon tracks, called muon Level-3. After this pre-selection more advanced reconstructions are run and a final event selection is applied (Final-Level).

For the scope of this thesis we take data taken between the years 2009 and 2017. In the early years IceCube was taking data in partial configuration in 2009-2010 with 59 strings (IC59) and in 2010-2011 with 79 strings (IC79). While the detector configuration is in its final state with 86 strings since 2011 (IC86), the Level-2 and Level-3 processing was changed from the season 2011-2012 to the season starting in 2012. Due to the change in detector configuration and Level-2 and Level-3 processing different event selections had to be developed for the seasons IC59, IC79 and IC86-2011. Due to the nearly unchanged processing in 2012 the event selection stays unchanged for the years 2012-2017 (IC86-2012/16).

The event selection for IC59 was developed by A. Schukraft [157] and for IC79 by J. Pütz [242]. The event selections for the seasons IC86-2011 [241] and IC86-2012/16 [154] have been developed by L. Rädel. In the following we summarize the Muon Level-3 and Final-Level event selection for the IC86-2012/2016 seasons [154].

5.5.1 Muon Level-3

The Muon Level-3 selection is split in two branches, one covering the Northern hemisphere and one the Southern Hemisphere, where the Hemispheres are split at a zenith angle of $\theta = 85°$. We are interested in the Northern hemisphere only where the events are dominated by mis-reconstructed muons, because muons can not penetrate more than 13 km w.e.. A pre-cut is applied using the total charge of an event Q_{tot} which is a rudimental energy estimator and the averaged charge weighted DOM distance to the track $d_{\mathrm{Qavg.}}$. The pre-cut is $Q_{\mathrm{tot}} \geq 100\,\mathrm{PE}$ or $d_{\mathrm{Qavg.}} \leq 90\,\mathrm{m}$ and should reduce mis-reconstructed low energy events. In addition, the criteria in Eq. 5.1 on the first successful reconstruction of MPE, SPE with two iterations, SPE and LineFit, where all fits use the Pandel approximation.

It is possible that multiple events are recorded within a single readout of the detector due to the readout time of microseconds. The reconstruction hypothesis however is a single particle hypothesis and thus reconstructions can be fouled by coincident events. The HiveSplitter algorithm described in [243] is used, which searches for causally connected hits in a defined volume of the detector. The splitting algorithm can split single events into sub-events, even if they originate from the same event, e.g. if no light was detected in the dust-layer. Therefore, the algorithm CoincSuite [243] is applied which tries to recombine falsely split single events. After splitting the MPE, SPE and LineFit reconstructions using the Pandel approximation are applied to all sub-events.

For the quality of the reconstruction unscattered photons are of great relevance and thus the number of unscattered photon n_{dir} observed in a small time window of [-15 ns, +250 ns] around the expected arrival time is a measure of the reconstruction quality. Moreover the distance along the track between the first and last DOM with unscattered photons l_{dir} can be used as quality variable [204].

Another measure of the reconstruction quality can be obtained from the reconstruction likelihood value $\mathcal{L}$ itself. A quality parameter is the reduced likelihood $\mathcal{L}_{\mathrm{reduced}} = -\mathcal{L}/\mathrm{ndof}$, where $\mathrm{ndof} = N_{\mathrm{DOMs}} - 5$ for a through-going track hypothesis and N_{DOMs} is the number of DOMs which detected light in an event. Another quantity $\hat{\mathcal{L}}_{\mathrm{reduced}} = -\mathcal{L}/\hat{N}_{\mathrm{free}}$ with $\hat{N}_{\mathrm{free}} = N_{\mathrm{DOMs}} - 3$ has empirically a better separation power [244].

The final muon Level-3 selection criterion is:

$$\Big(\big((l_{\mathrm{dir}}/180\,\mathrm{m})^2 + (n_{\mathrm{dir}}/10)^2\big) > 2\,\mathrm{and}\,n_{\mathrm{dir}} > 6\Big)\ \mathrm{or}\,\mathcal{L}_{\mathrm{reduced}}/\mathrm{ndof} < 9\,\mathrm{or}\,\hat{\mathcal{L}}_{\mathrm{reduced}}/\mathrm{ndof} < 7.5\,. \tag{5.11}$$

After the muon Level-3 selection 89.0% of a benchmark neutrino flux following a power law with spectral index of -2 and 8.7% of atmospheric muons remain in the region of the Northern hemisphere [154].

5.5.2 Final Event Selection

The event rate after the muon Level-3 is of a few Hz and still dominated by atmospheric muons [154]. The rate of atmospheric neutrinos is more than three orders of magnitude smaller. Multi-variate methods are used to reduce the remaining mis-reconstructed atmospheric muons.

Additional to variables used in the Muon Level-3 selection more topological and quality variables are used within the multi-variate selection. To this quantities belongs the Center of Gravity (COG) $\vec{\mathrm{COG}} = \sum_{i=0}^{n_{\mathrm{DOMs}}} q_i \vec{x}_i / \sum_{i=0}^{n_{\mathrm{DOMs}}} q_i$, which can be calculated using the charge q_i and position $\vec{x}_i$ of all hit DOMs [154, 204]. This COG can be expressed in cylinder coordinates by COG_z and COG_ρ and gives the position of the event. The distance between the $\vec{\mathrm{COG}}$ of the first and last 25% of time-order hit DOMs within 150 m distance around the track is called l_{sep}. For through-going tracks l_{sep} is expected to be large while for events that only pass though a corner of the detector it is expected to be short. A quantity to identify mis-reconstructed events is obtained by the likelihood ratio between an up-going H_u and down-going H_d event hypothesis. The change in likelihood $\Delta\mathrm{LLH}_{\mathrm{bayes}} = \log\Big(\mathcal{L}(\hat{H}_u)\Big) - \log\Big(\mathcal{L}(\tilde{H}_d)\phi(\tilde{\theta})\Big)$, where $\phi(\theta)$ is a prior for down-going atmospheric muons [204, 245, 246] is expected to be large in case of truly up-going events while it is small for down-going events. For a given track hypothesis the position of closest approach to a DOM position can be calculated. Using these points, the variable $s_{\mathrm{dir}} = \max_j \frac{j-1}{N-1} - \frac{l_j}{l_N}$ can be calculated which is a measure of how smooth direct hits are distributed along the track [154]. Here N is the number of direct hit DOMs and l_j is the distance along the track from closest approach [204]. Another variable using the points of closest approach is l_{empty}, which gives the maximum distance between two successive positions along the track. For starting muon events the first part of the event is distorted by the hadronic cascade. Splitting the hit DOMs in two equally large sets along the track, reconstructions can be performed on the first and second set. The reconstructed zenith angle $\cos\theta^2_{\mathrm{geo}}$ of the second half set, using the SPE likelihood with two iterations and the Pandel approximation, can be used as another quality parameter.

Before the multi-variate methods are applied a pre-cut is performed to reduce the number of uninteresting events [154]:

$$n_{\mathrm{DOMs}} > 12 \,\mathrm{and}\, n_{\mathrm{dir}} > 6 \,\mathrm{and}\, l_{\mathrm{dir}} > 200\,\mathrm{m} \,\mathrm{and}\, l_{\mathrm{empty}} < 400\,\mathrm{m} \,\mathrm{and}\, \cos\theta^2_{\mathrm{geo}} < 0.2\,. \tag{5.12}$$

For the selection of well reconstructed muon neutrinos two Boosted Decision Trees (BDT) are trained and their score is calculated.

A first BDT using the AdaBoost algorithm [247], aims at separating atmospheric muons simulated with CORSIKA from CC muon neutrino interaction which have an angular reconstruction of better than 5° to their truth [154]. For training the neutrino events have been weighted to an E^{-2} power law. The BDT takes the topological variables COG_z, COG_ρ and $\cos(\theta)$ as well as the reconstruction quality variables l_{sep}, n_{DOMs}, $\Delta\mathrm{LLH}_{\mathrm{bayes}}$, $\mathrm{L}_{\mathrm{reduced}}/\mathrm{ndof}$, n_{dir}, l_{dir}, s_{dir} and the uncorrected $\sigma_{\mathrm{paraboloid}}$ into account [154]. The cut at the BDT score has been chosen to Score ≥ 0.9 as a compromise between background rejection and signal efficiency [154].

The second BDT also using the AdaBoost algorithm, aims at separating cascade like events simulated by electron neutrino interactions with nuclei from CC muon neutrino interaction which have an angular reconstruction of better than 5° to their truth [154]. For this BDT the topological variables COG_z, COG_ρ and $\cos(\theta)$ as well as the reconstruction quality variables l_{sep}, $\mathrm{L}_{\mathrm{reduced}}/\mathrm{ndof}$, n_{dir}, l_{dir} and the uncorrected $\sigma_{\mathrm{paraboloid}}$ are taken into account [154]. The cut at the BDT score has been chosen to Cascade Score ≥ 0.5, which reduced events with bad angular resolution [154].

For all seasons the SplineMPE-Max reconstruction is performed and the corresponding Sigma-Paraboloid is calculated.

5.6 Experimental Data

Experimental data are taken from the IceCube data taking season IC59 starting in 2009 until the end of the IceCube data taking season IC86-2016 which ended in 2017. As described the event selection differ for different sub-seasons as described in Sec. 5.5. The seasons IC86-2012

Season	Start Date	Livetime days	Events	Declination Range	$\log_{10}\left(\frac{E_\nu^{\text{astro}}}{\text{GeV}}\right)$ Range	$\log_{10}\left(\frac{E_\nu^{\text{atmos}}}{\text{GeV}}\right)$ Range
IC59	2009/05/20	353.39	21411	0° – +90°	3.02 – 5.73	2.37 – 4.06
IC79	2010/06/01	310.59	36880	−5° – +90°	2.96 – 5.82	2.36 – 4.04
IC2011	2011/05/13	359.97	71191	−5° – +90°	2.89 – 5.76	2.29 – 3.98
IC2012	2012/05/15	331.35	367590	−5° – +90°	2.91 – 5.77	2.29 - 3.91
IC2013	2013/05/02	360.45				
IC2014	2014/05/06	367.96				
IC2015	2015/05/18	356.18				
IC2016	2016/05/25	340.95				

Table 5.1: Data samples used in this thesis and some characteristics of these samples. For each sample start date, livetime, number of observed events, and energy and declination range of the event selections are given. The energy range, calculated using a spectrum of atmospheric neutrinos and astrophysical neutrinos, spans the central 90% of the selected events. Astrophysical neutrinos were generated using the best-fit values described in Sec. 5.8. Note that livetime values slightly deviate from Ref. [5, 6] as the livetime calculation has been improved.

to IC86-2016 do not differ in configuration and event selection and thus are treated as a single sample labeled IC86-2012/16.

The runs considered in the final experimental sample are chosen by the following criteria for the season IC86-2012/16 [248]:

- the length of the run exceeds 10 minutes,
- the run is not marked as ”test run”,
- the run did not fail completely and a good start and end times are set,
- there was no light in detector due to calibration runs,
- more than 73 non-DeepCore strings must be active,
- more than 4350 standard DOMs on non-DeepCore strings.

For the other seasons similar conditions are required for a run to be included in the final sample. All runs which fulfill the requirements are listed on a Good Run List (GRL). The start dates of each seasons is given in Tab. 5.1.

The livetime calculation is based on the runs that enter the Good Run List. The calculation of livetime is based on the events passing the Level-2 selection. For each run, the first and last event times of all Level-2 events are used to define the start and stop time. Due to the rate of 34 Hz [154], the livetime is accurate on the order of milliseconds. In addition, we check that there are no gaps in the event times exceeding 50 seconds. The livetime and number of observed events at final selection level for each season is listed in Tab. 5.1. In total about 340 000 events are selected within a live-time of about 2032 days.

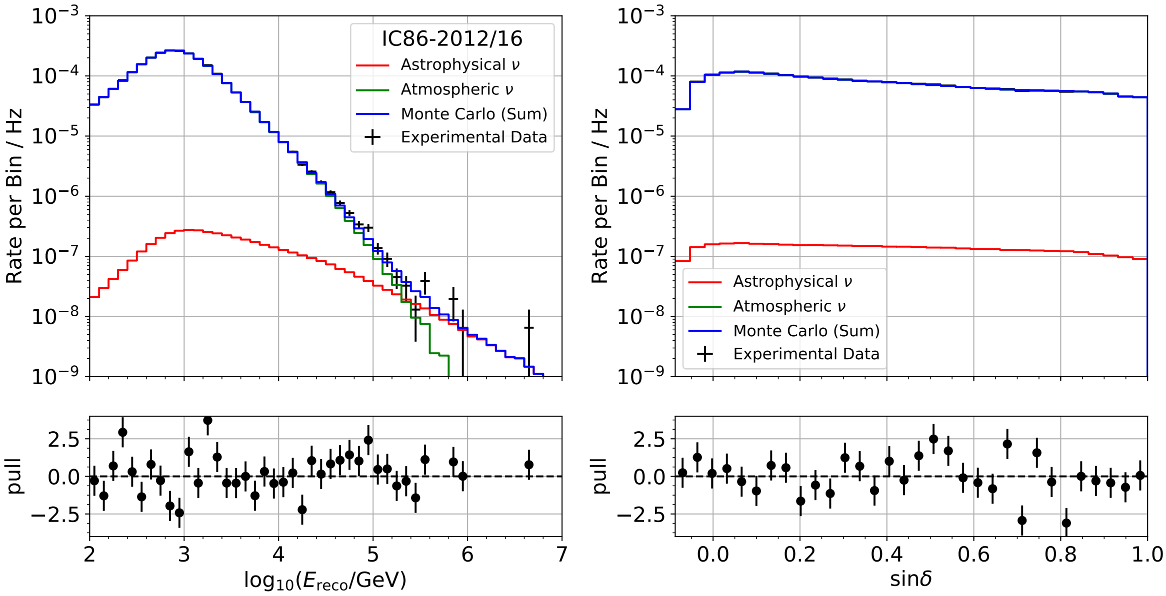

Figure 5.8: Reconstructed energy (left) and declination (right) distribution for the season IC86-2012/16. The experimentally observed rate is given by black error bars. The expected atmospheric (green) and astrophysical (red) component using the best fit parametrization (see Sec. 5.8) is shown as histograms. The contribution from *prompt* neutrinos is zero and the contributions from atmospheric muons are neglected. The pull relative to the total expected rate (blue) is shown in the lower panels. Plots for other sub-samples can be found in Appendix A.

5.7 Characteristics of the Data Sample

In this Section we calculate the characteristic quantities of the data sample with respect to a point-source analysis. The results shown in this section are mainly for the data sample from the season IC86-2012/16. Plots for other seasons can be found in Appendix A. For characterization we heavily rely on Monte Carlo simulation of detector response as described in Sec. 5.3 weighted to the atmospheric and astrophysical neutrino spectrum obtained by the best fit parametrization discussed in Sec 5.8. The experimental data can be well described by the best fit parametrization [154].

The purity defined by $N_\nu/(N_\nu + N_\mu)$, where N_ν and N_μ are the number of neutrinos and atmospheric muons in the sample, is about 99.7% [154] for the IC86-2012/2016 sample. The contamination of electron neutrino events is negligible [5, 154]. For the IC59 season, the purity has been evaluated to $99.85\% \pm 0.06\%(\mathrm{stat.}) \pm 0.04\%(\mathrm{sys.})$ [157] and for IC79 to $99.96\% \pm 0.013\%$ [242]. The remaining background is concentrated at low energies close to the horizon [154].

The reconstructed energy and declination are shown in Fig. 5.8. The reconstructed energy distribution peaks at energies close to 1 TeV and falls steeply to higher energies. At energies above ∼ 200 TeV the data exceed the background distribution of atmospheric neutrinos and the astrophysical neutrino component becomes dominant. While above about 200 TeV energy

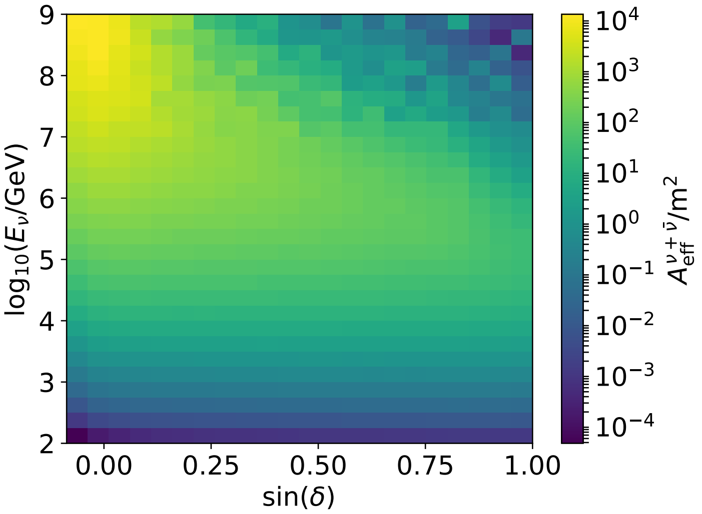

Figure 5.9: $\nu_\mu + \nu_{\bar{\mu}}$ effective area as a function of declination and neutrino energy for the season IC86-2012/16. The effective area is averaged over the parameter range covered by the bin. Plots for other sub-samples can be found in Appendix A.

the astrophysical neutrino spectrum is dominant it extends to lower energies assuming a single power law (see Sec. 5.8). The declination distribution peaks close to the horizon at $\delta \sim 0°$ with a steep decrease to negative declination. The distribution is relatively flat up to high declination. From the pull one can see that both the energy and declination distribution are well described by the best fit parametrization.

The sensitivity of a data sample is given by the efficiency of the detector and the event selection. This sensitivity is expressed by the effective area which is defined as the factor converting a particle flux into the number of observed events. When $\phi_{\nu+\bar{\nu}} = \phi_\nu + \phi_{\bar{\nu}}$ is the flux of neutrinos and anti-neutrinos at Earth and N is the number of observed events (both neutrinos and anti-neutrinos) within the energy range $[\mathrm{E}_{\mathrm{min}}, \mathrm{E}_{\mathrm{max}}]$, from the solid angle Ω and observed within the livetime T, than the effective area $A_{\mathrm{eff}}^{\nu+\bar{\nu}}$ is defined by:

$$N = \int_0^T \mathrm{d}t' \int_{\mathrm{E}_{\mathrm{min}}}^{\mathrm{E}_{\mathrm{max}}} \mathrm{d}E'_\nu \int_\Omega \mathrm{d}\Omega' \, \phi_{\nu+\bar{\nu}} \times A_{\mathrm{eff}}^{\nu+\bar{\nu}} \, . \tag{5.13}$$

The effective area depends on the neutrino energy and arrival direction. Note that the effective area depends on the considered particle flux, e.g. the muon flux or the neutrino and anti-neutrino flux as used here. Beside the effective area, the exposure of a data sample takes additionally into account the livetime of the data sample. As we do not distinguish between neutrinos and anti-neutrinos in the detection, we always consider the neutrino and anti-neutrino flux in the following.

The effective area for the seasons IC86-2012/16 is shown in Fig. 5.9 as a function of neutrino energy and declination angle. One can see that the effective area strongly increases with increasing neutrino energy and reaches about $1000\,\mathrm{m}^2$ at $10\,\mathrm{PeV}$ neutrino energy. In addition, one can see that the effective area is strongly reduced at high energies and neutrinos traversing

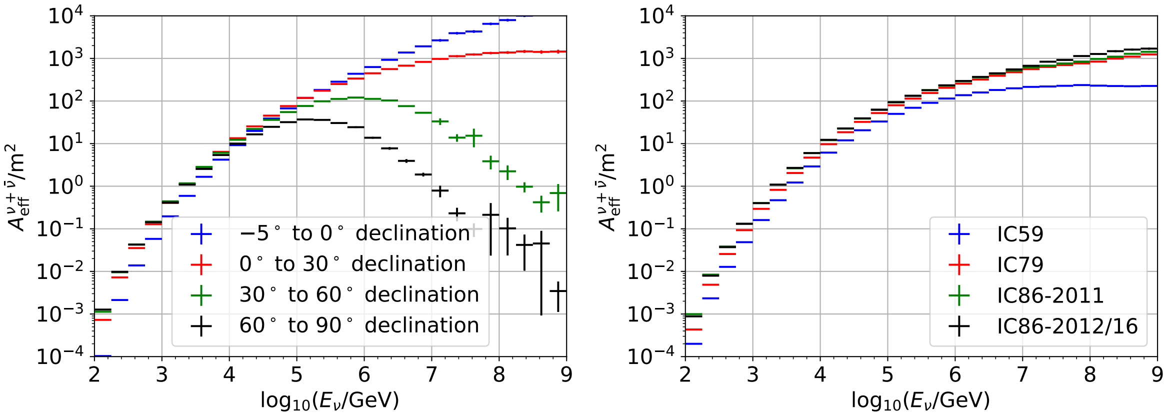

Figure 5.10: $\nu_\mu + \nu_{\bar{\mu}}$ effective area as a function of neutrino energy for the different declination (left) and different seasons (right). The effective area given in the left panel are averaged over the declination range given in the legend and are calculated for the season IC86-2012/16. The effective area given in the right panel are averaged over the full Northern hemisphere ($-5° \leq \delta \leq 90°$).

a large fraction of the Earth ($\sin(\delta) \sim 1$). This is an effect of the Earth absorption of neutrinos (see Sec. 4.1).

In Fig. 5.10 the effective area is shown as a function of neutrino energy. In the left panel the effective area is shown for the season IC86-2012/16 and averaged over different declination bands. Here the Earth absorption effect is clearly visible for energies above 100 TeV and declination larger than 30° declination. In the right panel of Fig. 5.10 the effective area averaged over the full Northern hemisphere is shown for all seasons. It can be seen that the effective area of IC59 is clearly reduced due to the smaller detector size.

Another interesting quantity is the main energy range contributing to the sample. In Fig. 5.11, the median and central 90% range of neutrino energy contributing is shown for different slices in $\sin\delta$ for the season IC86-2012/16. The left panel shows the energy range of atmospheric neutrinos while the right panel shows the energy range of astrophysical neutrinos. For atmospheric neutrinos, the energy range is is nearly constant of energy with a median of about 1 TeV and only increases slight close to the horizon. For astrophysical neutrinos the median neutrino energy lies above 10 TeV and especially the high energy tail extends to larger energies close to the horizon.

Further characteristics are the correlation of reconstructed and true parameters. For a search for point-like sources especially the point spread function (PSF) is of relevance. The point spread function is the distribution of the opening angle $\Delta\Psi$ between the true and the reconstructed event direction, also called angular resolution. In Fig. 5.12 the cumulative PSF distribution is shown for different slices in true neutrino energy. The median angular resolution decreases from about 3° at 100 GeV to 1° at 1 TeV and further to 0.3° at 1 PeV. Note that the kinematic opening angle between the initial neutrino and the muon produced in the CC muon interaction at high energies is much lower and is shown as Fig. 5.12 as well (compare Sec. 4.1 and Fig. 4.4).

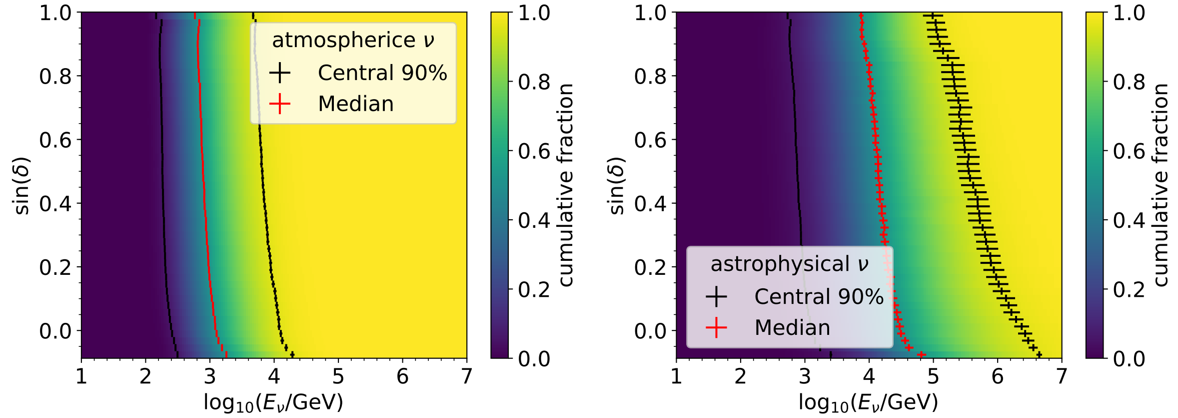

Figure 5.11: Cumulative neutrino energy distribution for different declinations for the season IC86-2012/16. The left panel shows the distribution for the best fit atmospheric neutrino spectrum and the right panel shows the distribution for the best fit astrophysical neutrino spectrum. The black error bars mark the central 90% energy range and the red error bars show the median energy. Plots for other sub-samples can be found in Appendix A.

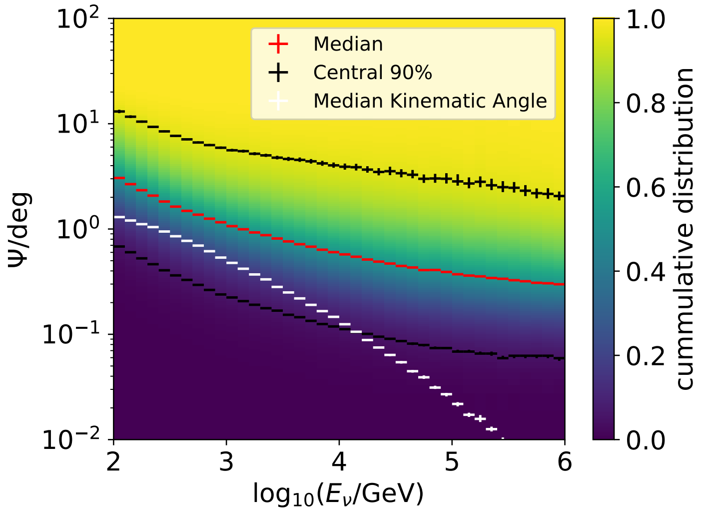

Figure 5.12: Cumulative distribution of the opening angle between true and reconstructed neutrino direction Ψ for different neutrino energies E_ν. The median Ψ and the central 90% range are indicated by red and black error bars. The median kinematic opening angle between the initial neutrino and the muon from a CC muon-neutrino interaction is shown in white (see Sec. 4.1 and Fig. 4.4). Plots for other sub-samples can be found in Appendix A.

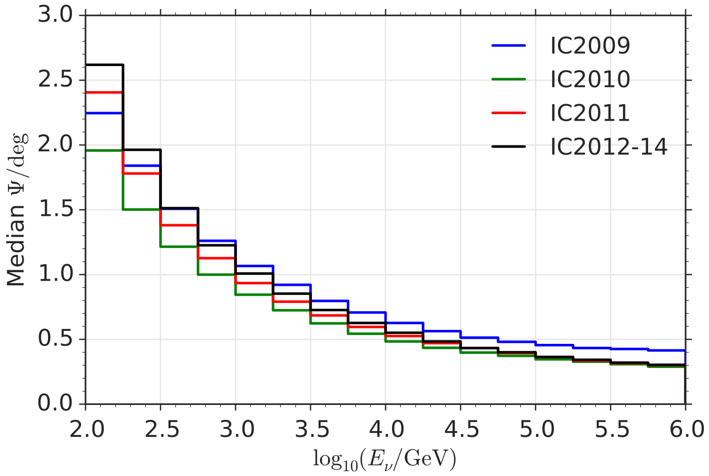

Figure 5.13: Median angular resolution as a function of neutrino energy for the different seasons labeled by the year.

Note that an improved reconstruction, resulting in a smaller angular resolution directly improves the sensitivity of the point source analysis. For this analysis we use the SplineMPE-Max reconstruction applied to all seasons, which gives the best performance in angular resolution. The previous point-source analysis [13] did use the SplineMPE for the latest season and did use the best reconstruction available at the time for previous seasons. Due to this change of reconstruction algorithm and thus an improved median angular resolution of up to 20% at highest energies, this analysis gains in sensitivity compared to previous analysis. A detailed comparison for the samples used in this thesis and in [13] is described in Appendix B. The median angular resolution for all seasons as a function of neutrino energy is summarized in Fig. 5.13.

To estimate the size of the angular reconstruction uncertainty we use the sigma paraboloid reconstruction. This variable is an estimator of the event individual reconstruction uncertainty. In Fig. 5.14 the median and central 68% range of opening angle $\Delta\Psi$ between the true and reconstructed neutrino direction is shown for different slices of pull corrected sigma paraboloid $\sigma_{\text{paraboloid}}$. Note that in Fig. 5.14 the median $\Delta\Psi$ is shown separately for successful and failed paraboloid fits. For a point spread function following a 2D Gaussian, the median is expected at 1.177σ (indicated as dashed line). A very good correlation between $\Delta\Psi$ and $\sigma_{\text{paraboloid}}$ can be seen.

Beside directional information also energy information of events are taken into account in the analysis. Therefore, the correlation between the reconstructed and true energy is of interest. In Fig. 5.15, the median and central 68% range of true neutrino energy and true muon energy are shown for different slices of reconstructed energy. Note that the energy measurement is based on the $\mathrm{d}E/\mathrm{d}x$ of the muon at the detector and the muon can loose an unknown fraction of energy even before reaching the detector. Therefore, the muon energy shown in the right panel of Fig. 5.15 is taken at the entrance of the detector. In addition, not the full neutrino energy is transferred into the created muon in a CC muon-neutrino interaction

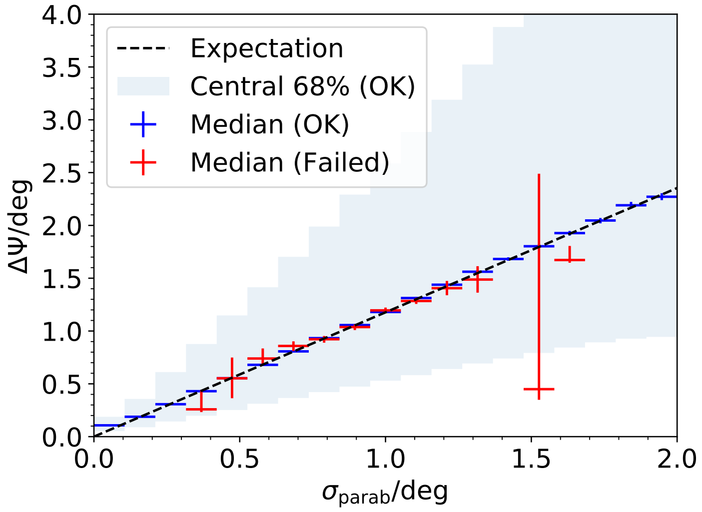

Figure 5.14: Median (error bars) and central 68% range (shaded area) of the opening angle Ψ between the true and reconstructed neutrino direction for different slices of pull corrected $\sigma_{\text{paraboloid}}$. The median opening angle ψ is expected to be at 1.177σ for a 2D Gaussian point spread function. The median ψ is shown separately for reconstructions with successful (blue) and failed (red) paraboloid fit. Events are for the seasons IC86-2012/16 and are weighted to the best fit astrophysical neutrino spectrum. Plots for other sub-samples can be found in Appendix A.

(compare Sec. 4.1 and Fig. 4.4) and thus the muon energy is just a lower bound on the neutrino energy. Therefore, the correlation of reconstructed neutrino energy and true neutrino energy depends on the assumed neutrino spectrum. In Fig. 5.15, the best-fit parametrization of the neutrino energy spectrum described in Sec. 5.8 is used.

5.8 Diffuse Best-Fit Parametrization

The data sample used in this thesis was analyzed for the existence of a diffuse astrophysical neutrino sample [5, 6, 150, 154]. This analysis is a 2 dimensional binned analysis based on the reconstructed muon energy and the reconstructed zenith angle. The analysis has taken into account:

- a *conventional atmospheric neutrino flux* from pion and kaon decay following the prediction of [187] modified to include effects of different cosmic ray flux models [32, 249] and the cosmic ray knee [157];
- a *prompt atmospheric neutrino flux* from charmed meson decay using the ESR model [250];
- a *diffuse astrophysical neutrino flux* modeled as an isotropic single power-law flux.

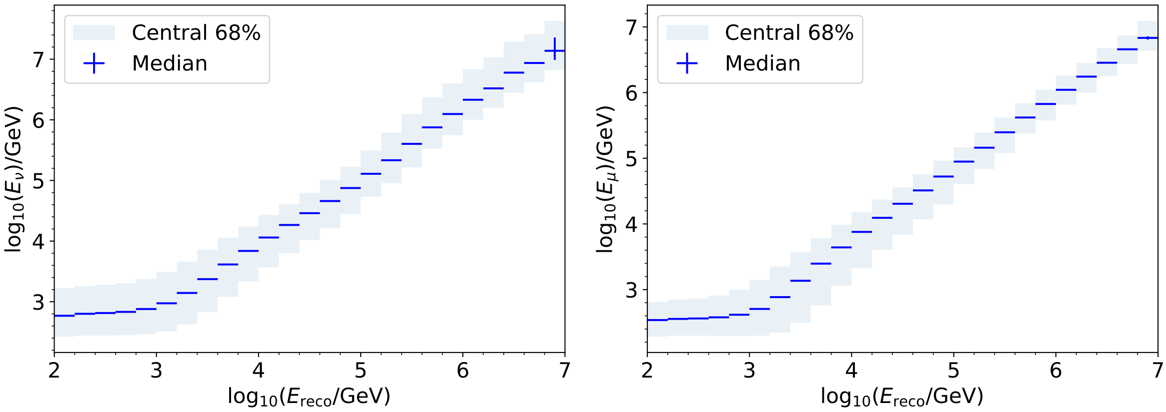

Figure 5.15: Median (error bars) and central 68% range (shaded area) neutrino energy (left) and muon energy (right) for different slices of reconstructed energy. The IC86-2012/16 data sample is used and events are weighted to the best fit (atmospheric + astrophysical) spectrum. The muon energy is the muon energy at the entrance of the detector. Plots for other subsamples can be found in Appendix A.

A modified Poisson likelihood taking into account the limit MC statistic [251] as described in [5] is used for each bin, resulting in a total likelihood

$$\mathcal{L} = \prod_i \left(\frac{\mu_i}{s_i/n_s}\right)^{s_i} \cdot \left(\frac{\mu_i}{d_i}\right)^{d_i}, \tag{5.14}$$

where n_s is the ratio of simulation and experimental livetimes, d_i is the number of data events and s_i is the number of simulated events in bin i. The expected events μ_i in bin i is given by:

$$\mu_i(\phi_{\mathrm{astro}}, \gamma_{\mathrm{astro}}, \phi_{\mathrm{prompt}}, \xi) = \mu_i^{\mathrm{conv}}(\xi) + \mu_i^{\mathrm{prompt}}(\phi_{\mathrm{prompt}}, \xi) + \mu_i^{\mathrm{astro}}(\phi_{\mathrm{astro}}, \gamma_{\mathrm{astro}}, \xi_{\mathrm{det}}) \tag{5.15}$$

where Φ_{astro} and Φ_{prompt} are the flux normalizations of the diffuse astrophysical neutrino flux and the prompt atmospheric neutrino flux, respectively, and γ_{astro} is the diffuse astrophysical spectral index. $\xi = \{\xi_{\mathrm{theo}}, \xi_{\mathrm{det}}\}$ denote nuisance parameters from the theoretical model predictions and detector effects. Due to the nuisance parameters, systematic uncertainties are included in the likelihood function. A detailed description of the nuisance parameters and their implementation can be found in [5].

The best-fit signal and nuisance parameters are obtained by maximizing the likelihood function in Eq. 5.14. Using Wilks' theorem [236] and the profile-likelihood technique, parameter uncertainties are obtained.

This likelihood fit was performed for the first six years of data in [5, 150, 154] and updated to eight years of data in [6]. Note that the eight year data sample is the same sample as used in this thesis.

The likelihood fit of the eight years sample prefers a contribution from diffuse astrophysical neutrinos with a significance of 6.7 σ over a pure conventional atmospheric neutrino sample [6].

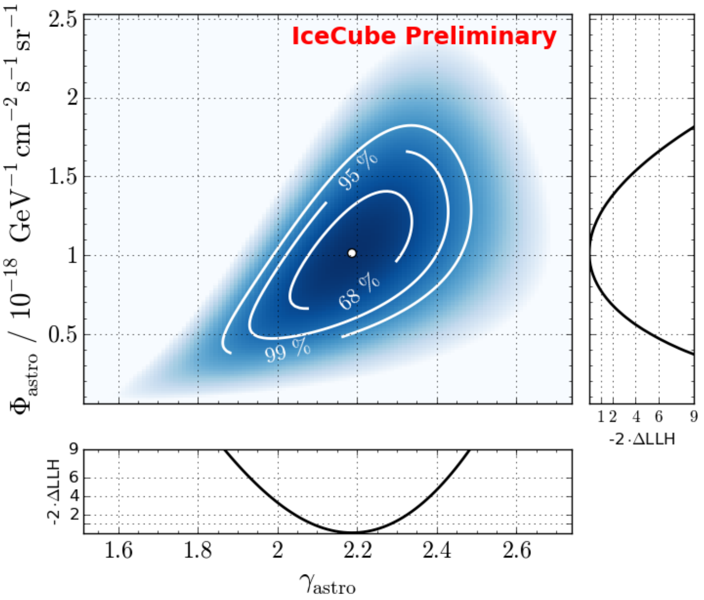

Figure 5.16: Scans of the profile likelihood for the astrophysical flux normalization Φ_{astro} and spectral index γ_{astro}. For each scan point all other parameters in the likelihood are optimized. The confidence intervals are based on Wilks' theorem. The best-fit point is marked with a white marker. Plot for [6].

The best-fit astrophysical spectrum is given by

$$\frac{\mathrm{d}\Phi_{\nu+\bar{\nu}}}{\mathrm{d}E} = (1.01^{+0.26}_{-0.23}) \cdot \left(\frac{E_\nu}{100\,\mathrm{TeV}}\right)^{-2.19\pm0.10} \cdot 10^{-18}\,\mathrm{GeV}^{-1}\mathrm{cm}^{-2}\mathrm{s}^{-1}\mathrm{sr}^{-1}\,. \tag{5.16}$$

Note that the prompt atmospheric neutrino flux normalization is fitted to zero [5, 6].

A scan of the profile likelihood in the astrophysical flux normalization and spectral index is shown in Fig. 5.16 [6]. The $1\,\sigma$, $2\,\sigma$ and $3\,\sigma$ confidence intervals are shown as well as the best fit parameters. Note that tests for a spectral cut-off of the astrophysical component are not significant at the moment [5, 6].

The best-fit parameters of the likelihood including the nuisance parameters can be used as a best-fit parametrization of the data sample. The parametrization can be evaluated for simulated Monte Carlo events individually resulting in a weight for each MC event and flux component. In this thesis we heavily rely on this parametrization to model the data sample. The prerequisite thus is a good data MC agreement between the best-fit parametrization and the experimentally observed data. The 1D event distributions on energy and declination are shown in Fig. 5.8 and Appendix A.

The fit quality of the two-dimensional fit was tested using the ratio of the likelihood in Eq. 5.14 and the saturated likelihood [5, 27]. The resulting ratio was tested against pseudo experiments based on the best-fit parametrization, yielding a p-value of 95.4% and thus indicates a very good agreement between data and MC [5]. The one dimensional distributions of reconstructed energy and zenith have been tested for data MC agreement using a Kolmogorov-

Smirnov test [252, 253] for each season resulting in p-values ranging from 9% to 85%, also showing a good data MC agreement [150]. Also the fitted nuisance parameters are consistent with their expectation within their uncertainty [5, 150].

Based on the best-fit astrophysical spectrum, the sample contains about 1000 astrophysical event [6]. Based on the central 68% central confidence interval (see Fig. 5.16) the number of astrophysical events ranges from 190 to 2415. Note that the number of astrophysical events is dominated by events at lower energies, which are buried below the astrophysical background and that the estimation of the number of astrophysical events is strongly influenced by the extrapolation of the single power law. A more constrained quantity is the number of astrophysical events above 200 TeV energy, because this is the region where the astrophysical flux starts to become dominant.

Even that most of the astrophysical events are buried under the background of atmospheric events, astrophysical neutrinos coming from a point-like source show spatial clustering. In the next Chapter we present the analysis method to search for point-like sources within the background of atmospheric and diffuse astrophysical neutrinos.

Chapter 6

Analysis Method

Declaration of Pre-released Publications The analysis method presented in this chapter have been previously published by the IceCube Collaboration in M. G. Aartsen *et al.* (IceCube Collaboration), "Search for steady point-like sources in the astrophysical muon neutrino flux with 8 years of IceCube data" The European Physical Journal C 79, 234 (2019). The author of this thesis has written this publication as a corresponding author. The author developed the estimation of probability density distributions based on Monte Carlo simulation and the diffuse best fit weights, the implementation of a prior on the spectral index and the definition of negative test statistic values. The test statistic was parametrizised by the author of this thesis.

In this Chapter, the analysis method to search for point-like neutrino sources is introduced, and improvements to the method are discussed. The likelihood for testing a celestial position for point-like neutrino emission is introduced in Section 6.1. In Section 6.2, the estimation of the signal and background probability density functions is explained and in Section 6.3, the combination of different sub-samples is discussed. The method presented in this thesis implements several modifications to previous likelihood analyses searching for point-like sources in IceCube. One is the addition of a prior to the likelihood to constrain the spectral index of the potential source which is discussed in Section 6.4. In Section 6.5, the test statistic of the analysis is introduced. The chapter ends with a discussion of the resulting p-value of the analysis in Section 6.6.

6.1 Search Strategy

The goal of this thesis is to test positions in the sky for the existence of a point-like neutrino source. To do this, the experimentally observed data, with reconstructed directions $\vec{x}_i$ and reconstructed energies E_i, are compared with a signal and a background hypothesis. For the scope of this thesis, the signal hypothesis is defined as

H_s: Data includes astrophysical neutrinos coming from a single emission region at $\vec{x}_S$ that seems to be point-like with respect to the detector resolution and exhibit a power-law energy spectrum with spectral index γ.

The null hypothesis H_0 is then defined as the complement of the signal hypothesis, which is

H_0: Data includes no cluster of astrophysical neutrinos, i.e. exclusively atmospheric neutrinos, and astrophysical neutrinos that are produced in a diffuse emission regions.

The likelihood to observe the data for a given signal and background hypotheses are $P(Data|H_s)$ and $P(Data|H_0)$, respectively. The method presented in this thesis uses a likelihood ratio test to discriminate between these two hypothesis. The analysis method is based on and described in [111]. The log of the likelihood ratio serves as test statistic:

$$TS = 2 \cdot \log \left(\frac{P(Data|H_s)}{P(Data|H_0)} \right) . \tag{6.1}$$

Given a set of N neutrinos with reconstructed directions $\vec{x}_i$, event based reconstruction uncertainty σ_i and reconstructed energy E_i, the source probability density of an individual event to originate from a true position $\vec{x}_s$ and being emitted by a source power law spectrum with spectral index γ is

$$S_i = S(\vec{x}_i, \sigma_i, E_i|\vec{x}_s, \gamma) . \tag{6.2}$$

The background probability density of events will not depend on the source parameters and is given by

$$B_i = B(\vec{x}_i, E_i) . \tag{6.3}$$

The construction of $S(\vec{x}, \sigma, E|\vec{x}_s, \gamma)$ and $B(\vec{x}, E)$ is discussed in Section 6.2.

Combining the source and background probability densities of all N observed events gives the likelihood function:

$$\mathcal{L}(\vec{x}_s, n_s, \gamma) = \prod_{i=1}^{N} \left(\frac{n_s}{N} S(\vec{x}_i, \sigma_i, E_i|\vec{x}_s, \gamma) + \left(1 - \frac{n_s}{N}\right) B(\vec{x}_i, E_i) \right) \cdot P(\gamma) , \tag{6.4}$$

where n_s/N gives the signal fraction of events relative to the total number of events in the sample N and $P(\gamma)$ is an additional prior term on the spectral index that incorporates external knowledge about the spectral index. The prior term in Eq. 6.4 is further discussed in Section 6.4.

For a given direction, the free parameters of the likelihood n_s and γ are unknown quantities. Thus, the likelihood is maximized with respect to these parameters to get the best-fit values $\hat{n}_s$ and $\hat{\gamma}$ for a celestial direction $\vec{x}_s$. Instead of maximizing the likelihood, the negative log likelihood is minimized using the L-BFGS-B minimizer [254] implemented in the *python* package *scipy* [255]. In addition, we use the software package *SkyLab* [256] that was co-developed within this thesis. The best-fit value $\hat{n}_s$ and $\hat{\gamma}$ are maximum likelihood estimators of n_s and γ, which are unbiased in the large sample limit and the variance of the estimators reach the minimal variance bound [257]. The estimators and the correlation with their true parameters are studied further in Section 7.2.

Once the best-fit parameters $\hat{n}_s, \hat{\gamma}$ are found for a celestial direction, the likelihood of the signal and background hypothesis can be expressed by the likelihood functions:

$$P(Data|H_S) = \mathcal{L}(\vec{x}_s, \hat{n}_s, \hat{\gamma}) \tag{6.5}$$

$$P(Data|H_0) = \mathcal{L}(\vec{x}_s, 0) \tag{6.6}$$

Note that for the background hypothesis there is no spectral index of the source, as there is no source in the hypothesis in the first place. In the same way also additional prior terms do not

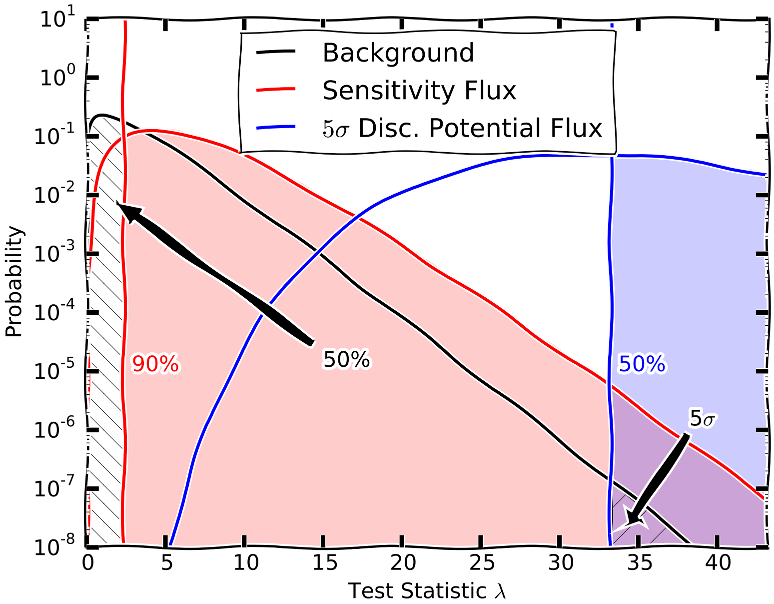

Figure 6.1: Sketch to illustrate the definition of the sensitivity and discovery potential. The background TS distribution is shown in black where the median and the 5σ quantile are marked. The signal TS distribution is given by the red line for the 90% CL sensitivity flux and in blue for the 5σ discovery potential flux.

show up in the likelihood of the background hypothesis. As $n_s = 0$ in the background case, the likelihood simplifies to

$$\mathcal{L}_0 = \mathcal{L}(\vec{x}_s, 0) = \prod_{i=1}^{N} B(\vec{x}_i, E_i)\,. \tag{6.7}$$

The test statistic can be written as

$$TS = 2\left[\sum_{i=0}^{N} \log\left(\frac{\hat{n}_s}{N}\left(\frac{S(\vec{x}_i, \sigma_i, E_i|\vec{x}_s, \hat{\gamma})}{B(\vec{x}_i, E_i)} - 1\right) + 1\right) + \log(P(\hat{\gamma}))\right], \tag{6.8}$$

which can be derived from Eq. 6.1 , Eq. 6.4 and Eq. 6.7. The test statistic is further discussed in Section 6.5.

The sensitivity and discovery potential flux normalization are a characteristic quantity that quantifies the performance of an analysis. The sensitivity and discovery potential are discussed in detail in Sec. 7.3, however it is helpful to introduce and define these quantities already here, before discussing the details of the likelihood and test statistic construction in the next sections. We define the sensitivity as the median expected flux upper limit in case of only background. Considering a 90% CL for the flux upper limit, the sensitivity flux normalization is determined by the flux normalization of a signal flux for which the 10%-quantile of the test statistic distribution coincides with the median of the test statistic distribution of only background. We define the discovery potential as the signal flux normalization that yields a 5σ deviation from the background hypothesis in 50% of all cases. Thus, the discovery potential flux

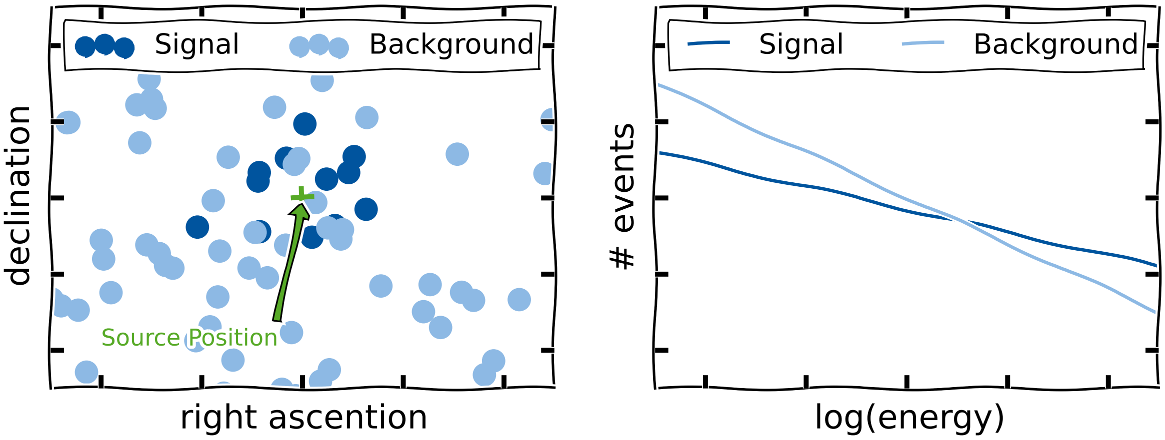

Figure 6.2: Sketch to illustrate the different likelihood contributions. Left: Event directions in equatorial coordinated. Signal events clustering around the source position (green cross) are marked in dark blue while uniform distributed background events are marked in light blue. Right: Energy distribution of astrophysical and atmospheric neutrinos. Both information can be used to suppress background.

normalization is determined by the flux normalization of a signal flux for which the median of the test statistic distribution coincides with the $1-5\sigma$-quantile of the test statistic distribution of only background. The test statistic distributions for only background and for signal flux normalization at the sensitivity and 5σ discovery potential are illustrated in Fig. 6.1. In the following, we use the 90% CL sensitivity and 5σ discovery potential for a source spectrum of E^{-2} as a benchmark and refer to the sensitivity flux normalization and discovery potential flux normalization simply as sensitivity and discovery potential.

6.2 Estimation of Probability Density Functions

The likelihood function in Eq. 6.4 and Eq. 6.7 depend on the individual probability densities $S(\vec{x}_i, E_i|\vec{x}_s, \gamma)$ of an event to originate from a source at position $\vec{x}_s$ and being produced by a power law spectrum with spectral index γ, and $B(\vec{x}_i, E_i)$ to originate from atmospheric background or diffuse astrophysical background.

Both probability densities, S and B are composed of a spatial and an energy probability term. The probability densities can be factorized into

$$\begin{aligned} S(\vec{x}, E|\vec{x}_s, \gamma) &= S^{\text{spat.}}(\vec{x}|\vec{x}_s) S^{\text{ener.}}(E|\gamma, \sin\delta)\,, && (6.9) \\ B(\vec{x}, E) &= B^{\text{spat.}}(\vec{x}) B^{\text{ener.}}(E|\sin\delta)\,. && (6.10) \end{aligned}$$

The spatial source probability density $S^{\text{spat.}}(\vec{x}|\vec{x}_s)$ describes the probability of an event reconstructed at celestial position $\vec{x}$ to origin from the celestial position $\vec{x}_S$. In case the reconstructed direction is estimated by a maximum likelihood method, as described in Section 5.4.1, $S^{\text{spat.}}(\vec{x}|\vec{x}_S)$ is directly given by the event reconstruction-likelihood landscape. As discussed in Section 5.4.2, the event reconstruction-likelihood landscape can be approximated by a paraboloid in the region close around the best-fit direction. Thus

$$S^{\text{spat.}} = \frac{1}{2\pi\sigma^2} e^{-\frac{|\vec{x}-\vec{x}_s|^2}{2\sigma^2}} \,, \tag{6.11}$$

can be used as approximation for the spatial source probability density, where σ_i is the $1\,\sigma$ radius of a paraboloid fitted to the likelihood landscape.

The energy probability density $S^{\text{ener.}}(E|\gamma, \sin\delta)$ of the source hypothesis, depends on the source spectrum and the observed declination angle δ of the event. The declination dependence is mainly a result of the propagation effect of neutrinos through the Earth and event selection effects. The probability density can be written as:

$$S^{\text{ener.}}(E_{\text{reco}}|\gamma, \sin\delta) = \int_{E_\nu} P(E_{\text{reco}}|E_\nu, \sin\delta) P(E_\nu|\gamma) \, \mathrm{d}E_\nu \,, \tag{6.12}$$

where $P(E_{\text{reco}}|E_\nu, \sin\delta)$ gives the probability density to observe an energy estimator E_{reco} for a neutrino with initial energy E_ν from declination δ (see Fig. 5.7). $P(E_\nu|\gamma)$ gives the probability density to get a neutrino with energy E_ν from the source with spectral index γ. The integral is performed over all possible neutrino energies. It is not evaluated explicitly, but the energy source probability density is calculated by using full detector Monte Carlo simulation, weighting the individual events to the source spectrum. The energy source probability density additionally depends on the sub-sample because $P(E_{\text{reco}}|E_\nu)$ depends on the event selection, energy reconstruction method and detector geometry. The energy source probability density is calculated for each sub-sample individually. To evaluate the full detector Monte Carlo simulation, the events are histogramized in $\log_{10}(E^{\text{reco}}/\text{GeV})$ and $\sin\delta$.

The binning of the different sub-samples is given in Tab. 6.1. The bin-size in $\sin\delta$ varies and is divided into three regions for which an equal spacing is used. The regions correspond to the near horizon region with $\sin\delta < 0.2$, the pole region with $\sin\delta > 0.9$ and a mid-range region. The regions are chosen because of the different amount of statistic in these regions, allowing for a finer binning in the near horizon region. This binning is taken from [258]. For $\log_{10}(E_{\text{reco}})$ an equal width binning is used with 40 bins over the full range of allowed energy proxies. The resulting energy source probability density depends on the spectral index of the source spectrum and on the declination of the event.

The source energy PDF is calculated for different spectral indices with a step width of 0.1. To evaluate the source energy PDF, a parabola is fitted to the closest spectral index and the two neighbouring spectral indices, for which the source energy PDF has been evaluated. The parabola is used to interpolate the source energy PDF between the different spectral indices.

Fig. 6.4 shows the source energy PDF for a spectral index of $\gamma = -2.0$ for the sub-sample IC86-2012/16. The PDFs for the other sub-samples can be found in Appendix C. The source energy PDF is normalized to 1 for each slice in $\sin\delta$. The maximal probability density is reached for an energy proxy between about $3 < \log_{10}(E_{\text{reco}}/\text{GeV}) < 4$. It is clearly visible that the probability density in the pole region $\sin\delta > 0.8$ and very high energies drops drastically. That is, because at highest energies the Earth absorbs neutrinos efficiently, as discussed in Section 4.1.

Sub-Sample	$\sin\delta$-binning		$\log_{10}(E_{\mathrm{reco}}/\mathrm{GeV})$-binning	
	# bins	$\sin\delta$-range	# bins	$\log_{10}(E_{\mathrm{reco}}/\mathrm{GeV})$-range
IC59	14 24 4	[0, 0.2] [0.2, 0.9] [0.9, 1.0]	40	[-1.5, 2]
IC79	24 24 4	$[\sin(-5°), 0.2]$ [0.2, 0.9] [0.9, 1.0]	40	[2.2, 7.2]
IC86-2011	24 24 4	$[\sin(-5°), 0.2]$ [0.2, 0.9] [0.9, 1.0]	40	[2.0, 7.0]
IC86-2012/16	24 24 4	$[\sin(-5°), 0.2]$ [0.2, 0.9] [0.9, 1.0]	40	[2.0, 7.0]

Table 6.1: Binning of probability density in sine of declination $\sin\delta$ and $\log_{10}$ of the energy proxy. The binning is given for each sub-sample. For both, $\sin\delta$ and $\log_{10}(E_{\mathrm{reco}}/\mathrm{GeV})$, the number of bins and the range is given. The bins have equal width in the given quantities. For $\sin\delta$ the size of the binning is different in three different regions.

The spatial background PDF, $B^{\mathrm{spat.}}(\vec{x})$, describes the declination and right ascension dependence of the atmospheric and diffuse astrophysical flux due to their production and acceptance of the detector. Because of the nearly continous operation of the IceCube detector, with an operational up-time of more than 99% [175], and IceCube special position at the geographical South Pole, any azimuth structure in the detector acceptance gets averaged out, when averaged over more than a few days by the Earth's rotation. Thus it is assumed, that the event directions of background events are uniformly distributed in right ascension. The declination dependence can be directly related to the zenith dependent acceptance of the detector, due to the detector's location. The zenith angle θ is linked to the declination angle δ by $\theta = \pi/2 - \delta$. The spatial background probability density is given by

$$B^{\mathrm{spat.}}(\vec{x}) = \frac{1}{2\pi} B^{\mathrm{dec}}(\delta) \,. \tag{6.13}$$

The declination or zenith detector acceptance has to be parametrized by a function $B^{\mathrm{dec}}(\delta)$. The parametrization is discussed in the following paragraphs.

Also the energy background PDF $B^{\mathrm{ener.}}(E|\sin\delta)$ has to be parametrized, taking into account the flux properties as well as the detector and event selection effects. To parametrize $B^{\mathrm{ener.}}(E|\sin\delta)$ and $B^{\mathrm{dec}}(\delta)$ there are two options. Either the PDFs are estimated using a physical motivated parametrization based on the full detector Monte Carlo simulation or the PDFs are estimated from experimental data. Both methods have advantages and disadvantages, which are discussed below. Before, the two methods are shortly introduced. Note that for $S^{\mathrm{ener.}}(E|\gamma, \sin\delta)$ the estimation from experimental data, is not possible, as no significant source has been discovered yet.

To build a physically motivated parametrization of the background distribution, three flux components are taken into account: atmospheric neutrinos from pion and kaon decay, atmospheric neutrinos from heavier meson decay and a diffuse astrophysical neutrino spectrum following a power-law distribution. In addition, several nuisance-parameters are introduced to absorb systematic uncertainties in the parametrization. The parametrization is fitted to experimental data. The fit procedure, parametrization and result is described in detail in [150, 154] and in Section 5.8. The latest update to this fit, which is based on the same data sample as used in this thesis, was reported in Ref. [6]. The best-fit parametrization exhibits a good data / MC agreement as shown in Section 5.8. Using the best-fit parameters of the flux components, including nuisance parameters, it is possible to derive individual weights corresponding to the flux contributions of conventional atmospheric neutrinos, prompt atmospheric neutrinos and astrophysical neutrinos for each simulated event from a full detector Monte Carlo simulation. Using this parametrization, the PDFs can be estimated by Monte Carlo events weighted to the background flux of atmospheric and diffuse astrophysical events.

In case the PDFs are estimated directly from experimental data, one has to assume that the contribution from signal to the experimental data is negligible. Furthermore, as discussed above the event direction in right ascension is expected to be uniformly distributed. By reassigning randomly generated detection times, and thus right ascension values, a possible auto-correlation in the spatial component get lost. However, the distributions in energy and declination are unaffected. Thus, these background PDFs can be estimated by histogramizing the experimental data with randomized detection times.

For both approaches the PDFs are obtained from histogramizing events, for the physically motivated parametrization these are MC simulated, weighted events and for experimental these are the experimentally observed events directly. The binning is given in Tab. 6.1. For $B^{\text{dec}}(\delta)$ the PDF is calculated from the 1D histogram in $\sin\delta$. The resulting PDFs are shown in Fig. 6.3 using both methods. The bin centers are used to construct an interpolation spline of order 2. The energy signal and background PDFs are shown in Fig. 6.4 generated with both methods. For $B^{\text{ener.}}(E|\sin\delta)$, the histogram is normalized to 1 for each $\sin\delta$ slice. Instead of evaluating the histogram directly, the ratio $W \equiv S^{\text{ener}}/B^{\text{ener.}}$ is evaluated[1], which is also shown in Fig. 6.4. This is done, since experimental data are used directly to generate the background energy PDF, there are several bins that do not contain any events. The ratio W is interpolated by a linear spline in the natural logarithm of W. For these bins, W is set to the largest W that is still defined. Note that at these points the PDF is never evaluated as the observed event energies and directions are the same as used for the background energy PDF construction.

To compare the PDFs, $B^{\text{dec}}(\delta)$ and $B^{\text{ener.}}(E|\sin\delta)$ estimated with the best-fit parametrization and estimated from randomized experimental data are shown in Fig. 6.3 and Fig. 6.4, respectively. The overall distributions are very similar, however in Fig. 6.4 the W distribution reaches much larger values, if the best-fit parametrization is used.

---

[1] The test statistic as written in Eq. 6.8 depends on the ratio S/B. Also, S/B can be factorized into the spatial and energy part, where the energy part is called W.

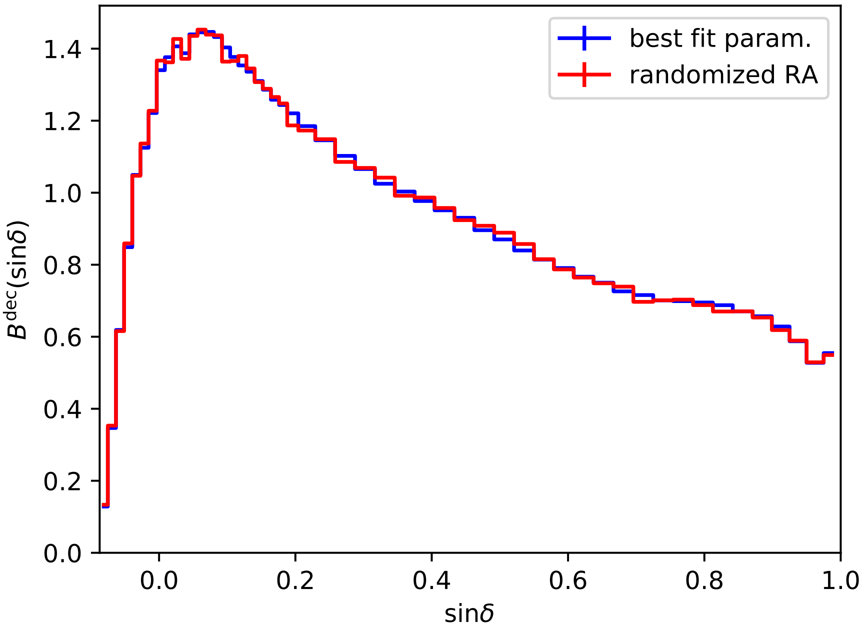

Figure 6.3: Spatial background PDF $B^{\mathrm{dec}}(\delta)$ estimated from Monte Carlo for the best-fit parametrization (blue) and experimental data (red) for the season IC86-2012/16. Similar plots for other seasons can be found in Appendix C.

The good agreement between both methods is based on the fact, that the physical motivated best-fit parametrization has been fitted to the same data. Since the fit shows reasonable agreement with the data, also the PDFs are very similar. However both methods have conceptual differences.

By building PDFs estimated from experimental data, the PDF converges to the true PDF by construction, in the limit of infinite statistics. However, the statistics of experimental data is limited, especially in sparsely populated regions, i.e. at highest energies and in the celestial pole region. By building PDFs from best-fit parametrization, the high-statistic data samples of full detector Monte Carlo can be used to reduce the statistical uncertainties in the PDF. However, in this method it is possible, that the best-fit parametrization does not describe the true distribution in every detail. Thus, choosing between the two approaches, one has to balance between statistical limitation and a non optimal PDF.

As shown in Section 5.8, the data MC agreement between experimental data and best-fit parametrization is in agreement within the 1D projections of the used variables. Thus, there is no obvious sign that the best-fit parametrization has serious problems to describe the data. However, we use the physical motivation to allow an extrapolation in the sparely populated regions. Note that beside the fact that the sample used in this thesis is limited to the Northern Hemisphere, also the PDF construction from best-fit parametrizations is currently limited only to the Northern Hemisphere, because of the leak of a precise parametrization of the neutrino samples from the Southern Hemispheres that shows reasonable data / MC agreement.

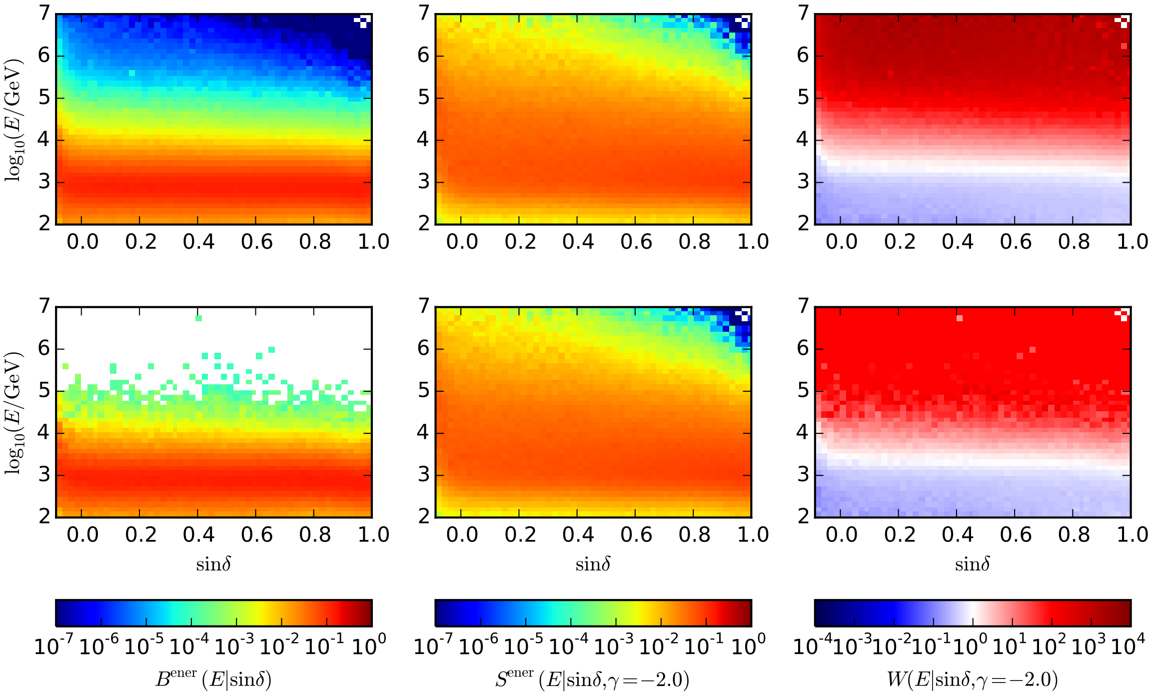

Figure 6.4: Background energy PDF $B^{\text{ener.}}(E|\sin\delta)$ (left), signal energy PDF $S^{\text{ener.}}(E|\sin\delta, \gamma = -2.0)$ for a spectral index of $\gamma = -2.0$ (middle) and ratio $W(\gamma = -2.0) = S^{\text{ener.}}(E|\sin\delta, \gamma = -2.0)/B^{\text{ener.}}(E|\sin\delta)$ (right) for the season IC86-2012/16 as a function of $\log_{10}(E/\mathrm{GeV})$ and $\sin\delta$. The background PDF is estimated from the best-fit parametrization (see Sec. 5.8) (top) and randomized right ascension (bottom). The signal PDF is the same (top and bottom) and are derived from Monte Carlo. Similar plots for other seasons can be found in Appendix C.

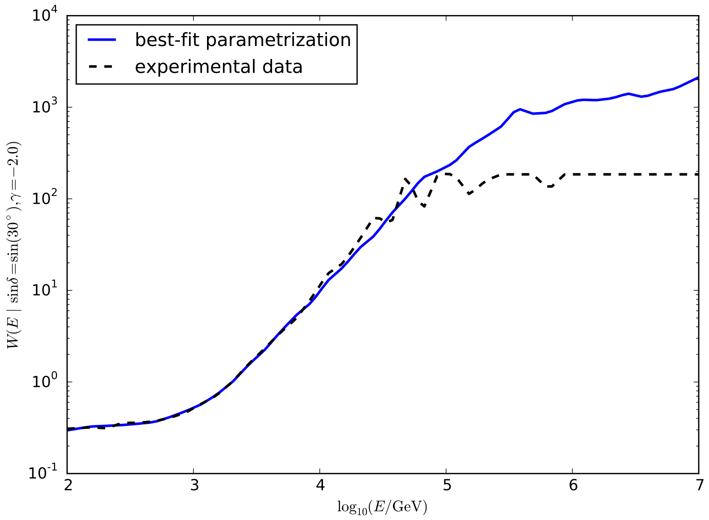

Figure 6.5: Ratio of signal and background energy PDF $W(E|\gamma = -2, \sin(30°)) = S^{\text{ener.}}/B^{\text{ener.}}$ estimated from best-fit parametrization (solid) and randomized data (dashed) for the season IC86-2012/16 as a function of $\log_{10}(E/\mathrm{GeV})$.

To see the power of using a physically motivated parametrization that can extrapolate into sparsely populated regions, Fig. 6.5 shows the energy weight W as a function of $\log_{10}(E/\mathrm{GeV})$ along a slice in $\sin\delta = \sin(30°)$ for both methods. One can see that for low energies both weight factors agree very well. In the region above 10 TeV, statistical fluctuations become dominant if scrambled experimental data are used. The weight from the best-fit parametrizations reaches much larger values, even before reaching a plateau, that is reached if the contribution of the atmospheric flux in the background energy PDF becomes negligible with respect to the astrophysical component.

Note that in case of randomized experimental data there is also a self-penalizing effect, that can be described as follows: once there is an event in a sparsely populated region, this event heavily influences the determination of the background and raises the PDF. Thus, the weighting factor for this event gets smaller.

Note that the effect of a systematically wrong PDF would not result in a systematically wrong p-value, but in a non-optimal sensitivity. However, the improvement in the sensitivity and discovery potential by reducing the statistical uncertainties can be even larger. The impact on the sensitivity and discovery potential can be seen from Fig. 6.6, where the differential sensitivity and discovery potential as a function of the true neutrino energy is shown for a declination of 12.55° and using PDFs constructed by both methods. It can be seen that for neutrino energies $< 100\,\mathrm{TeV}$, the differential sensitivity and discovery potential is the same no matter which method to construct the background energy PDF is chosen. Above 100 TeV however especially the discovery potential improves up to 20-30%.

The effect on the sensitivity and discovery potential depending on the choice of background PDF for an E^{-2} power-law spectrum can be seen in Fig. 6.7 as a function of declination. While the sensitivity improves by only a few percent if choosing the background energy PDF from

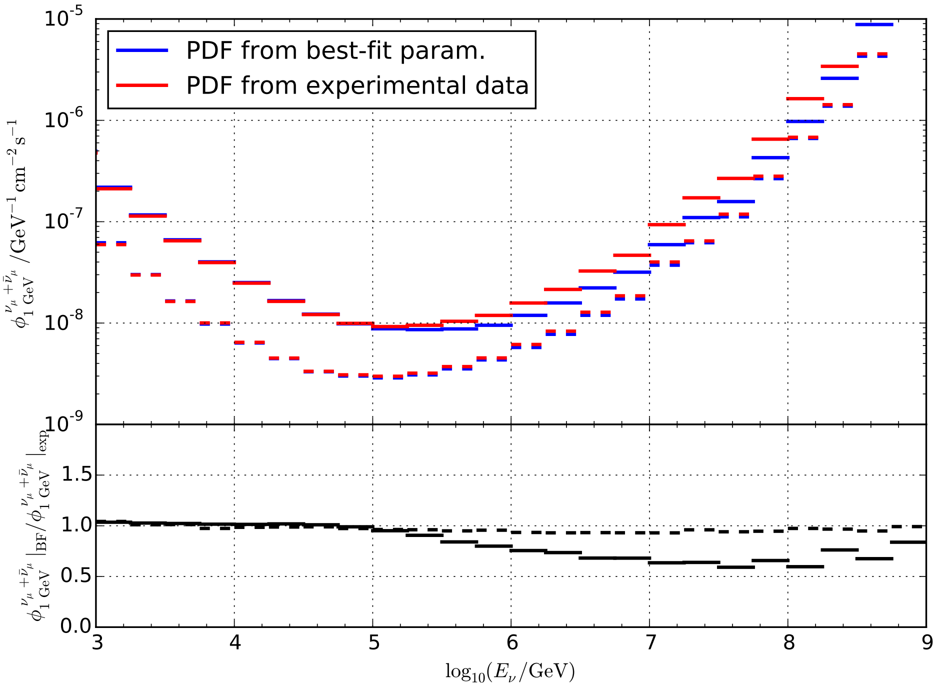

Figure 6.6: Differential sensitivity (dashed) and discovery potential (solid) flux normalization at 1 GeV calculated using background PDFs using the best-fit parametrization (BFP) and randomized experimental data (exp.) shown in blue and red respectively. The lower panel shows the ratio of the flux normalizations for the sensitivity flux and discovery potential flux. The differential sensitivity and discovery potential are calculated for a declination of 12.55°.

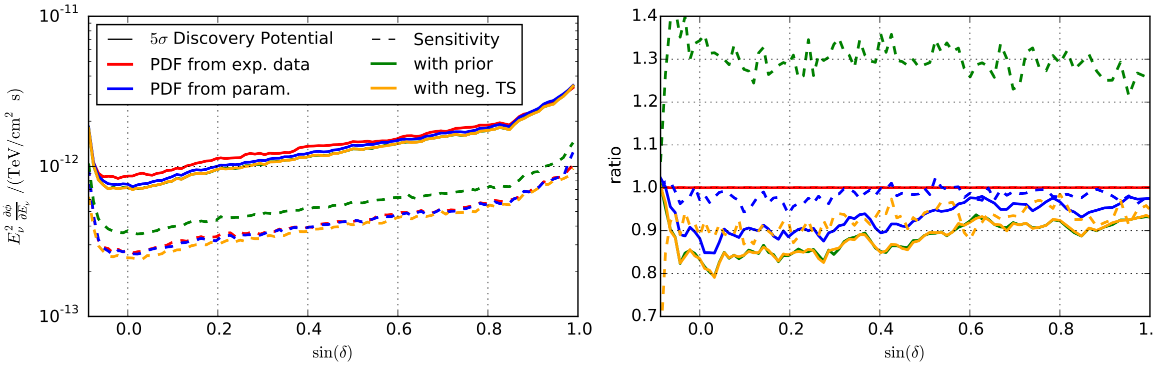

Figure 6.7: Sensitivity (dashed) and discovery potential (solid) of an E^{-2} power-law flux as a function of $\sin\delta$ (left). The sensitivity and discovery potential are calculated using different likelihood and test statistic formulations (see legend). The right panel shows the ratio of the sensitivity or discovery potential flux for different likelihood and test statistic formulations with respect to the reference flux. The reference flux is chosen to be calculated with PDFs estimated with experimental data, no prior and no definition of negative test statistic values (red). Note that the green solid line is hidden by the orange solid line. Note that the clear correlation in the declination dependence is caused by from using the same pseudo experiments. For the likelihood with prior but without the definition of a negative test statistic results in about 80% of $TS = 0$ fits and thus the sensitivity artificially gets worse.

best-fit parametrization, the discovery potential improves by up to about 10% depending on the declination. The largest improvement is reached for declinations close to the horizon, while the gain in discovery potential is not that strong for larger $\sin\delta$. For large $\sin\delta$, the absorption of very high-energy neutrinos in the Earth leads to a generally worse differential discovery potential.

Due to the gain in performance, for the scope of this thesis, we use the best-fit parametrization to construct the background PDFs.

6.3 Combination of Seasons

As the total analyzed data sample consists of several data-taking periods with different conditions and event-selections, the spatial and energy PDFs for these seasons differ. Thus, the PDF estimation and the likelihood function as described in Sec. 6.2 has to be done for each sub-sample individually. The combined likelihood of all sub-samples $\mathcal{L}_{\text{tot}}$ is given by the product of the likelihoods of the individual samples $\mathcal{L}_{\text{j}}$:

$$\mathcal{L}_{\text{tot}}(\vec{x}_s, n_s, \gamma) = \prod_{j}^{\text{season}} \mathcal{L}_j(\vec{x}_s, n_{s,j}, \gamma_j)\,. \tag{6.14}$$

Note that the likelihood of each sample depends on the parameters $\vec{x}_s$, $n_{s,j}$ and γ_j. As we always test the same celestial spot, $\vec{x}_s$ is the same in all samples, while γ_j and $n_{s,j}$ are free

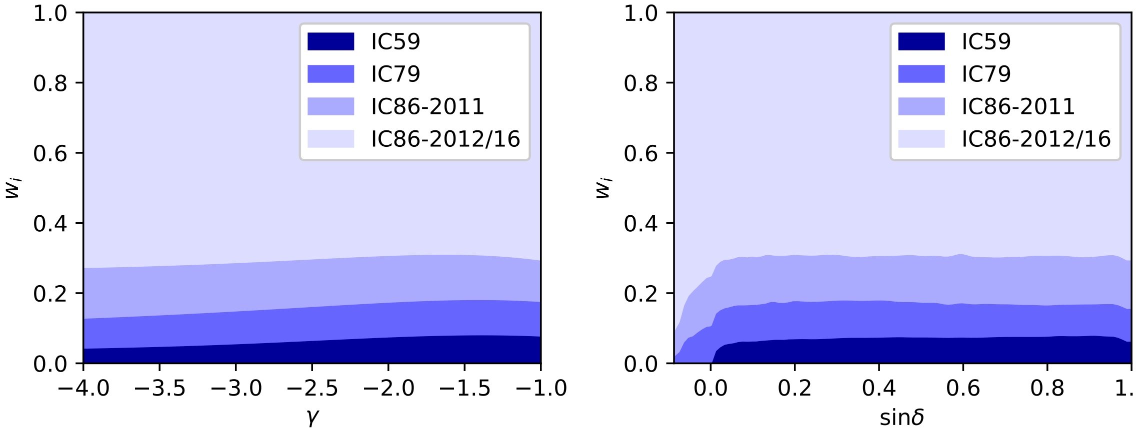

Figure 6.8: Relative weighting factor of all sub-samples to n_s as a function of the spectral index γ (left) for $\sin\delta = \sin(30°)$ and as a function of $\sin\delta$ (right) for a spectral index of $\gamma = -2.0$.

parameters of the likelihood. As γ is the spectral index of the astrophysical point source and the hypothesis to be tested is a steady source, γ can be assumed to be constant over all sub-sample, such that $\gamma_j = \gamma$ for all seasons.

The number of signal events in a single sub-sample j is $n_{s,j}$. Because the sub-samples have different exposures and acceptances and thus different effective areas, $n_{s,j}$ is different for each sub-sample. As the source is assumed to be steady, the sub-sample j contributes proportional to its live-time and its effective area to n_s. Thus, $n_{s,j}$ can be written as

$$n_{s,j} = n_s \times \frac{T_{\mathrm{life},j} \int_0^\infty A_{\mathrm{eff},j}(E_\nu) \cdot \phi(E_\nu) \mathrm{d}E_\nu}{\sum_k T_{\mathrm{life},k} \int_0^\infty A_{\mathrm{eff},k}(E_\nu) \cdot \phi(E_\nu) \mathrm{d}E_\nu} \equiv n_s \times \frac{w_j}{\sum_k w_k}\,, \tag{6.15}$$

where $A_{\mathrm{eff},j}$ is the effective area and $T_{\mathrm{life},j}$ is the live-time of the sub-sample j and $\phi(E_\nu)$ is the source flux. $w_j = T_{\mathrm{life},j} \int_0^\infty A_{\mathrm{eff},j}(E_\nu) \cdot \phi(E_\nu) \mathrm{d}E_\nu$ is the weighting factor of the sub-sample j. Thus, n_s is the only free parameter of the likelihood beside γ.

Note that because the effective area is declination dependent, also the integrals are declination dependent. In addition, the integrals depend on the source flux and thus on the spectral index γ, if an unbroken power-law is assumed.

In Fig. 6.8, the relative weighting factor of all samples is plotted as a function of the spectral index for $\sin\delta$, where the sum of all weighing factors adds up to one. For all values of γ and $\sin\delta$, the largest weight corresponds to the sub-sample IC86-2012/16 as this is by far the sample with the longest data taking period. The variation with respect to spectral index and $\sin\delta$ are small. For $\sin\delta < 0$ the sub-sample IC59 has no contribution because of its data selection, choosing only events from the upper hemisphere (see Sec. 5.6). Note that the prior term for the spectral index γ in Eq. 6.4 is only applied once.

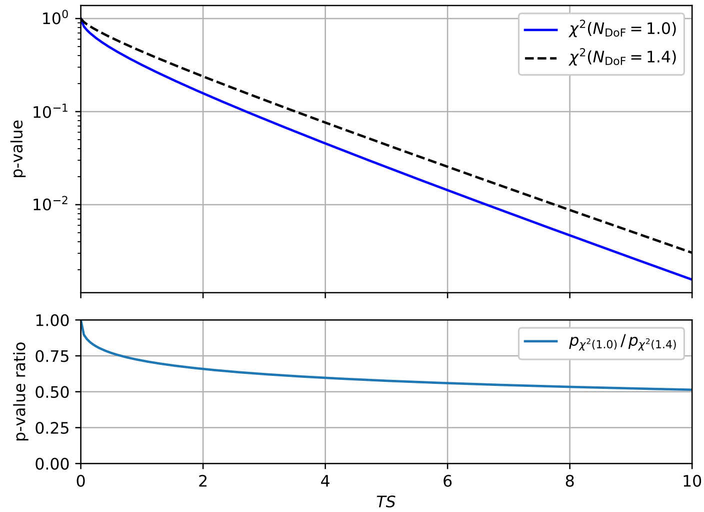

Figure 6.9: Top: P-value as a function of TS value for p_{χ^2} for $N_{DoF} = 1.0$ (fixed γ) and $N_{DoF} = 1.4$ (free γ). Bottom: Ratio of p-values for $N_{DoF} = 1.0$ (fixed γ) to $N_{DoF} = 1.4$ (free γ) as a function of TS value.

6.4 Constrained Spectral Index

The choice of the astrophysical point-source flux model that should be tested is to some extend arbitrary. However, the Fermi-mechanism discussed in Sec. 3.1, yields a generic power-law energy spectrum with spectral index of $-2.0 + \epsilon$, where ϵ is a small additional contribution in case of shock acceleration. Thus, often power-law spectra are analyzed as benchmark scenarios, with spectral indices ranging from -1.0 to -4.0, which is even softer than the spectrum of atmospheric neutrinos.

However, from the experimentally observed diffuse flux, it is known that the astrophysical component can be described by a single power-law with a spectral index of $\gamma_{\mathrm{astro}} = -2.19 \pm 0.10$ [6]. Within the scope of this thesis, we investigate the hypothesis that the spectra of all single sources are similar or equal to the observed spectrum.

If previous knowledge about free parameters of the likelihood is taken into account, the freedom of the likelihood to model the fluctuations in the data sample is reduced. In the likelihood defined in Eq. 6.4, there are two free parameters n_s and γ. These parameters are correlated to some extent. In particulat, γ is degenerated if n_s becomes zero. However, adding previous knowledge about γ by introducing a prior reduces this degeneracy. Moreover it increases the sensitivity.

This can be seen by a simplified case: The TS value that yields a likelihood with and without a prior term is the same, if the spectral index is fitted to the prior position even in case of no prior. By this $\hat{\gamma}$ is the same in both cases and from Eq. 6.8, one can see that the only difference is the prior term itself, which is $\log(P(\hat{\gamma})) = 0$. Thus, there is no difference in the test statistic value. However, by introducing a prior the background test statistic changes due to the reduced freedom of the likelihood. Assuming that in case of no prior n_s and γ

are free parameters, which are correlated resulting in a background test statistic distribution that can be approximated by a χ^2-distribution with $N_{\mathrm{DoF}} \approx 1.4$. Assuming that by adding a prior on γ, the spectral index gets effectively fixed, the only remaining free parameters is n_s and thus the background test statistic distribution can be approximated by a χ^2-distribution with $N_{\mathrm{DoF}} \approx 1$. Comparing the p-values resulting from the same TS value one finds that $p_{\chi^2, N_{\mathrm{DoF}}=1}(TS) < p_{\chi^2, N_{\mathrm{DoF}}=1.4}(TS)$. This means that by adding previous knowledge, the p-value becomes more significant in a signal like case. The gain in p-value for a signal like case is sketched in Fig. 6.9. One can see that the gain in p-value becomes a constant factor for large TS values.

On the other hand, if the added prior does not describe the realization in nature, the likelihood has not enough freedom to match the signal parametrization and the data. In this case we loose sensitivity to spectra that are not compatible with the added prior.

To focus the analysis performed in this thesis to those sources that produce the observed spectrum of astrophysical events, we add a Gaussian prior for the spectral index

$$P(\gamma) = \frac{1}{2\pi\sigma^2_{\gamma_{\mathrm{astro}}}} \exp\left(-\frac{(\gamma - \gamma_{\mathrm{astro}})^2}{2\sigma^2_{\gamma_{\mathrm{astro}}}}\right) . \tag{6.16}$$

The position and the width of the prior are taken from the latest update of the best-fit of [5, 6] and are $\gamma_{\mathrm{astro}} = -2.19$ and $\sigma_{\gamma_{\mathrm{astro}}} = 0.10$. Taking the log of the Gaussian prior yields:

$$\log P(\gamma) = -\frac{(\gamma - \gamma_{\mathrm{astro}})^2}{2\sigma^2_{\gamma_{\mathrm{astro}}}} + \mathrm{const} . \tag{6.17}$$

Note that the log of the normalization is a constant with respect to γ and thus does not influence the parameter estimation. In addition, the log of the normalization would also result in a constant shift in all TS values, which is irrelevant and thus the constant term is dropped in Eq. 6.17 and the following, such that $\log P(\gamma = \gamma_{\mathrm{astro}}) = 0$.

In Fig. 6.10, the likelihood landscape for right ascension 177.89° and declination 23.24° is shown as a function of the spectral index and flux normalization. On the left side one can see a scan of the likelihood landscape without a prior on the spectral index. One can see that there is a degeneracy in the likelihood landscape between the spectral index and the flux normalization. This results from the fact, that the majority of events in a source spectrum are located at lower energies, while the fit is more sensitive to higher energies. Thus, a small change at higher energies has a strong effect on the flux normalization at lower energies. On the right panel a prior was added. The best-fit shifts and is now close to the central value of the prior. Because the best-fit point for the likelihood without a prior is consistent with the spectral index of the prior at about the 1σ CL the results are compatible. Thus, as the source spectrum is not strongly constrained by the few events that contribute to the source, the prior has the largest handle on the fit of γ and thus the spectral index is effectively fixed allowing just for a small variation.

The effect on the sensitivity and discovery potential by adding the prior on the spectral index can be seen in Fig. 6.7. The ratio of the sensitivity and discovery potential relative to the sensitivity and discovery potential calculated from PDF estimated from experimental

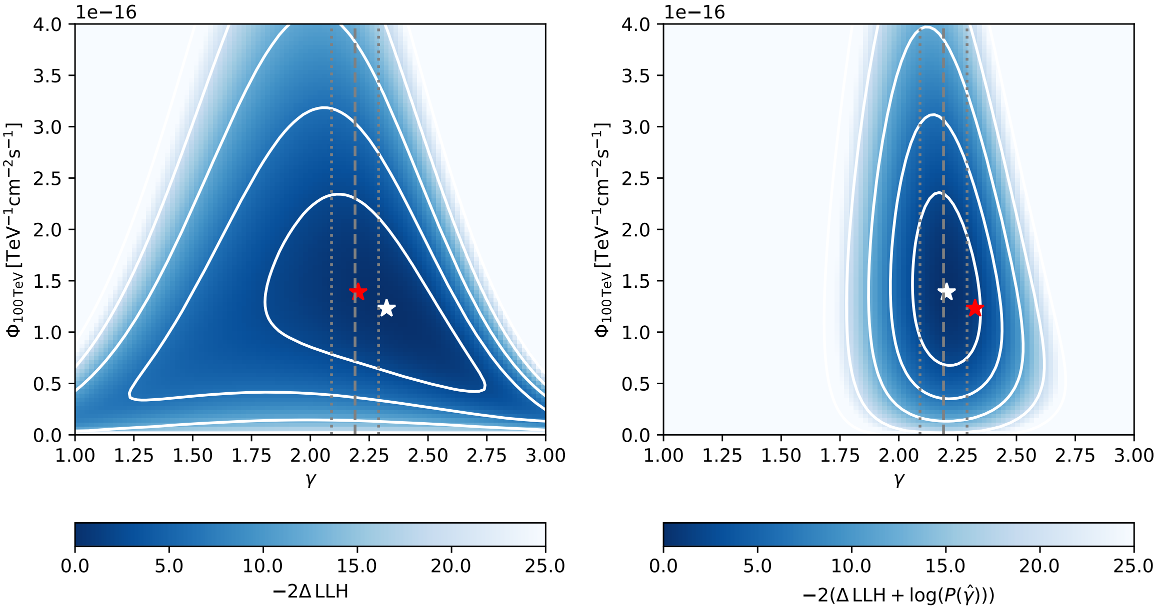

Figure 6.10: Scan of the likelihood landscape in spectral index γ and flux normalization for experimental data and the direction right ascension 177.89° and declination 23.24°, which is the host significant spot in the Northern sky (see Sec. 8.1.2). The left panel shows the scan without a prior on the spectral index while the right panel shows the scan with a prior on the spectral index. The position and the 1σ uncertainty range of the prior are indicated by gray dashed and dotted lines. The best-fit spectral index and flux normalizations are indicated by white stars, while contours show the central 1 to 5 sigma regions assuming Wilk's theorem with two degrees of freedom. The red star shows the best-fit of the respective other panel.

data without a prior is shown in the right plot of Fig. 6.7. The discovery potential reduces on average by about 11% relative to the discovery potential calculated with PDFs estimated from experimental data without a prior and on average by about 5% relative to the discovery potential calculated with PDFs estimated from the best-fit parametrization and without a prior. However, the behavior is different for the sensitivity. The sensitivity increases on average by about 30% relative to the flux required using PDFs estimated from experimental data and no prior and 32% when compared to the flux required by using PDFs estimated from best-fit parametrization and no prior.

The increase in flux normalization is a result of a degeneracy of the sensitivity definition. This can be explained by the fraction of trials that result in $\hat{n}_s = 0$ fits. Because of the definition of the TS in Eq. 6.8 the TS value for $\hat{n}_S = 0$ is $TS = 0$. Thus, once $\hat{n}_S$ is 0, which is the lower bound of the allowed $\hat{n}_S$ range, $TS = 0$. In Fig. 6.11 the fraction η of pure background trials that result in a $\hat{n}_s = 0$ fits is shown as a function of $\sin\delta$ using different definitions of the likelihood. In case the likelihood is defined without a prior, the fraction η is between 40%-50% except for declinations very close to the end of the sample, i.e. below the horizon and at the celestial pole at $\sin\delta \sim 1$. In case a prior on the spectral index is added the

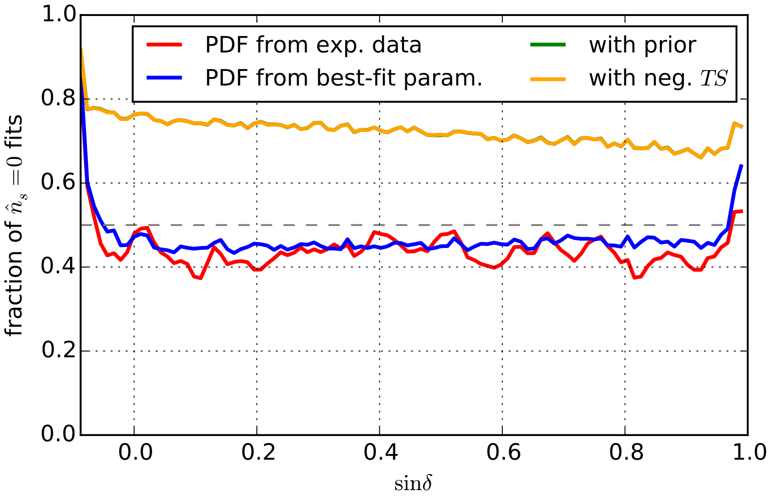

Figure 6.11: Fraction of pure background trials that result in a best-fit $\hat{n}_S = 0$ as a function of $\sin\delta$. For each declination about 10^4 trials have been generated. By adding a prior term on the spectral index the fraction of $\hat{n}_S = 0$ fits increases strongly. The gray dashed line indicates the fraction, where equally many trials result in $\hat{n}_S = 0$ and $\hat{n}_S > 0$. Note that the green line is hiden by the orange line, because the likelihood definition and thus the best fit parameters is the same, however the TS definition is different. Note that if we have $\hat{n}_S = 0$ we can define $TS \leq 0$.

fraction η increases up to about 70%-80%. The sensitivity is defined by the averaged upper limit, and thus depends on the median of the TS distribution of pure background. However, if more than 50% of trials result in $\hat{n}_s = 0$ and thus $TS = 0$ fits, the median of the background TS distribution is exactly zero. If even up to 80% trials result in $TS = 0$ the sensitivity flux has to generate a TS distribution that is even above the 80% quantile. Thus, the sensitivity is not comparable and under-estimated. In the next section a workaround for this problem is presented.

6.5 Test Statistics

For a potential source position, the likelihood is maximized with respect to n_s and γ with $n_s \geq 0$ and a likelihood ratio test is performed to compare the best-fit likelihood to the null hypothesis of no significant clustering with $n_s = 0$. The likelihood ratio as defined in Eq. 6.8 is called the test statistic TS. When using this definition, the TS distribution follows the shape of the red distribution in Fig. 6.12. A clear pile-up at $TS = 0$ can be seen. As discussed in Section 6.4, the fraction of background trials, that result in a test statistic value of 0, can be up to 80%. This would result in an under-estimation of the sensitivity because of the degeneration of the 50% quantile with other quantiles of the distribution.

A work-around to break the degeneracy is to spread the pile-up at $TS = 0$ over a certain test statistic range, where the test statistic gives the level of incompatibility of the data with

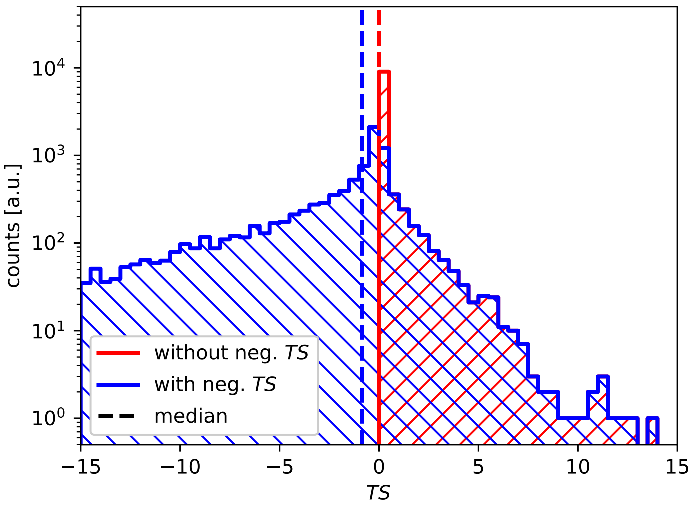

Figure 6.12: Test statistic distribution for pseudo experiments with only background. The TS definition as in Eq. 6.8 results in the red distribution that exhibits a prominent peak at $TS = 0$. In the blue distribution each trial that fits $\hat{n}_S = 0$ gets a negative TS definition given by Eq. 6.21. For each distribution the median is shown by a dashed vertical line.

the background hypothesis. Therefore, an alternative definition is required that should spread trials that fit $\hat{n}_S = 0$ to negative test statistic values.

In Fig. 6.13 the blue line is a sketch of a likelihood profile with respect to n_s for a normal case with $\hat{n}_S \approx 4$, that is given by the maximum of the likelihood. The test statistic value is proportional to the likelihood value at the best-fit point. In case of a local under-fluctuation, however, the likelihood will increase while approaching $n_s = 0$ from the right and thus once n_s reaches the parameter bound of $n_s = 0$ the test statistic value is $TS = 0$. However, the shape of the likelihood in the region around $n_s = 0$ can indicate the level of disagreement with the data.

A first estimate can be made by changing the allowed parameter space of $n_s = 0$ to $[\epsilon, \infty)$ where ϵ is a small positive number. In this case the best-fit parameter would be $\hat{n}_s = \epsilon$ and thus the test statistic would be $TS = 2 \cdot \Delta\mathcal{L}(\hat{n}_s = \epsilon)$. As the likelihood value at $\hat{n}_s = \epsilon$ will not be exactly the same for every trial the TS distribution will spread into the negative TS space. By this definition, the test statistic value is an approximation of the slope of the likelihood at $n_s = 0$ and ϵ is an arbitrary parameter.

A better definition would be to calculate the slope of the $\Delta \log \mathcal{L}$ at $n_s = 0$ analytically. This is possible and the first order derivative of the TS is given by

$$\left.\frac{\mathrm{d}\log\mathcal{L}}{\mathrm{d}n_s}\right|_{n_s=0} = \sum_{i=1}^{N} \frac{1}{N}\left(\frac{S_i}{B_i}W_i - 1\right) . \tag{6.18}$$

Note that by this definition the TS value is given by the slope of the likelihood while for $\hat{n}_s > 0$ the TS is given by a likelihood difference.

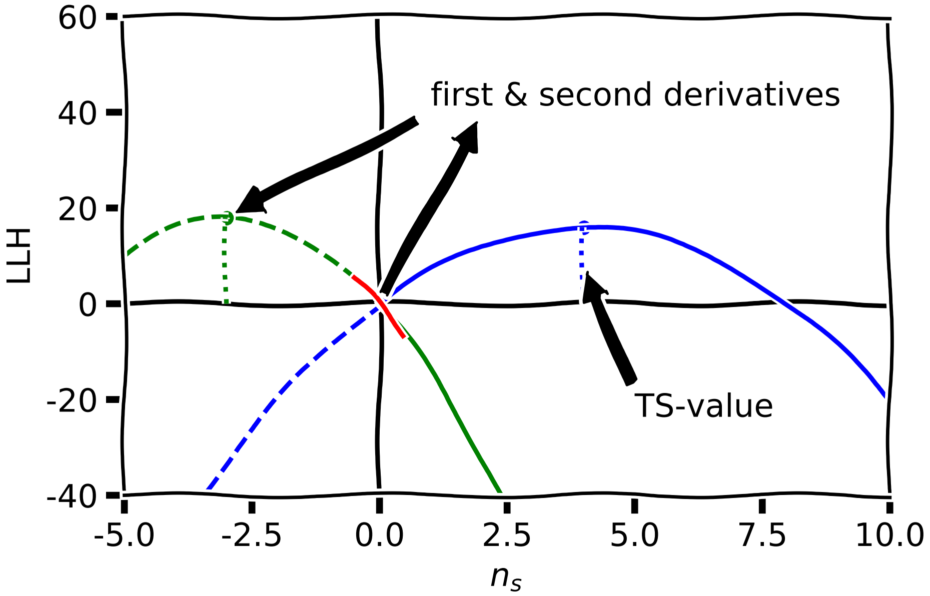

Figure 6.13: Sketch to illustrate the construction of TS values in case of background fits. The blue curve corresponds to a profile likelihood for a fit with $\hat{n}_s > 0$ and the TS value is proportional to the $\Delta \log \mathcal{L}$ value at the dashed blue line. The green curve corresponds to a profile likelihood for a fit with $\hat{n}_s = 0$.

Thus, to define test statistic values for $\hat{n}_s = 0$ with a similar meaning than for $\hat{n}_s > 0$ one can derive the following TS definition: Assuming the likelihood profile has a maximum in the unphysical region of $n_s < 0$, the likelihood profile around that maximum can be described by a Taylor-expansion of the likelihood profile. In a small region around the maximum the profile can be described by the leading terms of the Taylor-expansion, which is a parabola. If the maximum is not far in the unphysical region, the assumption of a parabola shape is still valid at $n_s = 0$. The parabola can be fully described by the first and second order derivative of the likelihood profile with respect to n_s. Like the first order derivative of the TS, also the second order derivative of the TS with respect to n_s can be calculated analytically:

$$\left.\frac{\mathrm{d}^2 \log \mathcal{L}}{\mathrm{d}^2 n_s}\right|_{n_s=0} = -\sum_{i=1}^{N} \frac{1}{N^2} \left(\frac{S_i}{B_i} W_i - 1 \right)^2 . \tag{6.19}$$

Thus, we expand the shape of the $\log \mathcal{L}$ function at $n_s = 0$ with a Taylor-expansion of second order to estimate the minimum TS value for negative n_s values resolving the peak at $TS = 0$. Note that just the derivative in n_s is used. The derivative of γ vanishes at $n_s = 0$.

In the following we derive the coefficients of the Taylor expansion, the minimum of the parabola and the value of the parabola at the minimum.

The tailor series around zero is given by:

$$-\log \mathcal{L}(n_s)|_0 \approx \underbrace{-\log \mathcal{L}(0)}_{\equiv c} - \underbrace{\left.\frac{\mathrm{d} \log \mathcal{L}}{\mathrm{d} n_s}\right|_{n_s=0}}_{\equiv b} n_s - \underbrace{\frac{1}{2} \left.\frac{\mathrm{d}^2 \log \mathcal{L}}{\mathrm{d} n_s^2}\right|_{n_s=0}}_{\equiv a} n_s^2 . \tag{6.20}$$

Note that $c = -\log \mathcal{L}(0)$ is the same as the likelihood of the background hypothesis $-\log \mathcal{L}_0$ and thus in the TS the constant value cancels. The extremum of the parabola is $\tilde{n}_s = -\frac{b}{2a}$ with a value of $-\log \mathcal{L}(\tilde{n}_s) = -\frac{b^2}{4a}$.

Thus, using Eq. 6.18 and Eq. 6.19, one can define the test statistic value for $\hat{n}_S = 0$ fits as

$$TS = -2 \cdot \log \mathcal{L}(\tilde{n}_s) = 2 \frac{\left(\sum_i \left(\frac{S_i}{B_i} W_i - 1\right)\right)^2}{2 \sum_i \left(\frac{S_i}{B_i} W_i - 1\right)^2} \,. \tag{6.21}$$

This definition is used to calculate TS values for the blue distribution in Fig. 6.12 which now has a long tail in the negative TS region. From Fig. 6.12 it can also be seen that the 50% quantile of the background distribution is now well defined and no longer degenerated. As a result, the sensitivity can be estimated as shown in Fig. 6.7 and a reduced sensitivity flux of on average about 8% compared to the likelihood defined with PDFs from experimental data and 5% compared to the likelihood defined with PDFs estimated from best-fit parametrization.

Note that this definition of the TS does not have any influence on fits that have $\hat{n}_S > 0$ and thus all TS values that are positive. Especially it has no effect on the discovery potential, which is defined by the 5σ quantile of the background TS distribution. This can be seen in Fig. 6.7 because the blue and orange discovery potential lines are exactly on top of each other. In addition, one can see from Fig. 6.11 that because of the fraction of $\hat{n}_s = 0$ fits does not exceed 80%, this definition does not change the TS values for all trials resulting in a p-value of less than 20%. By this, the definition does not change any significant result and does not interfere with any possible detection. However, it helps to quantify the median average upper limit and thus the sensitivity of the analysis in a comparable way.

Beside the TS distribution of pure background, also the TS distribution for pseudo experiments with injected signal from a point-like source is of interest. In Fig. 6.14, one can see the TS distribution once for only background and once with an injected signal of five events generated from an $E^{-2.0}$ power-law distribution. The signal events are injected at the tested source position. A clear shift to the right can be seen as it is expected for pseudo experiments with signal. The generation and injection of signal pseudo experiments is discussed in Section 7.1

6.6 Local p-Values

When testing a celestial point for the existence of a point-like neutrino source, the result are the best-fit parameters $\hat{n}_s$ and $\hat{\gamma}$ as well as the TS value for that point. The TS value can be translated into a local p-value, where the local p-value gives the probability to find an equal or larger TS value for this celestial point in case of only background. The p-value is the fraction of trials that result in an equal or larger TS value from the background TS distribution, which can be generated from background pseudo experiments.

Note that the TS may depend on the tested celestial direction. However, due to the daily rotation of the Earth and IceCube's special position at the South Pole, no dependence on the right ascension angle is expected. There is however a slight declination dependency. Thus, the background TS distributions has to be generated using pseudo experiments for several different

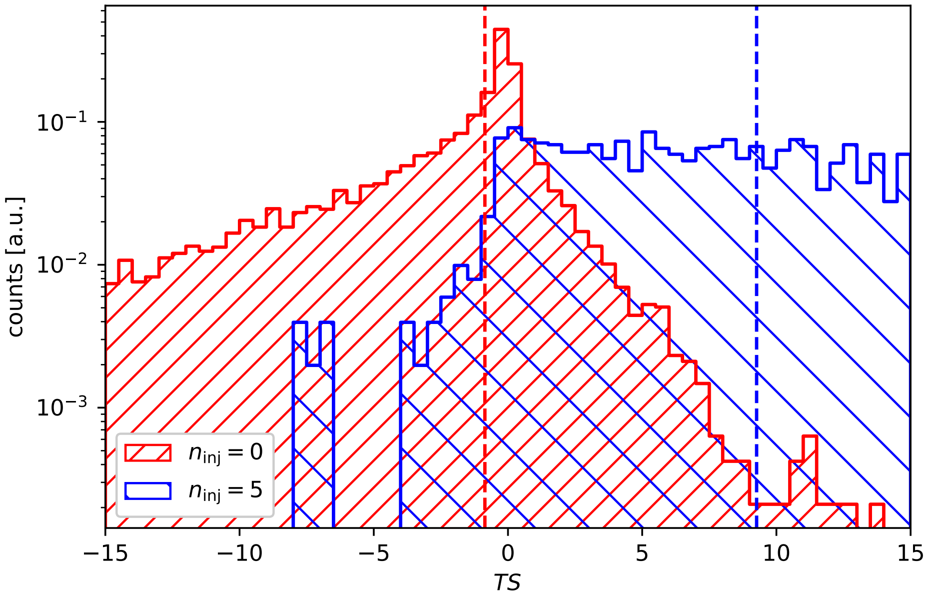

Figure 6.14: Test statistic distribution for only background (red) and an injected signal of five signal events generated from an $E^{-2.0}$ power-law spectrum. The median of each distribution is indicated by a dashed vertical line. The test statistic distribution has been generated for a declination of $\delta = 0°$.

declinations. In Fig. 6.15 (left) TS-distributions for five different declinations are shown. The local p-value as a function of the TS value is shown in Fig. 6.15 (right) for the same declinations. Due to a limited amount of generated pseudo experiments, a statistical uncertainty is shown for the local p-value. This uncertainty band is calculated based on binomial statistics. For the distributions shown in Fig. 6.15 at least 10^6 pseudo-experiments have been generated. The p-value is a smooth function of the test statistic. For reference, the one sided 1 to 5 sigma levels are indicated by dashed gray lines.

The p-value for testing a single direction in the sky is called a local p-value in the following. If multiple points in the sky are tested, the p-value has to be corrected for the number of trials. The calculation of this trial corrected p-value is discussed when the corresponding tests are presented in Chapter 8. Before, the generation of pseudo-experiments and a detailed performance study is presented in the next chapter.

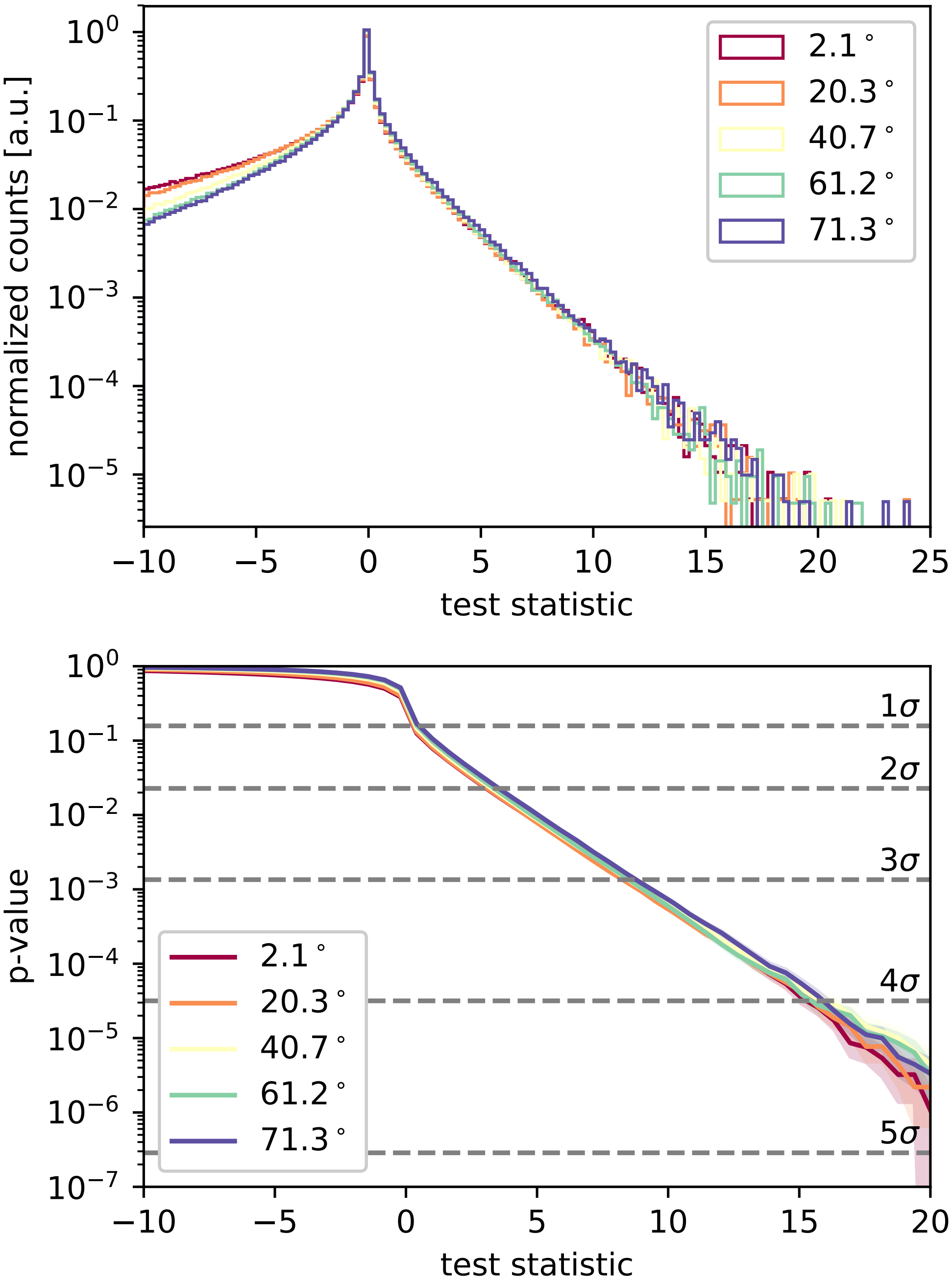

Figure 6.15: Test statistic histogram from only background pseudo experiments (top) and local p-value as a function of test statistic (bottom) for different declinations (see legend). The one sigma uncertainty band around the local p-value gives the binomial uncertainty due to the finite amount of generated pseudo experiments generated to calculate the p-value function. The gray dashed lines indicate the 1, 2, 3, 4 and 5 σ level.

Chapter 7

Final Analysis Performance

Declaration of Pre-released Publications The analysis performance presented in this chapter have been previously published by the IceCube Collaboration in M. G. Aartsen *et al.* (IceCube Collaboration), "Search for steady point-like sources in the astrophysical muon neutrino flux with 8 years of IceCube data" The European Physical Journal C 79, 234 (2019). The author of this thesis has written this publication as a corresponding author. The author contributed to the calculation of the analysis performance and the determination of systematic uncertainties.

In Chapter 6, the analysis method to test a celestial position has been presented. In this chapter, the performance of the analysis method is evaluated. Essential for the evaluation of the performance are the generation of pseudo-experiments, which is discussed in Sec. 7.1. The result of the likelihood fit as presented in Chapter 6, is the best-fit source spectral index and number of signal events which can be converted to the best fit flux. The relation of these parameters to their true physical counter-parts is discussed in Sec. 7.2. In Sec. 7.3, the potential to discover a point-like source and the potential to exclude signal parameters are discussed in more detail. The systematic uncertainties on these results are discussed in Sec. 7.4.

7.1 Generation of Pseudo Experiments

The basis to evaluate the performance of an analysis is the generation of pseudo-experiments. These pseudo-experiments should represent the data as realistic as possible and follow the same underlying distributions as the measured experimental data. These underlying distributions are usually a composite of the background contribution and some signal contribution. A pseudo-experiment that is composite of both signal and background is generated in a two step process: first the signal contribution is generated and then background is added. In Sec. 7.1.1, the generation of pure background pseudo-experiments is discussed and in Sec. 7.1.2 the generation of events coming from point-like sources is explained.

7.1.1 Generation of Background Pseudo Experiments

To generate background pseudo-experiments, there are different approaches similar to the approaches to estimates PDFs as discussed in Sec. 6.2.

The first approach relies on experimental data only. In this method, each experimentally observed event gets a new randomized right ascension assigned. By this, pseudo-experiments are generated, that have the same declination, energy and angular error estimate distributions as the experimental data. Any spatial correlation get lost due to the random right ascension

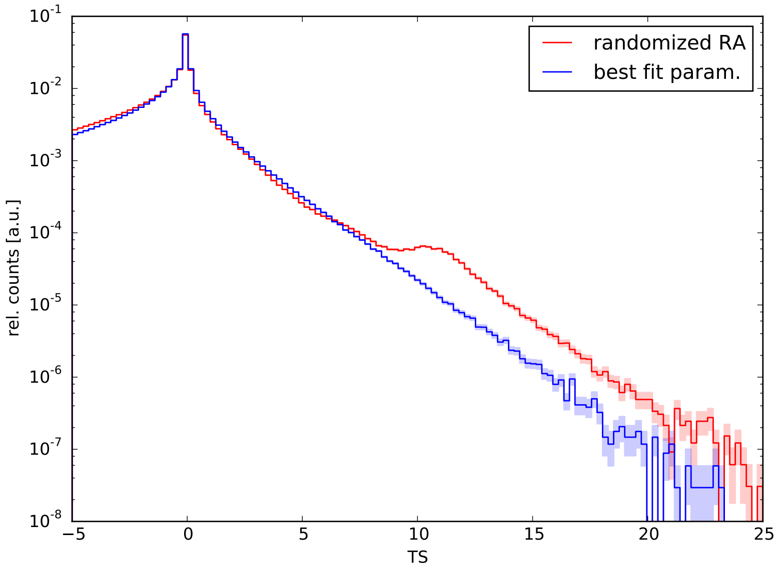

Figure 7.1: Test statistic distribution for background only at a declination of 11.4°. The red histogram is calculated from pseudo-experiments based on randomized experimental data. The blue histogram is calculated from pseudo-experiments generated from Monte Carlo using the best-fit parametrization of the sample.

value. It is expected that the right ascension distribution is uniform, due to the daily rotation of the Earth and the up-time of more than 99% of the detector. Note that randomizing the right ascension is a valid approach in cases where the data sample extends over a time-range that exceeds several days. For observation periods of few days or below, the azimuth structure of the detector acceptance does not average out when the right ascension is calculated. In that case, the pseudo-experiment has to be generated by assigning random observation times. For time-integrated analysis with long data taking periods this is equivalent to assigning random right ascensions. This method is robust as it does not depend on any Monte Carlo simulation or parametrization. In the following this method will be called "randomized right ascension" or short RRA.

Another approach relies on the best-fit parametrization of experimental data and full detector Monte Carlo simulation. In this case, Monte Carlo events are drawn from a Monte Carlo sample relative to their individual best-fit weight. The best-fit parametrization is composed of a conventional atmospheric neutrinos flux and an astrophysical neutrinos flux[1]. The resulting event sample will follow the best-fit parametrization, which is a parametrization of the zenith and energy spectrum. In this approach also the right ascension is generated from a uniform distribution. This approach will be called "best-fit parametrization" or short BFP.

In Fig. 7.1, one can see the background TS distribution for a declination of about 11° once generated from pseudo-experiments generated with the RRA-method (blue) and once with

---

[1] In principle also a prompt atmospheric neutrinos flux component is considered, however the flux normalization of this component is fitted to 0 in the diffuse best-fit (see Sec. 5.8).

the BFP-method (green). The distributions are very similar but not identical, especially the TS distribution from pseudo-experiments generated with the RRA-method shows a bump at $TS \approx 10$ which is not visible if using the BFP-method. The bump is caused by a single event that gets a very large energy-weight in the analysis [259], namely the most energetic event with a declination of 11.36°. Thus, in each pseudo-experiment where this event gets a right ascension value close to the tested direction, this event strongly contributes and leads to the peak in the TS. Such a peak does not appear in the TS distribution generated using the BFP-method as in these pseudo-experiments also the energy and declination varies and thus the contribution of such an event is not always the same. On average there will be similar many events with these high energies but their contribution gets smeared out and does not always appear at the same declination. Thus, the TS distribution is smooth and does not show peaks as in the RRA-method. This example shows a drawback of the RRA-method.

From a frequentist point of view, pseudo-experiments should produce different representations of the same underlying distributions. However, the generation of pseudo-experiments using the RRA-method always results in the exact same energy proxy, declination and angular uncertainty estimate value. Thus, this method can only be used to test the sub-hypothesis of uniform arrival directions under the condition that the declination, energy and angular uncertainty estimates are exactly the same. However, in case of the BFP-method the declination, energy and angular uncertainty estimators show fluctuations from pseudo-experiment to pseudo-experiment. Thus, the hypothesis is tested that events are distributed with respect to the underlying distribution which is the best-fit distribution. This hypothesis covers a larger phase space as tested by the RRA-method, as all event parameters are allowed to vary within their distribution. Especially the hypothesis tested with the BFP-method includes the hypothesis tested with the RRA-method and thus gives a more general answer.

Thus, the two methods give answers to two different questions, which are: "What is the probability that events show no sign of clustering given exactly the measured declination, energy and angular resolution values?" and "What is the probability that events show no sign of clustering give that declination, energy and angular resolution values follow the best-fit distribution?". Both questions are tightly coupled and will often give a very similar result as can be seen in Fig. 7.1.

On the other hand, the RRA-method has the advantage, that it is robust with respect to systematic uncertainties, because the randomized data describe the experimental distributions and correlations in all details. Thus, by choosing between both methods one has to balance between the effect of the specific realization of the energy, declination and angular error values and the risk of potential presence of systematic uncertainties in the best-fit parametrization. In the following, the best-fit parametrization will be used as the default method if not stated otherwise, because there is no sign of systematic mis-modeling of the experimental data by the best-fit parametrization [5, 150] (see Sec. 5.8).

Note that both approaches, RRA-method and BFP-method, are only valid if a signal, that is already in the experimental data, is small compared to the total detected sample and can be neglected. As no point-like source has been found in previous studies, the assumption is valid. However, this can only be assumed for testing individual source locations. Once the full sky

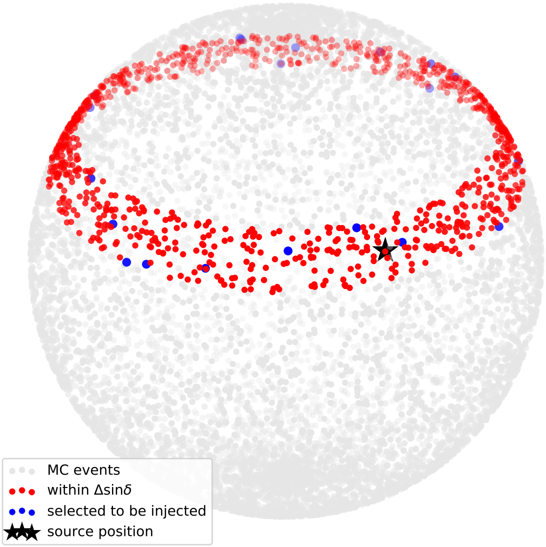

Figure 7.2: Sketch to illustrate the signal generation in pseudo-experiments. Monte Carlo event directions are indicated by circular marker. The source position is marked by a black star.

is tested, e.g. for a population of sources a potential signal contribution has to be considered (see Sec. 9.2.2).

7.1.2 Generation of Pseudo Experiments Including Signal

To study the performance of an analysis for a potential signal, events coming from a point-source have to be generated. This is only possible by relying on full detector Monte Carlo simulation, because no point-like source has been discovered so far. The signal events are generated depending on the signal parameters, which are the source position, the source spectrum shape and the source strength. In case the source spectrum is assumed to be a power-law spectrum, the spectral index has to be given to determine the shape and the flux normalization of the spectrum has to be given as for the source strength. For a given set of source parameters, signal events are generated by the following steps (see Fig. 7.2 for illustration):

- Events are generated using a full detector simulation uniformly distributed on a sphere (see gray markers in Fig. 7.2). This has to be done once and can be saved as a large pool of Monte Carlo events.

- Events within a small declination band with width $\Delta \sin \delta$ are selected (see red markers in Fig. 7.2). By this, it is required, that the events are representative for this declination and thus their correlations between declination, energy estimator and angular resolution is well described.

- The number of signal events corresponding to the signal flux strength ϕ_0, signal flux spectrum $\phi(E)$ and source declination δ are calculated. Therefore, the flux normalization ϕ_0 is converted using the flux distribution $\phi(E)$ and the effective area A_{eff} for the source declination δ into an expected number of signal events μ. The final number of signal events n_{inj} is drawn from a Poisson distribution with an expectation value of $\mu = \int \phi(E|\phi_0, \gamma) A_{\mathrm{eff}}(E|\delta)\,\mathrm{d}E_\nu$. The integral is performed over all neutrino energies. Note that the effective area also has to be calculated as an averaged effective area for a small declination band with width $\Delta \sin\delta$ as the effective area is also calculated from full detector Monte Carlo simulation.

- n_{inj} events are selected from the events within the declination band. The events are picked with respect to an energy dependent weighting factor corresponding to the source spectrum. Thus, it is achieved, that the picked events follow the source spectrum.
- For each selected event, a rotation matrix is calculated that rotates the true direction of the Monte Carlo event onto the source position. This rotation matrix is then applied to the reconstructed direction of the event. By that, it is achieved that the events are spread around the source position corresponding to the point-spread function (see Sec. 5.7).

Within the procedure above, the $\Delta \sin\delta$ is the only free parameter, once the source position, spectrum and strength are given. $\Delta \sin\delta = \sin(1°)$ is chosen as default value as motivated in Appendix D. In addition a systematic uncertainty on the sensitivity and discovery potential of ±8% has to be taken into account.

7.2 Bias of Fitted Parameters

Using pseudo-experiments with injected signal, it is possible to test the behaviour of the estimated parameters $\hat{n}_s$ and $\hat{\gamma}$ and their correlation with the true parameters n_s and γ. To characterize the behaviour of a parameter estimator one usually uses the quantities "consistency", "bias" and "efficiency" [257]. A maximum likelihood estimator is usually consistent [257] and in the large statistic limit the efficiency reaches the minimal variance bound, which is the smallest possible variance that can be achieved for an unbiased parameter bound. However, a maximum likelihood estimator is in most cases biased. An estimator is called unbiased, if the expectation value $\langle \hat{a} \rangle = a$ where a is the true value, otherwise it is called biased. Therefore, we will have a closer look at the bias of the parameters $\hat{n}_s$ and $\hat{\gamma}$.

In Fig. 7.3, the median and central 68% quantile of the best-fit parameters $\hat{n}_s$ and $\hat{\gamma}$ are shown as a function of the number of injected events n_{inj}. One can see that the $\hat{n}_s$ slightly over-estimates the injected number of events n_{inj}. This effect becomes stronger if the prior on the spectral index is applied and the bias increases with increasing n_{inj}. That $\hat{n}_s$ is over-estimated may depend on the injected signal spectrum. As the injected signal is harder than the prior on the spectral index, more events at higher energies are generated. Thus, the total number of events is over-estimated because the analysis is more sensitive to events at higher energies and additional events at lower energies do not penalize the likelihood strongly. However, as the bias in n_s is not that strong and a monotone function can be found for $\langle \hat{n}_s \rangle (n_{\mathrm{inj}})$ the best-fit

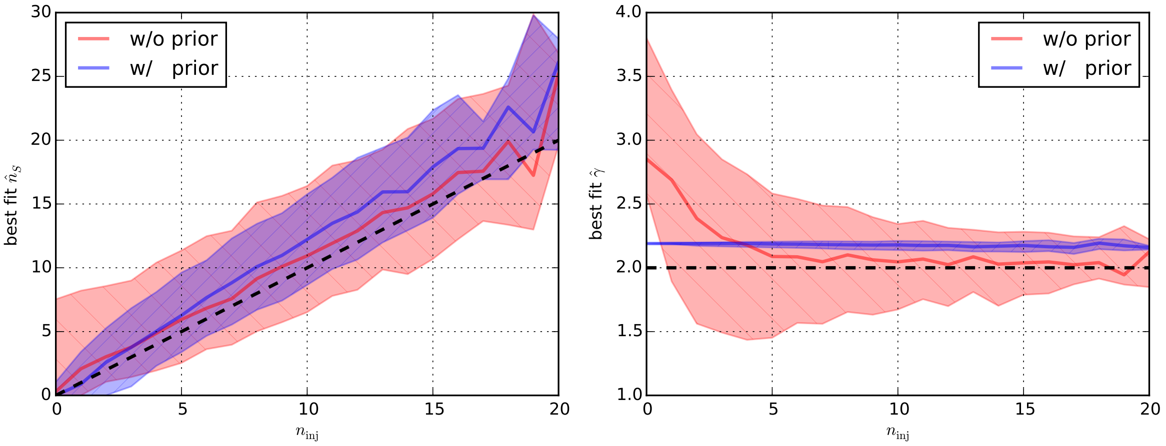

Figure 7.3: Median and central 68% quantiles of best-fit $\hat{n}_s$ (left) and $\hat{\gamma}$ (right) for a fixed number of injected events $n_{\rm inj}$. The curves are shown once for the likelihood defined with and without the prior (blue/red). The black dashed line shows the true injected parameters.

parameter can be corrected for the bias afterwards. The correlation coefficient between $\hat{n}_s$ and $n_{\rm inj}$ is 0.986.

For $\hat{\gamma}$ one can see that in the case where no prior is added on the spectral index, the estimator becomes unbiased for $n_{\rm inj} \gtrsim 10$. However, for small $n_{\rm inj}$ the best-fit parameter $\hat{\gamma}$ shows a strong bias to soft spectra. In case the prior on the spectral index is used, the parameter is strongly biased toward the central value of the prior. For $n_{\rm inj}$ up to 20 the best-fit γ is basically fixed by the prior. The additional constrain on this parameter due to the data is very weak. This is a result of the slight degeneracy between $\hat{n}_s$ and $\hat{\gamma}$ seen in Fig. 6.10. An anti-correlation with a correlation coefficient of -0.784 can be calculated between $\hat{\gamma}$ and $n_{\rm inj}$. Due to the prior on the spectral index, a statement about source individual γ based on $\hat{\gamma}$ is very limited.

Note that the bias on the parameters $\hat{n}_s$ and $\hat{\gamma}$ depend on the source spectrum and source strength and is shown in Fig. 7.3 only for a spectral index of -2.0. To calculate best-fit fluxes the corresponding best fit source spectrum is used to correct the bias on the number of signal events and thus the flux normalization.

The parameter $n_{\rm inj}$ can be converted to the flux normalization of the source spectrum by using the effective area. As the effective area is declination dependent, also the conversion from $n_{\rm inj}$ to ϕ_0 is declination dependent. The conversion factor from $n_{\rm inj}$ to ϕ_0 for a power-law spectrum with spectral index of -2.0 can be found in Fig. 7.4.

7.3 Sensitivity and Discovery Potential

The sensitivity and discovery potential quantify the performance of the analysis. While the discovery potential quantifies the ability to discover a deviation from the null hypothesis, the sensitivity quantifies the ability to exclude a certain signal parameter space of the alternative

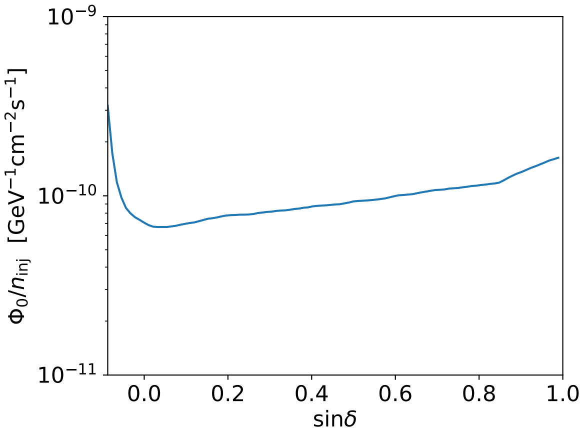

Figure 7.4: Flux normalization for an $E^{-2.0}$ spectrum per n_{inj} as a function of $\sin\delta$.

hypothesis.

In high-energy particle physics, the confidence level to "discover" a new effect or source is usually set to 5σ where this corresponds to a significance level of $p(5\sigma) = 2.867 \cdot 10^{-7}$ which is the one-sided p-value of a normal distribution at 5σ. The discovery potential gives the signal strength that on average (50%-quantile) results in a 5σ "discovery". Sometimes also the 3σ discovery potential is stated because the computation of the $1-2.867\cdot10^{-7}$ quantile needs large resources. A sketch to illustrate the definition of the discovery potential source flux is shown in Fig. 6.1. To calculate the discovery potential, pseudo-experiments with different signal strength are generated and the median TS as a function of the signal strength is compared to the $1 - 2.867 \cdot 10^{-7}$ quantile for pure background. The signal strength for which the median of the TS-distribution exceeds the 5σ-quantile is called the discovery potential.

The sensitivity quantifies the expected upper limit on signal parameters. When testing a celestial position,the result is a TS-value. Based on the TS-value, one can calculate confidence intervals on the signal parameters. In case the TS-value is non-significant, one calculates exclusion limits. Here we follow the procedure by Neyman to set exclusion limits on the signal strength [260]. For exclusion limits, we set a confidence level of $CL = 90\%$. Thus, by comparing the $1 - CL$ quantile of the TS-distributions as a function of the signal strength, one can find the signal strength that can be excluded for the given TS-value. If for a measured celestial position the experimental TS is used, this is the 90% CL upper limit on the flux. However, the performance of an analysis method should not depend on the experimental result. Instead one uses the median expected TS-value expected for pure background, which is determined by the 50%-quantile of the background TS-distribution.

Both the discovery potential and sensitivity are constrains on the source flux distribution. These constrains are usually expressed by the flux normalization at a pivot energy $E_0 = 1\,\mathrm{GeV}$. In the following, the flux normalization for which the source flux reaches the sensitivity or discovery potential is often also called sensitivity or discovery potential flux.

Note that the sensitivity and discovery potential are given for the test of a single position. The sensitivity corresponds to the median upper limit that can be obtained in case of back-

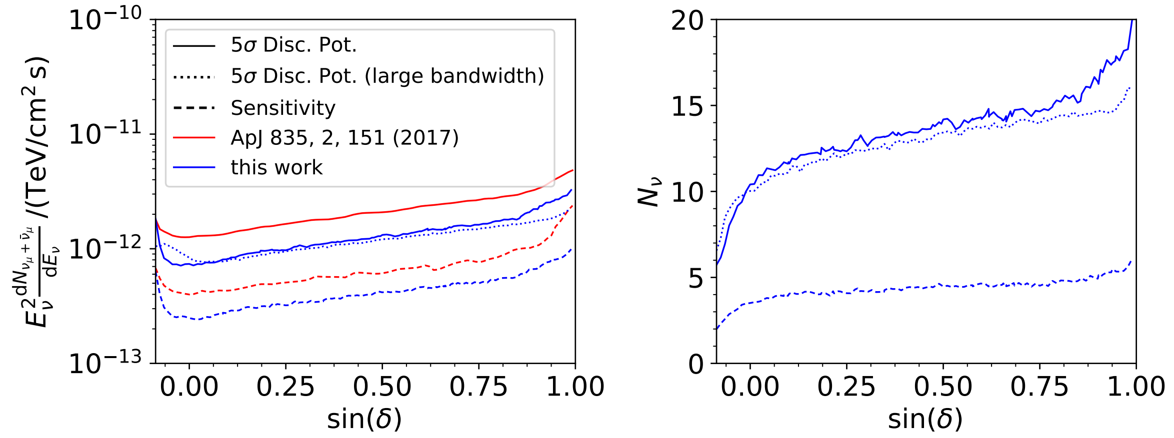

Figure 7.5: Sensitivity (dashed) and discovery potential (solid) on the flux normalization (left) and on the number of signal events (right) for an E^{-2} source spectrum vs sine of declination. The sensitivity and discovery potential for this analysis is shown in blue and for comparison the lines from [13] are shown in red. The effect of the bandwidth parameter on the discovery potential discussed in Sec. 7.1.2 is shown as dotted line.

ground only. The upper limit can be calculated of each point individually and a trial factor does not have to be taken into account. For the discovery potential a trial-factor should be considered if multiple points are tested. However the influence of a trial-factor is small for a significance level of 5σ. Because of this large significance level it is convention in IceCube to show the discovery potential of a test of a single point. Note that the trial-factor is taken into account in the calculation of p-values of a search if more than a single spot are tested. The calculation of the trial-corrected p-value is presented in Chapter 8 for each sub-analysis. Note, that because of the high significance level placed to claim a discovery in IceCube, also no trial factor is put on the results of different analyses.

7.3.1 Power Law Spectra

To evaluate the performance of the point-source analysis a baseline model with a power-law spectrum with a spectral index of $\gamma = -2.0$ is used. This allows to compare the analysis performance with other analysis, e.g. [13].

The sensitivity and discovery potential on the source flux normalization assuming an E^{-2} power law flux is shown in Fig.7.5. For comparison the sensitivity and discovery potential from [13] are shown. Despite of only one year more live-time, this analysis outperforms the analysis in [13] by about 20%-30% for multiple reasons: 1. the use of an improved angular reconstruction, 2. a slightly better optimized event selection near the horizon, 3. the use of background PDFs in the likelihood that are optimized on the parametrization from [5] which improves sensitivity especially for higher energies, 4. the fact that due to the prior on the spectral index the number of source hypotheses are reduced which results in a steeper falling background TS distribution and 5. the use of negative TS values which prevents the under-

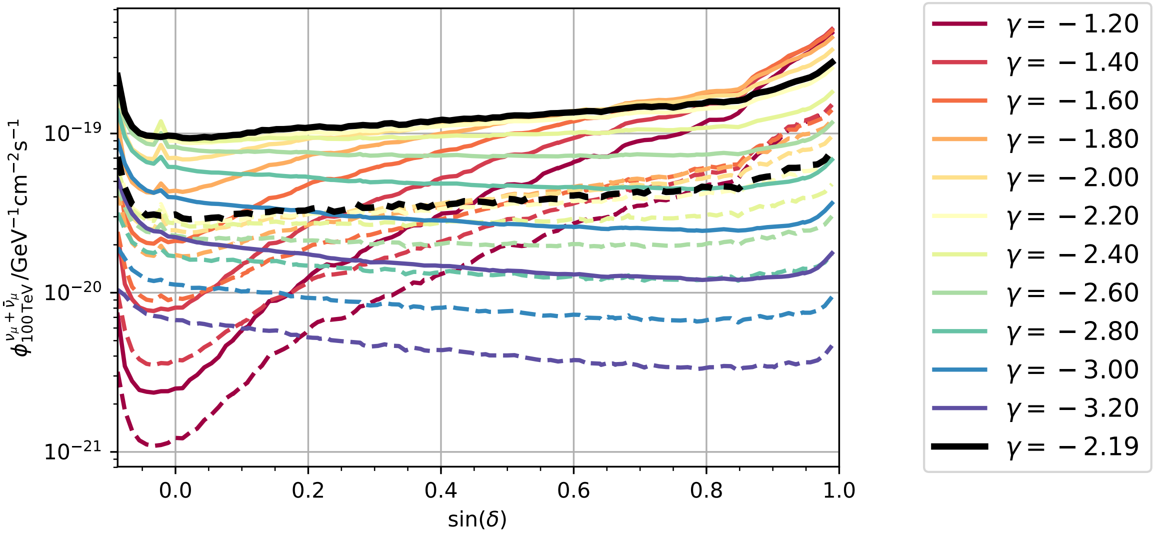

Figure 7.6: Sensitivity (dashed) and discovery potential (solid) on the flux normalization at 100 TeV for source spectra of different spectral indices (see legend).

estimating of the sensitivity especially near the pole ($\sin\delta \sim 1$) where the background changes strongly.

As this analysis is optimized for an $E^{-2.19}$ spectrum it is also of interest to evaluate the sensitivity and discovery potential for this spectrum. The sensitivity and discovery potential is shown in Fig. 7.6 (black line) as a function of sin declination. Note that this time the pivot energy is at 100 TeV. In addition, the sensitivity and discovery potential of the flux normalization for power-laws with spectral indices of -1.0, -1.2, -1.4, -1.6, -1.8, -2.0, -2.2, -2.4, -2.6, -2.8. -3.0 and -3.2 are shown as well.

As this search is optimized for source-spectrum with an spectral index of about -2.19, it does not outperform the analysis in [13] for soft-spectrum sources, e.g. E^{-3}.

7.3.2 Differential Sensitivity and Discovery Potential

The sensitivity and discovery potential has to be calculated for each different spectrum, e.g. for each spectral index or any other shape of the source spectrum. To show the energy dependence of the analysis independent of the energy spectrum, one can calculate the so called *differential* sensitivity and discovery potential.

To calculate the differential sensitivity or discovery potential events are not generated from the full source spectrum, but only in a small injection energy range $[E_{\mathrm{min}}, E_{\mathrm{max}}]$. Within this energy range the events are injected as signal like in the normal case. As only events from that small energy range can contribute to make up a significant source, the flux normalization $\phi_0^{\mathrm{diff},i}$ has to be larger than for the full spectrum. The sensitivity and discovery potential flux normalization can be calculated for each injection interval $[E^i_{\mathrm{min}}, E^i_{\mathrm{max}}]$ for any other source spectrum. The resulting sensitivity and discovery potential flux normalization can than be shown as a function of the injected energy interval $[E^i_{\mathrm{min}}, E^i_{\mathrm{max}}]$.

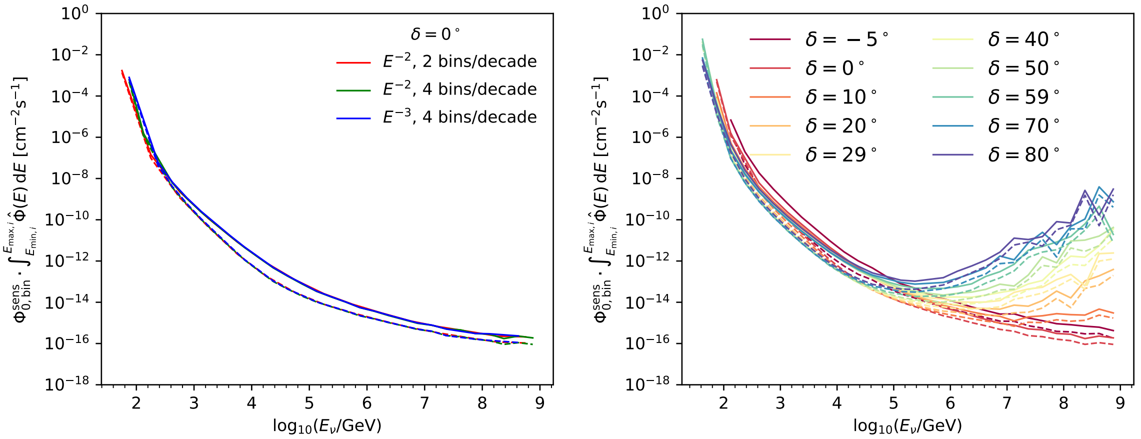

Figure 7.7: Differential sensitivity (dashed) and discovery potential (solid) as a function of neutrino energy E_ν. In the left panel, the flux normalization has been calculated for different injection spectra and injection energy ranges. In the right panel sensitivity and discovery potential is shown for different declinations.

In Fig. 7.7, the differential sensitivity and discovery potential is shown, where the flux normalization is expressed as the flux normalization multiplied with the integrated flux from the injected energy interval. As can be seen from the left panel of Fig. 7.7, this quantity is invariant under the chosen injection spectrum and the width of the injection energy interval, at least if the injection energy interval is small with respect to the energy resolution of the detector. In the right panel of Fig. 7.7, one can see the sensitivity and discovery potential for several declination. Below about 100 TeV the differential sensitivity and discovery potential is approximately independent of the declination. Above these energies one can see that the sensitivity and discovery potential increases for increasing declination. This is an effect of neutrino absorption in the Earth for very high-energy neutrinos as discussed in Sec. 4.1.

The differential sensitivity and discovery potential flux can be used to approximate the sensitivity and discovery potential flux for any other source spectrum. This approximation is derived in Appendix E. The sensitivity and discovery potential on the flux normalization ϕ_0 for any spectrum $\phi(E_\nu)$ can be calculated by

$$\frac{1}{\phi_0} = \sum_i \frac{1}{w_i \cdot \phi_0^{\mathrm{diff},i}}\,, \tag{7.1}$$

where i is running over all injection intervals $[E^i_{\mathrm{min}}, E^i_{\mathrm{max}}]$, and $\phi_0^{\mathrm{diff},i}$ is the flux normalization calculated for the corresponding injection interval. The factor $w_i = \frac{\int_{E_{\mathrm{min},i}}^{E_{\mathrm{max},i}} \hat{\phi}(E)\,\mathrm{d}E}{\int_{E_{\mathrm{min},i}}^{E_{\mathrm{max},i}} \hat{\phi}'(E)\,\mathrm{d}E}$ is a weighting factor calculating the ratio of the integrated flux spectrum of the spectrum of interest $\phi(E)$ and the generation spectrum $\phi'(E)$ of the differential sensitivity.

7.3.3 Arbitrary Spectra

Beside the generic power-law flux model, there are several source specific models in the literature. Also for these models a sensitivity and discovery potential can be calculated. What is required to calculate the sensitivity and discovery potential, is the source flux as a function of neutrino energy. Based on this source spectrum one can assign a weight to each Monte Carlo event corresponding to the likelihood that this event is generated by the source flux. Again by injection events from the source spectrum the sensitivity and discovery potential on the flux normalization is calculated.

In case there is also an absolute prediction of the neutrino flux from the source of interest, the model rejection factor (MRF) can be calculated, which is defined as:

$$\mathrm{MRF} = \frac{\phi^{\mathrm{sens}}(E_{\mathrm{pivot}})}{\phi^{\mathrm{model}}(E_{\mathrm{pivot}})} \,. \tag{7.2}$$

The MRF is the ratio of the sensitivity / discovery potential flux ϕ^{sens} and the source model flux ϕ^{model} at a pivot energy E_{pivot}. Note that the MRF is independent of the pivot energy, because for the calculation of the sensitivity / discovery potential flux ϕ^{sens} the spectral shape is assumed to follow ϕ^{model}. The MRF is 1 if the flux normalization at sensitivity level equals the absolute prediction. In case the MRF is two, the flux normalization at sensitivity level is the double of the absolute prediction.

Note that, as in model prediction often the shape or flux normalization depends on model parameters of the source, constrains on these parameters can be calculated. Again the Neyman method to set upper limits at 90% CL will be used. The discussion of specific source models is continued in Sec. 10.1.

7.3.4 Extended Sources

This analysis focuses on point-like sources where point-like means that the size of the emission region is much smaller than the angular resolution of the detector. Even though we focus on the point-like scenario, the analysis has some sensitivity to slightly extended sources, however this sensitivity is reduced with respect to the point-like scenario.

To test the sensitivity to slightly extended sources, sources are simulated with different extensions. The emission profile follows a tophat profile with constant emission strength at each point. We characterize the tophat by its radius r_{ext}. The likelihood is kept unchanged.

The resulting sensitivity and discovery potential depend on the source extension. In Fig. 7.8 (left panel), the sensitivity and discovery potential are shown for different source extensions as a function of declination. The ratio of sensitivity and discovery potential with respect to the point-like scenario is shown in the right panel of Fig. 7.8. Here values larger than one indicate a reduced sensitivity to extended sources. One can see, that the sensitivity gets weaker by up to a factor of eight for a source with a tophat emission profile with a radius of 2°. The increase in sensitivity flux is declination dependent and the sensitivity flux increases faster for small declinations while it is less effected at higher declinations.

Note that the chosen emission profile is a conservative choice. Any emission profile that

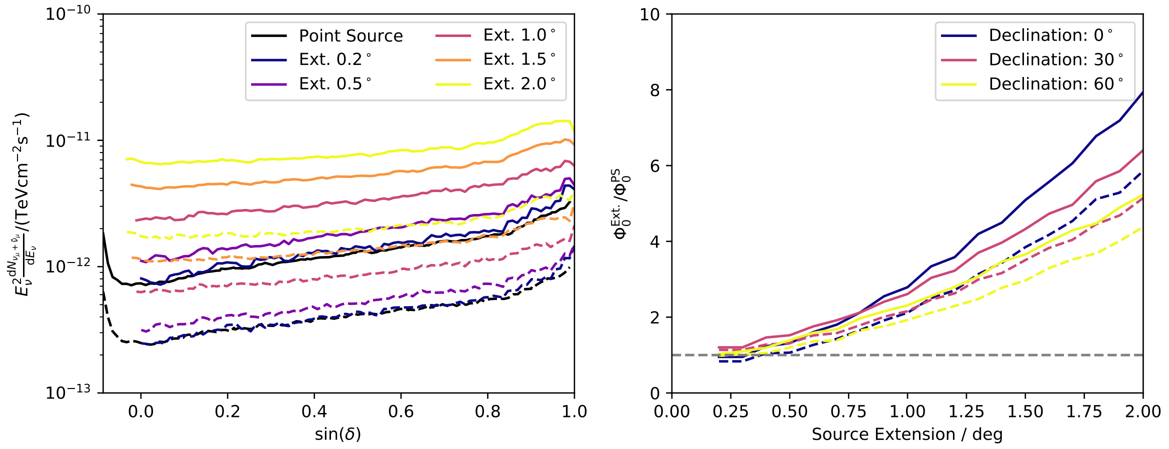

Figure 7.8: Sensitivity (dashed) and discovery potential (solid) for extended sources. The left panel shows the sensitivity and discovery potential as a function of declination for different source extensions (see legend). The black line gives the sensitivity and discovery potential for a point-like source. The right panel, shows the sensitivity and discovery potential flux ratio relative to the point-like scenario as function of source extension for different declinations. Note that small fluctuations are cause by a reduced computation precision.

is more peaked at the center, e.g. like a Gaussian emission profile, will lead to a reduced sensitivity flux compared to the tophat emission profile.

7.4 Systematic Uncertainties

When testing a sky position for the existence of a point-like neutrino source, the result will be a p-value and the best-fit signal strength – either given as number of source events or given as flux normalization – and the spectral index.

The p-value itself is not a physical quantity and thus has no uncertainty in the classical sens. When pseudo-experiments and thus the background test statistic distribution are calculated from randomized right ascension, by construction the p-value can not show any deviation from the underlying distributions of experimental data. In Sec. 7.1 also the generation of pseudo-experiments from Monte Carlo weighted to best-fit parametrization has been introduced. Note that this method is less affected by statistical fluctuations but has the potential to be affected by systematic uncertainties. Thus, the good agreement between parametrization and experimental data is a prerequisite of this method. The best-fit parametrization has been fitted to the experimentally observed data including several nuisance parameters to account for systematic uncertainties. This best-fit result shows a very good agreement to the experimental data as discussed in Sec. 5.8. To cross-check the results of both methods the p-values reported in Chapter 8 are calculated and given for both methods. As can be seen in Chapter 8, the p-values from both methods are very similar.

The best-fit spectral index is basically fixed due to the prior on the spectral index, as discussed in Sec. 7.2. Due to that and no correlation of the best-fit spectral index with its true value, the spectral index should not be interpreted as a physically observed value, at least for small fluxes. Therefore, it is also not necessary to give an systematic uncertainty on this fit parameter.

The remaining parameter is the best-fit signal strength. The signal strength can be expressed as number of required signal events or as flux normalization of the source spectrum. The flux normalization is calculated based on full detector Monte Carlo which can be affected by systematic uncertainties. The sensitivity on the flux normalization depends on the effective area, the point spread function of the events and the observed energy proxy for a given true neutrino energy. Thus, by mis-modeling the effective area, the point spread function or the energy proxy systematic uncertainties are introduced in the best-fit flux normalization. The dominant systematic uncertainties in the Monte Carlo generations result from photo-nuclear interaction cross sections of high energy muons [155, 161, 261, 262, 263, 264, 265], the optical properties of the South Pole ice [196], like absorption and scattering coefficients and the optical efficiency of the Cherenkov light production and detection in the DOMs [199].

To calculate the systematic uncertainties in the flux normalization, the calculation of sensitivity, discovery potential and upper limits is repeated in the full analysis chain starting with a re-simulation of the full detector Monte Carlo with modified input properties. The resulting detector Monte Carlo simulation is than used to generate injected signal as described in Sec. 7.1.2. The analysis is performed on pseudo-experiments with these modified injected signals and sensitivities, discovery potentials and upper limits are re-calculated for signal energy spectra with a spectral index of -2.0 which can be seen in Fig. 7.9 (left). To quantify the effect of systematic uncertainties flux normalization with changed input values and baseline input values are compared and their ratio is build (see Fig. 7.9, right). Note that because there is no consistent set of systematic re-simulation of the full detector Monte Carlo for all seasons, the study in this section is based on data for IC86-2012/16 only.

To calculate the systematic uncertainties due to photo-nuclear interactions of high energy muons, the models in Ref. [155, 161, 261, 262, 263, 264, 265] are used. These models represent the extreme cases from common literature and are partly outdated. However, due to the spread in these models the estimated uncertainties on the flux normalization can be assumed to be conservative. In Fig. 7.9 these models are labeled *BBHard* and *ALLM91*. The sensitivity and discovery potential change by ±4.2% averaged over all sine of declination.

To study the influence of ice properties on the flux normalization, the absorption and scattering length are varied. For the parametrization determined in [196] the uncertainties have been quoted to be at the 5% level. However, taking into account that the model itself has specific assumption, e.g. isotropic ice, it is expected that absorption and scattering length are known to better than 10%. Therefore, three points with (+10%, 0%), (0%, +10%) and (-7.1%, -7.1%) in absorption and scattering length are tested. The resulting influence of the changed input parameters on the flux normalization is ±5.3%. Note that this test does not test for any anisotropic effect.

Another main contribution comes from the optical efficiencies that can be described by the optical efficiency of the DOMs, but can also include other effects. In Ref. [199], the uncertainty on the absolute efficiency of the PMT in the DOMs is about 7.7%. By changing

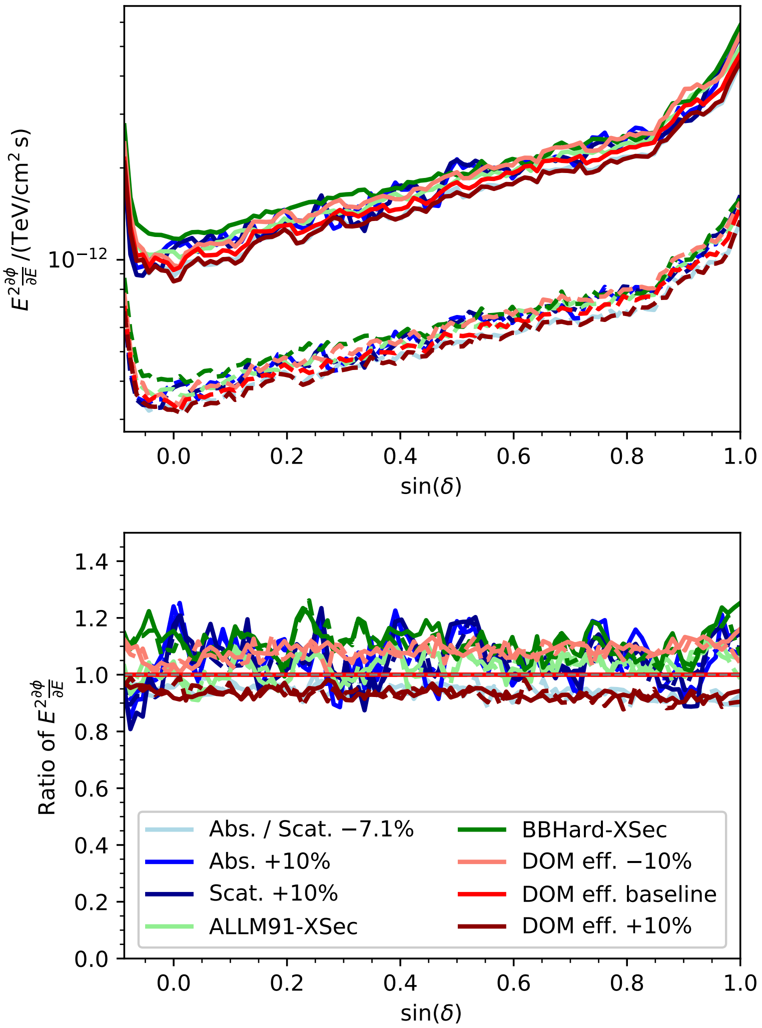

Figure 7.9: Sensitivity (dashed) and discovery potential (solid) on the flux normalization for an E^{-2} power law spectrum as a function of sine of declination (left). Sensitivity and discovery potential have been calculated based on different input parameters for the optical efficiency (DOM eff.), ice properties like absorption (Abs.) and scattering (Scat.) and different photonuclear cross-sections of high energy muons (*-XSec). Ratio of the flux normalization from the left panel relative to the flux normalization calculated with baseline input values (right).

Input Parameter	Variation	Change in Sens.	Change in Disc. Pot.
Ice Abs./Scat.	+10% / ±0%	-5.2%	-5.7%
Ice Abs./Scat.	±0% / +10%	-4.5%	-4.8%
Ice Abs./Scat.	-7.1% / -7.1%	5.7%	6.0%
Ice		±5.3%	
Optical eff.	-10%	-7.7%	-8.6%
Optical eff.	+10%	6.9%	6.7%
Optical eff.		±7.4%	
Cross-Section	ALLM91**	-2.7%	-2.7%
Cross-Section	BBHard**	-10.3%	-11.8%
Cross-Section		±4.2%	
Overall Detector		±10.5%	
$\Delta \sin \delta$			±8%
$\nu_\tau + \bar{\nu}_\tau$		(2.6–4.3)%	
$\nu_e + \bar{\nu}_e$		negligible	

Table 7.1: Systematic change in flux normalization due to changed input parameters. Given are the input parameter, the changed value relative to the default and the change in sensitivity and discovery potential flux for an $E^{-2.0}$ spectrum averaged over the full sine of declination range. ** Note that for the changed cross-section parametrizations also other input parameters have been changed in the full detector Monte Carlo and thus the effect on the flux normalization is shifted and does not contain the baseline flux. Therefore, only the spread for these models is used as maximal spread and the absolute shift was discarded.

the optical efficiency by ±10% the estimated systematic uncertainty is conservative and can account for additional uncertainties that would also manifest in a changed light yield. By varying the optical efficiency by ±10% the flux normalization changes by ±7.5% averaged over all declination.

Note that the influence of systematic uncertainties is energy dependent. This can be seen from Fig. 7.10 which shows the differential discovery potential for 30° declination calculated with different input values. It can be seen that the influence of systematic uncertainties becomes smaller with increasing energy up to 10^5 GeV. Above about 10^5 GeV a clear conclusion can not be drawn as this region is influenced by statistical fluctuations due to limited Monte Carlo statistics. As a result, the influence of systematic uncertainties will depend on the assumed energy spectrum. The above estimated uncertainties are given for an $E^{-2.0}$-spectrum.

Since the sample is assumed to be purely muon neutrino and muon anti-neutrino events, only $\nu_\mu + \bar{\nu}_\mu$ fluxes are considered. However, $\nu_\tau + \bar{\nu}_\tau$ may also contribute to the observed astrophysical neutrinos in the data sample. Taking ν_τ and $\bar{\nu}_\tau$ fluxes into account and assuming an equal flavor ratio at Earth (see Sec. 2.4.1), the sensitivity of the per-flavor flux normalization improves, depending on the declination, by 2.6% - 4.3% as can be seen in Fig. 7.11. The expected contamination from ν_e and $\bar{\nu}_e$ is negligible [150].

The systematic uncertainties are summarized in Tab. 7.1. These detector uncertainties can

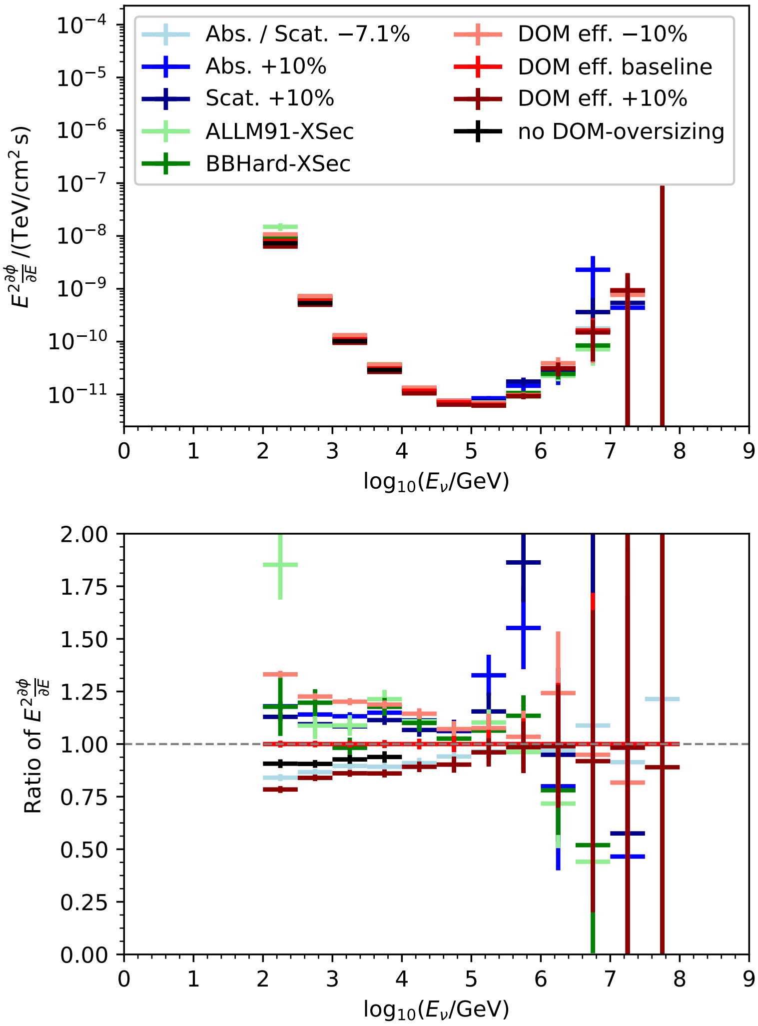

Figure 7.10: Differential discovery potential on the flux normalization for 30° declination (left). The discovery potential has been calculated based on different input parameters for the optical efficiency (DOM eff.), ice properties like absorption (Abs.) and scattering (Scat.) and different photo-nuclear cross-sections of high energy muons (*-XSec). The ratio of the flux normalization from the left panel relative to the flux normalization calculated with baseline input values is shown in the right panel. Note that above $\sim 10^6$ GeV statistical fluctuations become strong. The calculation is based on IC86-2012/16 MC data only.

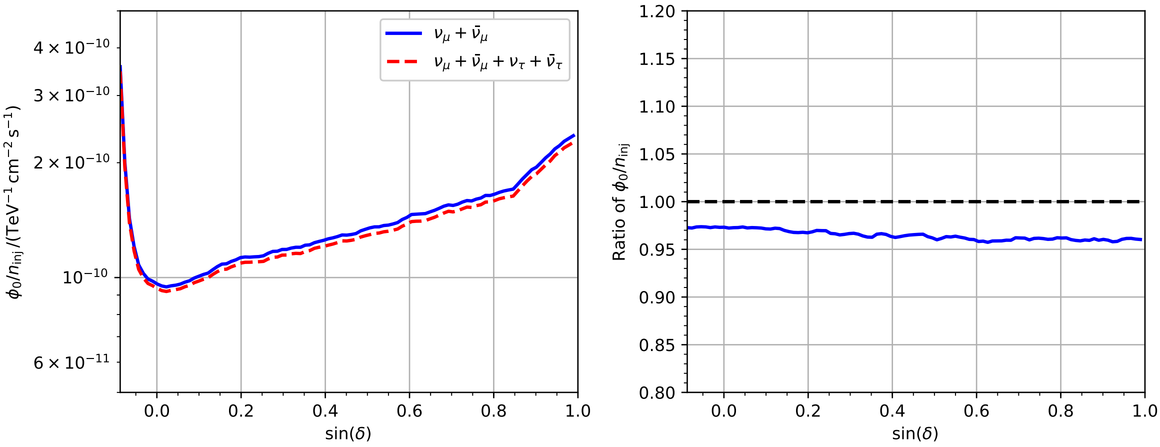

Figure 7.11: Source flux per injected event as a function of sine of declination, once assuming a pure $\nu_\mu + \bar{\nu}_\mu$ flux, and once including the $\nu_\tau + \bar{\nu}_\tau$ flux, assuming an equal flavor ratio at Earth. The lower panel shows the ratio of the flux per event.

be assumed to be independent and thus the total systematic uncertainty of ±10.5% for the $\nu_\mu + \bar{\nu}_\mu$ flux normalization is calculated by adding the individual contributions squared. In addition, the modeling of point-like sources as discussed in Sec. 7.1.2 and Appendix D yields an uncertainty of about ±8%.

Chapter 8

Tested Hypotheses and Experimental Result

Declaration of Pre-released Publications The experimental results presented in this chapter have been previously published by the IceCube Collaboration in M. G. Aartsen *et al.* (IceCube Collaboration), "Search for steady point-like sources in the astrophysical muon neutrino flux with 8 years of IceCube data" The European Physical Journal C 79, 234 (2019). The author of this thesis has written this publication as a corresponding author. The author contributed to the analysis method, and the application of the analysis to experimental data. The all-sky scan, the source list search and the test for steady neutrino emission from the direction of the blazar TXS 0506+056 have been performed by the author of this thesis. The test for steady neutrino emission from the direction of the blazar TXS 0506+056 has been used as an internal cross-check for the results published in M. G. Aartsen *et al.* (IceCube Collaboration), "Neutrino emission from the direction of the blazar TXS 0506+056 prior to the IceCube-170922A alert," Science 361, 147 (2018).

In the previous chapters the method and the performance of the analysis have been presented. The likelihood ratio test tests for a point-like neutrino source resulting in an excess above background for a given celestial position. In this chapter, the tested hypotheses, i.e. the tested celestial positions, are introduced and the experimental result is presented.

The full analysis chain, including the selection of celestial positions to test, has been developed in a blind procedure, i.e. without looking at the experimental data. After all details of the analysis procedure have been fixed and reviewed by the IceCube Collaboration, the experimental result has been calculated.

This chapter is split into three parts, each presenting a test for point-like sources, based on different strategies. In Sec. 8.1 a scan of the full Northern Hemisphere is presented, which is an unbiased and the most generic strategy to search for point-like sources. However, this search suffers from the large number of individual tested celestial positions (spatial trials), such that the local p-value of the most significant source has to be very small, to result in a significant trial-corrected p-value. Therefore, in Sec. 8.2 a test of a pre-defined source catalog is presented. This source catalog comprises potential neutrino source candidates that are motivated by gamma-ray observations and thus the multi-messenger approach. Because the pre-defined source catalog has been developed years ago, recent progress in the field is not reflected in this catalog. Therefore, Sec. 8.3 presents a test for a source called TXS 0506+056 that recently got increasingly popular, because an extrem-high-energy neutrino was measured in coincidence with a flare of this blazar [19].

Each section presents a motivation for the tested hypothesis, defines the construction of the final p-value, reports the experimentally observed results and gives results from further investigations. The discussion of astrophysical implications of the observed results is postponed to Chapter 10.

8.1 All-Sky Scan

The most generic search strategy, that does not take into account any external information, is to test all positions in the entire sky. Therefore, every direction will be tested individually. By this approach the result will not be influenced by prior knowledge.

However, in this analysis, the event sample only extends over the Northern Hemisphere and also the best-fit parametrization is only available for this sample. Therefore, only the Northern Hemisphere can be tested. The result of this search is the direction, best-fit parameter and p-value of the most significant spot on the Northern Hemisphere.

In the following, the selection of the most significant spot and the final p-value of the test are explained.

8.1.1 Final p-Value Construction

To test the entire Northern Hemisphere a scan is performed. The grid of the scan is generated using the HEALPix pixelization schema[1] [266], which provides pixels with equal area. The resolution parameter of the HealPix pixilization schema is given by the parameter N_{side}.

The scan is done in an iterative process with two iterations. In a first scan, the entire sky is scanned with a resolution parameter of $N_{\mathrm{side}} = 256$, which corresponds to a pixel size of $(0.23\,\mathrm{deg})^2$. In a second iteration, the scan is repeated with a resolution parameter of $N_{\mathrm{side}} = 512$, corresponding to a pixel size of $(0.11\,\mathrm{deg})^2$, on the 25% most significant pixels. The scan is done for all pixels with a declination larger than $-5°$. For each tested pixel the TS is calculated as described in Chapter 6.

In Sec. 6.6 it is discussed, that the background TS distribution has to be generated from pseudo-experiments for each tested source declination to calculate the local p-value. Here, this is not applicable due to two reasons: 1. The large number of trials requires a good description of the TS distribution up to a corresponding local p-value of $\sim 10^{-6}$ and above. Thus, at least 10^7 to 10^8 pseudo experiments have to be generated per declination. 2. Due to the very fine scan a lot of different declination are tested. Both reasons lead to an enormous amount of trials that would have to be generated, which goes to the computational limit. Therefore, the TS distribution is generated for 135 different declination with $5 \cdot 10^5$ trials each. The p-value is read from trials directly for $TS < 5$. For $TS \geq 5$ the distribution is parametrizied by an exponential function and p-values are calculated using this parametrization. The fit of the parametrization is described in detail in Appendix F.

The most significant spot is selected based on the smallest p-value. Therefore, the declination range from $-3°$ to $90°$ is considered, because due to the end of the experimental sample at $-5°$ and thus fast changing PDFs at the end of the tested sample, numerical problems arise close to $-5°$. Note that testing the region up to $90°$ is only possible, due to the use of pseudo-experiments generated using the Best Fit Parametrization (BFP)-method. If pseudo

---

[1] Hierarchical Equal Area isoLatitude Pixelation of a sphere, `http://healpix.sourceforge.net/`

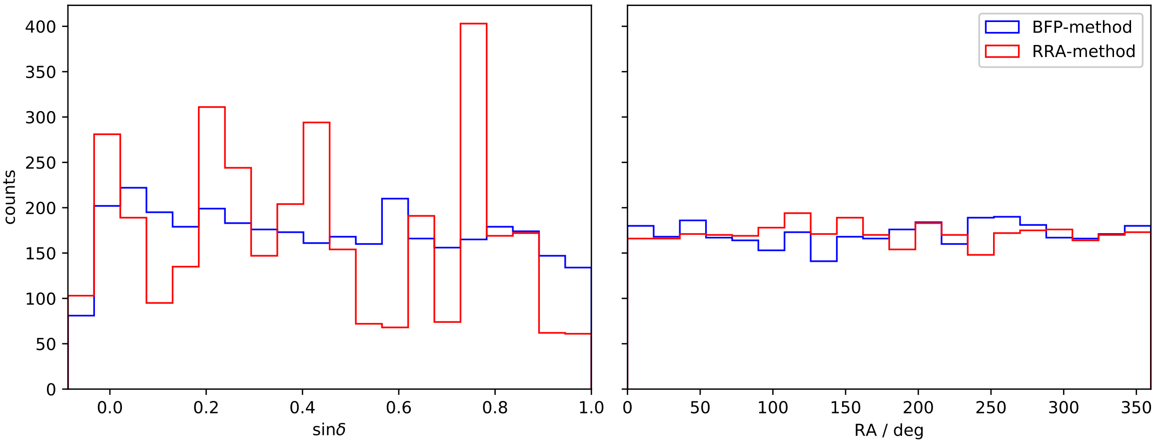

Figure 8.1: Histogram of $\sin\delta$ and right ascension of the most significant spot in pseudo experiments. The blue and red histograms show pseudo-experiments generated using the Best Fit Parametrization (BFP)- and Randomized Right Ascension (RRA)-method, respectively.

experiments are generated by randomized right ascension, events in the pole region are not shifted much and an excess in the data will lead also to an excess in all pseudo experiments. By using pseudo-experiments using the BFP-method, this effect is reduced. Also the background TS distribution accounts for this effect and thus a local p-value will be conservative. As this will not lead to an overestimated p-values it is save to include also this region in the selection of the most significant spot and no arbitrary bound has to be set.

In Fig. 8.1 the position of the most significant spot from $\sim$ 3500 pseudo-experiments is shown for pseudo-experiments generated using the BFP-method and the RRA-method, respectively. For only background fluctuations, one expects that the most significant spot is randomly distributed in the sky. One can see that for both methods the right ascension distribution is flat. On the other hand the distribution of $\sin\delta$ shows distinct peaks for the RRA-method. Within this method the declination and energies of events are fixed and thus high energy events, which are a seed for local hot-spots, are always at the same declination. For the BFP-method the distribution of $\sin\delta$ is much more flat.

In Fig. 8.2 the distribution of the local p-value from the most significant spots is shown (left) for only background pseudo-experiments generated with the Best Fit Parametrization (BFP)- and Randomized Right Ascension (RRA)-method. In the right panel the fraction of pseudo-experiments that give an equal or smaller local p-value, also called post-trial p-value p_{post}, are shown as a function of the local p-value of the hottest spot. The lower right panel shows the ratio of p_{post} calculated with pseudo-experiments using the RRA-method and BFP-method, respectively. It can be seen that the resulting post-trial p-value based on the BFP-method is slightly smaller than the p-value from the RRA-method. However, from the ratio of the p_{post} one can see that this difference is at a few 10% level and reaches at maximum a factor of two in the region with low statistics. Note, that even with a factor of two in the p-value the significance does not change much if the significance is large. A two sample Kolmogorov-Smirnov test, to test if the two representations originate from the same distribution, results in

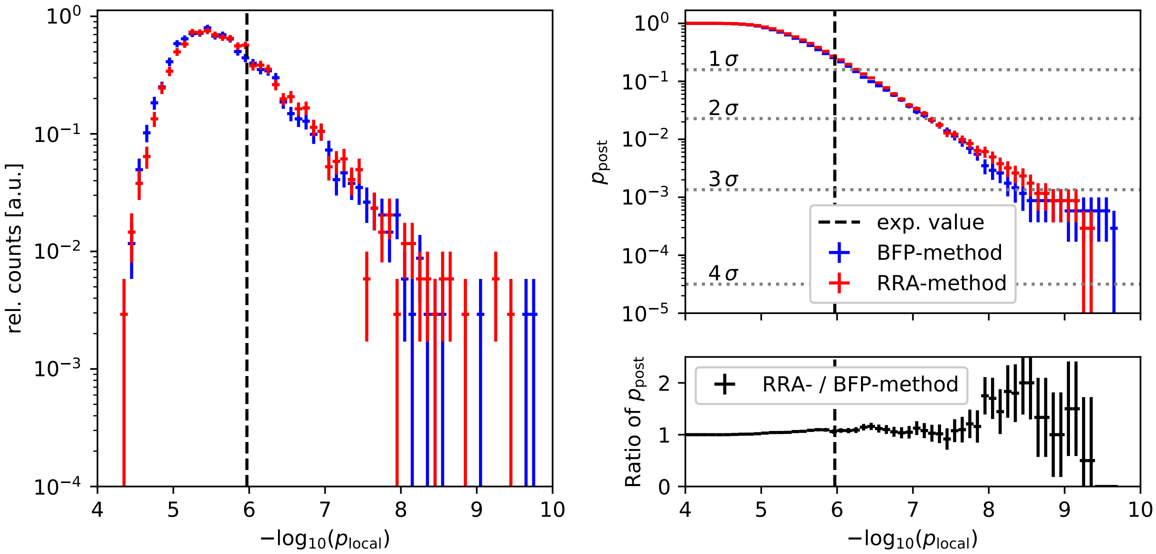

Figure 8.2: Local p-value distribution of most significant spot in all-sky scans (left) and post-trial p-value as a function of local p-value distribution of most significant spot (right). The blue and red histogram is calculated from ~ 3500 pseudo-experiments using the best-fit parametrization (BFP) method and the randomized right ascension (RRA) method, respectively. The black vertical line shows the experimentally observed value. The lower right panel shows the ratio of p_post using the two different pseudo experiment methods.

a two-sided p-value of 0.567%.

A rough approximation of the local p-value distribution of the most-significant spot can be obtained by the function:

$$\mathrm{d}\mathcal{P} = N \cdot (1 - p_\mathrm{local})^{N-1} \mathrm{d}p_\mathrm{local} \tag{8.1}$$

which is a binomial distribution where $k = 1$ and N is the effective number of independent trials. Note that N is not the total number of scan points, because neighbouring scan points are correlated. Fitting Eq. 8.1 to the distribution shown in Fig. 8.2 (left) yields $N \approx 237000$ and $N \approx 258000$ in case of pseudo experiments using the BFP-method and RRA-method, respectively. Even though the fit does not describe the tail of the distribution perfectly, the fit can be used to estimate the number of independent trials.

The number of independent trials can also be estimated by a rough approximation using the tested solid angle of the Northern Hemisphere of $\sim 2\pi$ and a typical angular resolution of $\sim 0.3°$, which gives the scale at which scan points are correlated. The ratio $2\pi/(0.3°)^2 \approx 229000$ of the solid angle and the typical angular resolution squared gives a similar order of magnitude for the number of independent trials.

8.1.2 Experimental Result

The local p-value sky map of the experimentally observed events is shown in Fig. 8.3. The most significant spot is indicated by a black circle and is located at 177.89° right ascension and

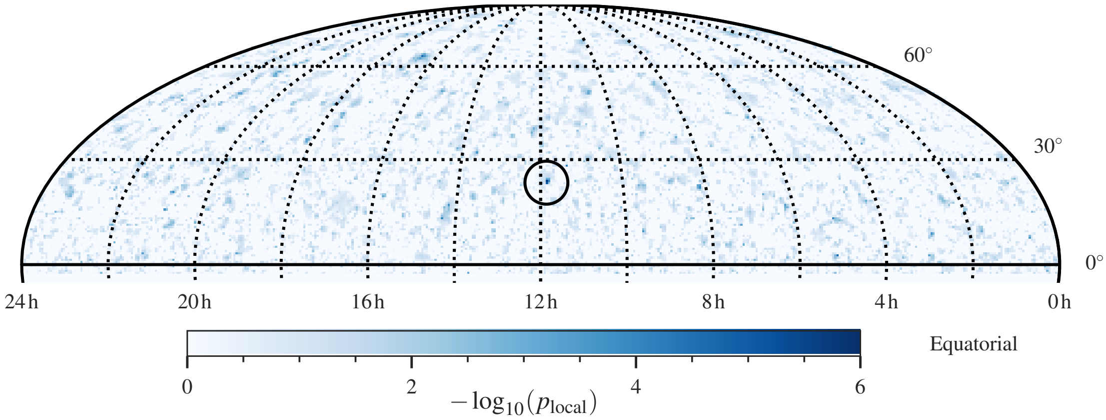

Figure 8.3: Sky map of local p-values in equatorial coordinates (J2000). The color gives the negative $\log_{10}$ of the local p-values. The most significant point is indicated by a black circle.

23.23° declination (J2000). In galactic coordinates the most significant spot is at $b_{\mathrm{gal}} = 75.92°$, $l_{\mathrm{gal}} = -134.33°$. The TS value at the most significant spot is 21.63 which corresponds to a local p-value of $10^{-5.97}$ for that declination.

A zoom into the p-value landscape around the most significant point is shown in Fig. 8.4, where in addition the arrival directions of the experimentally observed events are shown as black circles. The size of the circles is proportional to the median $\log_{10}$ of the neutrino energy assuming the diffuse best-fit spectrum. The shape of the most significant spot is slightly elongated to higher declination.

In Fig. 8.4 (right), a scan of the likelihood as a function of the fit parameters γ and $\Phi_{100\,\mathrm{TeV}}$, the flux normalization at 100 TeV which corresponds to a fixed n_s for a given γ, are shown. The best fit parameters of the most significant spot are $\hat{\gamma} = -2.20$ and $\hat{n}_s = 21.32$ and indicated by a white star. The corresponding flux normalization assuming an $E^{-2.20}$ spectrum is $\Phi_{100\,\mathrm{TeV}} = 1.4 \cdot 10^{-19} \mathrm{GeV}^{-1}\,\mathrm{cm}^{-2}\,\mathrm{s}^{-1}$.

The post trial p-value can be read of from Fig. 8.2 by the intersection of the vertical black dashed line and the distributions. It is 26.5% using the BFP-method and 29.9% using the RRA-method. Both p-values agree and are non significant. Thus, there is no indication for a significant excess above background only.

8.1.3 Further Investigations

Even that the most significant spot in the sky scan is non significant, it is still interesting to have a closer look at the hottest spot location itself.

From pseudo experiments with signal injected similar to the best-fit parameters, it was found that the best fit position is within less than 0.2° within the true source position in 90% of all cases. This can be read of from Fig. 8.5 where the cumulative distribution of distances between best fit direction and true direction of injected sources are shown.

The closest source from the Fermi Large Area Telescope (LAT) third source catalog (3FGL) [267]

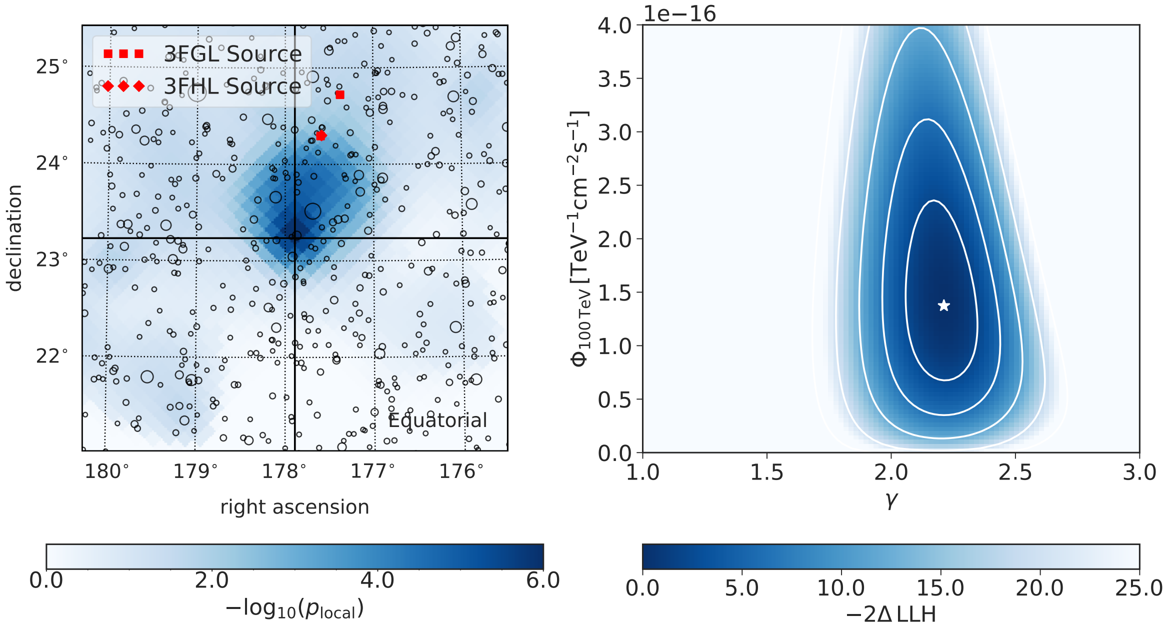

Figure 8.4: Local p-value landscape around the most significant spot in the sky scan in equatorial coordinates (J2000) (left). Neutrino event arrival directions are indicated by small circles where the area of the circles is proportional to the median decadic logarithm of neutrino energy assuming the diffuse best-fit spectrum. Sources of the 3FGL and 3FHL catalog are indicated by red markers [267, 268]. Likelihood landscape scan at the hottest spot position for different flux spectral indices and normalization (right). The best-fit position is indicated by a white star. Contours correspond to the 1, 2, 3, 4 and 5σ CL assuming Wilk's theorem with 2 degrees of freedom.

and the third catalog of hard Fermi-LAT sources (3FHL) [268] is called J1150.3+2418 with an angular distance to the most significant spot of 1.1°. The chance probability to fine a 3FGL or 3FHL source closer than 1.1° for only background pseudo-experiments is $\sim 25\%$ and thus there is no significant correlation between the closest source and the hottest spot.

8.2 *A-Priori* Source List

The all-sky search suffers from the large number of effective trials, that are made by testing each sky position. Thus, a local p-value of $10^{-5.97}$ becomes insignificant with a trial-corrected p-value of about 26.5%. To reduce the number of trials, a pre-selection of celestial positions is needed. The selection of these sky position has to be based on other messenger particles and thus assumes a correlation between the different messenger-particles as it is motivated in Chapter 2. By setting up a source list of potential neutrino sources the number of trials is reduced to at most the number of sources within the catalog.

In this section the *a-priori* source list which has been developed by the IceCube and ANTARES collaborations over many years will be tested, see e.g. [13]. The source list was

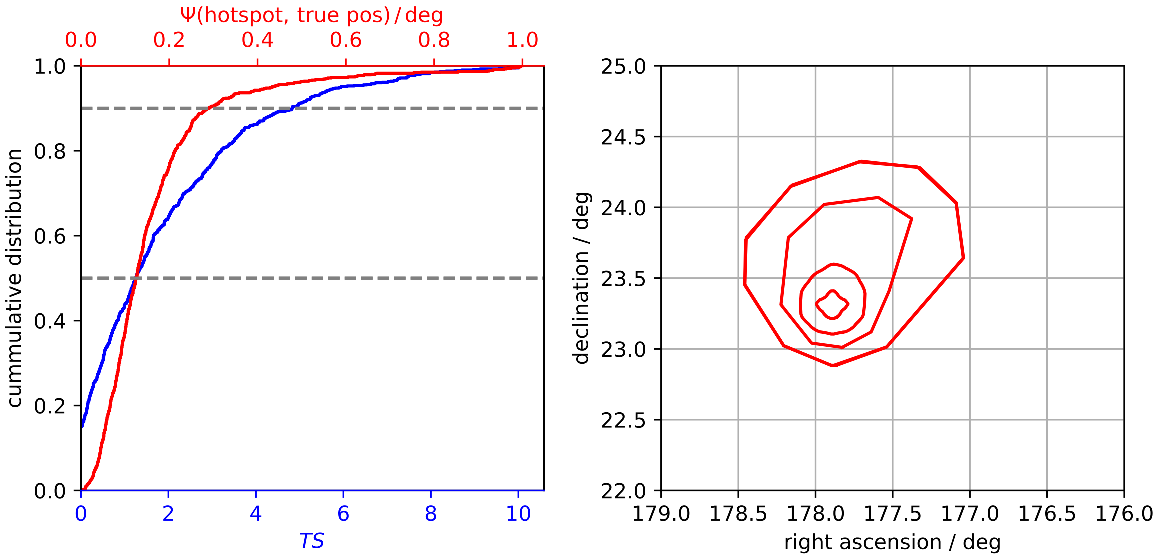

Figure 8.5: Cumulative distribution of angular distances (red) and TS difference (blue) between most significant spot and true direction. Sources are injected at the best-fit properties of the experimentally observed hottest spot in the all-sky scan. The 50% and 90% quantiles are marked by dashed gray lines. The right panel shows the 1σ, 2σ, 3σ and 4σ contours for the best-fit source position assuming the best-fit parameters of the most significant spot.

first set up in a search for point-like neutrino sources using the predecessor of IceCube, AMANDA [118, 269, 270]. The source list has been motivated by gamma-ray observations where interesting sources have been compiled to a list. Since the first version in 2005, the list has changed multiple times, always incorporating knowledge that was present at the time of an analysis, and sources from the list have been dropped and new were included [113, 114, 116, 271]. Since 2012 the list has been kept fixed in all analyses, to not bias the experimental result by picking spots that show interesting p-values in the full sky scan.

The sources on the list are mainly high-energy γ-ray sources. The decision to include the source in the source list was done by source individual motivations. There has not been a fixed selection criteria that has been used to compile the source list. Thus, a simple update of the catalog is not possible by reapplying the selection criteria on up to date data.

In the current version this list comprises 74 sources from which 34 are located on the Northern Hemisphere. These 34 sources are used here to search for point-like neutrino emission reducing the trial factor to about 34. The sources are listed in Tab. 8.1 where the source names, celestial position and source type are given. A short introduction to each source can be found in Appendix G.1. The source catalog contains sources of the types BL Lacertae object (BL Lac), Flat Spectrum Radio Quasar (FSRQ), Pulsar Wind Nebula (PWN), Star Formation Region (SFR), Supernova Remnant (SNR), Starburst / Radio Galaxy (SRG), X-ray Binary and Micro-Quasar (XB/mqso) as well as Not Identified (NI) sources.

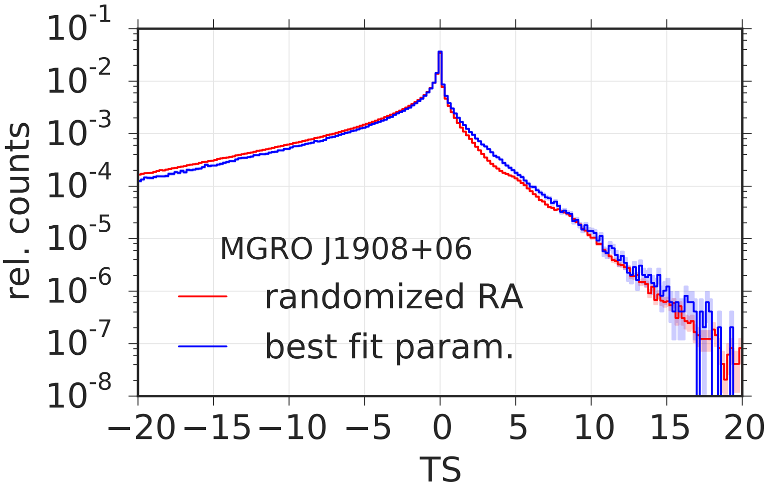

Figure 8.6: Background TS distribution for the source MGRO J1908+06. The histograms have been generated from 10^6 pseudo experiments once generated using the best fit parametrization method (blue) and once using the randomized RA method (red). The shaded band gives the statistical uncertainties of the distribution due to the finite statistics.

8.2.1 Final p-Value Construction

The source position of the sources are taken from Ref. [13]. Note that for some of these sources different gamma-ray experiments have measured slightly different source positions or that the source position has been updated by the experiments with more data. However, the source position for this list are kept fixed for all analysis. Note that in addition some of the sources in the source list show an extension of up to several degrees in gamma-rays, e.g. MGRO J1908+06, SS 433 or Geminga. For these sources a test for a point-like emission is non optimal as their extension is larger than IceCube's point spread function (compare Sec. 5.7). For the analysis presented in [112] the sensitivity for a source with a 1° extension has been 20% worse than for a point-like source.

For each source position only background pseudo experiments are generated. As an example the only background TS distribution is shown for the source MGRO J1908+06 in Fig. 8.6. The local p-value is calculated from trials directly by calculating the fraction of pseudo experiments that result in an equal or larger TS value than the experimentally observed value. Therefore, the TS distribution based on pseudo experiments generated using the BFP-method is used. As long as the experimental TS value for a source is not much larger than 15, the generation of 10^6 trials is sufficient. In case the TS value would be larger, more pseudo experiments have to be performed. The background TS distributions for each source can be found in Appendix G.2.

The best-fit parameters $\hat{n}_s$ and $\hat{\gamma}$, as well as the TS value and the local p-value are calculated for each source separately yielding 34 local p-values. To combine the results from these 34 local p-values the source with the smallest p-value is picked, which is the most likely source. To trial correct for picking the most significant source, the local p-value has to be compared with the local p-value from the most significant source in the list calculated on pseudo experiments.

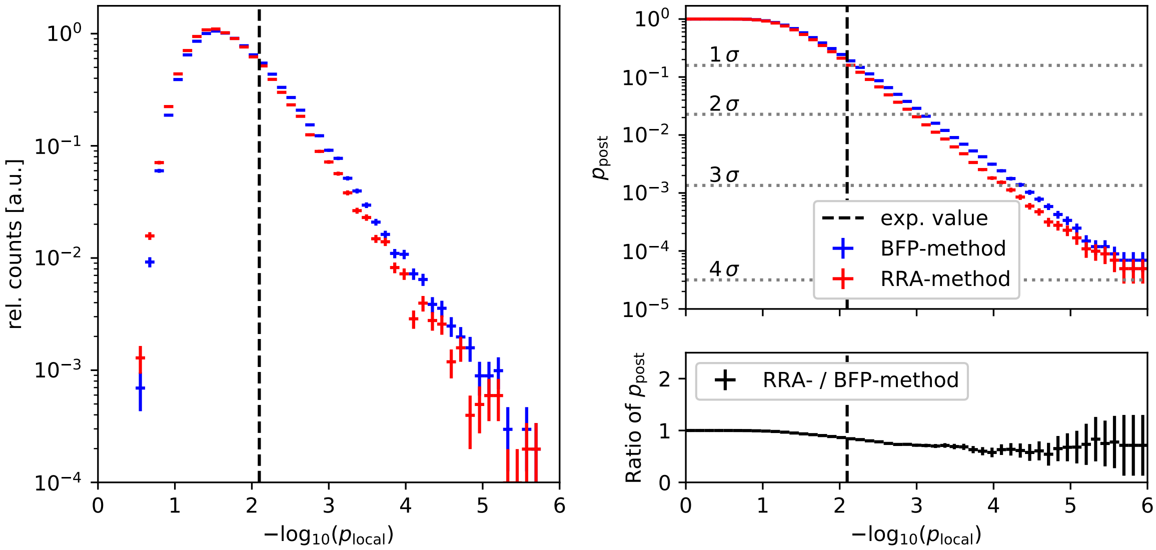

Figure 8.7: Local p-value distribution of most significant source in the source catalog (left) and post-trial p-value as a function of local p-value distribution of most significant source (right). The blue and red histogram is calculated from ~ 3500 pseudo-experiments using the best-fit parametrization (BFP) method and the randomized right ascension (RRA) method, respectively. The black vertical line shows the experimentally observed value. The lower right panel shows the ratio of p_{post} using the two different pseudo experiment methods.

The distribution of the local p-value of the most significant source in the source list in only background pseudo experiments can be seen in Fig. 8.7, along with the post-trial p-value as a function of the local p-value of the most significant source in the source list and the ratio of the post-trial p-value once calculated using the BFP-method and the RRA-method. From Fig. 8.7 it can be seen that the post-trial p-values obtained by pseudo experiments generated using the BFP-method is less significant than the p-value obtained from the RRA-method and thus more conservative. However, from the ratio of the p_{post} one can see that this difference is at most a factor of two. Note that even with a factor of two in the p-value the significance does not change much if the significance is large. A two sample Kolmogorov-Smirnov test, to test if the two representations originate from the same distribution, results in a two-sided p-value of 2.2×10^{-67}, leading to the conclusion that these distribution are not compatible.

8.2.2 Experimental Result

The 34 source on the source list are individually tested and the best fit parameter of $\hat{n}_s$ and $\hat{\gamma}$ as well as the TS value and the local p-value of each source are given in Tab. 8.1. Note that $\hat{\gamma}$ has only small deviations within the spectral index due to the prior on the spectral index.

The most significant source in the source list is 4C 38.41, which is a flat spectrum radio quasar (FSRQ) with a redshift of $z \approx 1.8$ [273, 280][2]. The local p-value of 4C 38.41 is 0.8%.

---

[2] http://simbad.u-strasbg.fr/simbad/sim-id?Ident=4C+38.41

Source Name	Type	α [deg]	δ [deg]	size [deg]	p-Value (local)	TS	$\hat{n}_s$	$\hat{\gamma}$	$\hat{\phi}_{100\,\mathrm{TeV}}$ $[\mathrm{TeV}^{-1}\mathrm{cm}^{-2}\,\mathrm{s}^{-1}]$	$\phi^{\mathrm{limit}}_{100\,\mathrm{TeV}}(E^{-2.0})$ $[\mathrm{TeV}^{-1}\mathrm{cm}^{-2}\,\mathrm{s}^{-1}]$	$\phi^{\mathrm{limit}}_{100\,\mathrm{TeV}}(E^{-2.19})$ $[\mathrm{TeV}^{-1}\mathrm{cm}^{-2}\,\mathrm{s}^{-1}]$
4C 38.41	FSRQ	248.81	38.13	—	0.0080	5.089	7.69	-2.19	$4.87 \cdot 10^{-17}$	$1.27 \cdot 10^{-16}$	$5.63 \cdot 10^{-17}$
MGRO J1908+06	NI	286.99	6.27	0.34 [272]	0.0088	4.793	2.82	-2.18	$1.85 \cdot 10^{-17}$	$7.62 \cdot 10^{-17}$	$4.65 \cdot 10^{-17}$
Cyg A	SRG	299.87	40.73	— [273]	0.0101	4.720	3.80	-2.18	$2.42 \cdot 10^{-17}$	$1.28 \cdot 10^{-16}$	$5.63 \cdot 10^{-17}$
3C454.3	FSRQ	343.50	16.15	— [273]	0.0258	2.967	5.03	-2.19	$3.24 \cdot 10^{-17}$	$8.08 \cdot 10^{-17}$	$4.83 \cdot 10^{-17}$
Cyg X-3	XB/mqso	308.11	40.96	— [274]	0.1263	0.570	4.33	-2.20	$2.71 \cdot 10^{-17}$	$8.20 \cdot 10^{-17}$	$5.58 \cdot 10^{-17}$
Cyg OB2	SFR	308.09	41.23	1.00 [275]	0.1706	0.255	2.82	-2.20	$1.77 \cdot 10^{-17}$	$7.64 \cdot 10^{-17}$	$5.77 \cdot 10^{-17}$
LSI 303	XB/mqso	40.13	61.23	— [272]	0.2056	0.175	2.37	-2.19	$1.48 \cdot 10^{-17}$	$9.93 \cdot 10^{-17}$	$6.98 \cdot 10^{-17}$
NGC 1275	SRG	49.95	41.51	— [272]	0.2447	0.023	0.50	-2.19	$3.14 \cdot 10^{-18}$	$6.96 \cdot 10^{-17}$	$5.71 \cdot 10^{-17}$
1ES 1959+650	BL Lac	300.00	65.15	— [272]	0.2573	0.072	1.70	-2.20	$1.05 \cdot 10^{-17}$	$9.86 \cdot 10^{-17}$	$7.24 \cdot 10^{-17}$
Crab Nebula	PWN	83.63	22.01	— [272]	0.3213	-0.020	0.00	—	0.0	$4.74 \cdot 10^{-17}$	$5.10 \cdot 10^{-17}$
Mrk 421	BL Lac	166.11	38.21	— [272]	0.3460	-0.021	0.00	—	0.0	$5.79 \cdot 10^{-17}$	$5.66 \cdot 10^{-17}$
Cas A	SNR	350.85	58.81	— [272]	0.3808	-0.017	0.00	—	0.0	$7.01 \cdot 10^{-17}$	$6.54 \cdot 10^{-17}$
TYCHO	SNR	6.36	64.18	— [272]	0.3893	-0.022	0.00	—	0.0	$7.98 \cdot 10^{-17}$	$7.43 \cdot 10^{-17}$
PKS 1502+106	FSRQ	226.10	10.52	— [276]	0.3931	-0.177	0.00	—	0.0	$3.57 \cdot 10^{-17}$	$4.83 \cdot 10^{-17}$
3C66A	BL Lac	35.67	43.04	— [272]	0.4265	-0.109	0.00	—	0.0	$5.44 \cdot 10^{-17}$	$5.93 \cdot 10^{-17}$
3C 273	FSRQ	187.28	2.05	— [277]	0.4285	-0.371	0.00	—	0.0	$2.72 \cdot 10^{-17}$	$4.38 \cdot 10^{-17}$
HESS J0632+057	XB/mqso	98.24	5.81	— [272]	0.5017	-0.760	0.00	—	0.0	$2.82 \cdot 10^{-17}$	$4.59 \cdot 10^{-17}$
BL Lac	BL Lac	330.68	42.28	— [272]	0.5378	-0.477	0.00	—	0.0	$4.78 \cdot 10^{-17}$	$5.77 \cdot 10^{-17}$
W Comae	BL Lac	185.38	28.23	— [272]	0.5961	-1.077	0.00	—	0.0	$3.88 \cdot 10^{-17}$	$5.36 \cdot 10^{-17}$
Cyg X-1	XB/mqso	299.59	35.20	— [272]	0.6170	-1.064	0.00	—	0.0	$4.31 \cdot 10^{-17}$	$5.43 \cdot 10^{-17}$
1ES 0229+200	BL Lac	38.20	20.29	— [272]	0.6257	-1.687	0.00	—	0.0	$3.41 \cdot 10^{-17}$	$5.04 \cdot 10^{-17}$
M87	SRG	187.71	12.39	— [278]	0.7054	-2.968	0.00	—	0.0	$3.26 \cdot 10^{-17}$	$4.84 \cdot 10^{-17}$
Mrk 501	BL Lac	253.47	39.76	— [272]	0.7214	-1.986	0.00	—	0.0	$4.58 \cdot 10^{-17}$	$5.63 \cdot 10^{-17}$
PKS 0235+164	BL Lac	39.66	16.62	— [273]	0.7494	-3.595	0.00	—	0.0	$3.33 \cdot 10^{-17}$	$5.02 \cdot 10^{-17}$
H 1426+428	BL Lac	217.14	42.67	— [272]	0.7587	-2.510	0.00	—	0.0	$4.86 \cdot 10^{-17}$	$5.83 \cdot 10^{-17}$
PKS 0528+134	FSRQ	82.73	13.53	— [273]	0.7788	-4.455	0.00	—	0.0	$3.18 \cdot 10^{-17}$	$4.90 \cdot 10^{-17}$
S5 0716+71	BL Lac	110.47	71.34	— [272]	0.7802	-2.071	0.00	—	0.0	$8.02 \cdot 10^{-17}$	$8.20 \cdot 10^{-17}$
Geminga	PWN	98.48	17.77	2.60 [272]	0.7950	-4.779	0.00	—	0.0	$3.41 \cdot 10^{-17}$	$5.01 \cdot 10^{-17}$
SS433	XB/mqso	287.96	4.98	$0.35^{\dagger}$ [272]	0.8455	-8.005	0.00	—	0.0	$2.71 \cdot 10^{-17}$	$4.62 \cdot 10^{-17}$
M82	SRG	148.97	69.68	0.18 [279]	0.8456	-3.557	0.00	—	0.0	$8.04 \cdot 10^{-17}$	$8.07 \cdot 10^{-17}$
3C 123.0	SRG	69.27	29.67	—	0.9056	-8.292	0.00	—	0.0	$4.11 \cdot 10^{-17}$	$5.33 \cdot 10^{-17}$
1ES 2344+514	BL Lac	356.77	51.70	— [272]	0.9518	-10.139	0.00	—	0.0	$5.28 \cdot 10^{-17}$	$6.30 \cdot 10^{-17}$
IC443	SNR	94.18	22.53	0.16 [272]	0.9620	-16.415	0.00	—	0.0	$3.63 \cdot 10^{-17}$	$5.25 \cdot 10^{-17}$
MGRO J2019+37	PWN	305.22	36.83	0.75 [272]	0.9784	-17.607	0.00	—	0.0	$4.54 \cdot 10^{-17}$	$5.61 \cdot 10^{-17}$

Table 8.1: Results of the *a-priori* defined source list search. Coordinates are given in equatorial coordinates (J2000). The fitted spectral index $\hat{\gamma}$ is not given if $\hat{n}_s$ is fitted to zero. The table is sorted by the local p-value of the sources. Source types abbreviation: BL Lacertae object (BL Lac), Flat Spectrum Radio Quasar (FSRQ), Not Identified (NI), Pulsar Wind Nebula (PWN), Star Formation Region (SFR), Supernova Remnant (SNR), Starburst / Radio Galaxy (SRG), X-ray Binary and Micro-Quasar (XB/mqso). † The TeV emission in SS 433 is located in two points seperated by 0.35°.

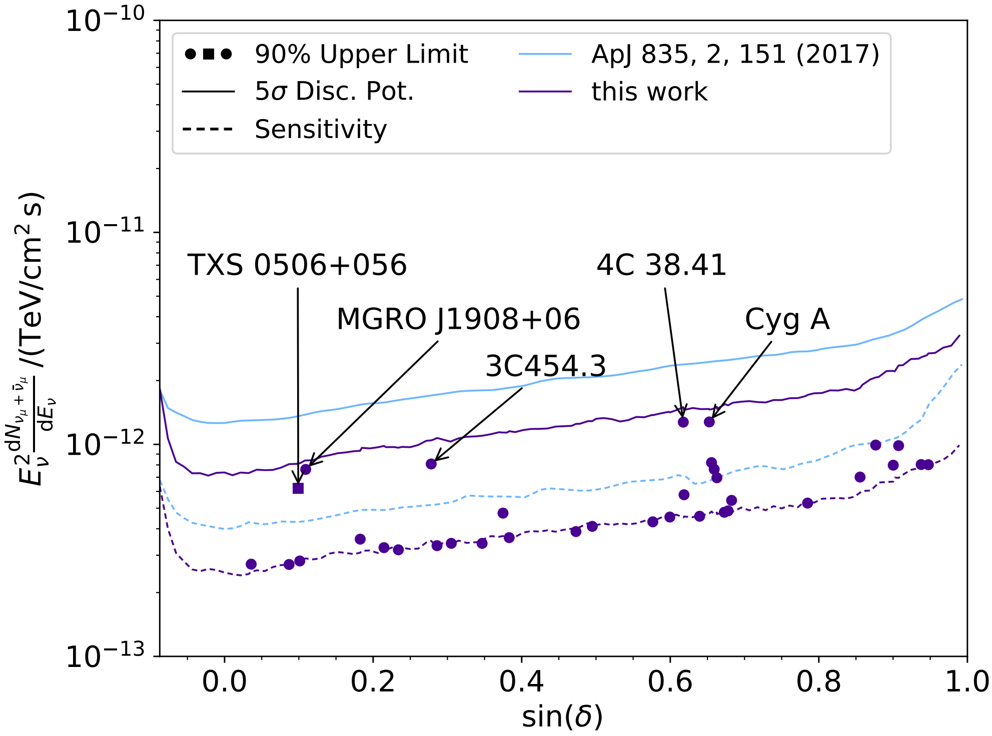

Figure 8.8: 90% CL upper limits on source flux for sources on the source list assuming an $E^{-2.0}$ spectrum. Upper limits that would be below the sensitivity level of the analysis are set to the sensitivity flux. For comparison, the sensitivity and discovery potential are shown.

This local p-value is indicated as black dashed vertical line in Fig. 8.7, and a post-trial p-value of 23.7% and 20.3% can be read of, using pseudo experiments generated using the BFP-method and the RRA-method, respectively. This post-trial p-value is non-significant and thus the result is compatible with only background.

As no significant deviation above background was found for any of the sources in the catalog, 90% upper limits on the flux normalization can be calculated assuming a fixed spectral shape. The upper limit calculation is described in Sec. 7.3. Here the 90% upper limits for a source spectrum of $E^{-2.0}$ and $E^{-2.19}$ is calculated for each source and listed in Tab. 8.1. In case the 90% upper limit would lie below the sensitivity of the analysis, the 90% upper limit is set to the sensitivity flux normalization.

The 90% upper limits on the flux normalization for each source are also shown in Fig. 8.8 as dots at the declination of the source. For comparison also the sensitivity and discovery potential on the flux normalization is shown. Note, that the 90% upper flux limit can exceed even the discovery potential flux, as long as the best-fit flux normalization lies below the discovery potential.

The best-fit flux normalization is calculated from the best-fit $\hat{n}_s$ taking into account the conversion of signal events to flux normalization for the best-fit spectral index, as discussed in Sec. 7.2.

8.2.3 Further Investigations

Within the source list there are four sources that have a local p-value of a few percent or even below. These sources are 4C 38.41, MGRO J1908+06, Cyg A and 3C454.3. Even though these sources are non significant, it is interesting to have a closer look at them.

4C 38.41 is an optically violent variable FSRQ at a redshift of $z = 1.813970 \pm 0.000155$ [273, 280][3], that had a big optical outburst in 2011 which was also detected in X-ray and in the UV band by Swift and in gamma-rays by Fermi [282, 283]. 3C 454.3 is also a FSRQ at redshift of z=0.859001 ± 0.000170 [273][4] and is the brightest gamma-ray blazar in the sky [284]. It also shows strong flares in radio and visible wavelengths and had a bright flare in June 2014 with an apparent magnitude of 13.4 [285][5]. Cygnus A is the closest ultra-luminous radio galaxy [286] with a redshift of $z = 0.056075 \pm 0.000067$ [273][6] and thus one of the strongest radio sources in the sky. Note that it has not been detected in gamma-rays so far [287]. Note, that the lobe of the extended radio jets which can be resolved in X-ray have a distance of about 0.05° and thus appear point-like. MGRO J1908+06 is a galactic extended TeV gamma-ray emission region with a standard deviation of $\sigma_{\mathrm{src}} = 0.44° \pm 0.02°$ [281]. It can be attributed to the pulsar PSR J1907+0602 at a distance of 3.2 kpc or the supernova remnant G40.5-0.5 at a distance of 3.4 kpc. It is one of few sources that have been detected in gamma-rays above 56 TeV by HAWC [288] and has been proposed to be a detectable neutrino source, e.g. in [289].

For each of these sources a zoom into the p-value landscape around the source position is shown in Fig. 8.9. It can be seen that for these sources a local hot-spot is near the source position. Note that MGRO J1908+06 is extended in TeV gamma rays and different experiments report different source positions [281, 290, 291]. Here the position as reported by the H.E.S.S. collaboration is used [290]. In Fig. 8.9 the contours of the H.E.S.S. excess map is overlayed to indicate the size and morphology of the source. The local hot-spot close to the tested position is fully contained by the H.E.S.S., VERITAS and HAWC contour and positioned at the center [281, 290, 292].

8.3 Testing the Position of Blazar TXS 0506+056

The source list discussed in Sec. 8.2 is kept fixed since several years, to not influence the selection of sources by neutrino observations itself. This is both an advantage and disadvantage at the same time, as the progress in the field is not reflected in the catalog. Not reporting about recently found interesting source candidates is also strange. Therefore, this Section discusses a test of the position of the Blazar TXS 0506+056, which is a source for that evidence for neutrino emission has been reported [20]. The analysis presented here is very similar to the time-integrated analysis presented in [20] and was done as a cross-check of the result prior to publication.

---

[3] http://simbad.u-strasbg.fr/simbad/sim-id?Ident=4C+38.41

[4] `http://simbad.u-strasbg.fr/simbad/sim-basic?Ident=3C+454.3`

[5] `https://www.aavso.org/lcg/plot?auid=000-BDC-612&starname=3C+454.3`

[6] `http://simbad.u-strasbg.fr/simbad/sim-basic?Ident=NAME+Cygnus+A`

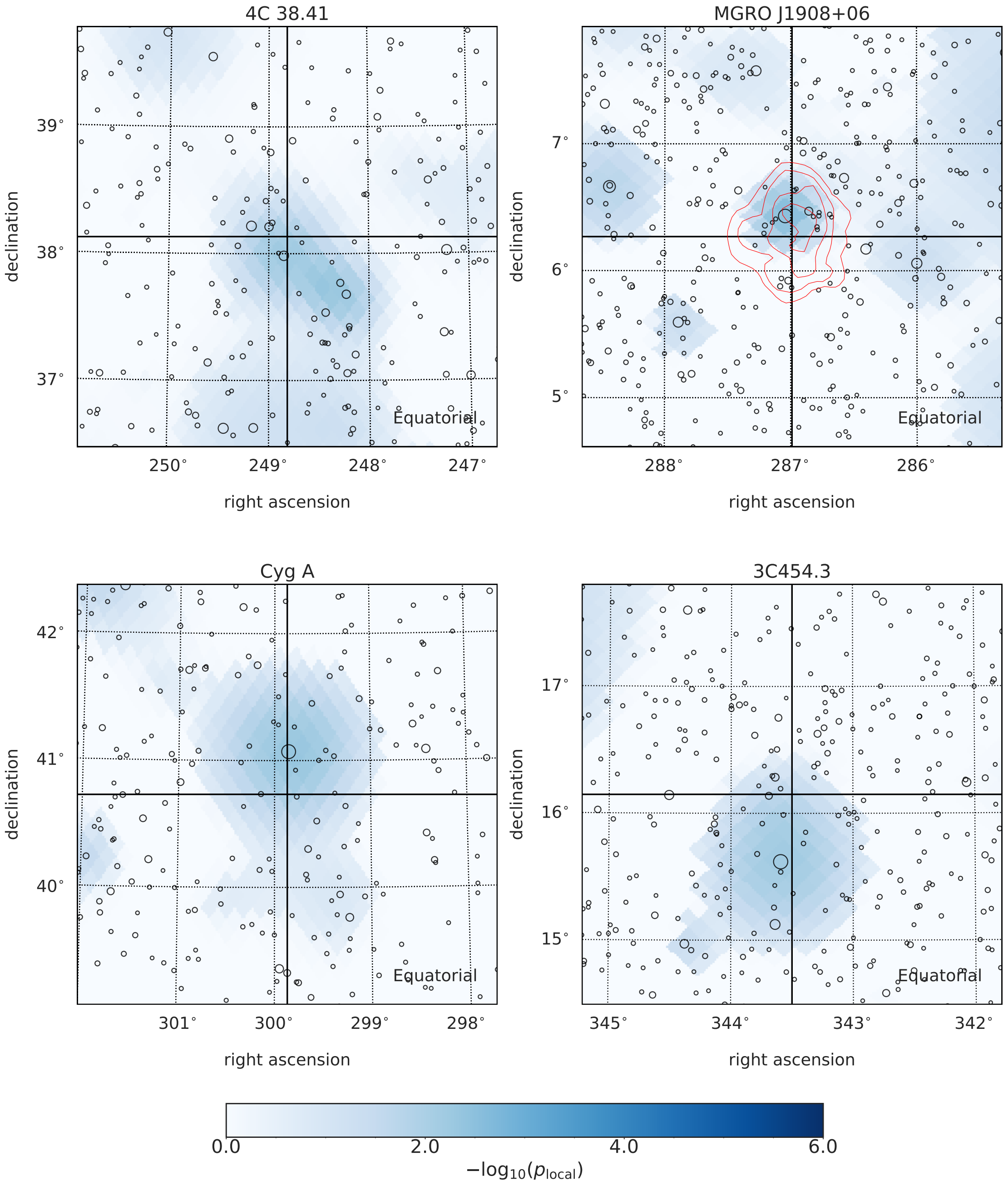

Figure 8.9: Local p-value landscape around 4C 38.41 (upper left), MGRO J1908+06 (upper right), Cyg A (lower left) and 3C 454.3 (lower right). The maps are given in equatorial coordinates (J2000) and are centred on the source position. Neutrino events are overlayed as circles where the size corresponds to the $\log_{10}$ of the median neutrino energy assuming the best fit spectrum. The red contours in the upper left panel show the 4σ, 5σ, 6σ and 7σ levels of the HESS excess map for MGRO J1908+06 [281].

8.3.1 Coincident Observation of IceCube-170922A and a Flare of Blazar TXS 0506+056

On September 22, 2017 the IceCube Neutrino Observatory detected an extreme-high-energy event that triggered the IceCube's realtime system [141] called IceCube-170922A. The realtime system checks the taken data of IceCube live at the South Pole for spectacular events. The event, IceCube-170922A, has a well reconstructed direction with an uncertainty of less than $(1\,\mathrm{deg})^2$ at 90% CL and deposited (23.7 ± 2.8) TeV energy within the IceCube detector. The neutrino energy of the event is 290 TeV assuming an $E^{-2.13}$ spectrum with a 90% CL lower limit of 183 TeV. The signalness of the events, and thus the probability to be of astrophysical origin, is calculated based on its energy and declination and is 56.5% [19].

IceCube's realtime system send out a Gamma-Ray Coordinates Network (GCN) notice[7] 43 seconds after the detection of event, encouraging follow-up observations by other telescopes. Few hours later a GCN report with refined direction of the event was issued [293].

On September 28, 2017 the Fermi collaboration reported that the source TXS 0506+056 is located inside the event uncertainties of the IceCube-170922A events, which is also listed in the 3FGL and 3FHL catalogs [267, 268]. In addition, the Fermi All-sky Variability Analysis (FAVA), that analyses light curves at energies above 800 MeV, using data from the Fermi Large Area Telescope (LAT), found that TXS 0506+056 was in a flaring state with an increased flux of about a factor 6 larger than its long time average flux with nearly the same spectrum [294].

Using monthly binned light curves above 1 GeV for 2257 extra-galactic sources that are contained in the Fermi-LAT catalog, a likelihood ratio test was performed comparing chance coincidences and correlated neutrino and gamma-ray emission. After correcting for the non-observation of a counter part in previous alerts (9 alerts and 41 events that would have resulted in an alert before the realtime system was deployed in April 2016), correlated emission is preferred over pure chance coincidence of a neutrino alert in spatial and temporal coincidence with a flaring extra-galactic source at the $3\,\sigma$ level [19].

As a follow-up the MAGIC collaboration also found the source TXS 0506+056 in a flaring state with energies up to 400 GeV around the arrival time of IceCube-170922A. The source has not been observed in VHE gamma-rays before. Further follow-up observations lead to the determination of the redshift of $z = 0.3365 \pm 0.0010$ [295]. An independent lower bound on the redshift of $z < 0.61 - 0.98$ at 95% CL could be derived from the observation of VHE gamma-rays, because they are not yet absorbed by interactions with the extra-galactic background light. With the measurement of the redshift of TXS 0506+056 it turns out that it is one of the most luminous blazar, known.

In Fig. 8.10 the spectral energy distribution at multi-wavelength obtained within 14 days of the detection of the neutrino alert IceCube-170922A is shown. The spectrum shows the typical non-thermal double-bump structure of a blazar. The first bump peaks in the optical-ultraviolet range and is considered to be caused by synchrotron radiation of relativistic electrons. The second bump peaks in the GeV range that can either be explained by inverse Compton scattering of leptons or by π^0 decays produced in hadronic interactions. For comparison an upper limit

---

[7] `https://gcn.gsfc.nasa.gov/notices_amon/50579430_130033.amon`

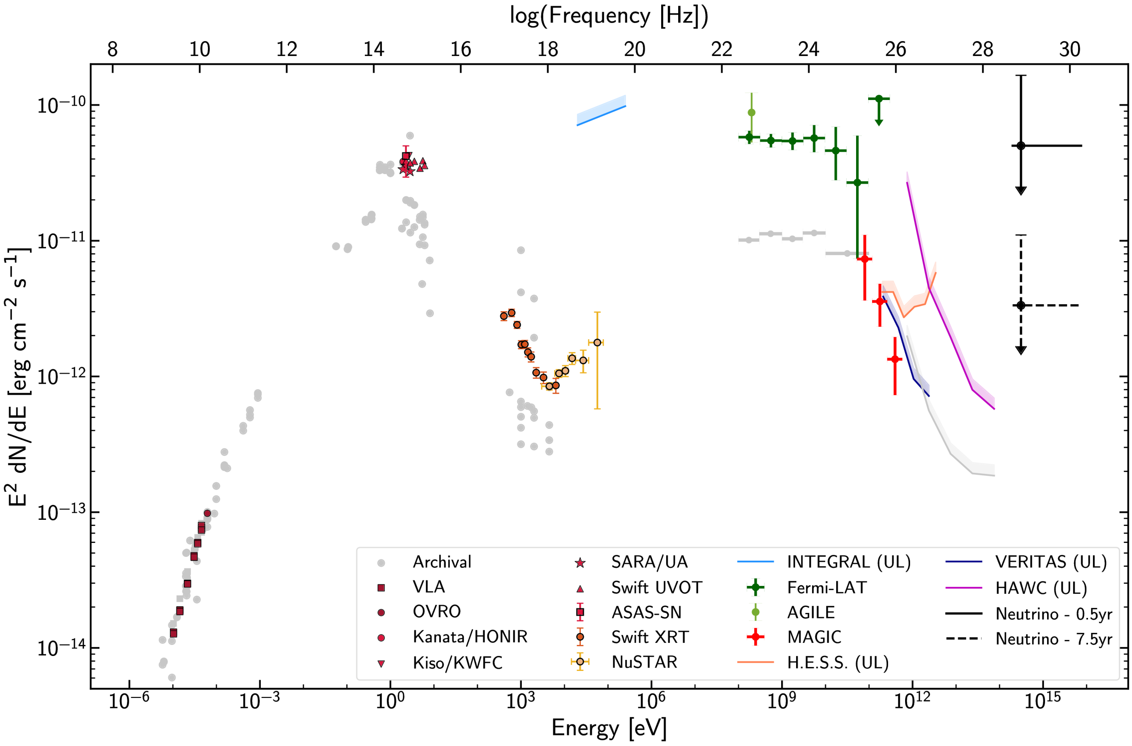

Figure 8.10: Broadband spectral energy distribution for the blazar TXS 0506+056. The spectrum has been multiplied by E^2 for better visualization of the structure. The SED is based on observations obtained within 14 days of the detection of the IceCube-170922A event. Archival observations are shown in gray. Differential flux upper limits (UL) are quoted at the 95% C.L. while markers indicate significant detections. The observations have not been corrected for absorption owing to the EBL and for Galactic attenuation. Figure taken from [19] and references there in.

for the $\nu_\mu + \bar{\nu}_\mu$ was calculated assuming an E^{-2} spectrum and based on the fact that one event like IceCube-170922A has been detected within a period of 0.5 years and 7.5, respectively [19]. Note that the chosen time range for this calculation is arbitrary and assumptions to calculate a flux from a single event are necessary. Gray data points show archival data and it can be seen that the gamma-ray flux is larger by a factor of six compared to the long time average in the energy range from $10^8\,\mathrm{eV}$ to $10^{10}\,\mathrm{eV}$. One also can see that at gamma-ray energies the spectral shape does not change and stays approximately $E^{-2.0}$. At about $10^{11}\,\mathrm{eV}$ the spectrum steeply drops due to interactions of VHE gamma-rays with the extra-galactic background but measurement of the flux reach up to 400 GeV.

8.3.2 Time-Integrated Analysis of Archival Data

The observation of a flaring blazar in spatial and temporal coincidence with a high-energy neutrino alert at the $3\,\sigma$ level motivates a test for neutrino emission prior to the alert. Therefore, in the scope of this thesis, the celestial direction of TXS 0506+056 is tested for neutrino emission as each other source on the source list discussed in Sec. 8.2. The resulting best fit parameters, the TS value and the local p-value are given in Tab. 8.2.

The celestial direction of TXS 0506+056 shows a mild excess with a p-value of 2.93% ($1.9\,\sigma$). The local p-value landscape around the position of TXS 0506+056 is shown in Fig. 8.11 where the reconstruction contours at the 50% and 90% CL of the IceCube-170922A alert are overlayed. Note that the test for point-like neutrino emission presented here is independent of the alert and the coincident observation of the flaring blazar, as the dataset used in this thesis was taken until May 2017, while the alert event was detected in September 2017. Thus, also the two significances of $3.0\,\sigma$ and the $1.9\,\sigma$ are independent. Also note that no additional trial-correction is done as it is done for the source list presented in Sec. 8.2.

In [20] a similar analysis is presented, that uses the analysis method and data sample as published in [13]. This sample consists of 7 years of IceCube data also taken prior to the neutrino alert, with a large overlap to the sample used in this analysis. The best-fit parameters are $\Phi_{100\,\mathrm{TeV}} = (0.9^{+0.6}_{-0.5}) \cdot 10^{-16}$ and $\hat{\gamma} = 2.1 \pm 0.3$ with a similar mild excess with a local p-value of 1.6% (2.1σ). The analysis presented in this thesis was used to cross-check this result. Note that a comparison with the 9.5 year result in [20] is not appropriate as this result includes the neutrino alert and thus is not an independent result.

In Fig. 8.12 the likelihood landscape of the fit parameter n_s and γ is shown once for the analysis presented in this thesis (left) and for the analysis presented in [20] (right). Note that the different shape of the landscape is a result of the prior on the spectral index in this analysis that is not present in [20] (Fig.4b). Taking the differences in the analysis method and the differences in the data sample into account, the results agree within uncertainties.

As no significant excess above only background has been observed, a 90% CL upper limit is calculated for TXS 0506+056 assuming an $E^{-2.0}$ spectrum as it is done for other source of the source list in Sec. 8.2.2 and is explained in Sec. 7.3. The 90% upper limit is listed in Tab. 8.2 and shown in Fig. 8.8.

Source Name	Type	α [deg]	δ [deg]	size [deg]	p-Value (local)	TS	$\hat{n}_s$	$\hat{\gamma}$	$\hat{\phi}_{100\,\mathrm{TeV}}$ $[\mathrm{TeV}^{-1}\mathrm{cm}^{-2}\,\mathrm{s}^{-1}]$	$\phi^{\mathrm{limit}}_{100\,\mathrm{TeV}}(E^{-2.0})$ $[\mathrm{TeV}^{-1}\mathrm{cm}^{-2}\,\mathrm{s}^{-1}]$	$\phi^{\mathrm{limit}}_{100\,\mathrm{TeV}}(E^{-2.19})$ $[\mathrm{TeV}^{-1}\mathrm{cm}^{-2}\,\mathrm{s}^{-1}]$
TXS 0506+056	BL Lac	77.38	5.69	—[2]	0.0293	2.647	7.87	-2.20	$5.08 \cdot 10^{-17}$	$6.19 \cdot 10^{-17}$	$4.57 \cdot 10^{-17}$

Table 8.2: Results of the *monitored* sources list search. Coordinates are given in equatorial coordinates (J2000). The table is sorted by the local p-value of the sources. We use the source types abbreviation BL Lac for BL Lacertae object.

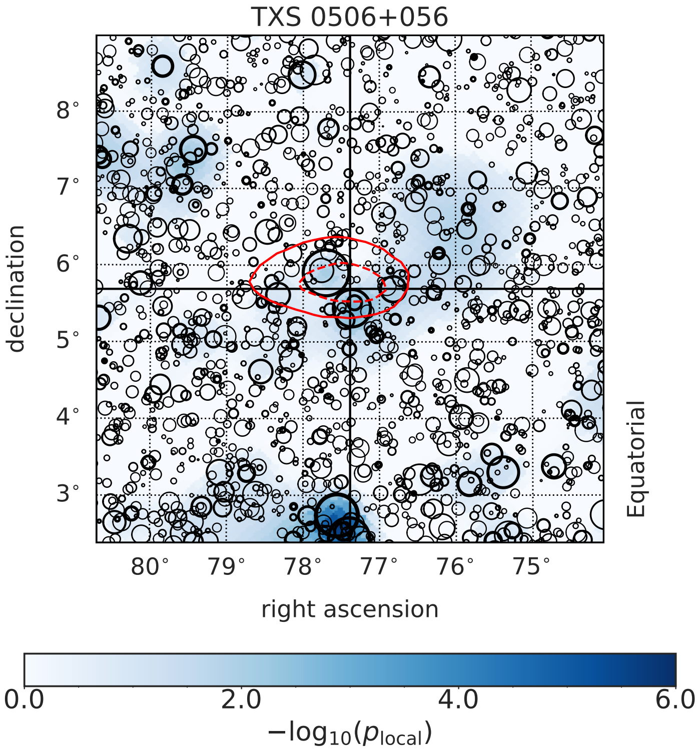

Figure 8.11: Local p-value landscape around TXS 0506+056. The map is given in equatorial coordinates (J2000) and is centred on the source position. Neutrino events are overlayed as circles where the circle radius scales with the inverse of the angular uncertainty estimate and the linewidth scales with $\log_{10}$ of the median neutrino energy assuming the best fit spectrum. In addition, the 50% (red, dashed) and 90% (red, solid) contours of the IceCube-170922A event are overlayed.

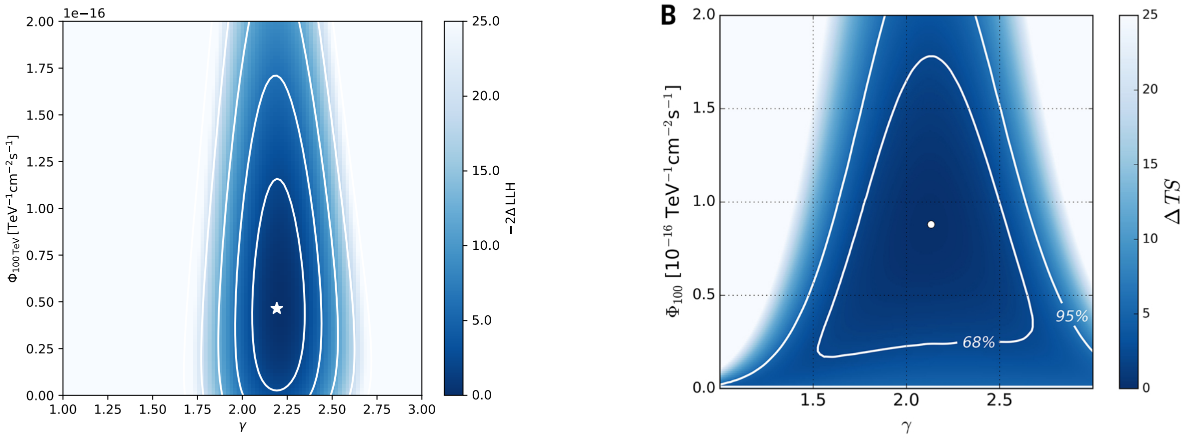

Figure 8.12: Log-likelihood landscape for a scan of the fit parameter n_s and γ for the celestial position of the blazar TXS 0506+056. The left panel shows the scan for the analysis as presented in this thesis while the right panel is taken from [20]. Contours correspond to the 1, 2, 3, 4 and 5σ CL assuming Wilk's theorem with 2 degrees of freedom.

8.3.3 Time-Dependent Analysis of Archival Data

Beside testing for time-integrated emission the location of TXS 0506+056 has been also tested for time-dependent emission in [20]. Therefore, the likelihood similar to the one presented in Sec. 6.1 is extended by adding a time-dependent probability density function. This time-dependent probability density function is flat for only background and has been characterized by a box-shaped or Gaussian probability density function for signal as a clear signal shape can not be determined. The signal probability distribution has additional free parameters which are the central time of the neutrino flare and the duration of the flare, which are either given by the width of the box or the standard deviation of the Gaussian distribution. Both parameters are additional free parameters and are fitted to determine the log likelihood.

In [20] the time-dependent analysis was performed once using a Gaussian shaped and once a box-shaped PDF. The analysis using the Gaussian-shaped PDF found an excess of neutrinos centered around the 13 December, 2014 ± 21 days with a width of 110^{+35}_{-24} days. The analysis results in a p-value of $1 \cdot 10^{-4}$ for only background, which corresponds to 3.7σ. The box-shaped analysis also found an excess centered around the 26 December 2014, with a width of 158 days. Also this analysis results in a p-value of $2 \cdot 10^{-4}$ for only background, which corresponds to 3.5σ. The excess in both analysis is 13 ± 5 events above background, where the background expectation in a circle with 1 degree radius is 5.8 events per 158 days. After correcting for choosing any of the two analysis results, this gives a trial corrected p-value of 3.5σ [20]. Note that the results of the time-integrated analysis is in agreement with the time dependent result, as the result becomes less significant if integrated over a longer time range.

Note that again this result is independent from the coincidence of the neutrino alert and the gamma-ray flare of the blazar. In addition, the neutrino alert had a probability to be of astrophysical origin on its own of 56.5%. Combining these results is however complicated as the alert event triggered the search for a point-like emission. Thus, if these results would be combined, the p-value of the search for a point-like emission in the archival data would have to be trial corrected.

Even without combining the results, the blazar TXS 0506+056 shows evidence for neutrino emission and would be the first source associated with high-energy neutrino emission.

Also before the IceCube-170922A alert event, IceCube performed systematic analysis for blazars and did a stacked search for blazars from the Fermi 2LAC catalog [296]. The search resulted in an upper limit that the sources of the 2LAC catalog contribute less than 27% to the measured astrophysical neutrino flux assuming an $E^{-2.5}$ spectrum [11]. If assuming an E^{-2} spectrum above $> 200\,\mathrm{TeV}$, the constraint weakens so that 2LAC sources contribute less than 40% - 80% to the astrophysical neutrino flux. Note that the best fit flux of TXS 0506+056 corresponds to 1% of the total astrophysical neutrino flux measured in 9.5 years.

With the measurement of the redshift of TXS 0506+056 it turns out, that it is one of the most luminous objects. TXS 0506+056 is located in the sweet spot for IceCube, as it is located at a declination close to the horizon, where the sensitivity and discovery potential for point-like neutrino sources is optimal as can be seen in Fig. 8.8.

To summarize, in all three tested hypothesis no significant time-independent neutrino source is found and upper limits for sources assuming an E^{-2} spectrum have been derived. Further constrains on individual source spectra resulting from these measurements are discussed in Chapter 10. Despite no source has been significant on its own, it may be possible to find an excess of small p-values due to a population of sources that are to weak to be detected on their own. Therefore, in Chapter 9 tests for populations of sub-threshold sources are presented.

Chapter 9

Testing for Populations of Sub-Threshold Sources

Declaration of Pre-released Publications The experimental results presented in this chapter have been previously published by the IceCube Collaboration in M. G. Aartsen *et al.* (IceCube Collaboration), "Search for steady point-like sources in the astrophysical muon neutrino flux with 8 years of IceCube data" The European Physical Journal C 79, 234 (2019). The author of this thesis has written this publication as a corresponding author. The author performed the experimental results of the population analysis of the sub-threshold sources in the source list method and the hot-spot population analysis.

All analyses presented in Chapter 8 test the existence of a single point-like source at a certain celestial position. These tests come out to be non significant after trial correction, which motivates the search for a population of sub-threshold sources. The tests presented in this chapter utilize that in case that data follow the background hypothesis, p-values are expected to be uniformly distributed between zero and one. The occurrence of multiple small p-values in a list of p-values thus hint to a population of weak sources. As pointed out in Sec. 8.2.3, there are four sources within the source list that have a small p-value below 2.6%, which however are not significant individually. Therefore, a test for a population of sub-threshold sources is discussed in Sec. 9.1.1, and the experimental result is given in Sec. 9.1.2. A similar method can be performed on the p-value map of the whole sky, as discussed in Sec. 9.2, and the corresponding method is presented in Sec. 9.2.1. In contrast to the tests in Chapter 8, where only single source locations are tested, pseudo-experiments have to take into account correlations over the entire sky. When testing for multiple sources distributed over the whole sky, pseudo experiments become computing intensive. Therefore, the generation of pseudo-experiments is revisited in Sec. 9.2.2. The experimental result is given in Sec. 9.2.3 and limits for the benchmark scenario of equal-strength sources are presented in Sec. 9.2.4. When testing for a population of very weak sources, the signal hypothesis becomes quasi-diffuse like with increasing number of sources. Therefore, the influence of a pure diffuse flux on the result of the hot-spot population analysis (HPA) is discussed in Sec. 9.2.5. The astrophysical implications of the HSP are discussed in Chapter 10.

9.1 Population of Sub-Threshold Sources in the Source List

9.1.1 Method

The source list tested in Sec. 8.2 contains 34 sources. In case that all tested spots consist of only background, the local p-values p_{local} are expected to be uniformly distributed between zero and one. If there is a population of sub-threshold sources in the catalog that are close to the detection threshold, there would be an excess of small local p-values.

When $p_{\text{local},i}$ is the local p-value of the ith source in the source list, and considering a threshold p-value p_{thres}, one can count the number of spots that have $p_{\text{local},i} < p_{\text{thres}}$. By counting the number of spots that are below the threshold, the statistic is binomial, as this is a yes-or-no question for each of the spots. The p-value to find k out of $N = 34$ sources with a local p-value smaller or equal to p_{thres} is

$$p_{\text{binom}} = \sum_{k}^{N} \binom{N}{k} p_{\text{thres}}^{k} \cdot (1 - p_{\text{thres}})^{N-k} \,. \tag{9.1}$$

The binomial p-value p_{binom} is a function of p_{thres}. $p_{\text{binom}}(p_{\text{thres}})$ has a local minimum, if $p_{\text{thres}} = p_{\text{local},k}$, where $p_{\text{local},k}$ is the p-value of the kth p-value in the list. This can be seen from Eq. 9.1, where the p_{binom} increases for increasing p_{thres} if no additional event is considered in the sum. Once p_{thres} exceeds the p-value of an additional event another summand has to be considered leading to a sawtooth function. Thus, it is sufficient to calculate the binomial p-values at p-value thresholds corresponding to the local p-values of the 34 tested source locations. The smallest p_{binom}, or equivalent the largest significance, is chosen as a test statistic for this test.

Because the number k that yields the smallest p_{binom} is not known a-priori, the result has to be corrected for the trials made for testing each possible value of k. This can be evaluated by running the analysis on pure background pseudo experiments. Note that it is important that all 34 source locations are evaluated on the same pseudo experiment to account for possible correlations of source locations that are close to each other.

The distribution of the local significance of the most significant binomial combination of p-values for pure background pseudo experiments is shown in Fig. 9.1 (left). Note that the tails are non-gaussian and thus post-trial p-value can slightly exceed the maximal local significance. The distribution slightly shifts to lower significance, if using pseudo experiments generated with the RRA-method compared to pseudo experiments generated with the BFP-method (see Sec. 7.1.1). A two-sample Kolmogorov-Smirnov-test [252, 253], to test that the two method are representations of the same underlying distribution, yields a p-value of 0. Fig. 9.1 (right) shows the post-trial p-value as a function of the significance of the most significant binomial combinations before trial correction. The lower panel shows the ratio of the post trial p-value calculated using the RRA-method and the BFP-method. One can see that the BFP-method yields slightly more conservative p-values.

9.1.2 Experimental Result

The result of all binomial combinations of local p-values from the source list shown in Tab. 8.1 are shown in Fig. 9.2. The binomial p-value is given in one sided Gaussian sigmas. When sorted by p-value, all sources from the source list with index > 9 are $\hat{n}_s = 0$ fits and thus are under-fluctuations. Even though the binomial test is defined for $k > 9$, the result can not indicate the existence of a sub-threshold population. The p-value threshold p_{thres} that gives the largest significance is given for $k = 3$ with a binomial p-value of $p_{\text{binom}} = 0.48\%$, corresponding to

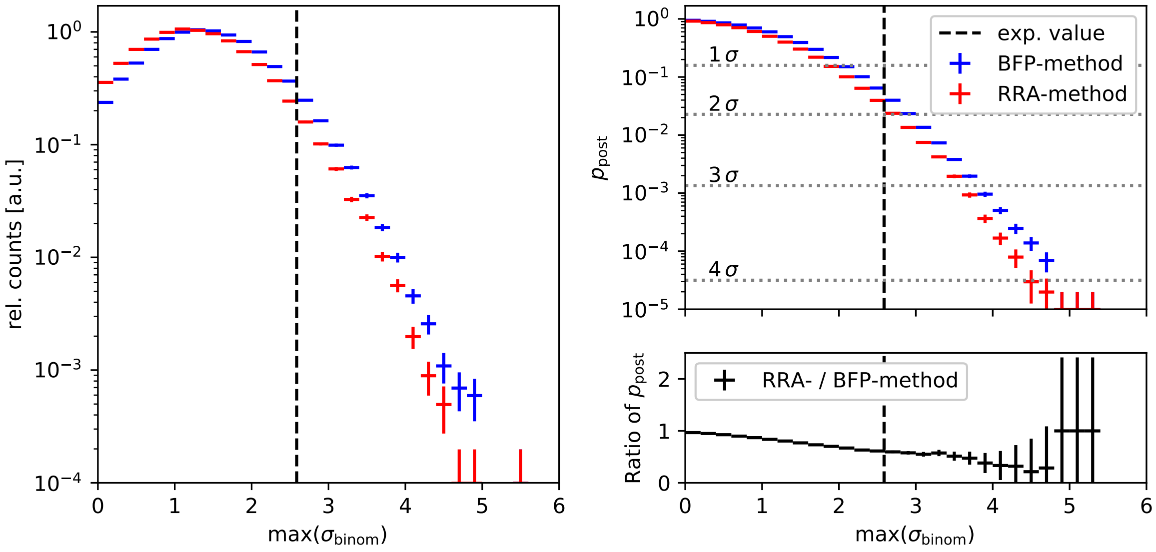

Figure 9.1: Local significance distribution of the most significant binomial combination of p-values for pure background pseudo-experiments (left), using the BFP-method (blue) and the RRA-method (red). Post-trial p-value as a function of the local significance of the most significant binomial combination (right). The lower right panel shows the ratio of post trial p-values calculated with the different methods. The experimentally observed value is indicated by a black dashed line.

2.59σ. The experimentally observed value is indicated by the black dashed line in Fig. 9.1. The post-trial p-value for the binomial combination of p-values in the source list is 6.6% ($1.51\,\sigma$) and 4.1% ($1.74\,\sigma$) using the BFP-method and the RRA-method, respectively.

Based on this result, the result is compatible with only background and thus there is no indication for a sub-threshold population of neutrino sources in the source list. Note that the test for the most significant source as defined in Sec. 8.2 can be seen as a sub-hypothesis of this test with $k = 1$ and a single trial. Thus, the result of the test for a population is a more general result and is not independent from the result presented in Sec. 8.2. Testing for only the most significant neutrino source in the source list in Sec. 8.2 is slightly more sensitive, as no trial-correction for picking k has to be applied.

The three sources contributing to the 2.59σ excess are 4C 38.41, MGRO J1908+06 and Cyg A. These sources are discussed in Sec. 8.2.3.

9.2 Hot-Spot Population Analysis

The hot-spot population analysis (HPA) presented in this section is based on the method presented in [13, 258].

When scanning the full sky, the number of independent trials is not known precisely. As shown in Sec. 8.1.1 the number of independent trial can be fitted to approximately 258 000. For $N \to \infty$ and $p_{\mathrm{thres}} \to 0$ the binomial distribution in Eq. 9.1 converges towards a Poisson

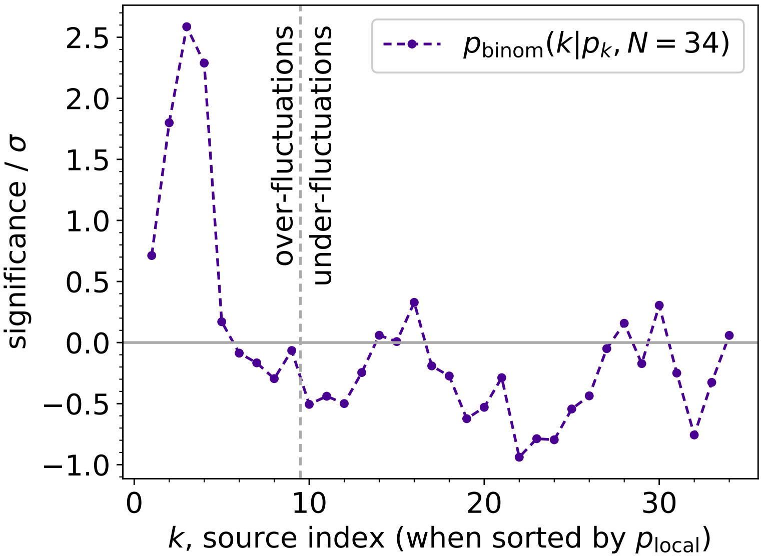

Figure 9.2: Local significance in Gaussian σ for binomial combinations of the k most significant sources in the *a-priory* source list. For $k \leq 9$ only local p-values of source with $\hat{n}_s > 0$ are combined, while for $k > 9$ also sources with $\hat{n}_s = 0$ are contributing (see gray dashed line).

distribution with mean $\lambda = N p_{\text{thres}}$ [257]. Thus, in case of only background it is expected, that the number of local hot-spots with a local p-value $p_{\text{local}} < p_{\text{thres}}$ is Poisson distributed with mean λ and $\lambda \propto p_{\text{thres}}$. Note that this assumption only holds, if the hot-spots and thus the local p-values in the all-sky scan are independent.

In case that Poisson statistic holds, the p-value to find n or more hot-spots with a local p-value below a threshold of p_{thres} is

$$p_{\text{local}}^{\text{HPA}} = p_{\text{poisson}} = \exp(-\lambda) \sum_{m=n}^{\infty} \frac{\lambda^m}{m!} \,. \tag{9.2}$$

Here $\lambda(p_{\text{thres}})$ is the expected number of hot-spots with $p_{\text{local}} \leq p_{\text{thres}}$. Using Eq. 9.2 and optimizing the p-value threshold, the full sky can be tested for an excess of hot-spots above the expectation. The test statistic for this test is thus:

$$TS_{\text{HPA}} = \max_{\lambda} \left(p_{\text{local}}^{\text{HPA}}(\lambda) \right) \tag{9.3}$$

Such an excess can be caused by a population of sub-threshold sources that are too weak to be detected individually.

9.2.1 Selection of Local Hot-Spots and Expectation

Before going further into the details of the analysis method, it has to be verified that indeed the Poisson statistic holds. Therefore, we first have to define how to select a local hot-spot.

The definition of a local hot-spot is based on the all-sky scan as discussed in Sec. 8.1. Using the scan grid, a scan point is called a local hot-spot, if its local p-value is smaller than the p-value of all neighbouring pixels. As neighbouring pixels we define the eight nearest pixels as defined by the function `get_all_neighbours` of the HealPy package [297]. In addition, we impose the second condition that two local hot-spots have to be separated by at least Ψ_{min}. Thus, if there are two local hot-spots with a distance of less than Ψ_{min}, the hot-spot with the larger p-value is excluded. Using this definition, an all-sky scan yields a set of hot-spots where for each spot the local p-value, declination and right-ascension are given.

A distribution of local hot-spots is extracted from 1000 all-sky scans of pure background pseudo experiments that were generated using the BFP-method. The histograms of the number of hot-spots with local p-values below different threshold p-values and $\Psi_{\mathrm{min}} = 1^\circ$ are shown in Fig. 9.3. For each histogram a Poisson distribution is shown using the maximum likelihood estimator of λ, which is the mean number of hot-spots. The $\Psi_{\mathrm{min}} = 1^\circ$ is chosen to get a resonable agreement between the histograms and the Poisson distributions, as can be seen in Fig. 9.3.

The histograms and the maximum likelihood estimator of λ are calculated for different p-value thresholds ranging from $10^{-2.0}$ to $10^{-7.0}$ and a step width of 0.1 in $-\log_{10}(p_{\mathrm{thres}})$. To quantify if the distribution of hot-spots is Poisson distributed, a Kolmogorov-Smirnov-test [252, 253] is performed for each tested p-value threshold. In addition, a KS-test is also performed to test the compatibility with a binomial distribution. In Fig. 9.3 (lower right), the p-values from the Kolmogorov-Smirnov-tests for each p-value threshold are shown. It can be seen that the assumption of a binomial and Poisson distribution for the number of hot-spots with p-values smaller than a threshold is valid at least in the range of $10^{-2} > p_{\mathrm{thres}} > 10^{-7}$. The expected number of hot-spots below a certain p-value threshold is shown in Fig. 9.4. The $\log_{10}(\lambda)$ is splined by a non-smoothing spline of order 1 as a function of $-\log_{10}(p_{\mathrm{thres}})$. Note that $\lambda(p_{\mathrm{thres}})$ slightly deviates from the simple assumption of $\lambda(p_{\mathrm{thres}}) \propto p_{\mathrm{thres}}$.

9.2.2 Generation of Pseudo Experiments

The test for populations of sub-threshold sources in the all-sky scan as described in this section requires a full scan of the Northern hemisphere as described in Sec. 8.1. However, this full scan is very computing intensive. Therefore, a more efficient way of generating pseudo experiments is needed to generate a large set of pseudo experiments.

Generation of Pure Background Pseudo Experiments

Using 1000 all-sky scans from pure background pseudo experiments, the hot-spots are extracted as defined in Sec. 9.2.1, yielding 1000 sets with p-values of local hot-spots. These p-values can be combined into a single large pool of background p-values which has the correct frequency of p-values as expected from pure background.

Only accounting for hot-spots with a local p-value $< 10^{-2}$, the total number of hot-spots in a sky map is Poisson distributed with mean $\lambda(10^{-2})$. Thus, we pick N_{tot}, the total number of hot-spots in a sky scan, from a Poisson distribution with mean $\lambda(10^{-2})$. As each hot-spot is independent we can pick N_{tot} p-values from the background pool and thus get a representation of local p-values of hot-spots as expected by pure background.

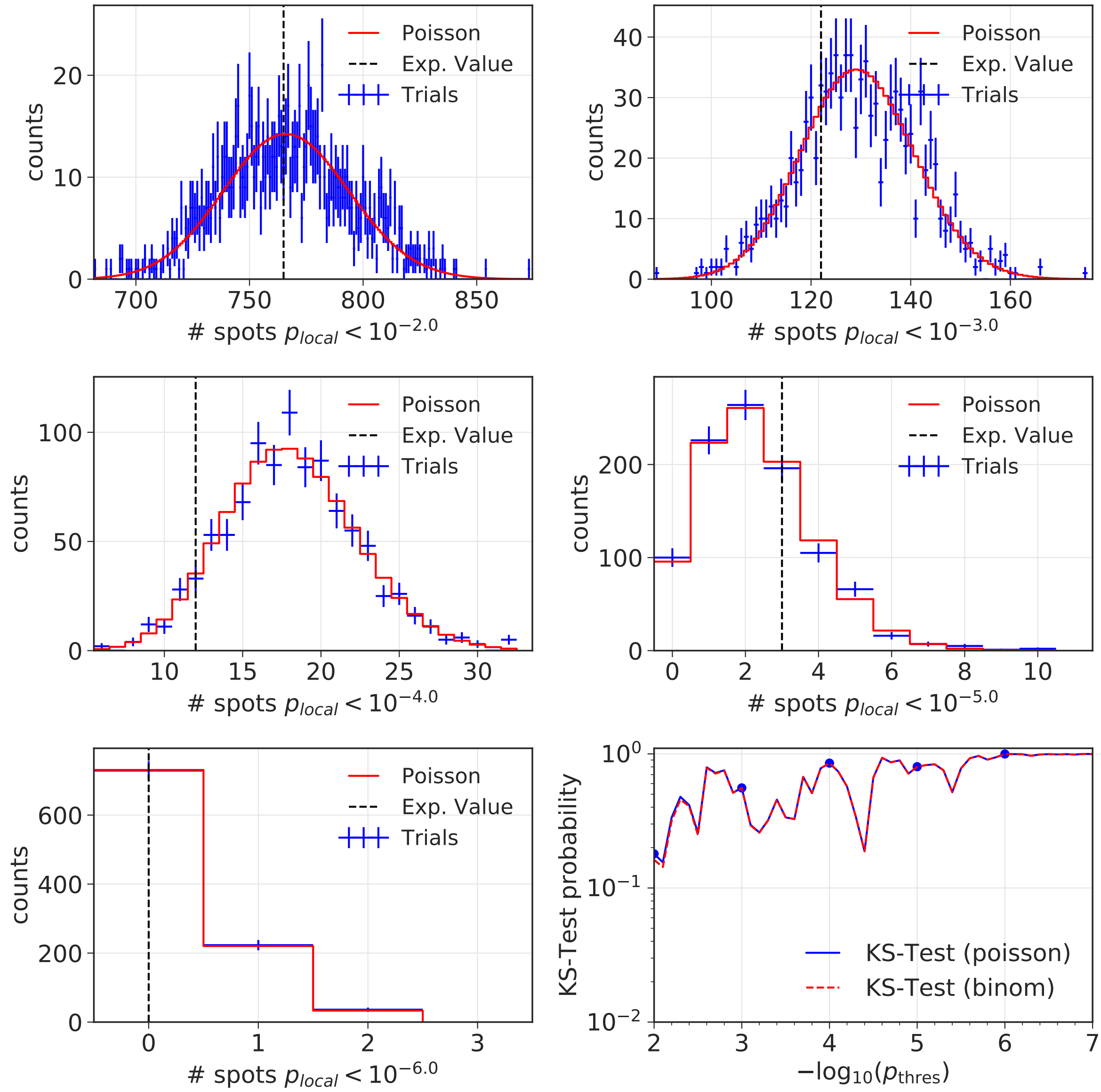

Figure 9.3: Number of local hot-spots with a local p-value smaller than $10^{-2.0}$ (upper left), $10^{-3.0}$ (upper right), $10^{-4.0}$ (middle left), $10^{-5.0}$ (middle right) and $10^{-6.0}$ (lower left). The histogram of the occurrence of local hot-spot p-values from the all-sky scans of pure background pseudo experiments is shown in blue. A Poisson distribution with fitted parameter $\hat{\lambda}$ is shown in red. The lower right panel shows the p-value of a Kolmogorov-Smirnov-test for different p-value thresholds. The markers correspond to p-values in other panels.

Using this procedure allows to generate background pseudo experiments for this population analysis in an efficient way.

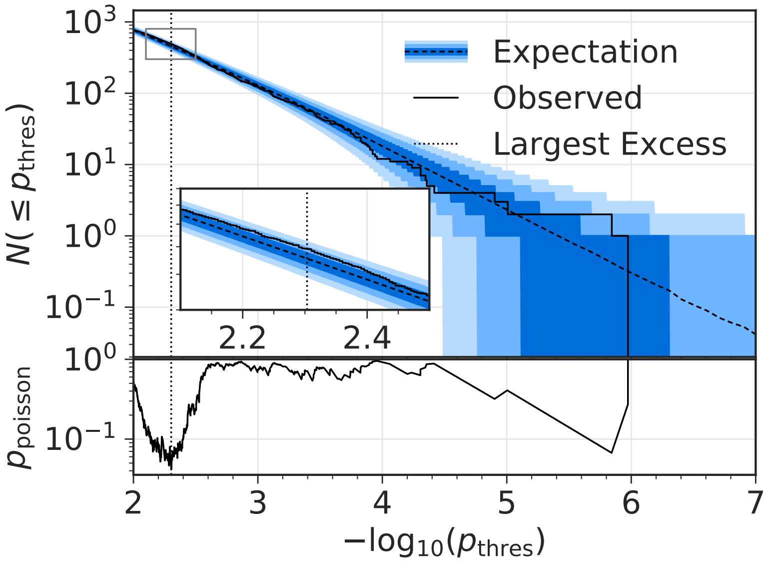

Figure 9.4: Number of local hot-spots in the all-sky scan with a local p-value smaller than the threshold p-value p_{thres}. The black line shows the experimentally observe hot-spots, while the black dashed line shows the expectation and the blue bands indicate the 1σ, 2σ and 3σ band. The lower panel shows the Poisson p-value where the most significant spot is indicated by a vertical dotted line. The insert shows the region around the most significant excess.

Generation of Pseudo Experiments with Signal Contribution

Beside generating pseudo experiments for pure background, also pseudo experiments including a signal contribution have to be generated to calculate the sensitivty of the analysis and to calculate exclusion limits. For a given set of sources with given position and flux, pseudo experiments are generated by the following procedure:

As described in Sec. 7.1 pseudo experiments for sources for different n_{inj} and declination are generated. The TS is evaluated at the position of the injected source and the resulting p-value calculated. This method is used to calculate e.g. the sensitivity as described in Chapter 7. To distinguish the pseudo-experiment generation in this section from Sec 7.1, we will refer to the test for a source at a single position as a single source test. Using this method, a large pool of local p-values for each set of n_{inj} and declination is generated. Fig. 9.5 shows the median of the negative $\log_{10}$ of the local p-value distribution of these single source trials as a function of $\sin\delta$ and n_{inj}.

Using the effective area and the source spectrum of the sources the flux of sources is converted in a number of expected events μ. This conversion is declination dependent as shown in Fig. 7.4 and has to be done for each source individually. The number of events to inject at the source position n_{inj} is drawn from a Poisson distribution with expectation value of μ. Based on the n_{inj} and declination of a source a local p-value is picked from the large pool of single source trials. If the local p-value is smaller than the threshold of 10^{-2} the p-value is considered as a local hot-spot.

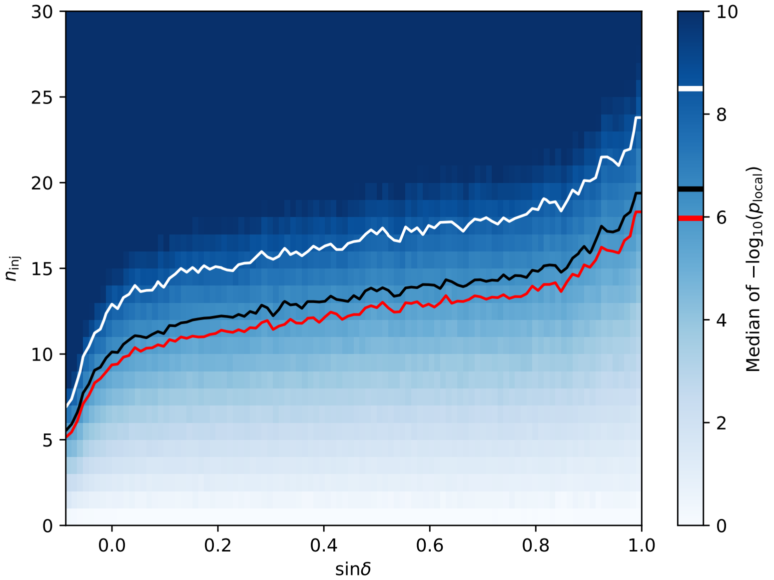

Figure 9.5: Median of the $-\log_{10}(p_{\mathrm{local}})$ distribution for single sources located and tested at $\sin\delta$ with n_{inj} injected events. The contour lines show the local p-values of the most significant spot in the sky scan (red, see Sec. 10.2 for further explanation), that is required for a 5σ local p-value (black), and for a 5σ post-trial p-value in the sky scan (white).

Note that by this procedure the p-value will be slightly overestimated, as the TS and thus the p-value is evaluated at the direction where the source has been injected. In a real scan a close-by spot may yield a slightly smaller p-value and would be chosen as the local hot-spot. However, by this approximation we can avoid a computational intensive scan and the sensitivity and upper limits are estimated conservatively.

When combining the list of p-values from sources and pure background one has to consider that hot-spots have to be separated by at least Ψ_{min}. Therefore, first a set of p-values from pure background is generated, where the total number N_{bgd} follows a Poisson distribution with mean $\lambda(10^{-2})$. For each p-value that has been calculated for sources a random number r is generated between 0 and 1 and the p-value is added to the set of p-values if $r > N_{\mathrm{spot}} \cdot \Omega_{\mathrm{spot}}/\Omega_{\mathrm{hemisphere}}$. Here, N_{spot} is the number of spots that are already in the set, $\Omega_{\mathrm{spot}} = \pi\Psi^2_{\mathrm{min}}$ and $\Omega_{\mathrm{hemisphere}}$ is the solid angle that is covered by the sky scan. If $r < N_{\mathrm{spot}} \cdot \Omega_{\mathrm{spot}}/\Omega_{\mathrm{hemisphere}}$ the p-value of the source is compared to a randomly picked p-value from the set and the larger one will remain in the set. This procedure takes into account that with increasing number of spots, hot-spots will occur closer to each other and thus not show up in the final p-value set.

9.2.3 Experimental Result and Post-Trial P-Value

The experimentally observed number of hot-spots as a function of the p-value threshold is shown in Fig. 9.4 as black solid line. Fig. 9.4 also shows the expected number of hot-spots as a function of the p-value threshold (black dashed line) together with the 1σ, 2σ and 3σ central regions expected from a Poisson distribution. The Poisson p-value p_{poisson} as defined in Eq. 9.2

is shown in the lower panel.

The most significant deviation from the number of expected hot-spots is found for a $p_{\text{thres}} = 0.5\%$, which is marked by a dotted line in Fig. 9.4. Here, 454.3 local hot-spots are expected and 492 have been observed. The Poisson p-value is $p_{\text{poisson}} = 4.17\%$.

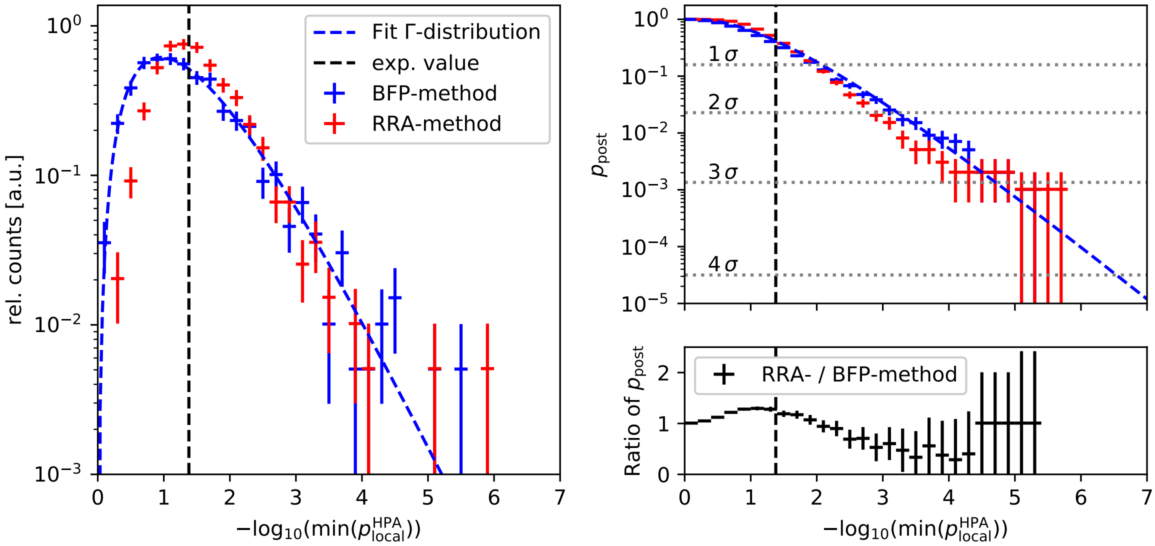

Figure 9.6: Histogram (left) and anti-cumulative distribution (right) of the minimal Poisson p-value from pure background pseudo experiments. The blue distributions are generated using pseudo experiments using the BFP while the red distributions are generated from pseudo experiments using the RRA method. A gamma distribution has been fitted to the blue histogram and is shown as dashed line. The experimentally observed value is shown as black vertical line.

Because the threshold p-value has not been chosen a-priory, a trial correction for picking the threshold that gives the most significant deviation has to be applied. Therefore, about 1000 pure background pseudo-experiments are generated using the BFP-method and the RRA-method, respectively. The histogram of the most significant Poisson p-value, which is the test statistic TS_{HPA} for this HPA, is histogramized in Fig. 9.6 (left) and the post-trial p-value p_{post} as a function of the most significant Poisson p-value is shown in Fig. 9.6 (right). The distribution generated using the BFP-method yields a slightly broader distribution. The distributions generated by the different methods are inconsistent with a p-value of $9.7 \cdot 10^{-15}$ from a two-sample Kolmogorov-Smirnov-test [252, 253]. A gamma distribution can be fitted to the histogram of the BFP of the most significant Poisson p-value and is shown as blue dashed line. The best-fit gamma distribution following $f(x) = x^{a-1}\exp(-x)/(s\Gamma(a))$ has a shape parameter $a = 3.32$ and a scale parameter of $s = 0.41$ where $x = -\log_{10}(\min(p^{HPA}_{\text{local}}))/s$ and a goodness of fit of 0.61 using a KS-test. The experimentally observed minimal Poisson p-value is marked by a black vertical line in Fig. 9.6. The post-trial p-value is 42.0% using the BFP-method and 54.3% using the RRA-method. These post-trial p-values are directly read off from trials, and thus do not rely on the fit of the gamma distribution. However, the gamma distribution is used to calculate the median, 3σ and 5σ quantiles of the background distribution, which are used in the upper limit calculation in Sec. 9.2.4.

The result is fully compatible with only background, but the fact that the most significant excess was found for a p-value threshold of $p_{\mathrm{thres}} = 0.5\%$ with 454.3 expected spots indicates that, if there is a population of sub-threshold sources, there are many very weak sources. Note that there is a similar significant spot for a p-value threshold of about $p_{\mathrm{thres}} \approx 10^{-5.8}$ where two spots are observed while only about 0.3 spots are expected. This excess is influenced by the most significant spot already discussed in Sec. 8.1.3. The second most significant spot is located at right ascension 77.52° and declination 2.61° with a local p-value of about $p_{\mathrm{local}} \approx 10^{-5.8}$.

9.2.4 Upper Limits for Equal-Strength Sources

In order to consider a flux distribution for the sources, we have to evaluate the power of the HPA presented in this section, and to place upper limits on source populations. A rather unrealistic, but simple benchmark scenario are sources that all produce the same neutrino flux at Earth. This scenario does not depend on any astrophysical assumptions and allows to directly compare sensitivities for different analyses without any uncertainties due to astrophysical models. More realistic scenarios are discussed in Sec. 10.3. For this section we use only the BFP for pseudo experiment generation.

A population of equal-strength sources is characterized by the number of sources N_{sources}, the source spectrum and the flux normalization per source at Earth $\phi_0 = \phi_{\mathrm{tot}}/N_{\mathrm{sources}}$. Here we consider a single power-law source spectrum with spectral index of $\gamma = -2.0$. The flux normalization per source can also be expressed by the averaged expected number of events per source μ by converting the flux normalization per source into the expected number of events averaged over all declinations.

Pseudo experiments are generated for different flux normalizations per source and different number of sources, as discussed in Sec. 9.2.2. The HPA as described in Sec. 9.2.1 is run on the resulting sets of p-values, yielding the most significant Poisson p-value for each pseudo experiment, which is the test statistic TS_{HPA}. In Fig. 9.7 the distribution of TS_{HPA} is shown for a populations with $N_{\mathrm{sources}} = 16$ as an example. The TS_{HPA} distribution is shown for three different flux normalizations per source corresponding to the sensitivity, 3σ and 5σ discovery potential. In the right panel of Fig. 9.7, the quantiles of the TS_{HPA} distributions are shown for different averaged events per source and for a population with $N_{\mathrm{sources}} = 16$. In addition, the median, 3σ and 5σ quantile of the background TS_{HPA} distribution are indicated by dashed vertical lines.

For a given number of sources, N_{sources}, the sensitivity on the flux normalization per source can be read off from the crossing point of the line showing the median background TS_{HPA} value and the 10% quantile as a function of the flux normalization per source. The 3σ discovery potential can be read off from the 3σ quantile line of the background TS_{HPA} and the median of the signal distribution. The 90% CL upper limit can also be read off by comparing the experimental TS_{HPA} value with the 10% quantile curve of the signal population. By this procedure the sensitivity, discovery potential and 90% CL upper limit are calculated on the flux normalization per sources as a function of the number of sources of the population.

In Fig. 9.8 the 90% UL on the flux normalization per source (left) and on the total flux

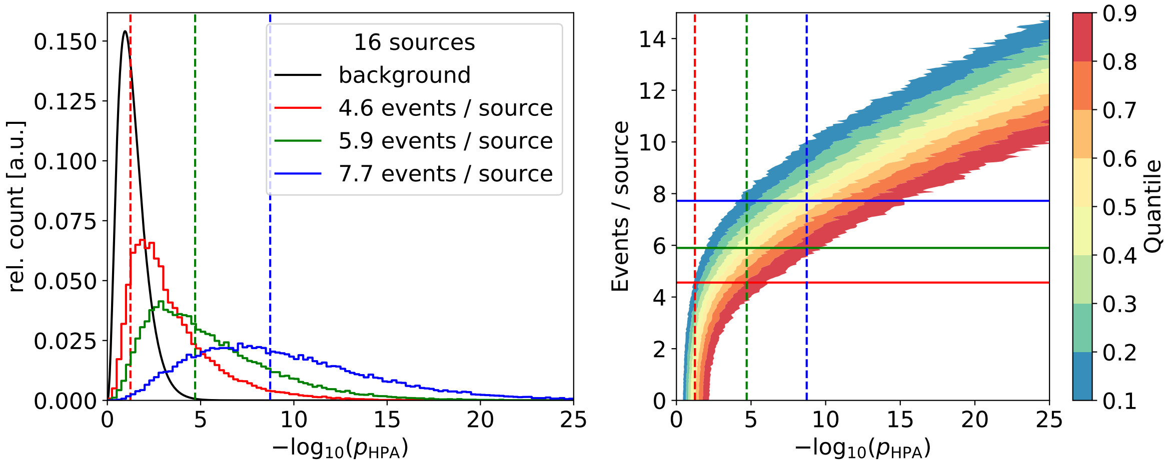

Figure 9.7: Left: Hotspot population analysis test statistic $TS_{\mathrm{HPA}} = -\log_{10}(p_{\mathrm{HPA}})$ for pseudo experiments including 16 sources with equal strength at Earth. The background test statistic distribution is shown in black and its median (red), 3σ (green) and 5σ (blue) quantiles are shown as dashed lines. The signal distributions are shown for three different values of flux per source, corresponding to the sensitivity (red), 3σ discovery potential (green) and 5σ discovery potential (blue). Right: Quantile of $TS_{\mathrm{HPA}} = -\log_{10}(p_{\mathrm{HPA}})$ for different number of events per source. The horizontal lines indicate the slices shown in the left panel. The dotted lines are the same as in the left panel.

(right) is shown as a function of the number of source in the population. The difference between the 90% UL and the different interpretation of the upper limits is discussed in the next section. In addition, an equal strength flux that saturates the diffuse flux is shown as dotted line.

9.2.5 Influence of a Pure Diffuse Flux on the Hot-Spot Population Analysis

For varying signal strength, the amount of diffuse astrophysical neutrinos in the background simulation would have to be adapted. However it is computationally not feasible to calculate the background expectation for different amount of diffuse astrophysical neutrino. Therefore, we limit the simulation of background to two cases: once without a contribution from diffuse astrophysical neutrinos and once with one times the best-fit diffuse astrophysical neutrino flux. In this section we discuss these limiting cases.

For populations with a lot of sources, the total neutrino flux from sources of the population becomes non-negligible with respect to the measured diffuse astrophysical flux. When generating pseudo experiments for source populations this has to be taken into account. In the limit of many sources, with a flux normalization per source corresponding to less than 1 event per source, the simulated population can also be described by a pure diffuse flux. Therefore, we investigate what the influence of single event sources and a pure diffuse flux has on the sensitivity of the population analysis.

To test the effect of single event sources, single source trials (see Sec. 7.1) are generated as described in Sec. 7.1 once for pure background ($n_{\mathrm{inj}} = 0$) and once injecting a single event

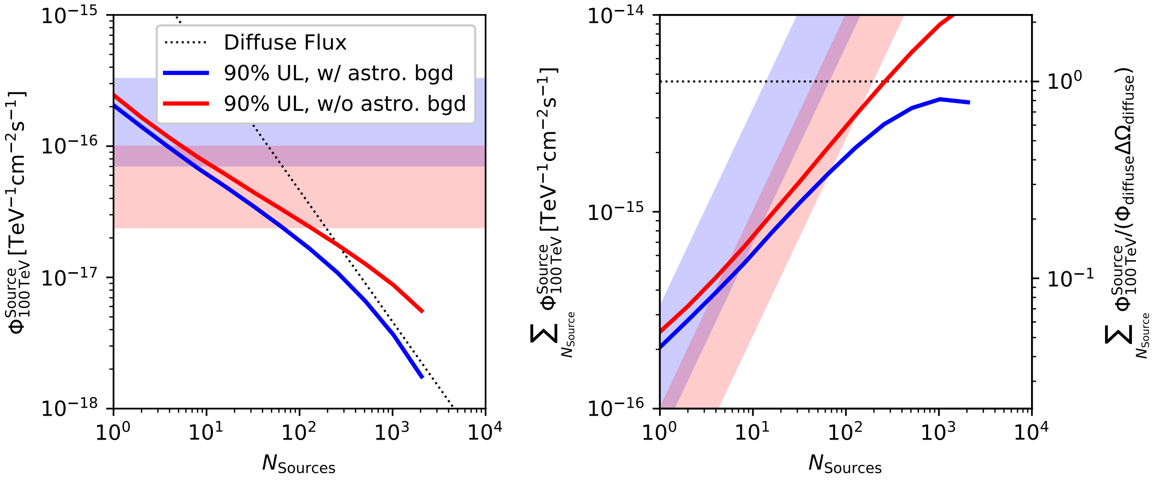

Figure 9.8: 90% CL upper limits on source populations that result in an equal flux per source at Earth. The limit is given on the flux per source (left) and total flux (right) as a function of the number of source in the population. The limit has been calculated once including (blue) and once excluding (red) an astrophysical component in the background simulation as explained in the text. The dashed gray line corresponds to the flux per source, if the diffuse flux came from N_{sources} sources. The shaded areas give range of pre-trial 5σ discovery potential (blue) and sensitivity (red) for a single source allowed for different declinations.

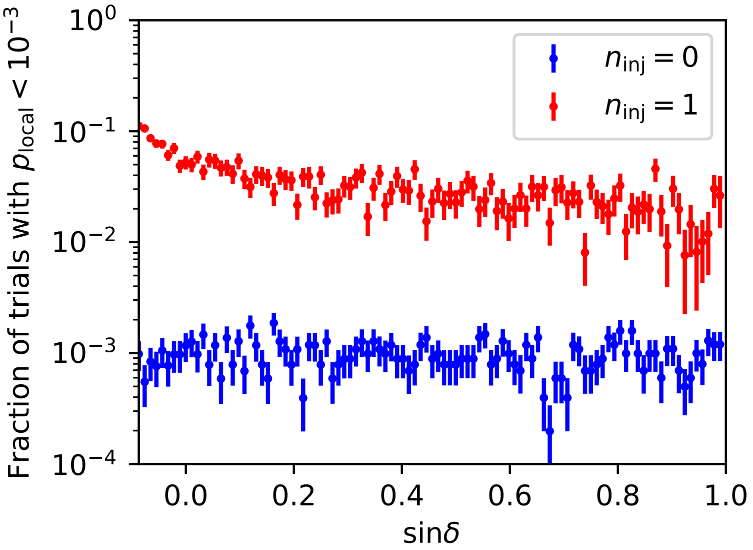

Figure 9.9: Fraction of single source trials, that result in a local p-value $< 10^{-3}$ once using pure background trials (blue) and once injecting one event following an E^{-2} power-law spectrum (red).

($n_{\mathrm{inj}} = 1$) following an $E^{-2.0}$ power-law spectrum. The TS and p-value are evaluated at the position of the injected source. Fig. 9.9 shows the fraction of trials with local p-values $< 10^{-3}$. It can be seen that for pure background the fraction of trials that result in $p_{\text{local}} < 10^{-3}$ occurs in $\sim 10^{-3}$ of all cases, independent of declination, as expected. If a single event is injected, the fraction of trials with $p_{\text{local}} < 10^{-3}$ is larger than 10^{-2} and increases for small declination to about 10^{-1}. The excess in the fraction of small p-values is caused by the addition of one event, which is not corrected for in background and the fact that the energy of this event is on average larger than the average energy of background events due to the harder spectrum. This shows that already single events can lead to an excess in small p-values.

To test if the pure diffuse flux also has an effect on the HPA, pseudo experiments as described in Sec. 7.1 are generated where the astrophysical component of the best-fit component is set to zero and to three times its best-fit value. 1000 pseudo experiments are generated for each of these settings and all-sky scans are performed. Using these all-sky scans, the HPA is performed using the expectation $\lambda(p_{\text{thres}})$ as derived in Sec. 9.2.1, where pseudo experiments with one times the best-fit astrophysical component are used.

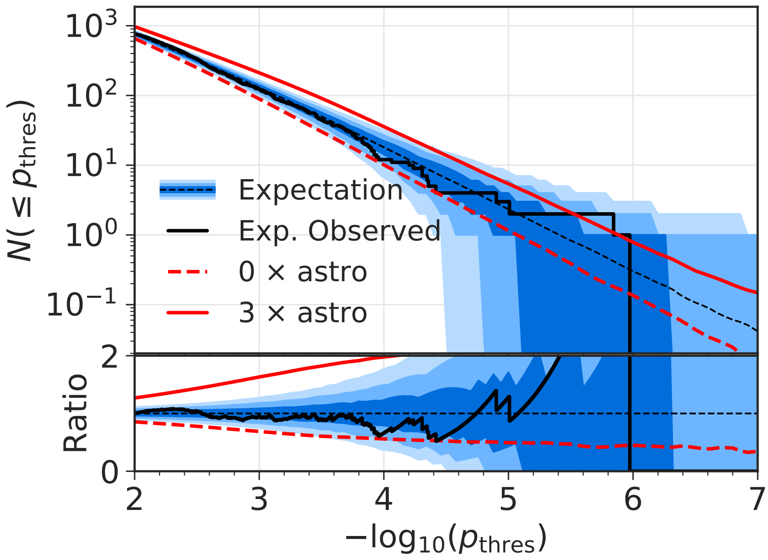

Figure 9.10: Number of expected local hot-spots as a function of p_{thres}. The expectation from pseudo experiments with 1× the astrophysical component is shown as black dashed line and the 1σ, 2σ and 3σ intervals are marked as blue bands. The expectation from 0× and 3× the astrophysical component is shown by the red dashed and red solid line, respectively. The lower panel shows the ratio with respect to the expectation from 1× the astrophysical component.

Fig. 9.10 shows the number of expected hot-spots as a function of the p-value threshold p_{thres}. The expectation has been calculated using 1000 pseudo experiments using the BFP-method, once using the best-fit astrophysical component (black dashed line), once without an astrophysical component (red dashed line) and once using three times the best-fit astrophysical component (solid red line). It can be seen that the expectation with zero times and three times the astrophysical component are not compatible with the expectation from one times the astrophysical component at the 3σ level. This leads to the conclusion that an additional diffuse flux that is not described by the best-fit parametrization leads to a significant excess in the HPA.

In Fig. 9.8, the 90% UL on the flux normalization per source (left) and on the total flux (right) as a function of the number of source in the population is shown, once including the diffuse astrophysical component in the background simulation and once excluding the diffuse astrophysical component in the background simulation.

For the limit of a large number of sources, the limits exclude that there is a flux from populations that corresponds to twice the diffuse flux. This can be seen as the blue line which gives the *additional* flux stays below the flux that corresponds to the best-fit diffuse astrophysical flux. For the limit of many sources, where the total flux from the population is not negligible compared to the diffuse flux, the limit calculation should be done without an astrophysical diffuse flux in the background component as it would be double counted (once by the signal population and once by the diffuse flux in the background simulation). On the other hand, if calculating upper limits in the limit of small number of sources, the limit will be conservative if the astrophysical component is not considered in the background simulation. As a gradual change of the astrophysical contribution in the background simulation would be computational very expensive we choose to calculate the upper limits without an astrophysical component in the background simulation. Thus, the upper limit is reasonable in the case of large N_{sources} and slightly conservative in case of small N_{sources}.

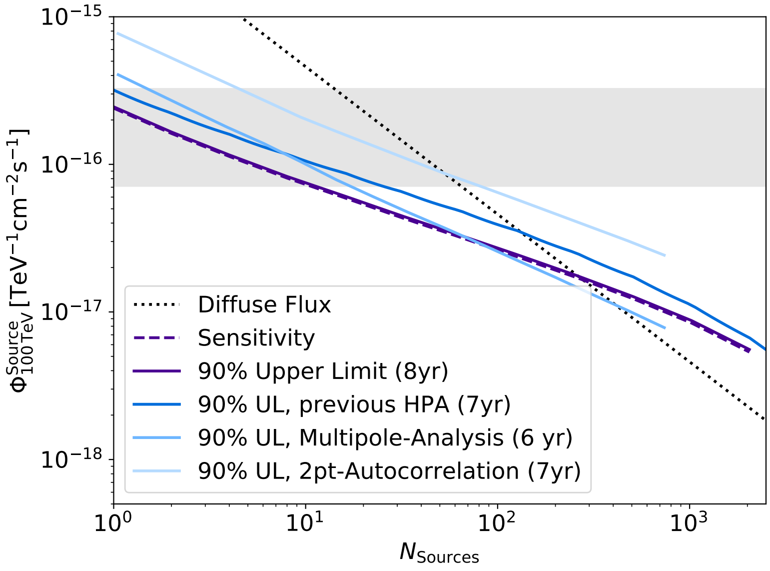

Figure 9.11: Sensitivity (dashed) and 90% upper limit (solid) on populations of equal strength sources. The sensitivity and upper limits are given on the flux per source as a function of the number of sources. For comparison also upper limits from other analysis are shown (see legend) [13, 130]. The flux per source that would saturate the diffuse flux is shown as dotted line [6]. The gray band indicates the range between minimal and maximal local 5σ discovery potential for single sources.

Although this benchmark scenario of equal-strength sources is unrealistic, it allows to compare the power of different analysis methods. Therefore, Fig. 9.11 shows the sensitivity and upper limit on the flux per source as a function of N_{sources} of this analysis, as well as the previous HPA presented in [13, 258] and the multipole and 2-point correlation analysis presented in [130]. Note that the analysis presented in this thesis is the most sensitive and sets the most stringent limits for populations with less than ~ 70 sources. For populations with $N_{\mathrm{sources}} > 70$ the multipole analysis presented in [130] is more stringent. For populations with more than 300 sources the upper limit from this analysis exceeds the best-fit diffuse astrophysical flux. Note that the upper limit from [13, 258] has been corrected, as in the original upper limit an incorrect detector acceptance was assumed [298]. The gain in sensitivity with respect to the analysis presented in [13, 258] is in agreement with the improved sensitivity for single point-like sources. Note that for the comparison the Northern Hemisphere sensitivities are used. The amount of data used in each analyses is noted in the legend of Fig. 9.11.

Constraints on more realistic, astrophysical source populations are discussed in Chapter 10.

Chapter 10

Astrophysical Implications and Constraints

Declaration of Pre-released Publications The constrains presented in this chapter have been previously published by the IceCube Collaboration in M. G. Aartsen *et al.* (IceCube Collaboration), "Search for steady point-like sources in the astrophysical muon neutrino flux with 8 years of IceCube data" The European Physical Journal C 79, 234 (2019). The author of this thesis has written this publication as a corresponding author. The author performed the limit calculation on specific source models and the calculation of the upper limits on the source density and effective luminosity for populations of sources.

All results presented in Chapter 8 and Chapter 9 are compatible with the background hypothesis, i.e. no strong single source and no population of sub-threshold sources can be reported. However, the result allows to put upper limits on chosen source parameters. Implications on the non-observation of a source in the source list are discussed in Sec. 10.1 and exclusion limits on predicted neutrino flux models for specific sources are calculated. Because the most significant spot in the all-sky scan is not significant, upper limits on the flux normalization for sources anywhere in the sky can be set. In addition, one can calculate exclusion limits for each scanned spot in the sky individually, assuming an $E^{-2.0}$ power-law spectrum, which is presented in Sec. 10.2. Also the non observation of a significant excess in the all-sky scan imposes constraints on populations of neutrino sources. Exclusion limits on populations of neutrino sources following realistic star formation rates are discussed in Sec. 10.3.

10.1 Specific Source Models

In Section 8.2, constraints on the flux normalizations of sources from the catalog list have been calculated assuming $\mathrm{d}N/\mathrm{d}E_\nu \propto E_\nu^{-2}$ and $\mathrm{d}N/\mathrm{d}E_\nu \propto E_\nu^{-2.19}$. However, more specific neutrino flux models can be obtained using γ-ray data. As discussed in Sec. 2.2.1, pion decays resulting from cosmic ray interactions can produce both neutrinos and γ-rays. Therefore, γ-ray data can be used to construct models for neutrino emission under certain assumptions. In the following, we therefore calculate exclusion limits for neutrino emission models for sources of the *a-priori* source list.

10.1.1 Calculation of Model Rejection Factor and Central Energy Range

The Model Rejection Factor (MRF) is calculated for each model, which is the ratio between the 90% CL upper limit and the predicted flux normalization. In addition, the expected result in case of pure background is also calculated, giving the MRF sensitivity. The central energy range that contributes 90% to the sensitivity has been calculated by dividing the source flux by

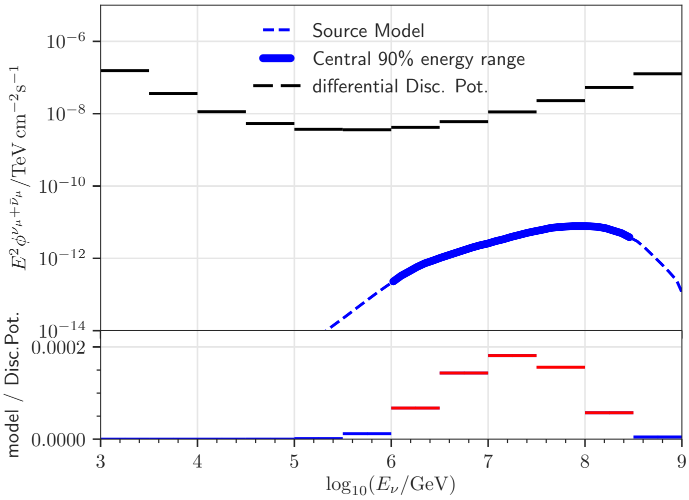

Figure 10.1: Source model flux for the blazar 3C273 as a function of neutrino energy (dashed line). The differential discovery potential for an E^{-2} power law is shown for a step size of 0.5 in $\log_{10}(E_\nu/\mathrm{GeV})$. The lower panel gives the ratio between the flux model and the differential discovery potential. The largest bins that add up to 90% of the total ratio are marked in red and define the central energy range.

the differential discovery potential for an E^{-2} generation spectrum and choosing the central region that makes up 90% of the sensitivity at the source position. The calculation of the energy range is illustrated in Fig. 10.1, where in the upper panel the source model and the differential discovery potential for the source declination is shown. The lower panel shows the ratio of source flux and differential discovery potential in arbitrary units. The central energy range is marked in red. Note that the given energy range is slightly too large due to the coarse bin width of the differential discovery potential.

In the following, we will discuss models for which the MRF sensitivity is smaller than 10 and neutrino flux predictions could be found in the literature.

10.1.2 The Crab Nebula

The first source considered is the Crab Nebula. The Crab Nebula is a Pulsar Wind Nebula (PWN) and the brightest source in our own galaxy in the TeV γ-ray sky. Despite the common understanding that the dominant γ emission from PWNe is of leptonic nature, see e.g. [299], neutrinos can be produced by subdominant hadronic emission processes. Here we consider the neutrino flux predictions from the Crab Nebula by Amato *et al.* [84] and Kappes *et al.* [61].

The prediction by Amato *et al.* assumes that pion production is dominated by pp interactions and the target density is given by

$$n_t = 10\mu M_{N_\odot} R_{\mathrm{pc}}^{-3}\,\mathrm{cm}^{-3}\,, \qquad (10.1)$$

where $M_{N_\odot}$ is the mass of the supernova ejecta in units of solar masses, R_{pc} is the radius of the supernova in units of pc and μ is an unknown factor of the order of $1 \leq \mu \leq 20$. This factor

μ takes into account e.g. the intensity and structures of magnetic fields within the PWN. For the model prediction, we assume $\mu = 20$ and a proton luminosity of 60% of the total PWN luminosity for Lorentz factors of $\Gamma = 10^4$, 10^5, 10^6, 10^7. Note that the resulting upper limits are complementary to the limits given in [84], because limits in [84] are calculated based of γ-ray data and here an independent observation channel with different systematic uncertainties is used.

The model prediction of the neutrino emission of the Crab Nebular by Kappes *et al.* [61], assumes a dominant production of γ-rays by *pp* interactions and used the γ-ray spectrum measured by the H.E.S.S. [300].

Type	Source Model	$\log_{10}(E/\mathrm{GeV})$	sensitivity	90% UL
Crab	Amato *et al.* [84] $\Gamma = 10^4$	1.5 - 9.0	23.38	31.47
	Amato *et al.* [84] $\Gamma = 10^5$	3.0 - 4.5	0.79	1.14
	Amato *et al.* [84] $\Gamma = 10^6$	4.0 - 5.5	0.16	0.21
	Amato *et al.* [84] $\Gamma = 10^7$	4.5 - 6.0	0.32	0.40
	Kappes *et al.* [61]	2.5 - 4.5	1.06	1.47
Blazar	3C273, Reimer [301]	6.0 - 8.5	0.39	0.42
	3C454.3, Reimer [301]	6.0 - 8.0	2.80	5.42
	Mrk421, Petropoulou *et al.* [302]	5.5 - 7.0	0.36	0.43
SNR	G40.5-0.5, Mandelartz *et al.* [303]	3.5 - 5.5	1.45	4.57

Table 10.1: Model rejection factors for source models in the source catalog. Given are source type, model reference, central 90% energy range, MRF sensitivity and MRF at 90% CL. Sources with MRF> 10 are not considered.

The models by Amato *et al.* ($\Gamma = 10^7$) and Kappes *et al.* are shown in Fig. 10.2. While the model by Amato *et al.* shows a bump in $E^2 \frac{\mathrm{d}N}{\mathrm{d}E}$ close to the maximal energy of 1 PeV, the model by Kappes *et al.* has a much softer spectrum and thus a larger flux at lower energies. The 90% CL upper limit on the MRF and the sensitivity on the MRF are calculated as described in Sec. 10.1.1. The values are listed in Tab. 10.1 and the source models scaled to the 90% CL upper limit and the sensitivity are shown in Fig. 10.2.

From Tab. 10.1 we can see that the model by Amato *et al.* can be excluded for $\Gamma = 10^6, 10^7$ for $\mu = 20$ and a proton luminosity of 60%. For $\Gamma = 10^5$ the limit is about 14% above the model prediction while the sensitivity is 21% below. For $\Gamma = 10^4$ the model predicts small neutrino energies such that the analysis is not sensitive and the MRF is therefore high.

The sensitivity to the model by Kappes *et al.* is close to the flux prediction, however as an over-fluctuation is observed for the Crab Nebula, the 90% CL upper limit is about 50% above the flux prediction.

10.1.3 Active Galactic Nuclei

Active galactic nuclei (AGN) and especially blazars are a promising class for high-energy neutrino production, due to their jetted emission, fast time variability and high radiation

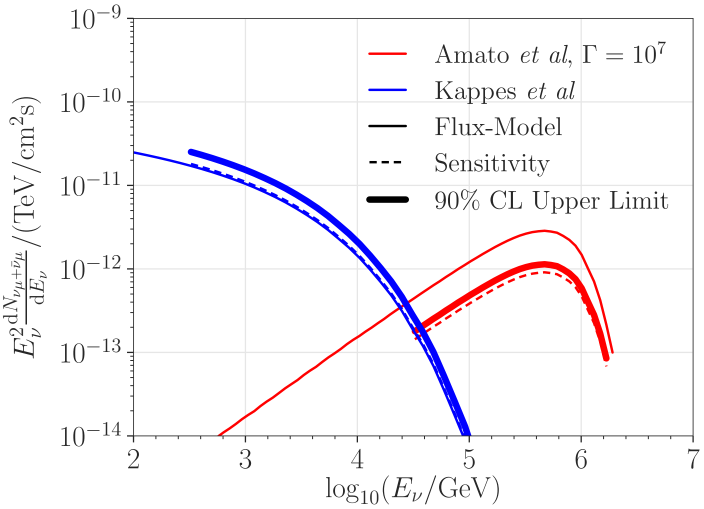

Figure 10.2: Differential source flux for the Crab Nebula as predicted by Amato *et al.* ($\Gamma = 10^7$) [84] and Kappes *et al.* [61]. Solid lines show the model prediction, thick lines give the 90% CL upper limit and the dashed lines indicate the sensitivity flux. 90% CL upper limit and sensitivity are shown in the energy range that contributes 90% to the sensitivity.

density. The high-energy hump of the typical double hump SED structure could be explained by inverse-Compton scattering, or decay of π^0 produced in hadronic interactions.

In Ref. [302], blazars in spatial and energetic agreement with high-energy starting events observed by IceCube are analyzed. One of these sources is Mrk 421, one of the two closest and brightest BL Lacertae objects (BL Lac). The broad-band SED is analyzed and fitted by a lepto-hadronic model with five stable particle populations. Beside magnetic fields, protons losing energy by synchrotron radiation, Bethe–Heitler pair production and photo-pion interactions, electrons and positrons losing energy by synchrotron radiation and inverse Compton scattering, photons gaining and losing energy in a variety of ways, neutrons, which can escape almost unimpeded from the source region, with a small probability of photo-pion interactions and neutrinos, which escape completely unimpeded are taken into account [302]. The neutrino spectrum is calculated using the SOPHIA Monte Carlo code [304] assuming photo-hadronic interactions ($p\gamma$) [302]. Other sources discussed in [302] are either located at the Southern Hemisphere, and thus outside of the range of this analysis, or have model predictions more than an order of magnitude below the sensitivity.

Models for 3C273 and 3C454.3, which are flat spectrum radio quasars (FSRQ), are derived in Ref. [301]. Therefore, the broad-band SED (containing at least optical/IR, X-ray and gamma-ray observations) are corrected for absorption in the extra-galactic background light (EBL) and fitted with a semi-analytical stationary hadronic blazar model [301]. The resulting neutrino spectra are again calculated using the SOPHIA Monte Carlo code [304] assuming photo-hadronic interactions ($p\gamma$) [301].

The models for the three blazars, the sensitivities and 90% CL upper limits are shown in Fig. 10.3 and the MRF are listed in Tab. 10.1.

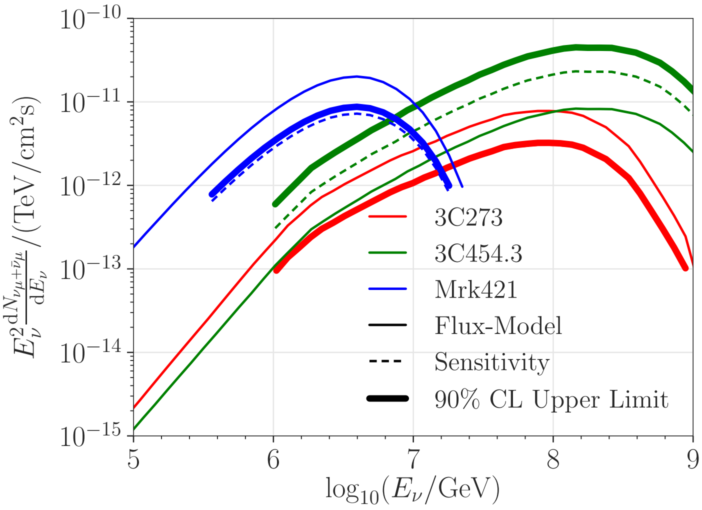

Figure 10.3: Differential source flux models for 3C273, 3C454.3 and Mrk 421. Solid lines show the model prediction, thick lines give the 90% CL upper limit and dashed lines indicate the sensitivity flux. 90% CL upper limit and sensitivity are shown in the energy range that contributes 90% to the sensitivity.

Due to the very similar physical model and construction of the predicted neutrino spectra, the shape of the three different spectra are similar with a peak close to the maximal energy in $E^2\,\mathrm{d}N/\mathrm{d}E$. However, the peak energy and the absolute flux predictions are different for the three blazars. For Mrk 421 and 3C273 the sensitivity is below the model prediction with a MRF of about 0.4. The 90% CL upper limit is close to the sensitivity and thus excludes the model prediction at the 90% CL. This indicates that the hadronic component is over-estimated in the considered model predictions.

The sensitivity to 3C454.3 is about a factor of 2.8 above the model prediction by [301]. This is caused by the very high peak flux in $E^2\,\mathrm{d}N/\mathrm{d}E$ at $> 100\,\mathrm{PeV}$, where the flux expectation is very small. With a local p-value of 2.58%, 3C454.3 is the fourth-smallest local p-value in the source list and a relatively strong over-fluctuation. Due to this small p-value, also the 90% CL upper limit on the flux prediction with a MRF of 5.42 lies clearly above the sensitivity and the source flux prediction. Thus, the source model can not be excluded.

10.1.4 The Unidentified Object MGRO J1908+06

As briefly described in Sec. 8.2.3, the morphology of the MGRO J1908+06 region is extended and a clear source of the high-energy gamma-ray flux is not identified. In Fig. 8.9 the high-energy gamma-ray excess measured by HESS is indicated. Several sources in the region might potentially contribute to the high-energy gamma-ray flux.

The galactic supernova remnant, G40.5-0.5, lies within the MGRO J1908+06 region and can be associated with the TeV source MGRO J1908+06, although the association of G40.5-0.5 with MGRO J1908+06 is not distinct [281]. In addition, the pulsar wind nebula powered by PSR J1907+0602 may contribute to the TeV emission of the MGRO J1908+06 region.

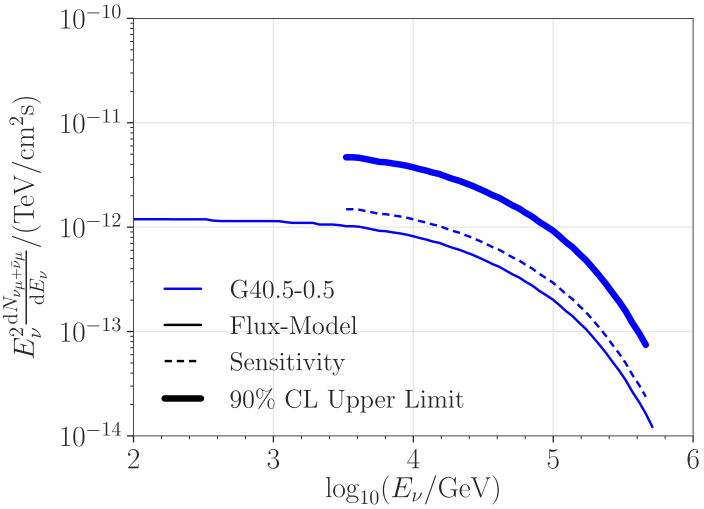

Figure 10.4: Differential source flux and MRF for the SNR G40.5-0.5. The solid line gives the model prediction, the thick line gives the 90% CL upper limit and the dashed line indicates the sensitivity flux. The 90% CL upper limit and sensitivity are shown in the energy range that contributes 90% to the sensitivity. Note that G40.5-0.5 is associated with MGRO J1908+06.

However, here we test the model for the SNR G40.5-0.5 as predicted in Ref. [303].

The model prediction from [303] for the SNR G40.5-0.5, the sensitivity MRF and the 90% CL upper limit MRF are shown in Fig. 10.4 and are listed in Tab. 10.1. With a sensitivity MRF of 1.45 the sensitivity is close to the model prediction. However, with a local p-value of $< 1\%$ for MGRO J1908+06, and thus the second-most significant source in the *a priori* source list, the 90% CL upper limit MRF is 4.57. Thus, the model prediction by [303] for the SNR G40.5-0.5 cannot be excluded.

10.2 Limits from the All-Sky Scan

In the previous section and in Sec. 8.2 90% CL upper limits are given for specific source positions. However, limits can also be calculated for any spot. These limits can be once derived from the observed p-value of the hottest spot, and on an individual basis for each scan point.

10.2.1 Limits from the Hottest Spot

The hottest spot is chosen to be the spot with the smallest p-value, because the distribution of TS values exhibits a slight declination dependence. Thus, any spot in the sky has a p-value larger than the p-value of the hottest spot. Based on the local p-value of the hottest spot, we can derive the TS value that is needed to reach that p-value by inverting the local p-value parametrization introduced in Sec. 8.1.1 and explained in Appendix F. Thus, for each declination band a TS is calculated from which a 90% CL upper limit on the flux normalization can

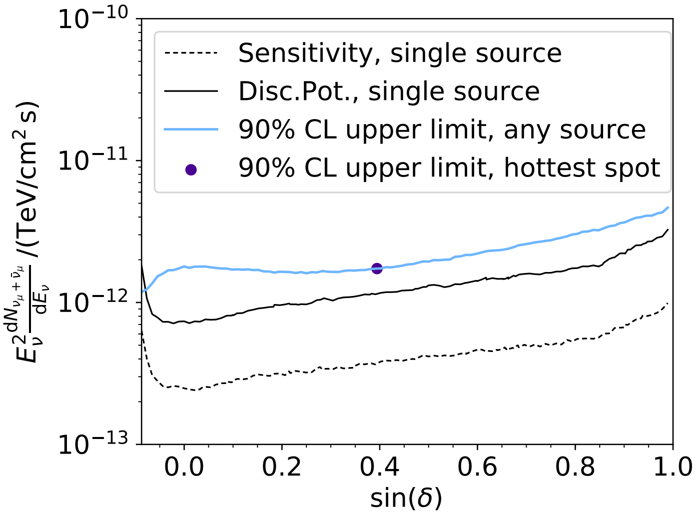

Figure 10.5: Upper bound on 90% CL upper limit on the flux normalization as a function of sine of declination for an E^{-2} spectrum. The 90% CL upper limit for the hottest spot is indicated by a blue marker. The single source sensitivity and discovery potential are shown as dashed and solid black lines for comparison.

be calculated following the procedure described in Sec. 7.3. A source with a flux normalization larger than this derived limit would lead to a more significant hottest spot than the observed one.

The resulting 90% CL upper limit is shown in Fig. 10.5 as a function of declination for an E^{-2} spectrum. The 90% CL upper limit does not depend on right ascension. The 90% CL upper limit for the hottest spot is marked by a dot. The 90% CL upper limit lies clearly above the discovery potential, however the discovery potential is not trial corrected and the 90% CL upper limit can exceed the discovery potential as long as the best-fit normalization lies below the discovery potential. Note that the difference in shape below the horizon ($\sin\delta < 0$) is caused by the small amount of events needed to be sensitive close to the edge of the sample.

Note that for all-sky positions, except the hottest spot, the 90% CL upper limit as calculated here is an upper bound for the 90% CL upper limit, because we only took into account that the p-value of these spots are larger than the p-value of the hottest spot. More stringent limits can be calculated taking into account the measured TS value for each spot individually.

10.2.2 Limits from each Spot Individually

Based on the pseudo experiments generated for the determination of the sensitivity and discovery potential as described in Sec. 7.3, another 90% CL upper limit can be calculated. The 90% CL upper limit is a function of the observed TS, which is shown in Fig. 10.6 for an E^{-2} spectrum and a declination of about 5°. The relative uncertainties on the 90% CL quantile is always in the range of a few percent for TS values between -10 and 30.

The 90% CL upper limit as a function of TS is parametrized by a linear interpolation

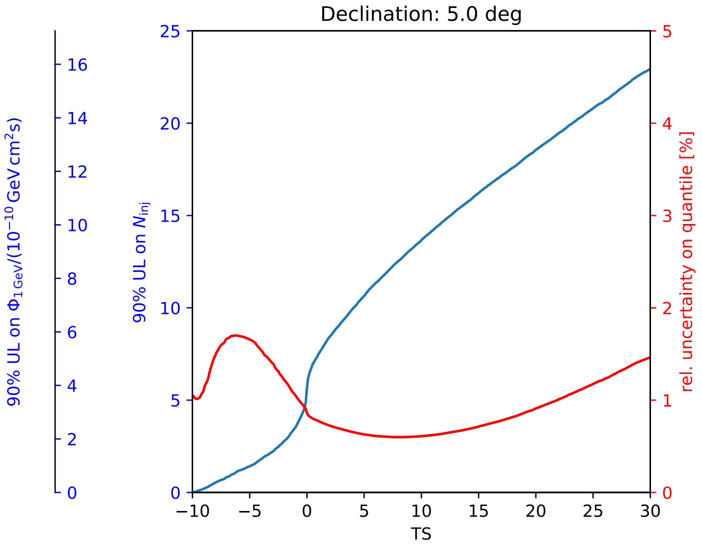

Figure 10.6: 90% CL upper limit on the flux normalization and number of events as a function of the observed TS value for 5° declination and an E^{-2} spectrum. The red line shows the relative uncertainty on the upper limit due to the finite statistic of simulated signal pseudo experiments.

spline for 100 different declinations uniformly distributed in $\sin\delta$. The parametrization of the upper limit as a function of TS for the closest generated parametrization is used to calculate an upper limit for a given declination. Note that by this upper limits close to the celestial pole may be slightly inaccurate, because the upper limit parametrization slightly changes for this declination.

Using this parametrization of upper limit in dependence of declination and TS, 90% CL upper limits can be calculated for each point in the all-sky scan individually. In Fig. 10.7, the TS sky map, the 90% CL upper limits on the number of events and the 90% CL upper limits on the flux normalization for an $E^{-2.0}$ power law are shown in equatorial coordinates. It can be seen that the 90% CL upper limits on the flux normalization are less stringent for high declinations than for low declinations. Note that the maximal 90% CL upper limit on the number of events is 23.

10.3 Source Populations

In Chapter 8 we presented different tests that analyzed individual locations for the existence of a single source. These tests are designed for scenarios that would correspond to a source count distribution

$$\frac{\mathrm{d}N_{\mathrm{source}}}{\mathrm{d}\phi} = \begin{cases} 1 & \text{if } \phi = \phi_x \\ 0 & \text{else} \end{cases}, \tag{10.2}$$

where ϕ_x is the flux normalization of the single source. Note that $\mathrm{d}N_{\mathrm{source}}/\mathrm{d}\phi \propto \mathrm{d}N_{\mathrm{source}}/\mathrm{d}\mu$. Such a source count distribution is illustrated in Fig. 10.8 (left panel).

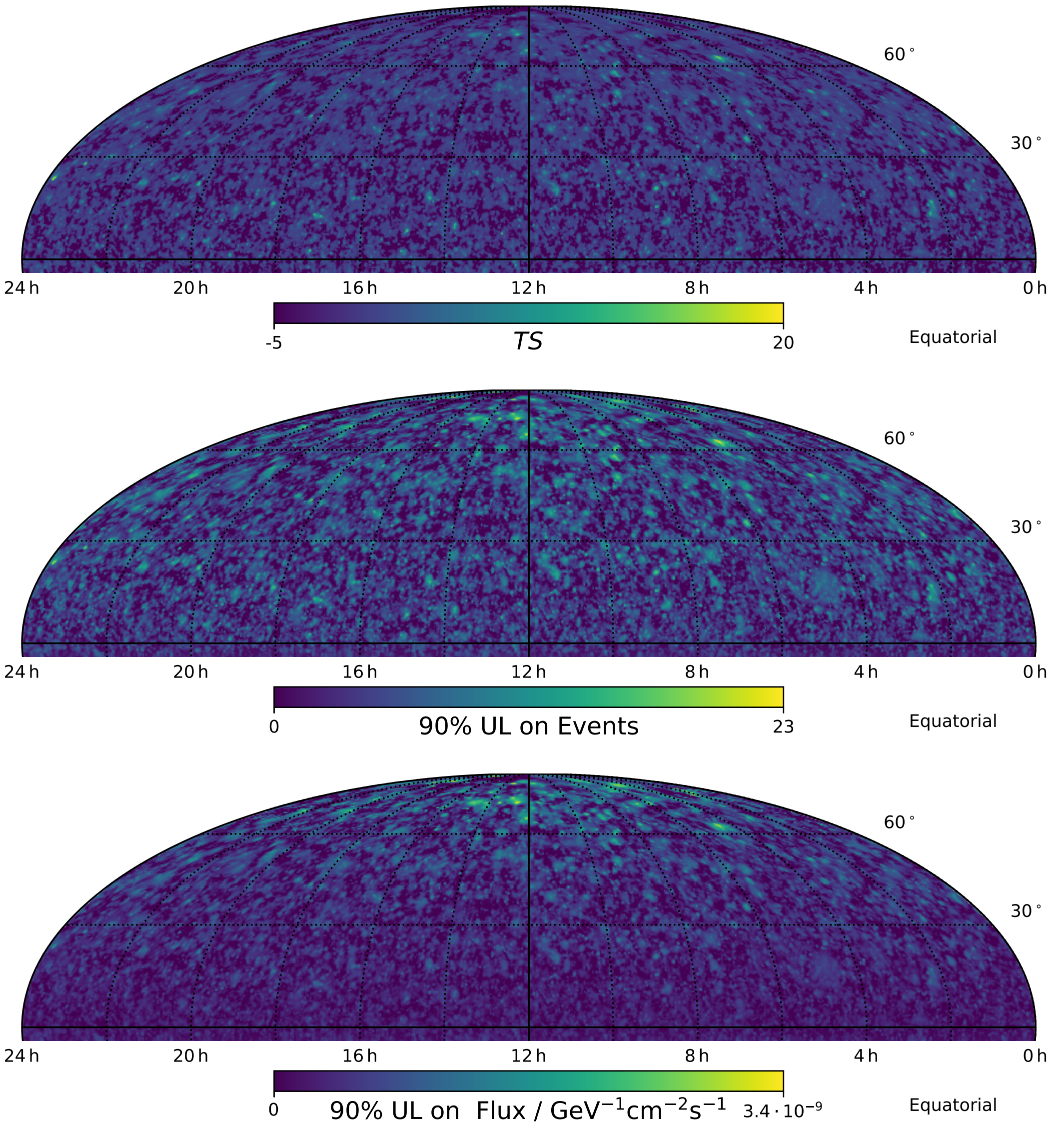

Figure 10.7: Sky map of TS (top), 90% CL upper limit on the number of events (middle) and 90% CL upper limit on the flux normalization (bottom) for each spot tested in the all-sky scan. The sky map is shown in equatorial coordinates. An E^{-2} spectrum is assumed. The color scale is linear.

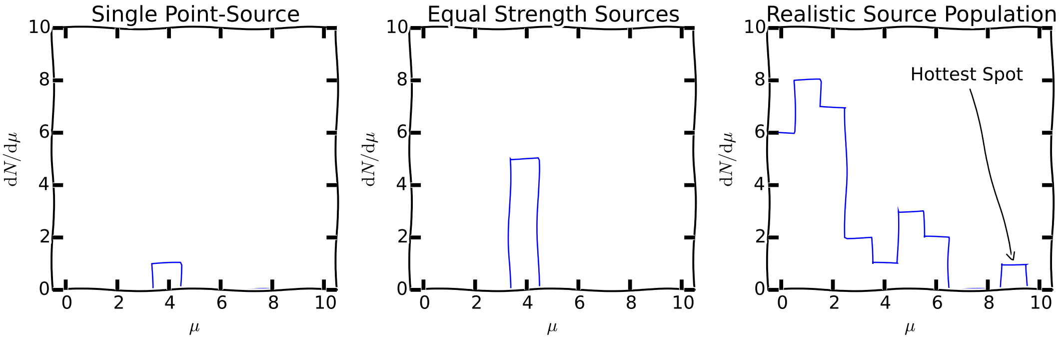

Figure 10.8: Sketch of source count distribution, to illustrate the different scenarios discussed in this thesis: a single point-source, population of equal-strength sources at Earth and realistic population of sources. The source count distribution $\mathrm{d}N_{\text{source}}/\mathrm{d}\mu$ gives the number of sources N_{source}, that produce μ neutrinos at Earth. The normalization corresponds to the total number of sources in the scenario. The source count distribution can also be given in dependence of the source flux at Earth ϕ since $\mu \propto \phi$.

In Chapter 9, the hot-spot population analysis (HPA) is introduced, which tests for a population of multiple weak sources. The result of this search is consistent with the background hypothesis (see Sec. 9.2.3). Thus, upper limits on the source flux of equal-strength sources at Earth are calculated in Sec. 9.2.4. This scenario is described by a source count distribution of

$$\frac{\mathrm{d}N_{\text{source}}}{\mathrm{d}\phi} = \begin{cases} N'_{\text{source}} & \text{if} \phi = \phi_x \\ 0 & \text{else} \end{cases} , \tag{10.3}$$

where ϕ_x is the flux normalization of the sources at Earth and N'_{source} is the number of sources of the population. Such a source count distribution is illustrated in Fig. 10.8 (middle panel). This scenario is well-suited to discuss and compare the performance of an analysis method. However, this scenario is rather unrealistic as the flux of a source at Earth depends on its luminosity and distance. If not all sources would have the same distance from Earth, the difference would have to be compensated by the source's luminosity.

In this section, more realistic source populations as illustrated in Fig. 10.8 (right panel) are discussed. Therefore, the calculation of more realistic source count distributions is described in Sec. 10.3.1. In Sec. 10.3.2 the construction of upper limits on the parameters of the population are presented and the dependence of the upper limits on the chosen parameters is discussed.

10.3.1 Construction of Source Count Distributions

A source with intrinsic neutrino luminosity L_ν at a redshift of z that emits neutrinos isotropically leads to a flux density S_{obs} at Earth:

$$S_{\text{obs}} = \frac{L_\nu}{4\pi d_L^2(z)} , \tag{10.4}$$

where $d_L(z)$ is the luminosity distance of the source. For a flat universe with a curvature constant $k = 0$, the luminosity distance is given by [305]:

$$d_L(z) = (1+z)d_H \int_0^z \frac{\mathrm{d}z'}{\sqrt{\Omega_M(1+z)^3 + \Omega_\Lambda}} \tag{10.5}$$

where Ω_M is the matter density relative to the critical density and $\Omega_\Lambda = 1 - \Omega_M = \frac{\Lambda c^2}{3H_0}$ is the energy density corresponding to the cosmological constant Λ. The Hubble distance is $d_H = \frac{c}{H_0} = \frac{c}{100h\,\mathrm{kms^{-1}Mpc^{-1}}}$, which depends on the speed of light c and the Hubble parameter H_0 which can be given as dimensionless parameter $h = H_0/(100\,\mathrm{km\,s^{-1}Mpc^{-1}})$[305].

The flux density can also be expressed by the observed flux density:

$$S_\mathrm{obs} = \int_{E_\mathrm{min}^\mathrm{obs}}^{E_\mathrm{max}^\mathrm{obs}} E\phi(E)\mathrm{d}E\,. \tag{10.6}$$

Here $E_\mathrm{min}^\mathrm{obs}$ and $E_\mathrm{max}^\mathrm{obs}$ are the minimal and maximal energy considered from the source as measured by the observer. Due to the propagation over astrophysical distances, the neutrinos lose energy due to redshift and are observed at a reduced energy of $E_\mathrm{obs} = E_\mathrm{emit}/(1+z)$. Note that $E_\mathrm{min}^\mathrm{emit}$ and $E_\mathrm{max}^\mathrm{emit}$ are the bounds of the energy range for which the luminosity of the source is defined.

By equating Eq. 10.4 and Eq. 10.6 and separating the source flux $\phi(E) = \phi_0\hat{\phi}(E)$ in a normalized distribution $\hat{\phi}(E)$ and the constant flux normalization ϕ_0, the flux normalization can be expressed as:

$$\phi_0 = \frac{L_\nu}{4\pi d_L^2(z)} \frac{1}{\int_{E_\mathrm{min}^\mathrm{emit}/(1+z)}^{E_\mathrm{max}^\mathrm{emit}/(1+z)} E\hat{\phi}(E)\mathrm{d}E} \tag{10.7}$$

Thus, we find that the flux normalization of a source ϕ_0 depends on the initial luminosity L_ν, the redshift z of the source and the initial source spectrum $\hat{\phi}(E)$.

To get a source count distribution as a function of the source flux, we need to know the luminosity distribution of sources $\mathrm{d}N/\mathrm{d}L$, the distribution of sources in the universe $\mathrm{d}N/\mathrm{d}V_\mathrm{c}$ and the initial source spectrum $\phi(E)$. Here, $\mathrm{d}V_\mathrm{C}$ is the differential comoving volume. In the following, we assume that the initial source spectrum $\phi(E) = \phi_0\left(\frac{E}{E_0}\right)^{-\gamma}$ is a power-law spectrum with spectral index γ.

The differential comoving volume is given by [305]:

$$\mathrm{d}V_C = d_H \frac{d_C^2}{\sqrt{\Omega_M(1+z)^3 + \Omega_\Lambda}} \mathrm{d}\Omega\mathrm{d}z\,, \tag{10.8}$$

where $d_C = d_H \int_0^z \frac{\mathrm{d}z'}{\sqrt{\Omega_M(1+z)^3+\Omega_\Lambda}}$ is the comoving distance [305]. Thus, the distribution of sources in the Universe can be factorized into a radial and a directional dependence using Eq. 10.8:

$$\frac{\mathrm{d}N}{\mathrm{d}z} = 4\pi d_H \frac{d_C^2}{\sqrt{\Omega_M(1+z)^3 + \Omega_\Lambda}} \frac{\mathrm{d}N}{\mathrm{d}V_\mathrm{C}}\,. \tag{10.9}$$

Here, the first term in Eq. 10.9 depends on the cosmological model and can be obtained from Eq. 10.8. The factor of 4π comes from considering sources from all directions. This leaves us to pick a suitable source count distribution with respect to redshift.

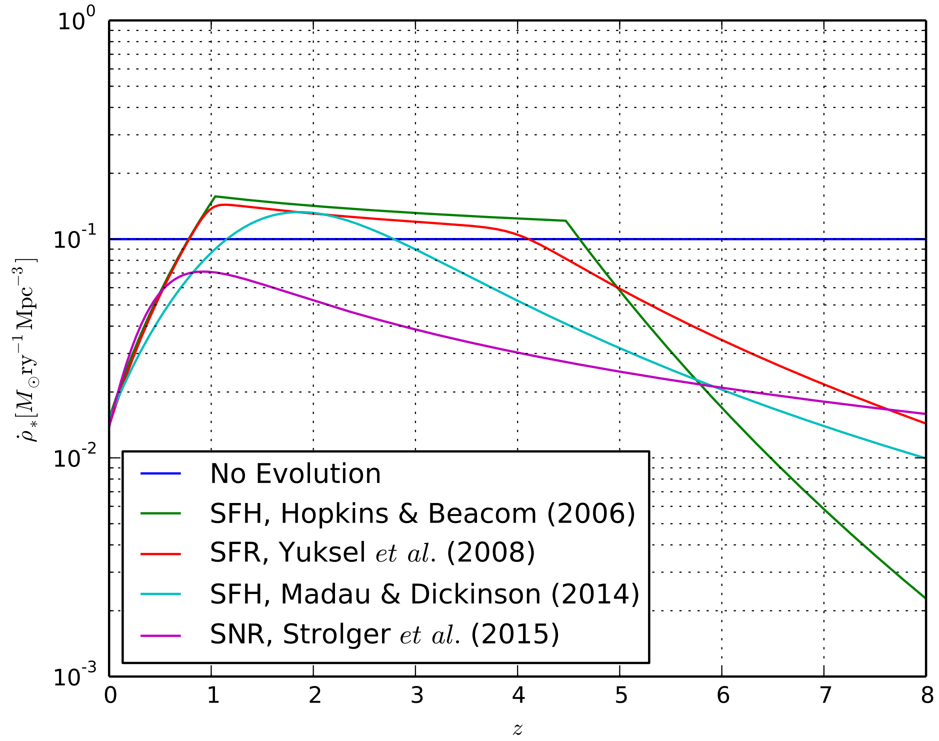

Figure 10.9: Star formation rate $\dot{\rho}_*$ as a function of redshift z. Different models are shown (see legend). The following abbreviations are used: Star-Formation-History (SFH), Star-Formation-Rate (SFR), Super Novae Rate (SNR).

A rather simple assumption is that there is no evolution in the number of sources with redshift at all. This no-evolution scenario can be described by $\mathrm{d}N/\mathrm{d}V_\mathrm{C} = \mathrm{const}$. More reasonable source count distributions have to be derived from electro-magnetic observations. E.g. the star formation rate $\dot{\rho}_*$ can be used as a tracer for neutrino production [306, 307]. Source count distributions are measured in the radio, ultraviolet and far-infrared electro-magnetic bands to $z > 6$. These measurements are sensitive especially to star formation rates and Core Collapse Supernovae rates. In Fig. 10.9, different parametrizations of the star formation history are shown. The star formation history from Hopkins & Beacom is a fit to ultraviolet and far-infrared measurements up to $z \approx 6$ compiled from several experiments [308]. The star formation rate from Yuksel *et al.* further incorporates measurements by Swift on the GRB rate which is related to the star formation rate and includes additional data at $4 < z < 7$ [309]. Other models, e.g. from core collapse supernovae with $z \leq 2.5$ measured by Candels and Clash, are modeled by [310] and a parametrization of ultraviolet and infra-red data up to $z = 8$ is parametrized in [311]. These parametrizations are shown as well in Fig. 10.9.

If the star formation rate $\dot{\rho}_*$ is used as a tracer for neutrino production, the shape of the source count distribution is determined by the chosen star formation history, however the absolute scaling of the neutrino rate is unknown. We parameterize this scaling by the local density of sources ρ_local within $z < \epsilon$. Making use of the local density, we find the total number of sources N_tot within $z < z_\mathrm{max}$ by:

$$N_\mathrm{sources} = \rho_\mathrm{local} V_C(z = \epsilon) \frac{\int_\Omega \int_0^{z_\mathrm{max}} \dot{\rho}_*(z) \mathrm{d}V_C}{\int_\Omega \int_0^{\epsilon} \dot{\rho}_*(z) \mathrm{d}V_C} \,, \tag{10.10}$$

which gives the normalization of the source count distribution $\mathrm{d}N/\mathrm{d}z$. The comoving volume up to a redshift of z is given by [305]:

$$V_C = \frac{4\pi}{3} d_C^3 = \frac{4\pi}{3} \left(d_H \int_0^z \frac{\mathrm{d}z'}{\sqrt{\Omega_M (1+z)^3 + \Omega_\Lambda}} \right)^3 . \tag{10.11}$$

Beside the source count distribution, also the luminosity distribution $\mathrm{d}N/\mathrm{d}L$ is required. In general, sources of one population can have different luminosities. It helps however, if one thinks of *benchmark* sources with a single luminosity, i.e. a standard candle luminosity. If the luminosity distribution $\mathrm{d}N/\mathrm{d}L$ is a broken power-law with spectral index $\alpha > -2$ below the break luminosity L_break and $\alpha < -2$ above the luminosity, sources with $L_\nu \approx L_\mathrm{break}$ will dominate the overall flux [312] due to the $\Phi_0 \propto d_L(z)^{-2}$ scaling in Eq. 10.7. Using an *effective* standard candle luminosity $L_{\nu,\mathrm{eff}}$ for a population, one can define the effective local source density $\rho_\mathrm{eff,local}$ [306, 312]:

$$\rho_\mathrm{eff,local} = \frac{1}{L_{\nu,\mathrm{eff}}} \int \mathrm{d}(\ln L_\gamma) L_\nu \frac{\mathrm{d}\rho}{\mathrm{d}\ln L_\gamma} \,, \tag{10.12}$$

where L_γ is the photon luminosity. Note that the *effective* number density gives the number density of sources that *dominate* the neutrino flux of the population. This effective density is the density which is constrained by the experimental result. Note that this quantity may be significantly smaller than the total density of the population [306].

We calculate experimental constraints on source populations depending on $L_{\nu,\mathrm{eff}}$ and $\rho_{\mathrm{eff,local}}$.

Note that Eq. 10.7 depends on E_{min} and E_{max}, which are the minimal and maximal energy of the energy band for which L_ν is defined. The neutrino luminosity per logarithmic energy interval is independent of E_{min} and E_{max} for an E^{-2} power law spectrum, i.e. the energy output per decade is constant. Therefore, often the luminosity is expressed as the luminosity per logarithmic energy interval $\frac{\mathrm{d}L_\nu}{\mathrm{d}\ln E_\nu}$ and an E^{-2} power-law spectrum is assumed. However, this quantity is not independent of E_{min} and E_{max} for spectral indices $\gamma \neq -2$. In the following, we define the neutrino luminosity in the energy range 10 TeV to 10 PeV if not stated otherwise.

To generate source count distributions for source populations we use the python package FIRESONG (FIRst Extragalactic Simulation Of Neutrinos and Gamma-rays)[1] [313, 314], which was co-developed within this thesis. Within FIRESONG, we model standard candle sources by log-normal distributions which are centered on their effective luminosity and have a width of 0.01 in $\log_{10}(L_{\nu,\mathrm{eff}})$. In the following we use these cosmological parameters as measured by Planck [91]: $\Omega_{M_0} = 0.308$, $\Omega_{\Lambda_0} = 0.692$, $h = 0.678$. As default source evolution, we use the star formation history by Hopkins & Beacom [308].

An example of a source count distribution generated with the FIRESONG package is shown in Fig. 10.10. As default parameter an $E^{-2.19}$ power-law spectrum, a source density of $10^{-9}\,\mathrm{Mpc}^{-3}$ and a standard candle luminosity distribution modeled by a log-normal distribution centered at $10^{52}\,\mathrm{erg/yr}$ is assumed. Sources are considered up to $z_{\mathrm{max}} = 10$.

From Fig. 10.10, it can be seen clearly that a change in neutrino luminosity leads to a shift of the source count distribution with respect to the source flux. One can also see that the source density scales the normalization of the source count distribution and the shape of the distribution is unchanged. The change due to evolution model is most prominent for the central peak and leads to a smear out especially to smaller flux values. The right tail of the source count distribution is similar for the models from Hopkins & Beacom (HB2006SFR) [308], Yüksel *et al.* (YMKBH2008SFR) [309] and Strolger *et al.* (CC2015SNR) [310]. Only if no source evolution is considered, the source count distribution is flatter at large source fluxes. The dependence on the spectral index is relatively weak, with only small differences for spectra with $\gamma = -2.0$, $\gamma = -2.19$ and $\gamma = -2.5$. The difference to the source count distribution of a spectrum with $\gamma = -3.0$ is mainly in the normalization.

Note that in a search for point-like sources the right tail of the source count distribution is the most relevant characteristic of a source count distribution, as this tail determines the occurrence of the strongest sources.

10.3.2 Constraints on Source Count Distributions

Source count distributions are generated using the FIRESONG package to calculate constrains on realistic source populations for different parameters as described in Sec. 10.3.1. Based on this source count distribution, pseudo experiments for the hotspot population analysis (HPA) are generated, following the prescription explained in Sec. 9.2.2. As default, we assume a power-law spectrum with a spectral index of $\gamma = -2.0$ and a source evolution following Hopkins &

---

[1] `https://github.com/ChrisCFTung/FIRESONG`

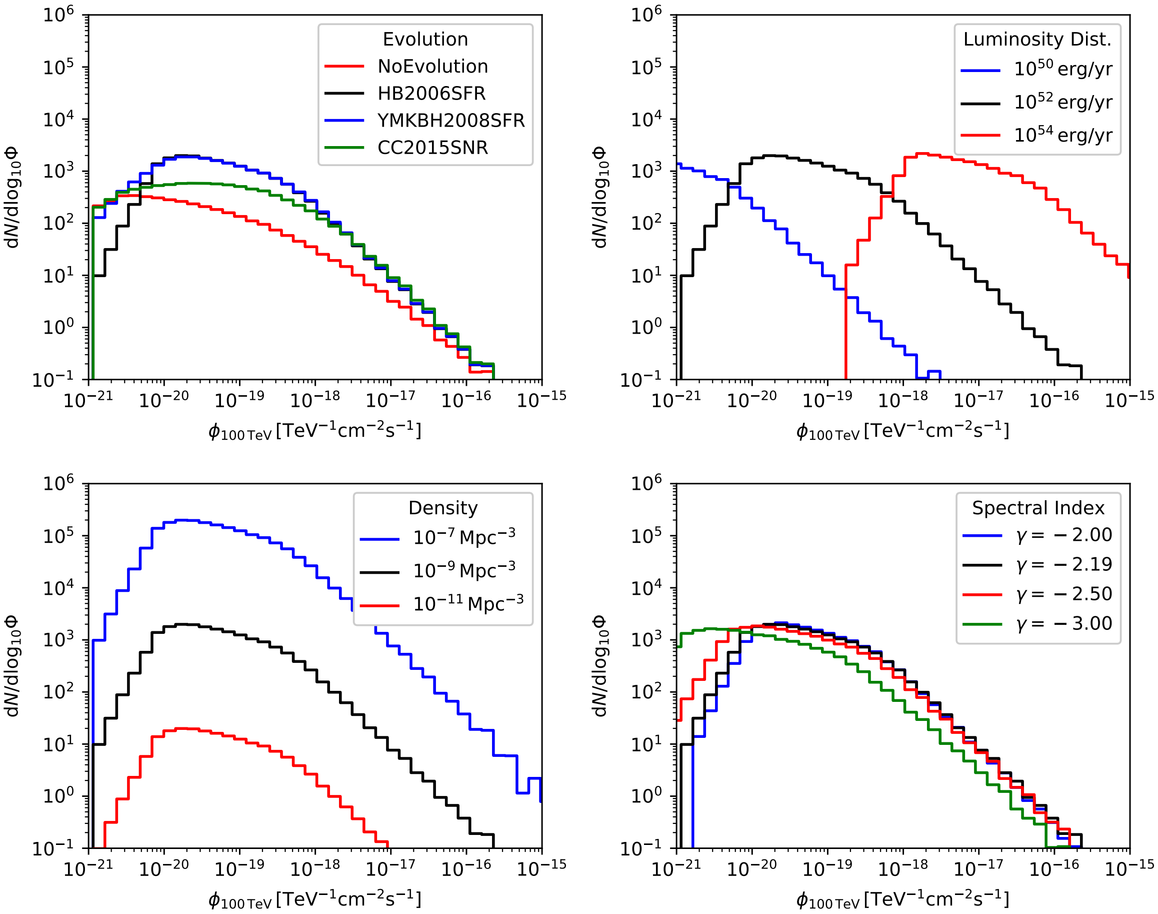

Figure 10.10: Source count distribution as a function of flux normalization at 100 TeV generated using the FIRESONG package. The source count distribution is shown for different source evolution models (upper left), different neutrino luminosities (upper right), different source densities (lower left) and different spectral indices (lower right). Note that the black distribution in the four panels are the same.

Beacom (HB2006SFR) [308]. We scan the parameter space in neutrino luminosity with a step width of 0.2 in $\log_{10}(L_\nu)$ and source density with a step width of 0.4 in $\log_{10}(\rho)$.

Within the simulation, it has to be taken into account that the source count distribution is given for the entire sky while the analysis is performed only on the Northern Hemisphere. Therefore, only the fraction of $\Omega_{\mathrm{NH}}/4\pi$ of sources is considered in the simulation, where Ω_{NH} is the solid angle analyzed in the HPA ranging from -3° to 90° declination.

For each pseudo-experiment, the HPA is performed as described in Sec. 9.2 and the HPA test statistic TS_{HPA} is calculated, as defined in Eq. 9.3. Note that no astrophysical background is considered in the pseudo-experiment generation, as discussed in Sec. 9.2.5.

Before we discuss the constraints resulting from the HPA itself, we note that already the result of the all-sky scan places an upper limit on the population of sources. We can already exclude all populations that result in a more significant hot-spot in the all-sky scan than the observed hottest spot with a local p-value of $p_{\mathrm{local}} = 10^{-5.97}$ (compare Sec. 8.1.2). The source density scales with the distance to the closest source like $\rho \propto d^{-3}$ and the source flux scales like $\phi \propto L/d^2$. Thus, the limit on the source density for a given neutrino luminosity is expected to scale like $\rho_{\mathrm{UL}} \propto L_\nu^{-3/2}$ [306, 312].

We construct the 90% CL upper limit resulting from the measured hottest spot by testing each point in the ρ-L_ν phase space and exclude it if more than 90% of an ensemble of pseudo experiments for a source population with fixed ρ and L_ν result in a smaller p-value than the experimentally observed value of $p_{\mathrm{local}} = 10^{-5.97}$. The resulting 90% upper limit is shown in Fig. 10.11 as dashed blue line. The upper limit is extrapolated above for neutrino luminosities below 10^{51} erg/yr, as the computational cost is too high to simulate corresponding pseudo-experiments. The extrapolation uses the expected $\rho \propto L_\nu^{-3/2}$ scaling and is shown as dotted line in Fig. 10.11. Note that all populations with source density and luminosity above the dashed line in Fig. 10.11 are excluded at the 90% CL.

For the same set of pseudo experiments, also the HPA is performed and the HPA test statistic TS_{HPA} as defined in Eq. 9.3 is calculated. In Fig. 10.12 the test-statistic distribution for three different source densities and a neutrino luminosity of $10^{51.2}$ erg/yr are shown. The 10% quantiles of the distributions are marked as dashed vertical lines. In addition, the experimentally observed value is marked by a black solid line.

Based on the 10% quantile of the HPA test-statistic distribution for different signal parameters, again upper limits are calculated as it was done above for the most significant spot in the all-sky scan. The resulting 90% upper limits are shown in Fig. 10.11 as solid lines in blue and red for an $E^{-2.0}$ and $E^{-2.19}$ spectrum, respectively.

From Fig. 10.11, it can be seen that for large neutrino luminosities ($L_\nu > 10^{52}$ erg/yr) the upper limit resulting from the HPA scales like the limit from the hottest spot in the all-sky scan and is slightly less stringent. This shows that for large neutrino luminosities the upper limit depends on the strongest source. The upper limit from the HPA is less stringent due to the trial correction that has to be done for choosing the most significant threshold p-value.

For neutrino luminosities below 10^{50} erg/yr the upper limit from the HPA scales like $\rho \propto L_\nu^{-1}$. Such a scaling is expected from a pure diffuse flux, as the diffuse flux is proportional to the source density and the neutrino luminosity of the sources and thus $\phi_{\mathrm{diffuse}} \propto \rho L_\nu$. From this it

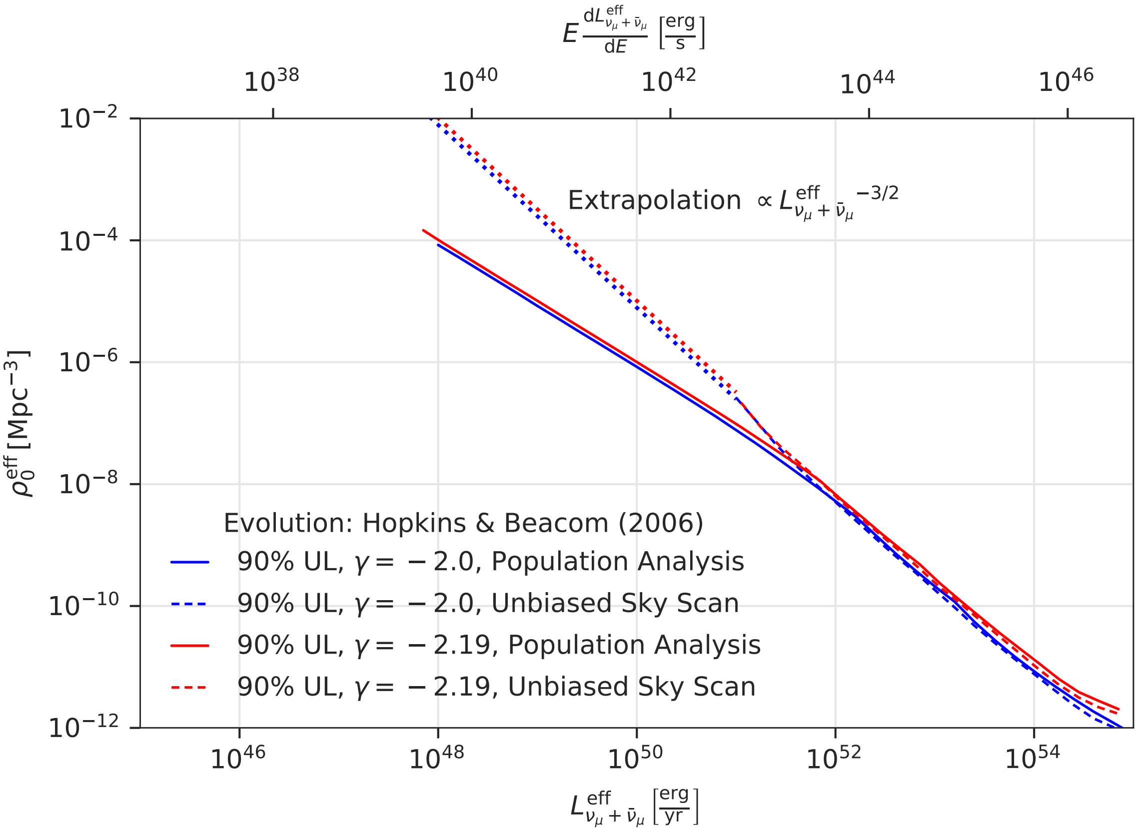

Figure 10.11: 90% CL upper limits on the local effective source density ρ_0^{eff} as a function of the local effective neutrino luminosity $L^{\mathrm{eff}}_{\nu_\mu+\nu_{\bar{\mu}}}$. Upper limits calculated from the most significant spot in the sky are marked by dashed lines and the upper limits are extrapolated by a $\rho_0^{\mathrm{eff}} \propto (L^{\mathrm{eff}}_{\nu_\mu+\nu_{\bar{\mu}}})^{-3/2}$ scaling for $L^{\mathrm{eff}}_{\nu_\mu+\nu_{\bar{\mu}}} < 10^{51}$ erg/yr (dotted lines). The upper limits from the hotspot population analysis (HPA) are shown as solid linex. The upper x-axis gives the local effective neutrino luminosity per logarithmic energy interval. A power law spectrum with spectral index $\gamma = -2.0$ (blue) and $\gamma = -2.19$ (red) and the source evolution from Hopkins & Beacom [308] are used.

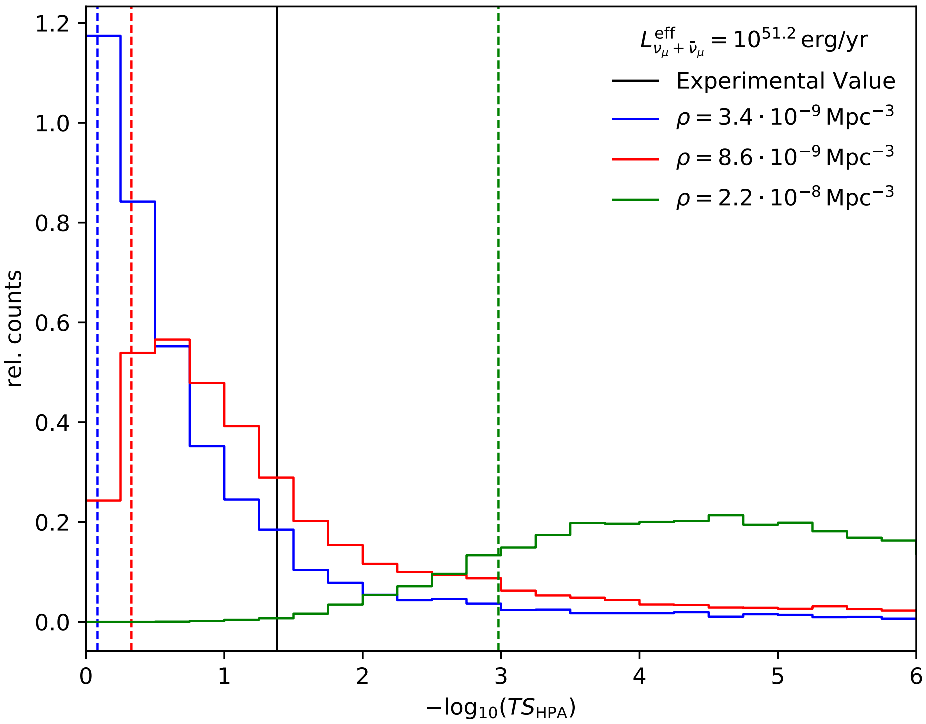

Figure 10.12: Test-statistic distribution of the HPA TS_{HPA} for different effective local source densities (see legend) and an effective local muon neutrino luminosity of $10^{51.2}$ erg/yr. The test statistic distribution is shown as negative decadic logarithm of TS_{HPA} which corresponds to the minimal poisson p-value. The 10% quantile of the test statistic distributions are indicated by vertical dashed lines. The experimentally observed test statistic value is shown as black solid line.

follows that for a measured diffuse flux the scaling is $\rho \propto \phi_{\mathrm{diffuse}}/L_\nu$. As discussed in Sec. 9.2.5, source populations with many weak sources that only produce single neutrinos per source are indistinguishable from a real diffuse flux. As shown in Sec. 9.2.5, the HPA is sensitive to such a diffuse-like population and thus allows to put upper limits on such diffuse-like populations.

From Fig. 10.11, it can be seen that the limits for source populations with source spectra with a spectral index of $\gamma = -2.0$ and $\gamma = -2.19$ are similar. As the different evolution models result in very similar source count distributions, as can be seen in Fig. 10.10, and the computation of the upper limits is computational very expensive, no other source evolution model is tested.

10.3.3 Discussion

As discussed in Sec. 10.3.2, the 90% CL upper limit resulting from the HPA results in a diffuse-like flux for small effective local neutrino luminosities. For each population we can calculate if they are consistent with the measured diffuse astrophysical flux, which was discussed in Sec. 5.8. The resulting diffuse flux normalization ϕ_{diffuse} from a source population can be calculated by:

$$4\pi\phi_{\mathrm{diffuse}} = \frac{N_{\mathrm{sources}}}{V_{\mathrm{C}}(z_{\mathrm{max}})} \int_0^{z_{\mathrm{max}}} \phi_0(L_\nu, z) \frac{\mathrm{d}N}{\mathrm{d}V_{\mathrm{C}}} \mathrm{d}z \,, \tag{10.13}$$

using Eq. 10.7, Eq. 10.9, Eq. 10.10 and Eq. 10.11. The factor 4π on the left-hand side takes the considered solid angle of the full sky into account. The right-hand site of Eq. 10.13 integrates the fluxes of sources at a distance z weighted by the distribution of sources in the Universe $\mathrm{d}N/\mathrm{d}V_{\mathrm{C}}$. The factor $\frac{N_{\mathrm{sources}}}{V_{\mathrm{C}}(z_{\mathrm{max}})}$ gives the averaged source density. Note that because $N_{\mathrm{source}} \propto \rho_0^{\mathrm{eff}}$ and $\phi_0 \propto L^{\mathrm{eff}}_{\nu_\mu+\nu_{\bar{\mu}}}$ we find $\rho_0^{\mathrm{eff}} L^{\mathrm{eff}}_{\nu_\mu+\nu_{\bar{\mu}}} = \mathrm{const}$ and thus $\rho_0^{\mathrm{eff}} \propto (L^{\mathrm{eff}}_{\nu_\mu+\nu_{\bar{\mu}}})^{-1}$ which was already mentioned above.

The populations that are consistent with the diffuse flux measured in [6] at the 1σ and 3σ level are shown as bands in Fig. 10.13. In the calculation, the spectral index and the diffuse flux normalization following the 1σ and 3σ contours from Fig. 3 in [6] are used, as well as a source evolution following Hopkins & Beacom [308] and standard candle luminosities.

From Fig. 10.14 one can see that the scaling of the upper limit from the HPA is the same as for the diffuse flux for neutrino luminosities $L_\nu < 10^{51}\,\mathrm{erg/yr}$. In addition, the 90% upper limit from the HPA coincides with the 3σ bound from the diffuse flux for neutrino luminosities $L_\nu < 10^{51}\,\mathrm{erg/yr}$. From this we can conclude that populations that lead to a higher neutrino flux than allowed by the 3σ confidence interval would lead to an excess in the HPA. This is the same observation as discussed in Sec. 9.2.5.

For neutrino luminosities $L_\nu > 10^{53}\,\mathrm{erg/yr}$, the 90% upper limit from both the hottest spot in the all-sky scan and the HPA are below the band which is compatible with the diffuse flux. For these populations we can exclude at 90% confidence level that the population is responsible for 100% of the diffuse flux.

Note that above we calculated experimental constraints on source populations depending on $L_{\nu,\mathrm{eff}}$ and $\rho_{\mathrm{eff,local}}$. However, to calculate model predictions for sources of a specific class, using their photon luminosity distribution $\mathrm{d}\rho/\mathrm{d}L_\gamma$, the scaling of neutrino luminosity to photon luminosity has to be given in addition, which is typically $L_\nu \propto L_\gamma^\alpha$ [306, 312]. The exact scaling

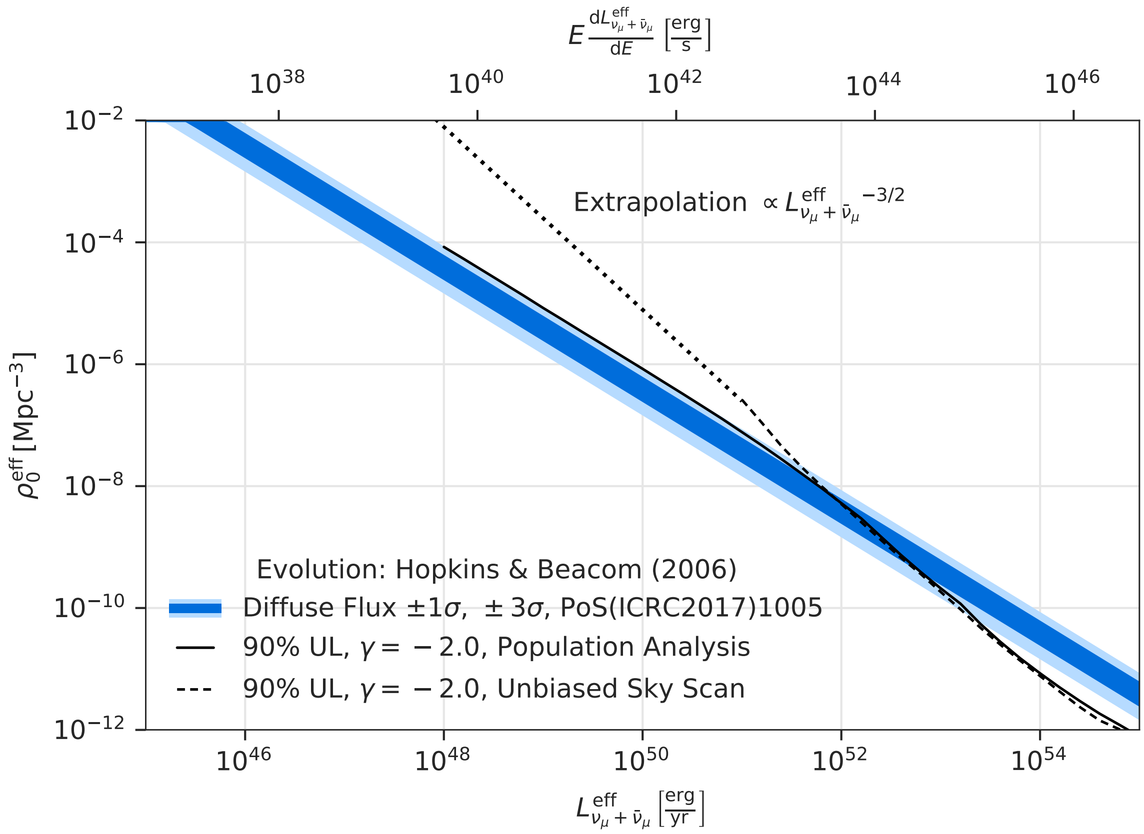

Figure 10.13: 90% CL upper limits on the local effective source density ρ_0^{eff} as a function of the local effective neutrino luminosity $L^{\mathrm{eff}}_{\nu_\mu+\nu_{\bar{\mu}}}$. Upper limits calculated from the most significant spot in the sky are marked by dashed lines and the upper limits are extrapolated by a $\rho_0^{\mathrm{eff}} \propto (L^{\mathrm{eff}}_{\nu_\mu+\nu_{\bar{\mu}}})^{-3/2}$ scaling for $L^{\mathrm{eff}}_{\nu_\mu+\nu_{\bar{\mu}}} < 10^{51}$ erg/yr (dotted line). The upper limits from the HPA are shown as solid line. The upper x-axis gives the local effective neutrino luminosity per logarithmic energy interval. A power-law spectrum with spectral index $\gamma = -2.0$ and the source evolution from Hopkins & Beacom [308] are used. Populations consistent at the 1σ and 3σ level with the diffuse astrophysical flux measured in [6] are shown as blue band.

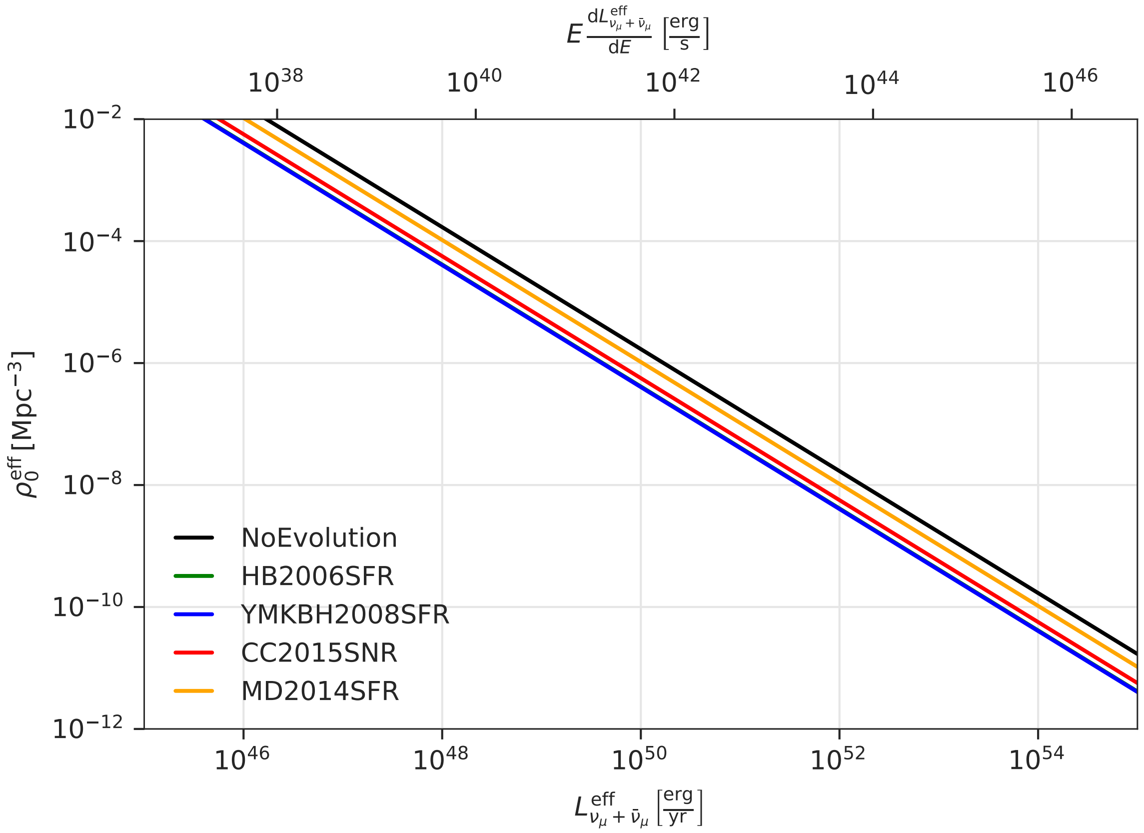

Figure 10.14: Local effective source density ρ_0^{eff} and local effective neutrino luminosity $L^{\mathrm{eff}}_{\nu_\mu+\nu_{\bar{\mu}}}$ of populations that correspond to the best-fit diffuse flux with a flux normalization at 100 TeV of $1.01 \cdot 10^{-18}\,\mathrm{GeV}^{-1}\mathrm{cm}^{-2}\mathrm{s}^{-1}\mathrm{sr}^{-1}$ and a spectral index of -2.19 for different source evolutions (see legend). The upper x-axis gives the local effective neutrino luminosity per logarithmic energy interval.

and normalization has to be discussed for each type of source class individually and depends on the process in which photons and neutrinos are produced.

As explained in Sec. 2.2.1, it is assumed that astrophysical high-energy neutrinos are produced in decays of charged pions in hadronic interactions of cosmic rays either with matter, also called proton-proton interaction (pp), or with radiation, also called proton-photon interaction ($p\gamma$). As also discussed in Sec. 2.2.1, photons produced by cosmic rays have about double the energy of neutrinos produced by cosmic rays with the same energy and thus $E_\gamma \simeq 2E_\nu$ [312].

In addition, one finds from the branching ratios of pions and kaons that the intensities of the neutrino flux and the gamma-ray flux are linked by [312, 315, 316]:

$$\begin{aligned} &I_\nu(E_\nu) \simeq K I_\gamma(E_\gamma)\,, \\ &E_\gamma \simeq 2E_\nu\,, \end{aligned} \tag{10.14}$$

where $K \simeq 2$ for pp-interaction and $K \simeq 1$ for $p\gamma$-interaction. Thus, given a photon luminosity function with a characteristic benchmark luminosity, we can calculate the corresponding effective benchmark neutrino luminosity and the effective source density.

In the following, we will used the values for source classes and shortly describe their derivation as done in [312] (Appendix C):

> **Starburst galaxies:** Neutrinos are produced by pp interaction in starburst galaxies. It is found that the infrared luminosity in the $[8, 10^3]\,\mu$m band is related to the γ-ray luminosity measured by Fermi in the $[0.1, 100]$ GeV band [317]. Using this relation and the infrared luminosity distribution from [318], the gamma-ray luminosity is calculated, the benchmark gamma-ray and neutrino luminosities are calculated. The local effective density is take from [312, 317].
>
> **Cluster of galaxies:** Neutrinos are produced by pp-interaction in clusters of galaxies. Using the phenomenological luminosity-mass relation found in [319]. The benchmark effective neutrino luminosity is found by extrapolating the expected neutrino luminosities from five galaxy clusters in [319] and averaging them. The effective local source density is taken from [312, 319].
>
> **Flat-spectrum radio quasars (FSRQs):** Neutrinos are produced by $p\gamma$ interaction in flat-spectrum radio quasars. Using the gamma-ray luminosity distribution by Fermi in the energy band [0.1, 100] GeV [320], the benchmark gamma-ray luminosity is found to be close to the break luminosity, from which the effective neutrino luminosity is derived [312]. The effective neutrino density is derived by Eq. 10.12 [312].
>
> **BL Lacs:** Neutrinos are produced by $p\gamma$ interaction in BL Lacs. Using the gamma-ray luminosity distribution by Fermi in the energy band [0.1, 100] GeV [321], the benchmark gamma-ray luminosity is found to be close to the break luminosity, from which the effective neutrino luminosity is derived [312]. The effective neutrino density is derived by Eq. 10.12 [312].
>
> **Fanaroff-Riley galaxies (FR-I and FR-II):** Using the correlation of radio-loud luminosity function and the gamma-ray luminosity function, as well as the radio-loud

Source class	ρ_0^{eff} [Mpc^{-3}]	L_ν [erg s^{-1}]
Starburst galaxies	2.5×10^{-5}	1.4×10^{40}
Clusters of galaxies	6.8×10^{-6}	3.3×10^{42}
FSRQs	5.6×10^{-11}	3.3×10^{45}
BL Lacs	1.5×10^{-8}	3.6×10^{44}
FR-I	3.2×10^{-8}	2.0×10^{40}
FR-II	2.0×10^{-7}	2.8×10^{41}
LL-AGN	1.0×10^{-3}	1.0×10^{39}

Table 10.2: Effective local density and muon neutrino luminosity of various astrophysical steady sources producing high-energy neutrinos in the same energy range as the IceCube neutrino events; adopted in [312].

luminosity functions at 5 GHz for FR-I and FR-II galaxies from [322], the benchmark luminosity is given by the break luminosity. Assuming *pp* interaction for FR-1 galaxies and $p\gamma$ interactions for FR-2 galaxies, the effective neutrino luminosities are calculated. The effective source densities are taken from [312, 322].

Low-luminosity active galactic nuclei (LL-AGN): The benchmark neutrino luminosity is taken from [323] where different acceleration mechanisms have been studied and the luminosity distribution is adopted from the Hα luminosity distribution from nearby LL-AGN [324]. The effective density is taken from [306, 312].

The effective muon neutrino luminosities per logarithmic energy interval and the effective source densities as taken from [312] (Appendix C) are listed in Tab. 10.2 and are plotted as markers in Fig. 10.15. Note that there are relatively large astrophysical model uncertainties and estimates can deviate by few orders of magnitude (compare e.g. the estimates in [306]). Therefore, no firm conclusions can be made but a qualitative picture can be drawn.

From Fig. 10.15 we can conclude that rare but strong sources are challenged by the non observation as a hottest spot in the all-sky scan. This is especially the case for BL Lacs and FSRQs. Note that already in [11] it was found that sources from the Fermi 2LAC catalog can make up at maximum 27% of the total astrophysical neutrino flux assuming an $E^{-2.5}$ spectrum. In addition, we can conclude from Fig. 10.15 that all populations that would result in a much larger flux than the diffuse astrophysical best-fit spectrum can be excluded (e.g. galaxy clusters). Such an additional diffuse like flux would have caused an excess in the HPA. Note that several source classes are close to the band that is consistent with the diffuse astrophysical flux. However e.g. a population of FR-I sources can not be probed as it is several orders of magnitudes below the current upper limits.

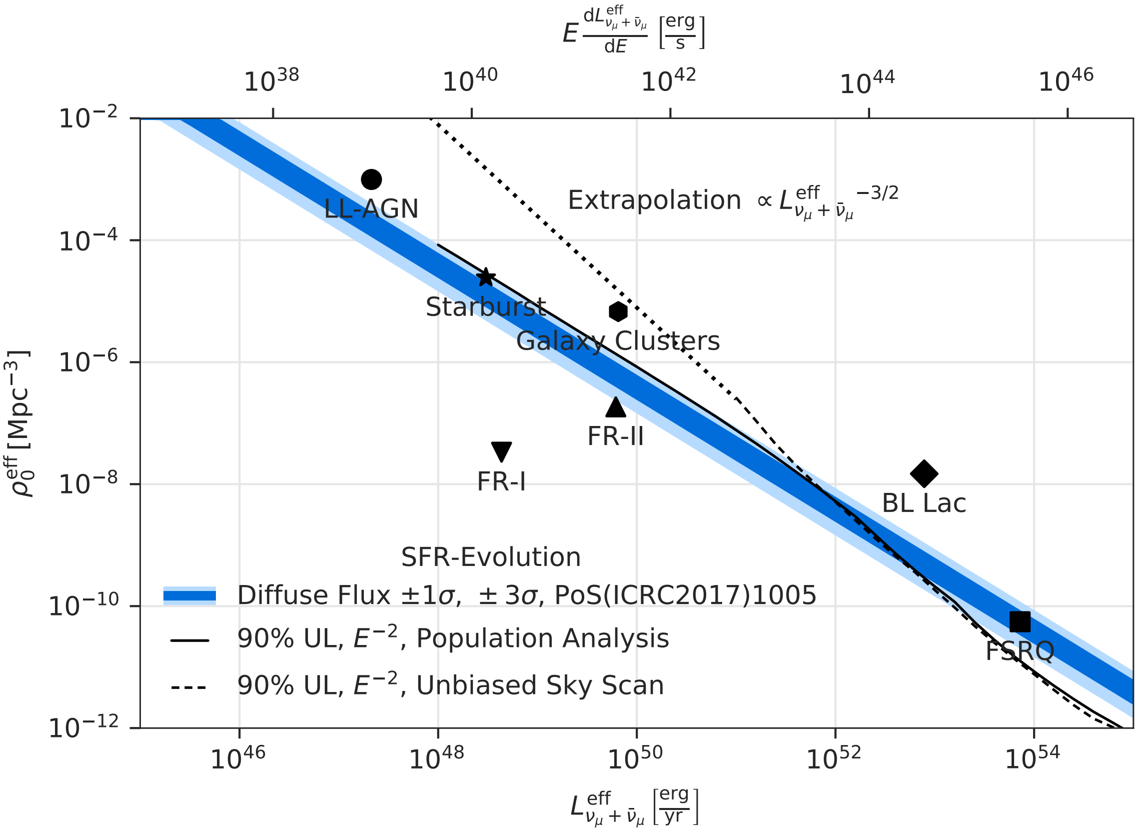

Figure 10.15: 90% CL upper limits on the local effective source density ρ_0^{eff} as a function of the local effective neutrino luminosity $L^{\mathrm{eff}}_{\nu_\mu+\nu_{\bar{\mu}}}$. Upper limits calculated from the most significant spot in the sky are marked the dashed line and the upper limit is extrapolated by a $\rho_0^{\mathrm{eff}} \propto (L^{\mathrm{eff}}_{\nu_\mu+\nu_{\bar{\mu}}})^{-3/2}$ scaling for $L^{\mathrm{eff}}_{\nu_\mu+\nu_{\bar{\mu}}} < 10^{51}\,\mathrm{erg/yr}$ (dotted line). The upper limits from the HPA are shown as solid line. The upper x-axis gives the local effective neutrino luminosity per logarithmic energy interval. A power-law spectrum with spectral index $\gamma = -2.0$ and the source evolution from Hopkins & Beacom [308] are used. Populations consistent at the 1σ and 3σ level with the diffuse astrophysical flux measured in [6] are shown as blue band. Estimates of typical effective source densities and effective neutrino luminosities for different source classes are shown by different markers [312].

Chapter 11

Conclusion and Outlook

11.1 Summary

In this thesis we aimed to find sources of high-energy astrophysical neutrinos by testing for spatial clustering. Therefore, an unbinned likelihood method was used and several improvements have been introduced in Chapter 6. During this process a special focus was put on sources that have the same spectrum as the observed astrophysical neutrino flux. We found that the gain in sensitivity and discovery potential is of the order of 20%-30% compared to the latest published analysis, depending on the declination of the source hypothesis.

We analysed in total eight years of IceCube data, where we selected well-reconstructed through-going muon tracks from the Northern hemisphere. This high statistics and high purity sample with about 500 000 neutrino events was tested for the existence of a point-like neutrino source anywhere in the Northern hemisphere. In addition, an a-priori selected source catalog containing 34 sources, which are thought to be likely neutrino sources, has been tested for point-like neutrino emission. Both tests remain insignificant. In the sky scan of the Northern Hemisphere the most significant spot was found at 177.89° right ascension and 23.23° declination (J2000) with a local p-value of $10^{-5.97}$. This local p-value reduces to a post-trial p-value of 26.5% when correcting for the number of trials. The most significant source from the source catalog is the flat spectrum radio quasar 4C 38.31 with a local p-value of 0.8% which results in a post-trial p-value of 23.7% when corrected for trials.

Based on these observations, upper limits on the flux normalization for sources following a power law spectrum have been computed. For sources from the source catalog, for which a neutrino flux model exists and the flux prediction is within a factor of five of the sensitivity of this analysis, model rejection factors have been computed. Thus the neutrino flux model for the Crab Nebula by Amato *et al.* [84] could be constrained for specific parameters as well as the models for 3C273 by Reimer [301] and Mrk 421 by Petropoulou *et al.* [302]. Based on the all-sky scan, source populations could be constrained such that the strongest source of a population can not exceed the observed test statistic of the most significant spot in the all-sky scan. These upper limit have been calculated for source populations in dependence of their benchmark neutrino luminosities and source density.

A special test for time-independent neutrino emission in the direction of the blazar TXS 0506+056 has been performed, resulting in a compatibility with background of only 2.93%. This blazar was found in flaring state in coincidence with the detection of an extreme-high-energy neutrino event alert IceCube-170922A [19]. An uncorrelated emission from the flaring blazar with the neutrino alert event is disfavoured at the 3σ level [19]. The result for time-independent neutrino emission obtained in this thesis was used as a cross-check to the analysis presented in [20] which obtained a compatible result. A time-dependent analysis found a neutrino flare in December 2014 with a duration of about 110 days and disfavours the background hypothesis at the 3.5σ level [20]. The independent result of the neutrino alert in temporal and spatial correlation with the flaring blazer and the additional neutrino flare from the direction of TXS 0506+056 mark the first evidence for an astrophysical neutrino source.

Beside the tests for individual sources, special tests for populations of sub-threshold sources have been developed and applied to the source catalog and the skymap of the all-sky scan. These analyses, testing for an excess of small p-values, are non significant with a p-value of 6.6% for the source catalog and 42.0% for the all-sky scan. Based on the observed test statistic value of the population test, constraints on source populations have been calculated. These upper limits have been calculated in dependence of the effective neutrino luminosity and the effective neutrino source density. The upper limits challenge the hypothesis that the full population of flat spectrum radio quasars and BL Lacs are the source of astrophysical neutrinos.

11.2 Outlook

With 8 years of livetime, no significant steady neutrino source could be found so far. To estimate the scaling with livetime, we calculated the sensitivity and discovery potential for different livetimes and for sources with different spectral index and declination. For livetimes smaller than the full livetime discussed in this thesis, the sample is cut down, while for extrapolation to longer livetimes the additional events follow the latest event selection. The resulting sensitivity and discovery potential for a source at 0° declination and an $E^{-2.0}$ spectrum is shown in Fig. 11.1. To estimate the scaling with livetime, a power law is fitted to the calculated sensitivity and discovery potential (dashed line in Fig. 11.1) as a function of livetime. While for background-free samples the analysis performance should scale like T^{-1} and for background-dominated samples the analysis performance should scale like $T^{-0.5}$, we find a scaling of $T^{-0.92}$ for the sensitivity and $T^{-0.86}$ for the discovery potential for a source at 0° declination and an $E^{-2.0}$ spectrum. The exponents of the fitted power laws are shown in the lower panel of Fig. 11.1 as a function of declination and for different source spectral indices. While for hard spectral indices the scaling nearly approaches the background-free case, the scaling for soft sources is nearly following the background-dominated case. While the sensitivity and discovery potential for point-like sources will decrease with further livetime, a steady point source should slowly emerge from the background with time. However this is not yet the case and thus we can expect that there will be no significant steady point-source within the next years without any significant improvements.

To improve the sensitivity and discovery potential to (steady) point-like sources there are several options. By improvements in the reconstruction of single events, the spread of the point spread function can be decreased. This would have a strong effect on the sensitivity and discovery potential as the relative improvement in the median angular resolution would lead to a similar relative improvement in sensitivity and discovery potential. Note that this will not only help with additional data, but as the reconstruction can be re-applied to already recorded data, this would effect the full sample.

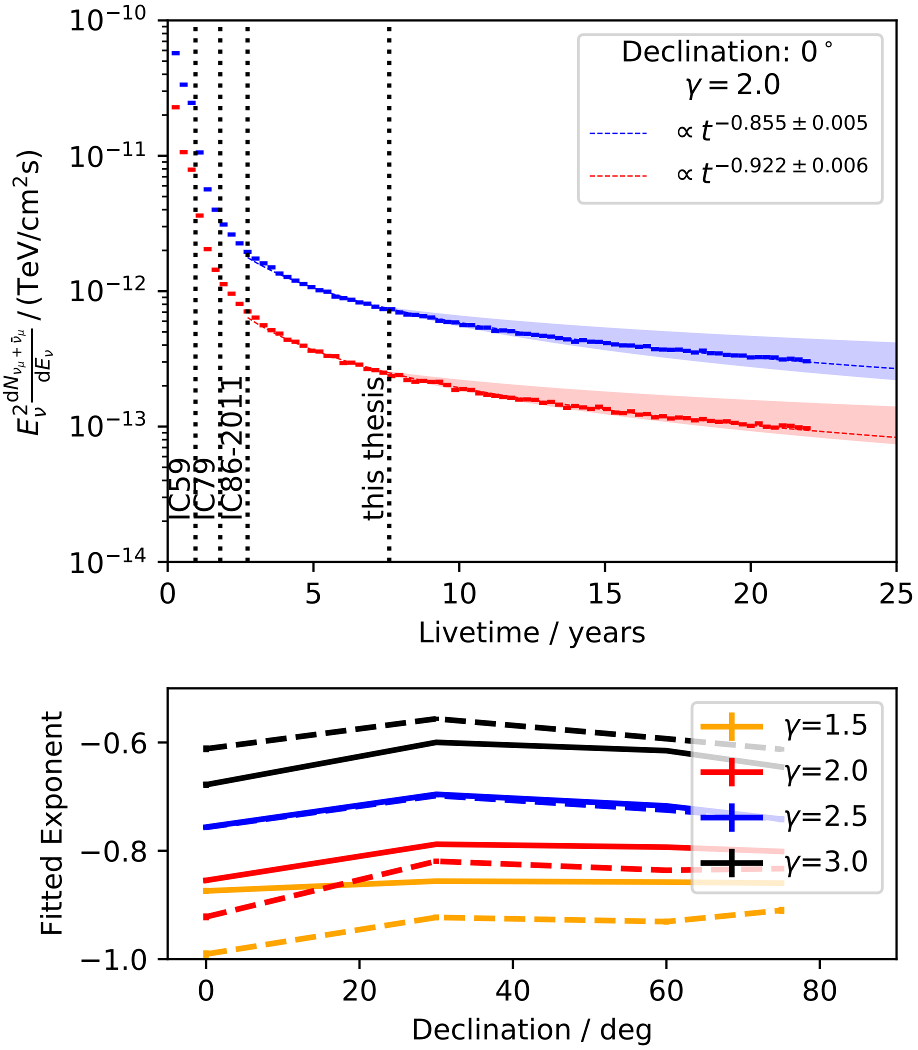

Figure 11.1: Upper panel: Sensitivity and discovery potential (errorbars, bars smaller than the linewidth) for a source at 0° declination and an $E^{-2.0}$ spectrum as a function of livetime. The change of sub-samples are indicated by vertical black dashed lines, where the line labeled ”this thesis” corresponds to the current sample. For extrapolated livetimes, the additional sample is following the latest event selection. The dashed line gives the result of a power law fit to the sensitivity and discovery potential as a function of livetime. The shaded areas give the extrapolation based on a $T^{-0.5}$ and a T^{-1} scaling and a fixed point at the current livetime. Bottom: Fitted exponent of the sensitivity and discovery potential scaling with livetime (see legend in upper panel) as function of source declination and for different source spectral indices.

Minor improvements can be made on the method, like more precise treatment of angular reconstruction uncertainty or estimating probability density function using kernel density estimation. Also the event selection approaches a very efficient level and improvements in purity or efficiency are expected to be minor.

To significantly improve the discovery potential for a source, we have to consider temporal information in addition to the spatial clustering. This can be seen e.g. at the example of TXS 0506+056, where the significance of the time-dependent analysis is much larger than the one obtained by a steady point-source analysis.

While these generic searches are not relaying on external information and thus are completely independent, they suffer from a large number of trials, which has to be corrected for in the final p-value. The discovery potential for source populations or individual sources thus can be increased if the number of trials is reduced e.g. by pre-selection of sources, stacking or cross-correlation. In this context the field of multi-messenger astronomy is very important.

Beside improvements in reconstruction and analysis methods, also an improved and larger detector will lead to a gain in sensitivity. An upgrade called IceCube-Gen2 is proposed for IceCube [178]. This upgrade should enhance the detection volume by a factor of ten and lead to an improved sensitivity to steady point sources of at least a factor of five [178]. A first step in this direction is the Phase1 Upgrade [325], that will be an infill array to the IceCube-DeepCore detector. Phase1 is designed to lower IceCube's energy threshold to allow improved measurements of particle physics properties, but at the same time is used to demonstrate the capabilities of new light sensors and study systematic effects especially of the antarctic ice.

Both with the first successes in multi-messenger astronomy and the construction of an improved detector in the next years, interesting times for neutrino astronomy are ahead of us.

Appendices

Appendix A

Characterisation of All Sub-Samples

In this Appendix we present plots that characterise the individual sub-samples use within this thesis. The corresponding figures for the season IC86-2012/16 can be found in Sec. 5.7 along with explanations to the individual plots. The figures shown in this appendix are for the seasons IC59, IC79 and IC86-2011. For details on the quantities shown in the figures see Sec. 5.7.

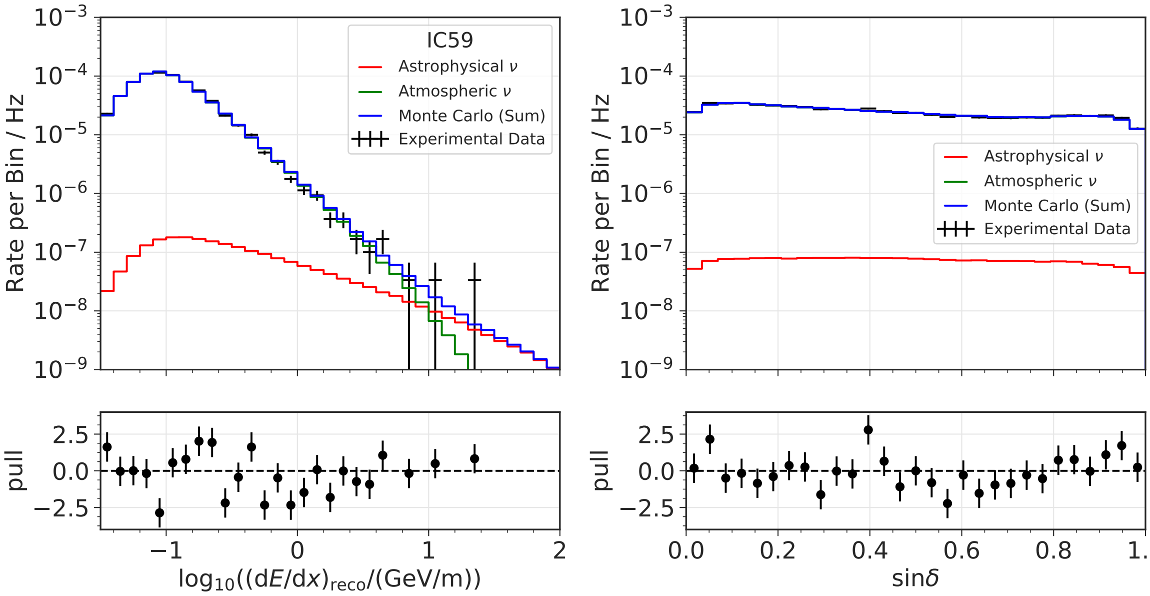

Figure A.1: Reconstructed energy (left) and declination (right) distribution for the season IC59. The experimentally observed rate is given by black error bars. The expected atmospheric (green) and astrophysical (red) component using the best fit parametrization (see Sec. 5.8) is shown as histograms. The contribution from *prompt* neutrinos is zero and the contributions from atmospheric muons are neglected. The pull relative to the total expected rate (blue) is shown in the lower panels.

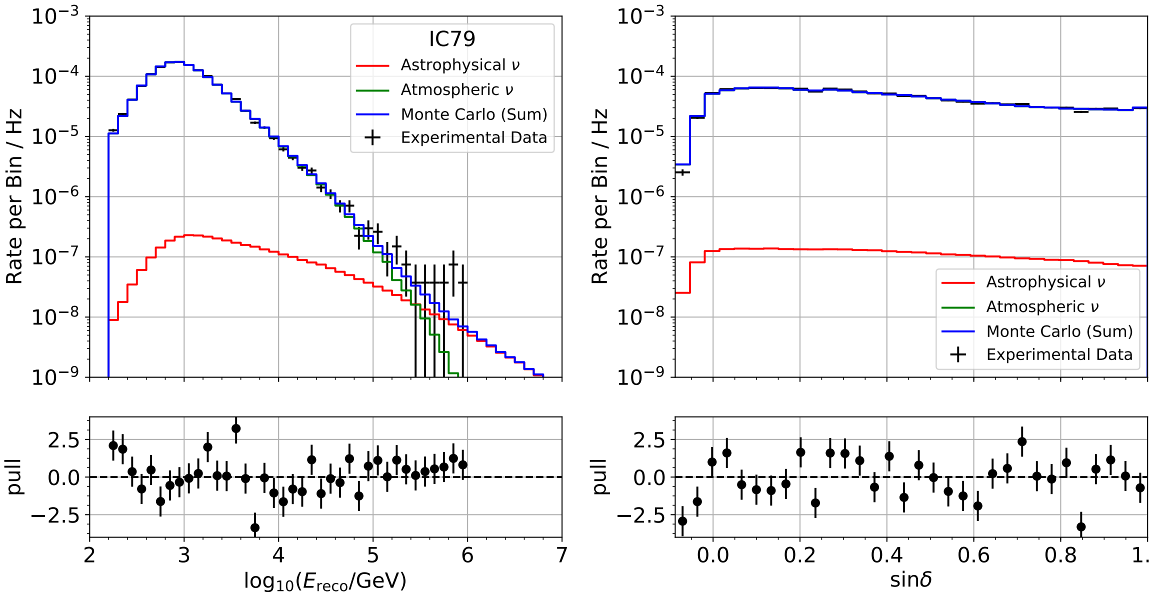

Figure A.2: Same as Fig. A.1 but for the season IC79.

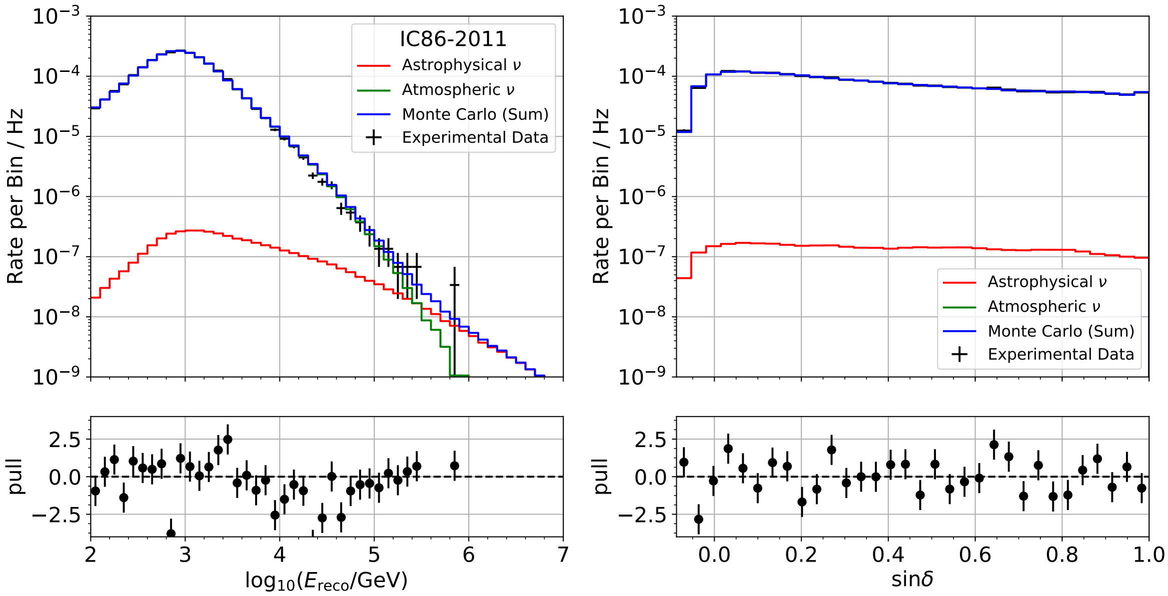

Figure A.3: Same as Fig. A.1 but for the season IC86-2011.

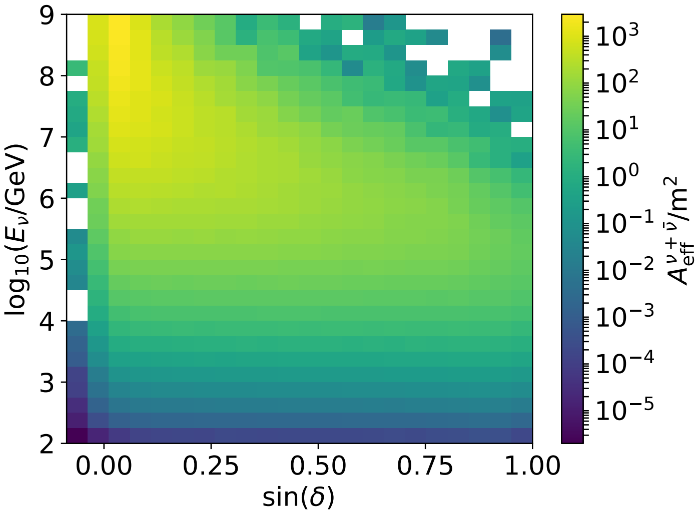

Figure A.4: $\nu_\mu + \nu_{\bar{\mu}}$ effective area as a function of declination and neutrino energy for the season IC59. The effective area is averaged over the parameter range covered by the bin.

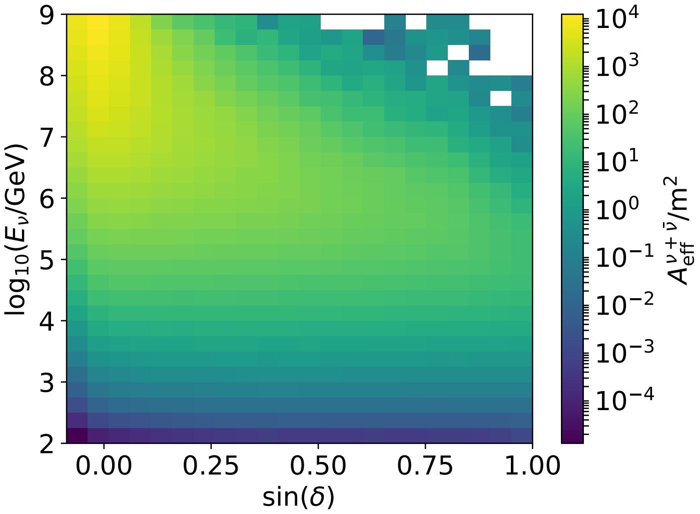

Figure A.5: Same as Fig. A.4 but for the season IC79.

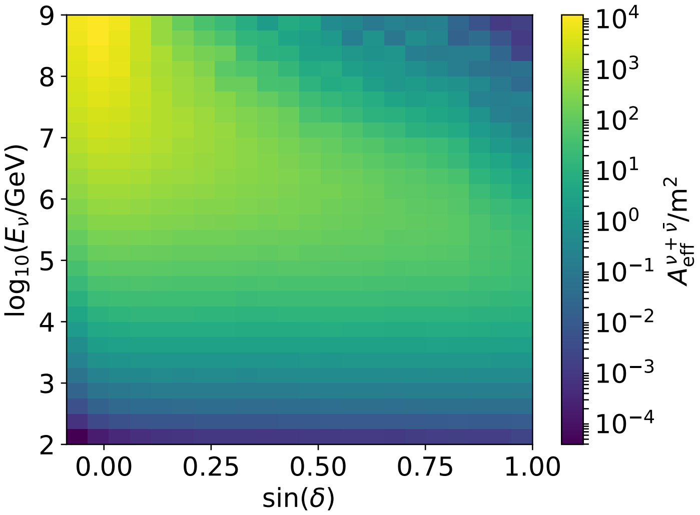

Figure A.6: Same as Fig. A.4 but for the season IC86-2011.

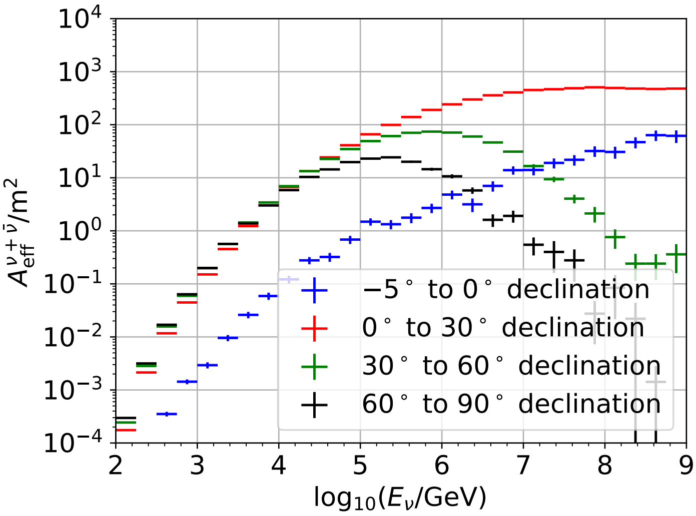

Figure A.7: $\nu_\mu + \nu_{\bar{\mu}}$ effective area as a function of neutrino energy for the different declination. The effective areas are averaged over the declination range given in the legend and are calculated for the season IC59.

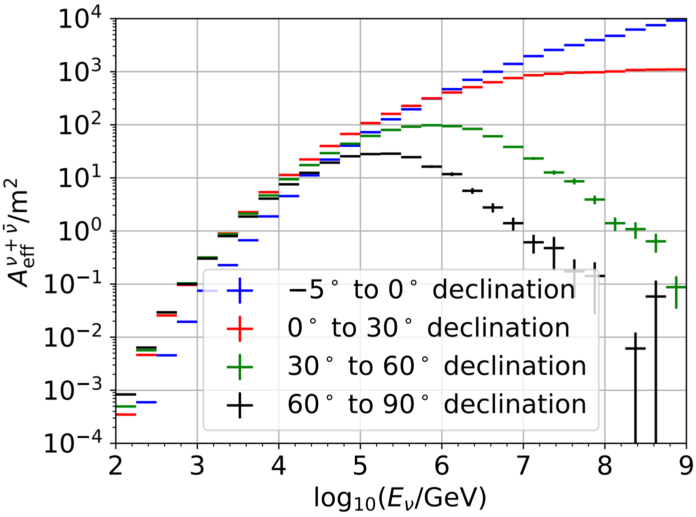

Figure A.8: Same as Fig. A.7 but for the season IC79.

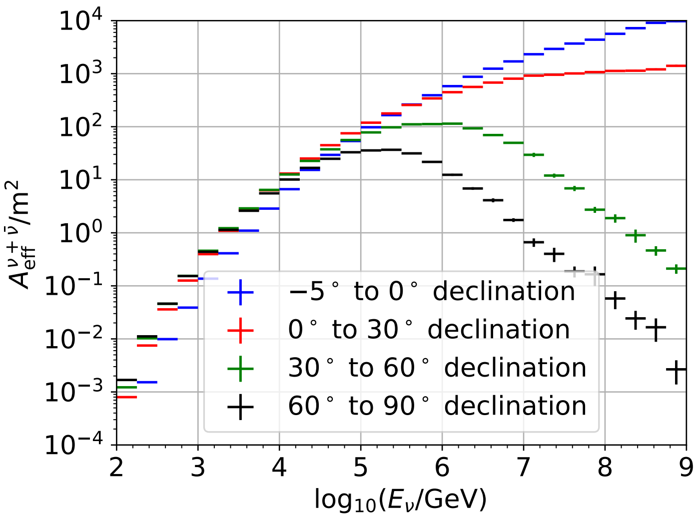

Figure A.9: Same as Fig. A.7 but for the season IC86-2011.

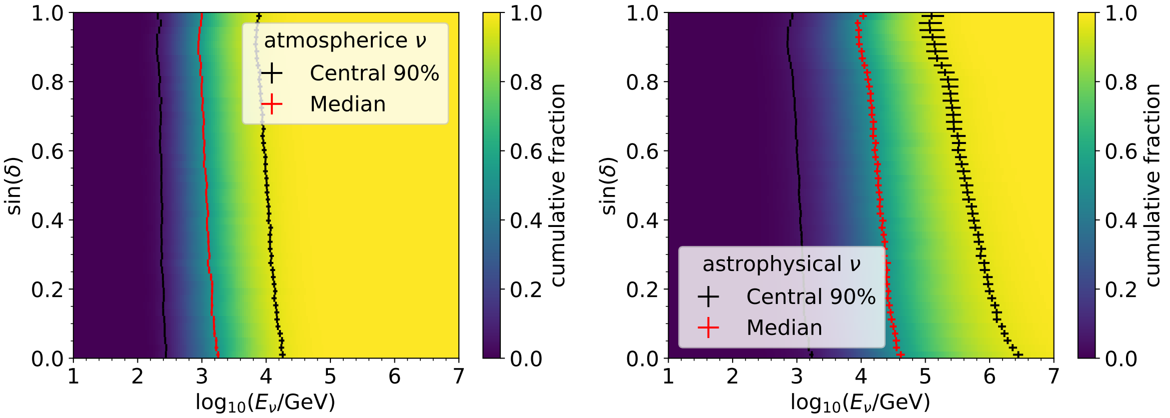

Figure A.10: Cumulative neutrino energy distribution for different declination for the season IC59. The left panel shows the distribution for the best fit atmospheric neutrino spectrum and the right panel shows the distribution for the best fit astrophysical neutrino spectrum. The black error bars mark the central 90% energy range and the red error bars show the median energy.

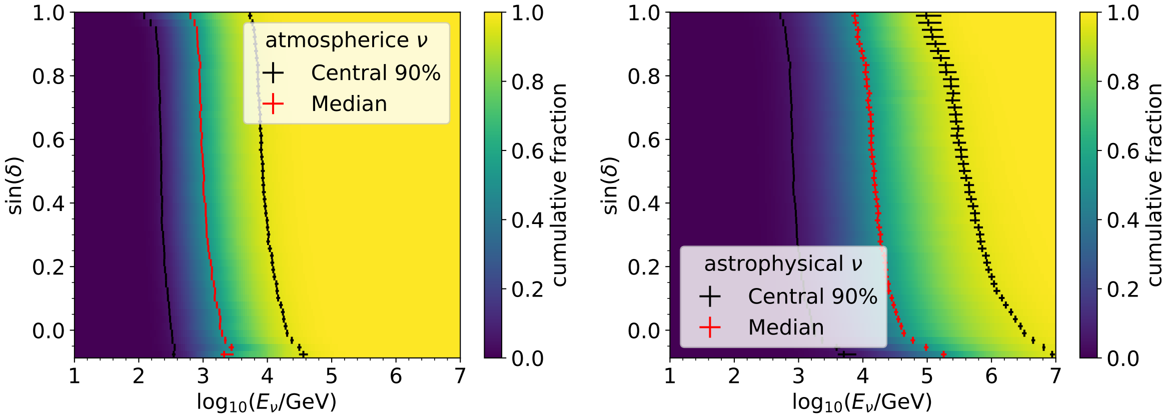

Figure A.11: Same as Fig. A.10 but for the season IC79.

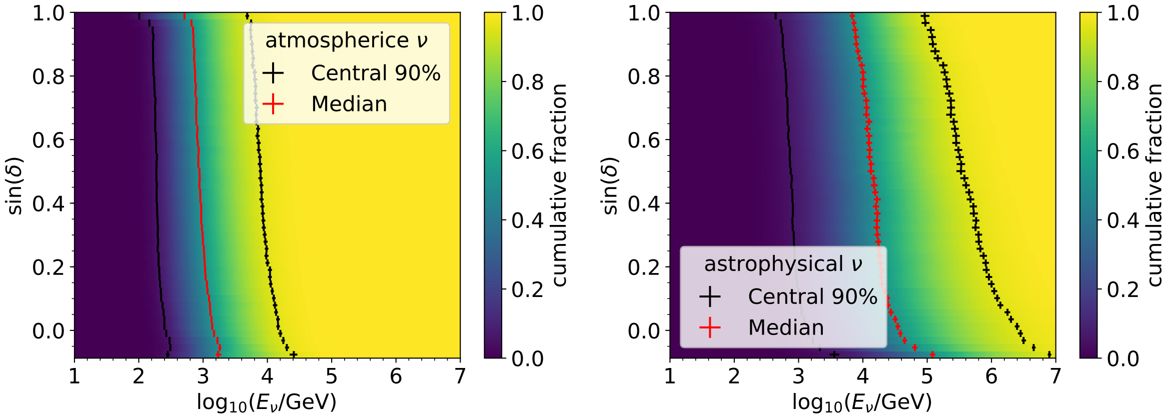

Figure A.12: Same as Fig. A.10 but for the season IC86-2011.

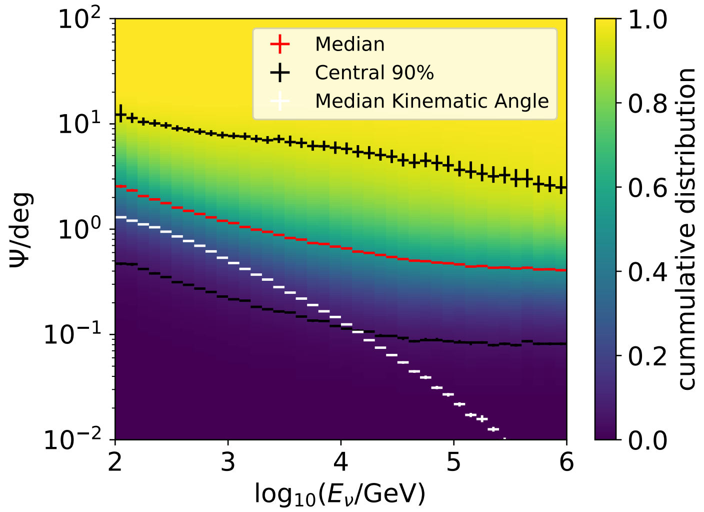

Figure A.13: Cumulative distribution of the opening angle between true and reconstructed neutrino direction Ψ for different neutrino energies E_ν for the season IC59. The median Ψ and the central 90% range are indicated by red and black error bars. The median kinematic opening angle between the initial neutrino and the muon from a CC muon-neutrino interaction is shown in white (see Sec. 4.1 and Fig. 4.4).

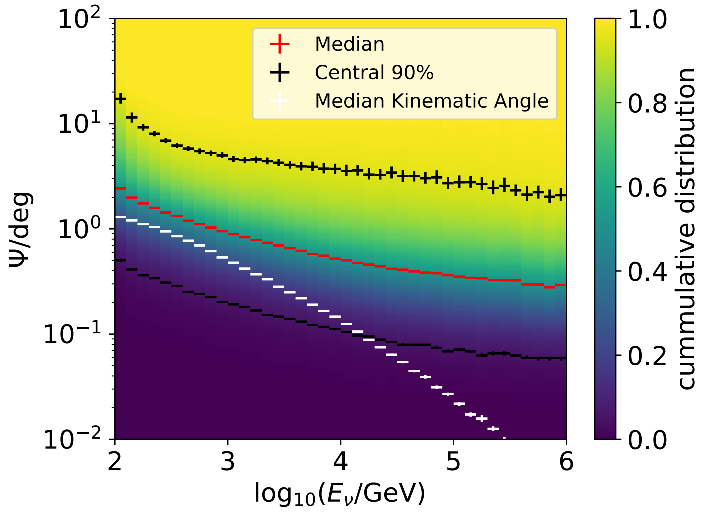

Figure A.14: Same as Fig. A.13 but for the season IC79.

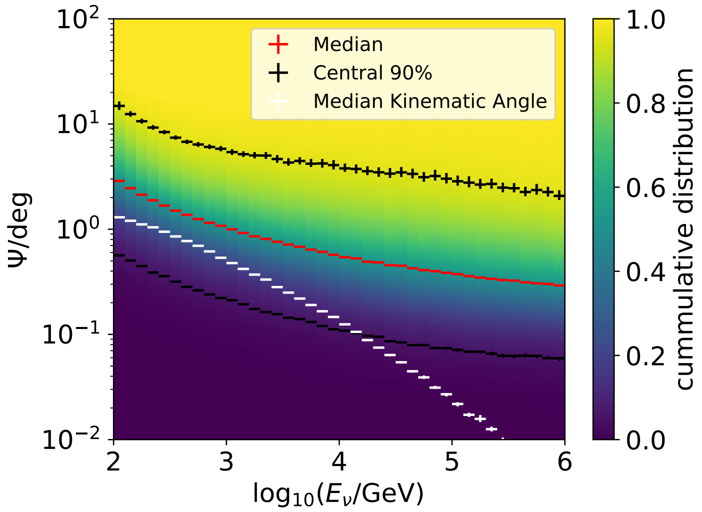

Figure A.15: Same as Fig. A.13 but for the season IC86-2011.

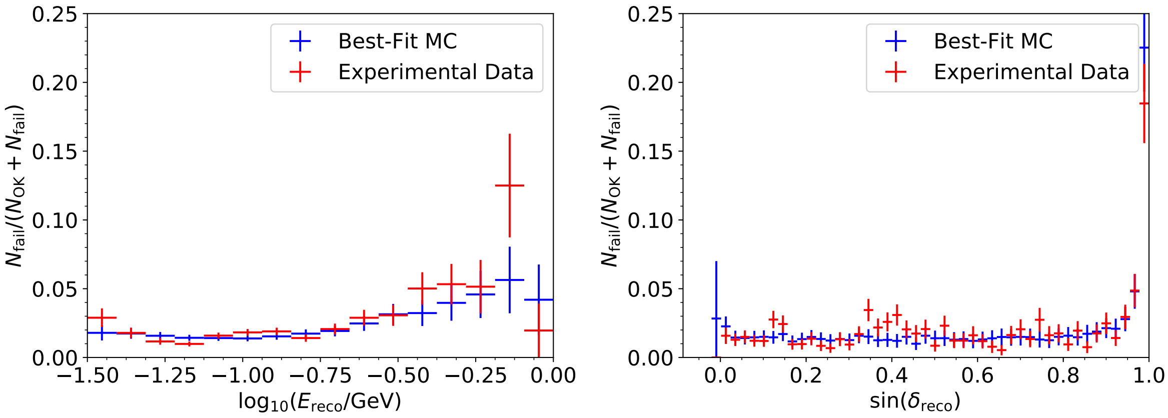

Figure A.16: Fraction of failed paraboloid fits as a function of reconstructed energy (left) and sine of declination (right) for the season IC59.

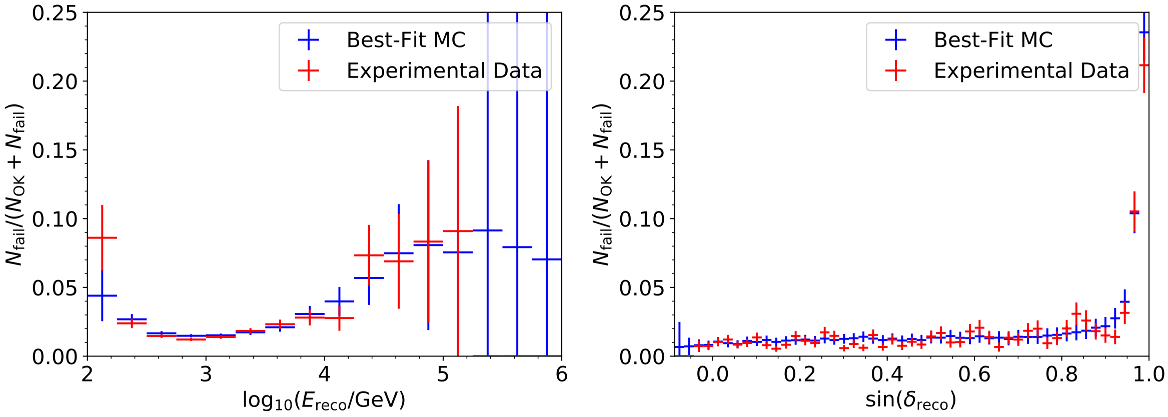

Figure A.17: Same as Fig. A.16 but for the season IC79.

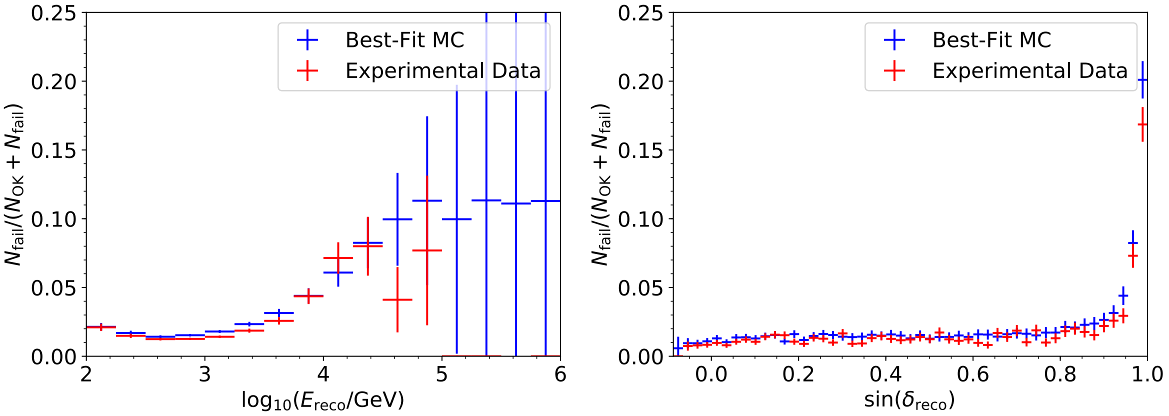

Figure A.18: Same as Fig. A.16 but for the season IC86-2011.

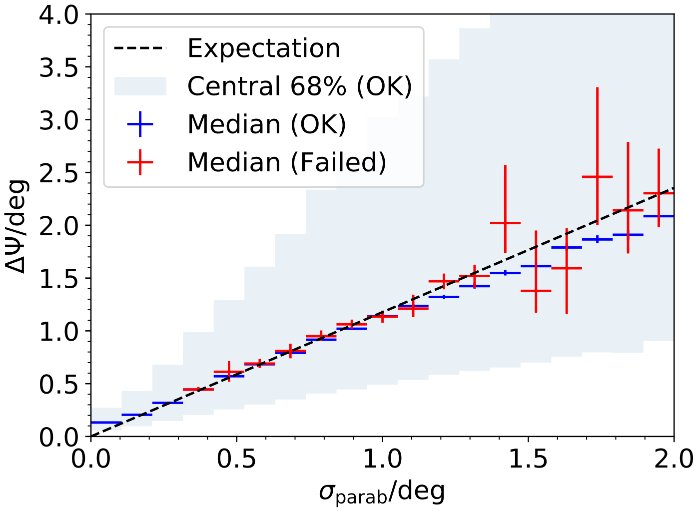

Figure A.19: Median (error bars) and central 68% range (shaded area) of the opening angle Ψ between the true and reconstructed neutrino direction for different slices of pull corrected $\sigma_{paraboloid}$. The median opening angle ψ is expected to be at 1.177σ for a 2D Gaussian point spread function. The median ψ is shown separately for reconstructions with successful (blue) and failed (red) paraboloid fit. Events are for the seasons IC59 and are weighted to the best fit astrophysical neutrino spectrum.

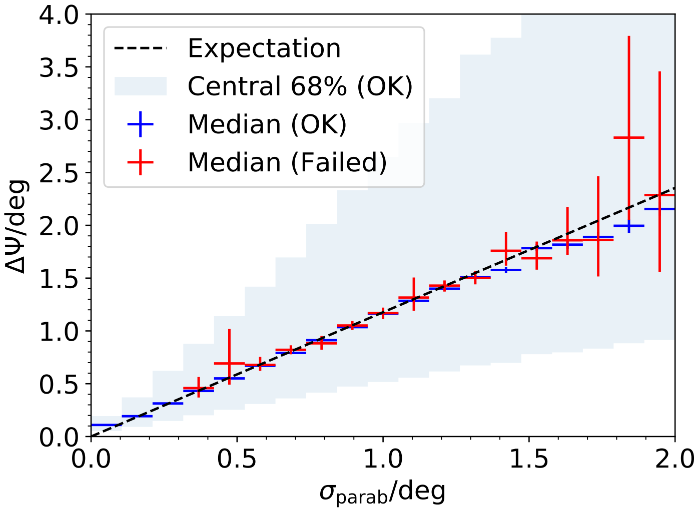

Figure A.20: Same as Fig. A.19 but for the season IC79.

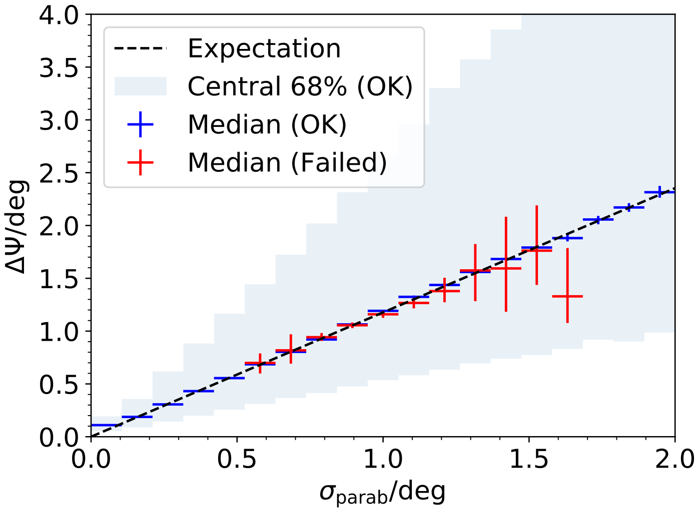

Figure A.21: Same as Fig. A.19 but for the season IC86-2011.

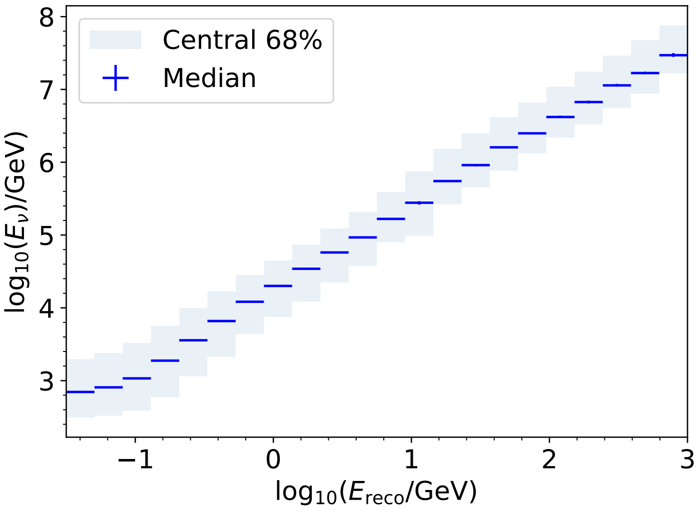

Figure A.22: Median (error bars) and central 68% range (shaded area) of neutrino energy for different slices of reconstructed energy. The IC59 data sample is used and events are weighted to the best fit (atmospheric + astrophysical) spectrum. The muon energy is the muon energy at the entrance of the detector.

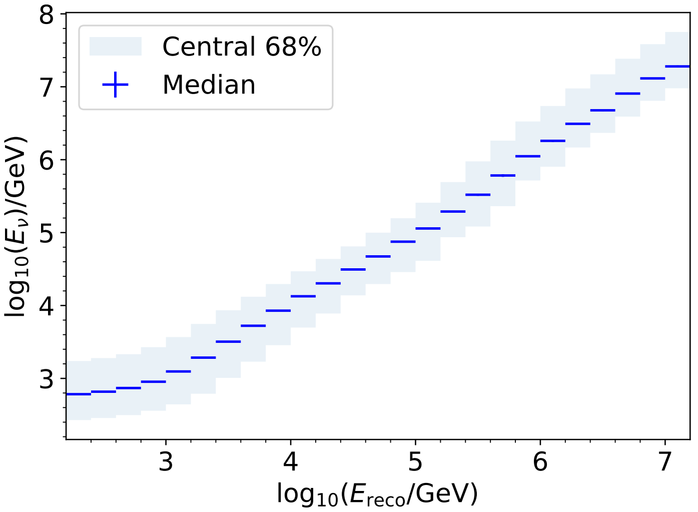

Figure A.23: Same as Fig. A.22 but for the season IC79.

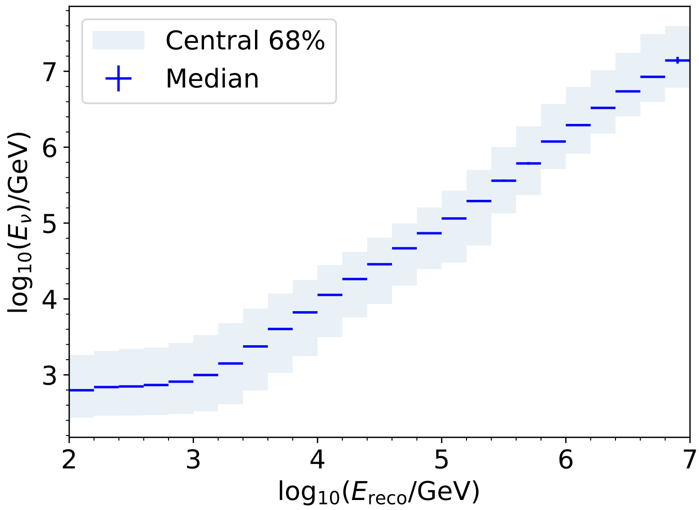

Figure A.24: Same as Fig. A.22 but for the season IC86-2011.

Appendix B

Sample Comparison

In previous searches for point-like sources using data from the IceCube detector [13] uses a different data sample than used in this thesis. In this appendix we will discuss the difference in performance of the two sample.

The different sub-samples used in [13] are listed in Tab. B.1, where the different sub-samples and their individual livetimes are given. In addition a reference is given where the event selection for the sub-sample is described in detail. Note that the event selection for the sub-sample IC79 was update in [230] and used in the later publications.

For a detailed comparison we focus on the sub-sample IC86-2012 as this sample is the latest (and thus most advanced event selection) and has the largest livetime. For a point-source analysis, the performance of the sample can be given by its livetime, the effective area, the point-spread function and the background contamination. For convenience we call the event selection IC86-2012/13/14 from [13] as "PS" and the event selection for IC86-2012/16 used in this thesis as "Diffuse" in this appendix.

The experimental data sample for IC86-2012 contains 69468 and 73553 events using the "Diffuse" and the "PS" event selection, respectively. 57386 events are selected by both event selections, which corresponds to an overlap of 82.6% and 78.0% for the "Diffuse" and the "PS" event selection. Thus 17.4% of the diffuse sample are not in the PS sample and 22.0% of the "PS" sample are not in the diffuse sample.

To compare the event selections in more detail we apply both selections to a common set of Monte Carlo events. Base on this we can sub-divide the selection into three categories: 1. the overlap of the sample which includes events selected by both selections, 2. the exclusive PS sample that contains events that are only selected by the PS selection and 3. the exclusive Diffuse sample that contains events that are only selected by the Diffuse selection. Because both event selections make use of slightly different reconstruction settings, the overlap sample

Season	Livetime	Sample Selection Reference
IC40	376 days	[114]
IC59	348 days	[113]
IC79	316 days	[113, 230]*
IC86-11	333 days	[112]
IC86-12/13/14	1058 days	[13]

Table B.1: IceCube configuration, livetime and reference in which the sample selection is described for the sample used in Ref. [13]. * The IC79 has been revisited after the initial publication.

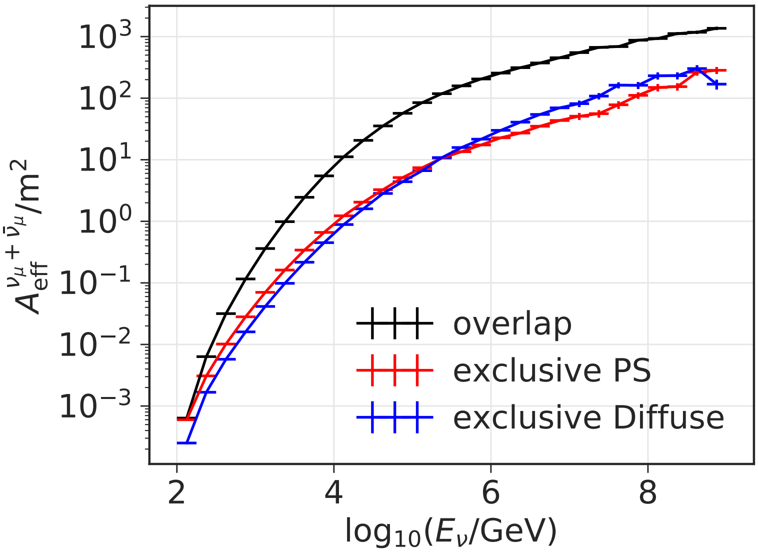

Figure B.1: Muon neutrino and anti-neutrino effective area as function of neutrino energy for the IC86-2012 PS and diffuse data sample. The selection used in this thesis and described in Sec. 5.5.2 and Ref. [5, 154] is labeled as "Diffuse" while the selection used and described in Ref. [13, 258] is labeled as "PS". The overlap of both selections is shown in black while the exclusive parts are shown in red and blue. The effective area is averaged over the Northern Hemisphere (-5° to 90° declination).

has different reconstructions for the PS selection and Diffuse selection.

For the "PS" event selection, the rejection of atmospheric muons at final selection level is stated to be $\sim 99.94\%$ with 90% signal efficiency [13, 258]. This number can be compared to the purity of the "Diffuse" event selection, of $\sim 99.7\%$ [5, 154]. Note to compare these numbers, we have to take the initial ratio of atmospheric muons and neutrinos into account. Assuming a rate difference of two orders of magnitude between atmospheric muons and neutrinos in the Northern hemisphere, the purity of the "PS" event selection is $\sim 93.75\%$[1].

Note that traditionally the "PS" event selection allows for a small background fraction in the data sample and is focused on a selection with maximal signal efficiency. This philosophy is driven by the fact that small background contamination does not reduce the sensitivity to clustering. The "Diffuse" event selection however was developed to maximize the sample purity and puts the signal efficiency at second priority. This difference in priority can be seen in the final sample purity.

The signal efficiency is characterized by the effective area (see Sec. 5.7). The muon neutrino and anti-neutrino effective area averaged over the Northern hemisphere is shown in Fig. B.1 for the overlap of the event selection and the exclusive parts, respectively.

---

[1] Assuming the background and signal rate before the selection is b_1 and s_1 and after the selection is b_2 and s_2, respectively. The background rejection can be defined by $r = 1 - b_2/b_1$, the signal efficiency is $\epsilon = s_2/s_1$ and the purity of the sample after the cut is $p = s_2/(s_2 + b_2) = \frac{1}{1+\frac{1-r}{\epsilon}\frac{b_1}{s_1}}$. Using an rate ration of $b_1/s_1 = 10^2$ after the muon L3, the purity is 93.4%.

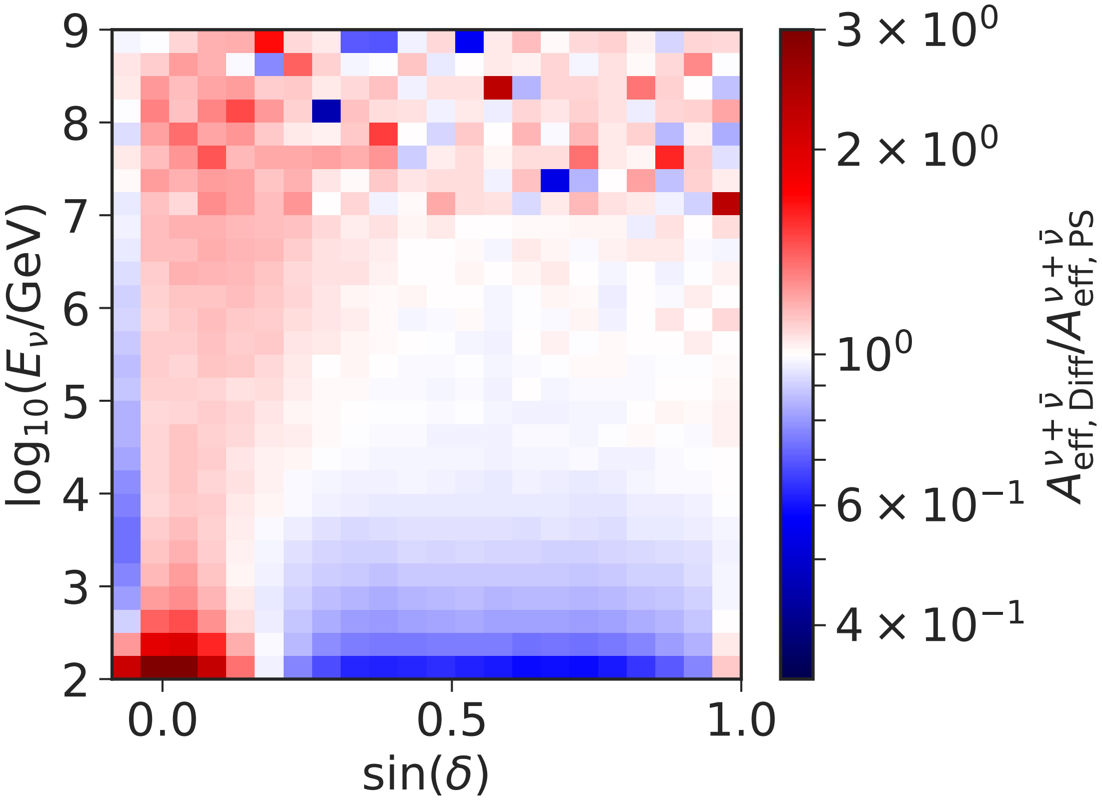

Figure B.2: Ratio of muon neutrino and anti-neutrino effective area for the "PS" and "Diffuse" event selection as function of declination and neutrino energy. The selection used in this thesis and described in Sec. 5.5.2 and Ref. [5, 154] is labeled as "Diffuse" while the selection used and described in Ref. [13, 258] is labeled as "PS". The ratio is plotted such that white colors correspond to equal effective areas, blue corresponds to a larger effective area for the "PS" selection and red corresponds to larger effective area for the "Diffuse" selection.

It can be seen that the dominant fraction of signal events would be contained in both event selections. The exclusive samples have a effective area which is about an order of magnitude reduced compared to the overlap sample. The effective area for the PS exclusive sample is slightly larger at energies below $\sim 100\,\mathrm{TeV}$, while the effective area for the Diffuse exclusive sample is slightly larger above $\sim 100\,\mathrm{TeV}$.

In Fig. B.2 the ratio of the effective areas of the PS and the Diffuse event selection is shown as function of neutrino energy and declination. It can be seen that each event selection has certain regions where the effective area is increased with respect to the other. While the PS event selection has a larger effective area at high declinations and lower energies, as well as at the transition of the hemispheres at -5° declination, the Diffuse event selection has a larger effective area close to the horizon and at energies above 1 PeV.

Another characteristic of the event sample is the point spread function (PSF, see Sec. 5.7). Note that the PSF is effected by both the event selection, due to the selection of event topolo-

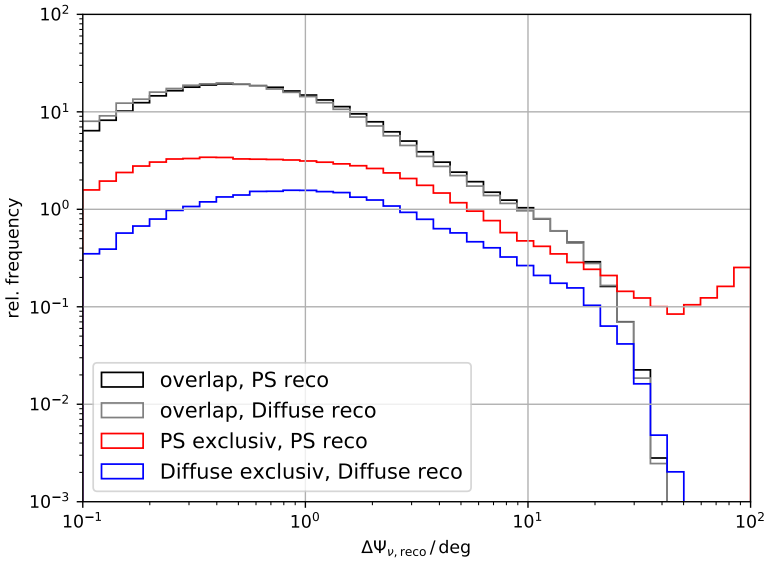

Figure B.3: Point spread function for the "PS" and "Diffuse" event selection and reconstruction. The selection used in this thesis and described in Sec. 5.5.2 and Ref. [5, 154] is labeled as "Diffuse" while the selection used and described in Ref. [13, 258] is labeled as "PS". For the overlap of the sample the point spread function is shown for both reconstructions, while for the exclusive parts of the samples only the available reconstruction is shown.

gies, and the reconstruction algorithm. In Fig. B.3 the PSF is shown for the overlap of the event selection and the exclusive parts, respectively. For the overlap sample, the PSF is shown using once the reconstruction as used in the PS event selection and once the reconstruction as used in the Diffuse event selection. By this comparison the difference in the PSF can only be effected by the reconstruction algorithm. It can be seen, that for the overlap sample the PSF is very similar. For the exclusive samples the PSF is in general slightly larger. Especially the exclusive PS sample PSF shows a long tail with angles $> 40°$. Such a tail does not appear in the diffuse exclusive sample, because the BDT event selection uses only tracks which are better reconstructed within 5° around their true position as signal definition and has a separate BDT to identify cascade like events like corner clippers which have a bad angular resolution.

In Fig. B.4 the median of the PSF is shown as function of neutrino energy. One can see that for the overlap sample the reconstruction associated with the diffuse event selection performs slightly better over all energy. The median PSF of the diffuse reconstruction improves at 10 TeV by about 10% and up to 20% at higher energies with respect to the PS reconstruction. The median PSF of the exclusive samples are much larger than the median PSF of the overlap sample.

For a final comparison we take exactly 365 days of livetime from each event selection and calculate the sensitivity and discovery potential to a point-like source with an E^{-2} power law spectrum. The likelihood function used to calculate the sensitivity and discovery potential is the same as in [13], which uses background PDFs estimated from experimental data, with does not use a prior on the spectral index of the source and does not allow for negative TS values

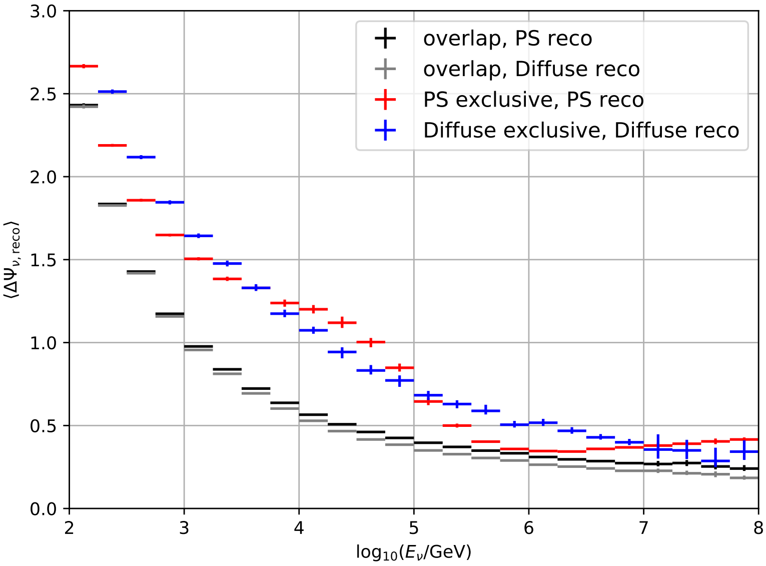

Figure B.4: Median point spread function as function of neutrino energy for the "PS" and "Diffuse" event selection and reconstruction. The selection used in this thesis and described in Sec. 5.5.2 and Ref. [5, 154] is labeled as "Diffuse" while the selection used and described in Ref. [13, 258] is labeled as "PS". For the overlap of the sample the median point spread function is shown for both reconstructions, while for the exclusive parts of the samples only the available reconstruction is shown.

(see Chapter 6).

In Fig. B.5 the sensitivity and discovery potential for 365 days of livetime using the PS and the diffuse event selection is shown. In the upper panel the sensitivity and discovery potential flux is shown as function of declination. The lower panel shows the ratio of sensitivity and discovery potential calculated using the diffuse event selection and using the PS event selection. Note that the computation precision is reduced for this calculation which yields slight fluctuations for different declinations. It can be seen that for all declination the sensitivity and discovery potential flux is reduced if the diffuse event selection is used, except at the transition between the hemispheres at $-5°$ declinations. The mean ratio in discovery potential and sensitivity is 0.865 and 0.867, respectively. With this the sensitivity and discovery potential to point-like sources improves by 13.5% only by change of the event selection. This is mainly a result of the improved angular reconstruction. Note that in addition the effective area close to the horizon is larger (see Fig. B.2) in the diffuse sample, which is also the region where the best sensitivity is reached.

Note that only the PS event selection covers the Southern Hemisphere, which is not discussed here. Also note that due to the larger background contamination of atmospheric muons and problems in modeling this background correctly, no precise parametrization of the PS event selection is available.

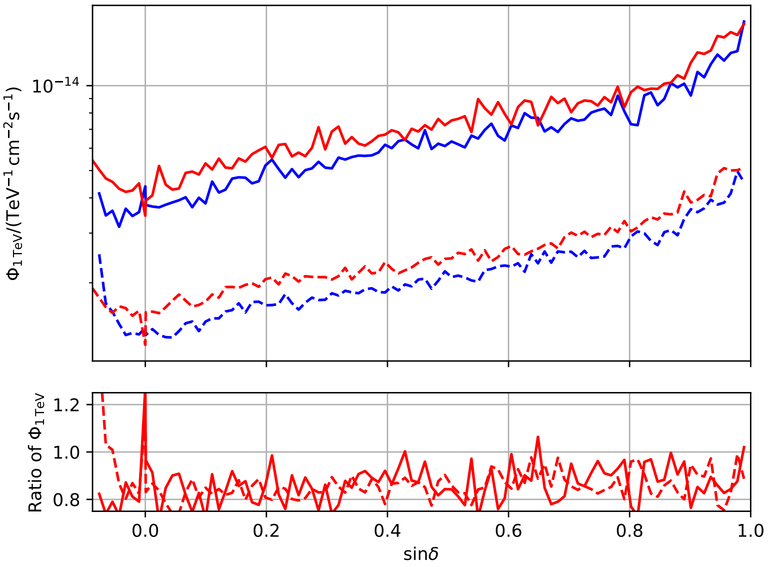

Figure B.5: Sensitivity and discovery potential for 365 days of livetime using the "PS" and "Diffuse" IC86-2012 event selection. The selection used in this thesis and described in Sec. 5.5.2 and Ref. [5, 154] is labeled as "Diffuse" while the selection used and described in Ref. [13, 258] is labeled as "PS". The upper panel shows the sensitivity and discovery potential as function of declination. The lower panel shows the ratio of sensitivities and discovery potentials calculated for both event selections. An E^{-2} power-law is used for the source flux. Fluctuations are due to reduced computational precision.

Appendix C

Estimation of Probability Density Functions for All Seasons

In this appendix we show the probability functions as defined in Sec. 6.2 for the different sub-samples. The PDFs for the seasons IC86-2012/16 are shown in Sec. 6.2. The binning differes for each sub-sample and is given in Tab. 6.1. For more details and an explanation of the shown quantities see Sec. 6.2.

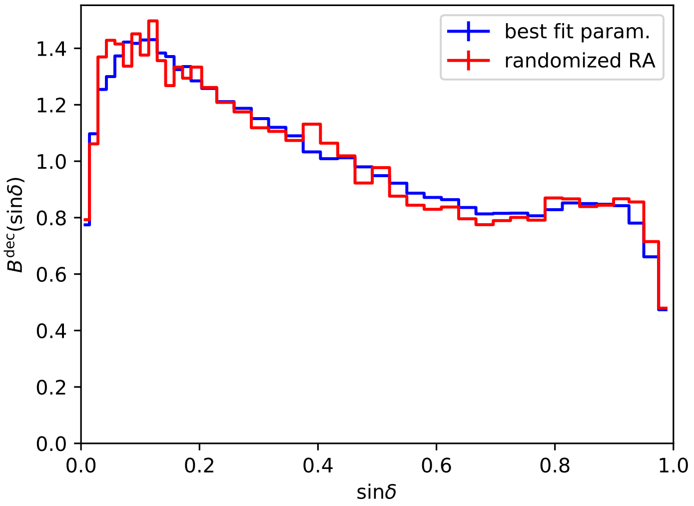

Figure C.1: Spatial background PDF $B^{\mathrm{dec}}(\delta)$ estimated from Monte Carlo for the best-fit parametrization (blue) and experimental data (red) for the season IC59.

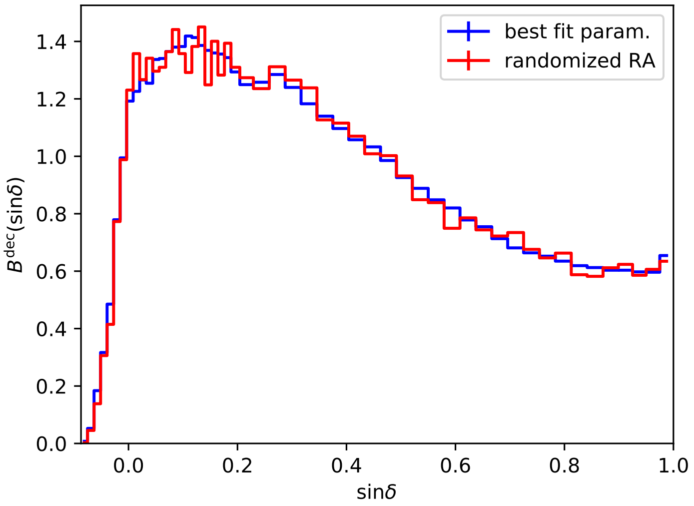

Figure C.2: Same as Fig. C.1 but for the season IC79.

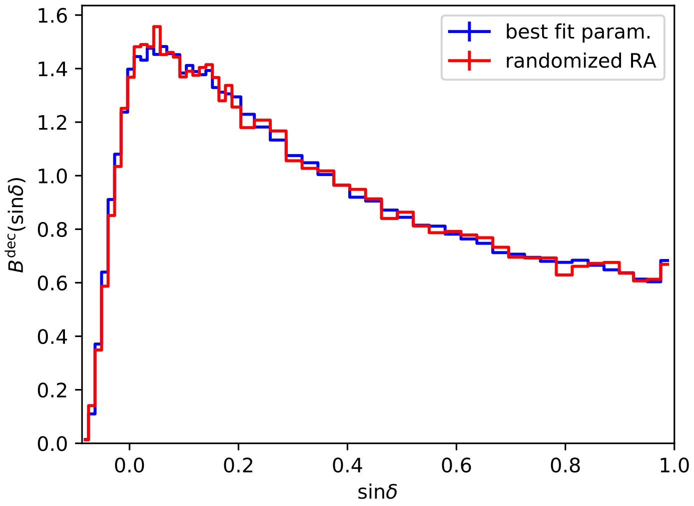

Figure C.3: Same as Fig. C.1 but for the season IC86-2011.

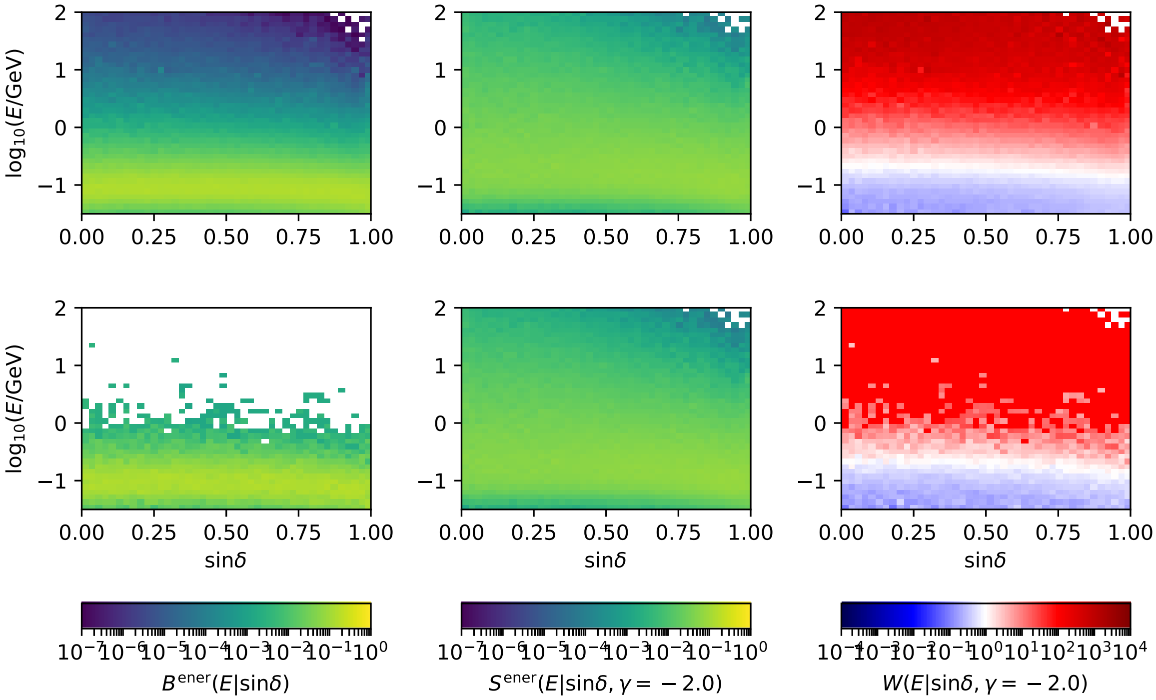

Figure C.4: Background energy PDF $B^{\mathrm{ener.}}(E|\sin\delta)$ (left), signal energy PDF $S^{\mathrm{ener.}}(E|\sin\delta, \gamma = -2.0)$ for a spectral index of $\gamma = -2.0$ (middle) and ratio $W(\gamma = -2.0) = S^{\mathrm{ener.}}(E|\sin\delta, \gamma = -2.0)/B^{\mathrm{ener.}}(E|\sin\delta)$ (right) as a function of $\log_{10}(E/\mathrm{GeV})$ and $\sin\delta$ for the season IC59. The background PDF is estimated from the best-fit parametrization (see Sec. 5.8) (top) and randomized right ascension (bottom).

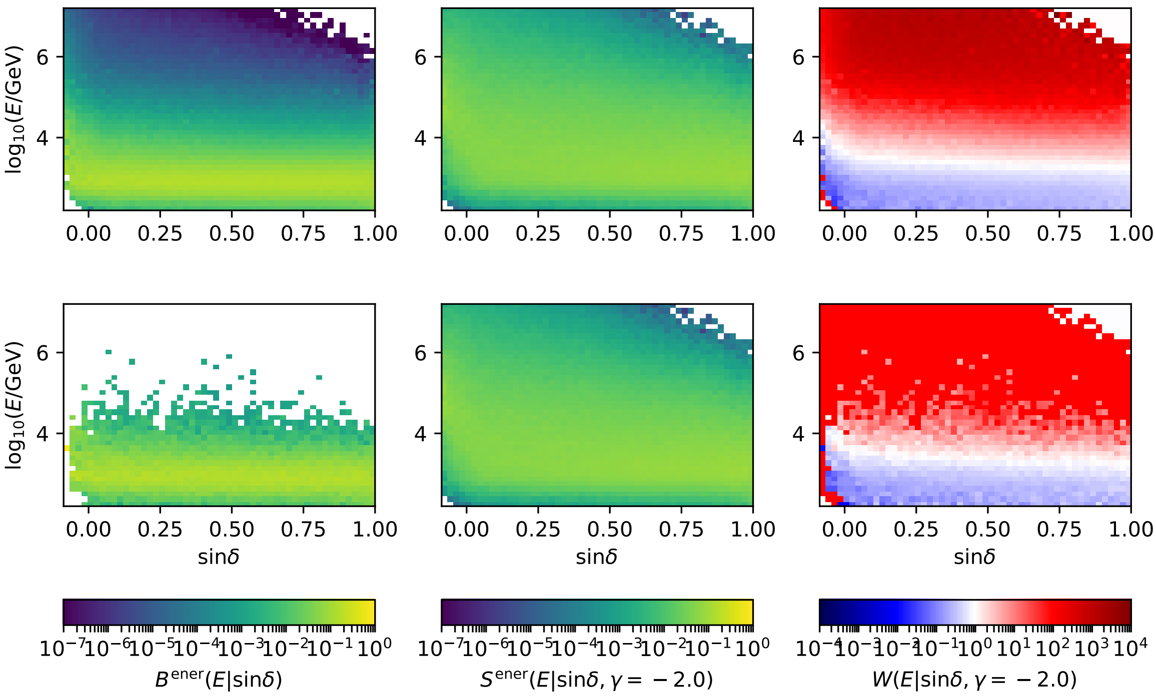

Figure C.5: Same as Fig. C.4 but for the season IC79.

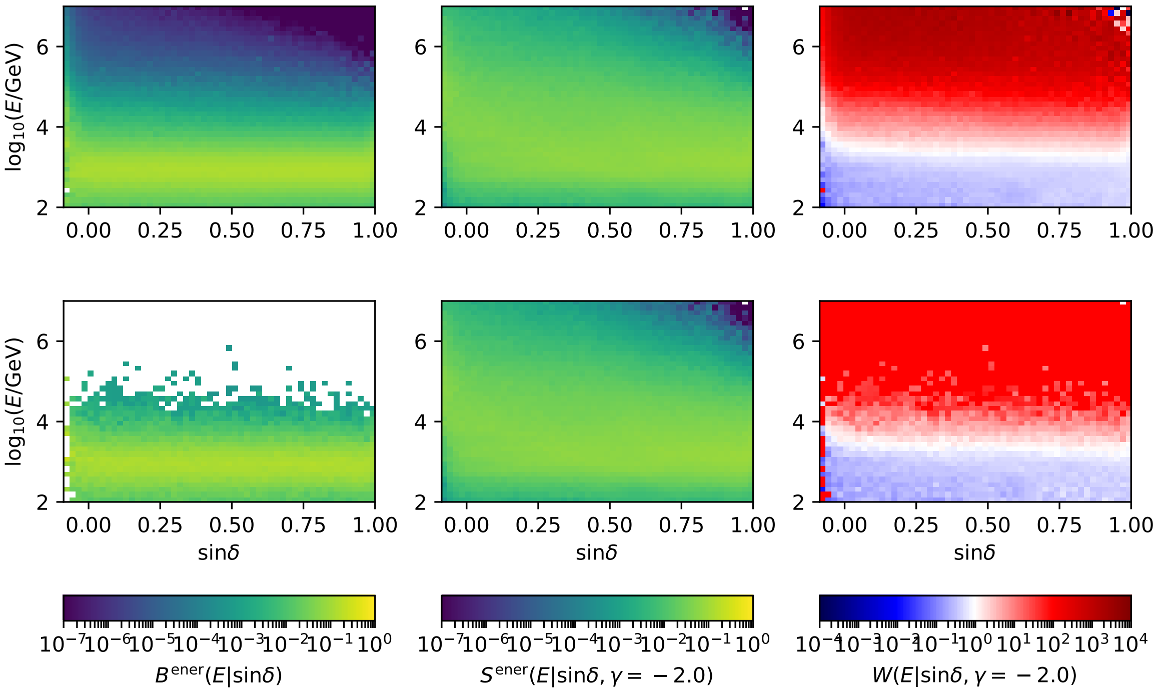

Figure C.6: Same as Fig. C.4 but for the season IC86-2011.

Appendix D

Optimization of the Bandwidth Parameter in Signal Pseudo-Experiment Generation

Within the signal pseudo-experiment generation explained in Sec. 7.1.2, $\Delta \sin \delta$ is the only free parameter, once the source position, spectrum and strength are given. $\Delta \sin \delta$ is the bandwidth of the selected events. To select this band-width there are two concurrent effects. If the bandwidth is chosen too small, only few events are taken into account when picking events for a source. Especially, if the bandwidth is chosen that small that just a handful of events are considered, double picking of events becomes very likely. In addition, the uncertainty on the effective area increases, as also the effective area is calculated within that small declination band. On the other hand, if the bandwidth is chosen to large, the events are no longer representative for the source declination. Correlations between parameters may get distorted. In addition, the effective area is averaged over a too large declination range and thus can be systematically over- or under-estimated.

To choose a reasonable value for $\Delta \sin \delta$, the sensitivity and discovery potential for five different declination are calculated for several $\Delta \sin \delta$ values between $\sin\left(10^{-4}\,\mathrm{deg}\right) < \Delta \sin \delta < \sin\left(10^{1}\,\mathrm{deg}\right)$. In Fig. D.1 (left) the ratio of the sensitivity and discovery flux normalization relative to the sensitivity and discovery flux normalization calculated with $\Delta \sin \delta = \sin(0.1^\circ)$ as a function of $\Delta \sin \delta$ is shown. Note that $\Delta \sin \delta$ translates in a different bandwidth in declination for different declination. From Fig. D.1 (left) it can be seen that with a bandwidth $\Delta \sin \delta \lesssim 5 \cdot 10^{-4}$ statistical fluctuations become large. In the region between $5 \cdot 10^{-4} \lesssim \Delta \sin \delta \lesssim 3 \cdot 10^{-2}$ the ratio becomes relatively flat. For $\Delta \sin \delta \gtrsim 3 \cdot 10^{-2}$ the ratio of sensitivity starts to change, depending on the declination. $\Delta \sin \delta = \sin(1^\circ)$ is chosen as default value, because it is in the region where the flux ratio is still flat but allows for a large sample of events when drawing events.

In Fig. D.1 (right) the sensitivity and discovery potential as a function of declination is shown for two different $\Delta \sin \delta$. The declination values in Fig. D.1 (left) are indicated as vertical lines. The choice of $\Delta \sin \delta$ changes the shape of the curves especially at the horizon and in the celestial pole region. Note that in previous IceCube analysis e.g. in Ref. [13, 258] the larger $\Delta \sin \delta = 0.017$ value has been used. This has to be taken into account when comparing the sensitivity and discovery potential curves.

Because the choice of $\Delta \sin \delta$ is still to some extent arbitrary, a systematic uncertainty on the sensitivity and discovery potential flux has to be taken into account. From Fig. D.1 (left) we find an 8% uncertainty when comparing the sensitivity for $\Delta \sin \delta = \sin(0.1^\circ)$ and $\Delta \sin \delta = \sin(1^\circ)$ and averaged over the five shown declination.

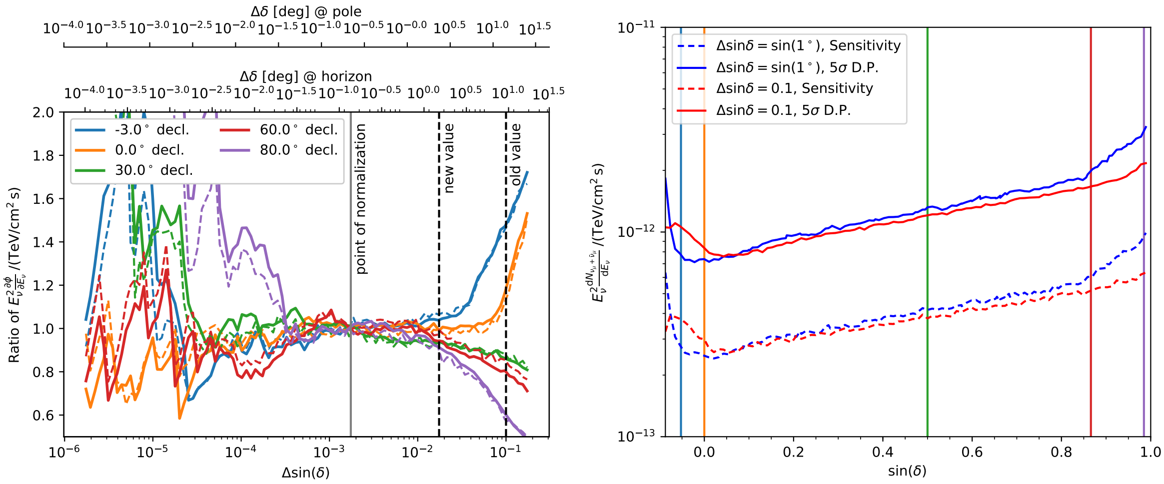

Figure D.1: Sensitivity and discovery potential of flux normalization calculated using pseudo-experiments with different $\Delta \sin \delta$ as a function of $\sin \delta$ (right). The left panel shows the flux normalization ratio relative to the flux normalization calculated with $\Delta \sin \delta = \sin(0.1°)$ for five different declination (see legend). The curves for different declination in the left plot are indicated by colored lines in the right plot.

Appendix E

Derivation: Combination of Differential Fluxes

When testing a celestial position $\vec{x}$ for the existence of a point-like source, the source flux $\phi(E)$ will lead to an excess of neutrino events compared to only background. The number of signal events n_{sens} at *sensitivity* level is defined as the number of events that are needed, so that the 10% quantile of the test statistic distribution is equal to the median of the test statistic distribution in case of only background. Note that n_{sens} is always the same if requiring a certain confidence level, e.g. here the sensitivity.

If the analysis takes the energy information of events into account by weighting high energy events stronger than low energy events, we can use the effective number of events instead of the true number of events. This means that e.g. an event at high energy can effectively count like two events at lower energies. To calculate the number of effective events n_{eff} we weight the events at energy E_ν with a weighting factor $w(E_\nu)$. This weighting factor includes several factors like the effective area, but also the contribution of events with energy E_ν to the analysis response.

Given the neutrino flux $\frac{\mathrm{d}N}{\mathrm{d}E} = \phi(E) = \phi_0 \cdot \hat{\phi}(E)$ of the source, with ϕ_0 the flux normalization and $\hat{\phi}(E)$ the normalized flux distribution (see Fig. E.1 for illustration), the number of effective events is:

$$
\begin{aligned}
n_{\text{eff}} &= \int_0^\infty \phi(E) \cdot w(E)\,\mathrm{d}E && \text{(E.1)}\\
&= \int_0^\infty \phi_0 \cdot \hat{\phi}(E) \cdot w(E)\,\mathrm{d}E && \text{(E.2)}\\
&= \sum_i^{\text{bins}} \int_{E_{\text{min},i}}^{E_{\text{max},i}} \phi_0 \cdot \hat{\phi}(E) \cdot w(E)\,\mathrm{d}E && \text{(E.3)}\\
&= \phi_0 \cdot \sum_i^{\text{bins}} \int_{E_{\text{min},i}}^{E_{\text{max},i}} \hat{\phi}(E) \cdot w(E)\,\mathrm{d}E && \text{(E.4)}\\
&= \phi_0 \cdot \sum_i^{\text{bins}} \int_{E_{\text{min},i}}^{E_{\text{max},i}} \hat{\phi}(E) \cdot w(E)\,\mathrm{d}E \frac{\int_{E_{\text{min},i}}^{E_{\text{max},i}} \hat{\phi}'(E) \cdot w(E)\,\mathrm{d}E}{\int_{E_{\text{min},i}}^{E_{\text{max},i}} \hat{\phi}'(E) \cdot w(E)\,\mathrm{d}E} && \text{(E.5)}\\
&\approx \phi_0 \cdot \sum_i^{\text{bins}} \tilde{w}_i \cdot \int_{E_{\text{min},i}}^{E_{\text{max},i}} \hat{\phi}(E)\,\mathrm{d}E && \text{(E.6)}\\
&\overset{!}{=} n_{\text{sens}} && \text{(E.7)}
\end{aligned}
$$

The sum in Eq. E.3 runs over all energy intervals $[E_{\text{min},i}, E_{\text{max},i}]$, so that the union of all intervals gives the interval $[0, \infty]$.

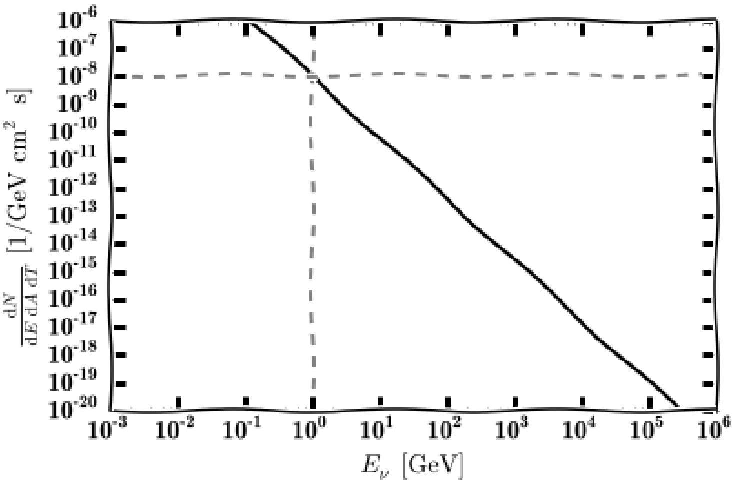

Figure E.1: Neutrino flux spectrum of a point-like source. The normalization of the spectrum can be read of at a pivot energy (gray dashed lines). The flux normalization for which the effective number of neutrinos from the full spectrum is equal to n_{sens} is called *sensitivity*.

The approximation in Eq. E.6 is valid, if $w(E_\nu) \approx \tilde{w}_i = \text{const}$ is nearly constant in the energy interval $[E_{\text{min},i}, E_{\text{max},i}]$. This approximation can be achieved e.g. by small energy bins. If the size of the energy bins is similar to the detector's energy resolution this approximation should hold.

The flux normalization at sensitivity level is defined by $\phi_0 = \phi_{\text{sens}}$ which is determined by requiring that $n_{\text{eff}} \overset{!}{=} n_{\text{sens}}$. Note again that n_{sens} is always the same if requiring a certain confidence level, e.g. here the sensitivity.

The differential sensitivity ϕ^i_{sens} is defined by the sensitivity flux of the spectrum $\phi(E)$ if only the energy range $[E_{\text{min},i}, E_{\text{max},i}]$ contributes (see Fig. E.2 for illustration). Note that the analysis always integrates over all energies and gives a single test statistic value for a specific position. Thus, no matter of the energy range that contributes to the signal flux, the number of effective events to reach the sensitivity level n_{sens} stays the same as the background is integrated over all energies. The differential sensitivity ϕ^i_{sens} is defined by:

$$n_{\text{sens}} \overset{!}{=} \phi^i_{\text{sens}} \cdot \int_{E_{\text{min},i}}^{E_{\text{max},i}} \hat{\phi}'(E) \cdot w(E)\,\mathrm{d}E \tag{E.8}$$

$$\approx \phi^i_{\text{sens}} \cdot \tilde{w}'_i \cdot \int_{E_{\text{min},i}}^{E_{\text{max},i}} \hat{\phi}'(E)\,\mathrm{d}E \tag{E.9}$$

If the same confidence level and thus n_{sens} is used to construct the differential sensitivity and the sensitivity for the full spectrum, Eq. E.5 and Eq. E.8 combine to:

$$\frac{n_{\text{sens}}}{\phi_{\text{sens}}} = \sum_i^{\text{bins}} \frac{n_{\text{sens}}}{\phi^i_{\text{sens}}} \frac{\int_{E_{\text{min},i}}^{E_{\text{max},i}} \hat{\phi}(E) \cdot w(E)\,\mathrm{d}E}{\int_{E_{\text{min},i}}^{E_{\text{max},i}} \hat{\phi}'(E) \cdot w(E)\,\mathrm{d}E}\,. \tag{E.10}$$

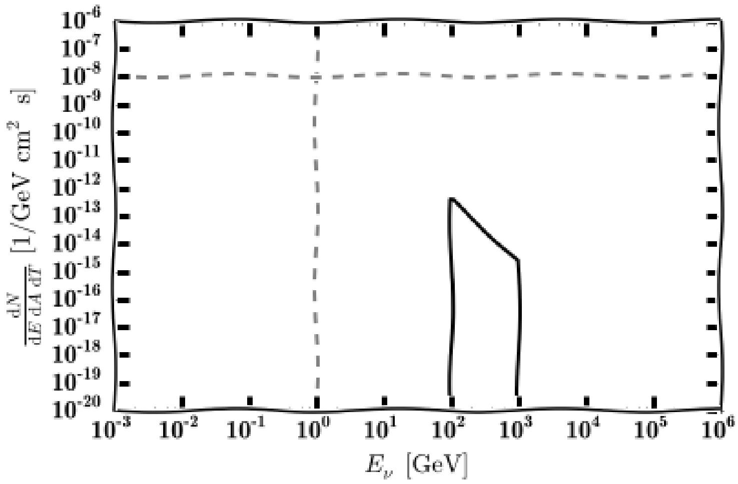

Figure E.2: Spectrum used to determine the *differential* sensitivity ϕ^i_{sens} in the energy interval $[E_{\text{min},i}, E_{\text{max},i}]$.

Note that because the same confidence level and thus the same n_{sens} is required in Eq. E.5 and Eq. E.8, n_{sens} cancels in the above Eq. E.10. The exact value of n_{sens} will depend on the normalization of $w(E)$ and the meaning of n_{eff}. However, because n_{sens} cancels, the exact value is not of interest here.

In case of same spectra $\hat{\phi}(E) = \hat{\phi}'(E)$, Eq. E.10 reduces to:

$$\frac{1}{\phi_{\text{sens}}} = \sum_i^{\text{bins}} \frac{1}{\phi^i_{\text{sens}}} \,. \tag{E.11}$$

In case of different spectra $\hat{\phi}(E) \neq \hat{\phi}'(E)$, we can use the approximation in Eq. E.6 and Eq. E.9 which yields:

$$\frac{1}{\phi_{\text{sens}}} \approx \sum_i^{\text{bins}} \frac{1}{\phi^i_{\text{sens}}} \frac{\tilde{w}_i \cdot \int_{E_{\text{min},i}}^{E_{\text{max},i}} \hat{\phi}(E)\,\mathrm{d}E}{\tilde{w}'_i \cdot \int_{E_{\text{min},i}}^{E_{\text{max},i}} \hat{\phi}'(E)\,\mathrm{d}E} \,. \tag{E.12}$$

Note that because $\hat{\phi}(E) \neq \hat{\phi}'(E)$ also $\tilde{w}_i \neq \tilde{w}'_i$. However, by the same argument as before $\tilde{w}_i \approx \tilde{w}'_i \approx$ const for small energy bins. Thus, we get:

$$\frac{1}{\phi_{\text{sens}}} \approx \sum_i^{\text{bins}} \frac{1}{\phi^i_{\text{sens}}} \underbrace{\frac{\int_{E_{\text{min},i}}^{E_{\text{max},i}} \hat{\phi}(E)\,\mathrm{d}E}{\int_{E_{\text{min},i}}^{E_{\text{max},i}} \hat{\phi}'(E)\,\mathrm{d}E}}_{\equiv k_i} \,. \tag{E.13}$$

Here k_i is a correction factor for each energy interval that depends on the generation spectrum of the differential flux $\phi'(E)$ and the target spectrum $\phi(E)$. There may be better correction factors depending on the exact shape of $w(E)$. However, without further knowledge we have to use Eq. E.13 as an approximation.

Note that k_i can be easily calculated either analytically or numerically for given generation and target spectra. Assuming the generation spectrum $\phi(E)'$ and the target spectrum $\phi(E)$ are power law spectra with spectral indices of $\gamma_1 \neq 1$ and $\gamma_2 \neq 1$ the correction factor k_i can be calculated analytically:

$$k_i = \frac{\gamma_2 - 1}{\gamma_1 - 1} E_0^{\gamma_1 - \gamma_2} \frac{\left(E_{\mathrm{min},i}^{-\gamma_1+1} - E_{\mathrm{max},i}^{-\gamma_1+1}\right)}{\left(E_{\mathrm{min},i}^{-\gamma_2+1} - E_{\mathrm{max},i}^{-\gamma_2+1}\right)} . \tag{E.14}$$

For $\gamma_1 = 2.0$, $\gamma_2 = 3.0$, $E_{\mathrm{min},i} = 10^{4.5}\,\mathrm{GeV}$, $E_{\mathrm{max},i} = 10^{5.0}\,\mathrm{GeV}$ and $E_0 = 10^5\,\mathrm{GeV}$ we get $k_i = 0.480506$. For $\gamma_1 = 2.0$, $\gamma_2 = 3.0$, $E_{\mathrm{min},i} = 10^{4.5}\,\mathrm{GeV}$, $E_{\mathrm{max},i} = 10^{5.0}\,\mathrm{GeV}$ and $E_0 = 1\,\mathrm{GeV}$ we get $k_i = 4805.06$.

Appendix F

TS Parametrization for the All-Sky Scan

For the all-sky scan presented in Sec. 8.1, the test statistic TS has to be parametrized to convert a TS value into a local p-value. Due to the large number of trials and the various declinations tested in an all-sky scan, the generation of TS distributions from pseudo experiments only goes to the computational limit. Therefore, in this appendix we present the parametrization of theses TS distributions.

To construct the parametrization, the TS distributions are generated using $5 \cdot 10^5$ pseudo-experiments for 135 different declinations. The declinations are chosen such that 100 different declinations are equally spread in sine of declination. In addition the declination of sources used in the source list search (see Sec. 8.2) are added. One example of such a TS distribution is shown in Fig. F.1.

Note that in principle one expect that TS follows a χ^2 distribution, however it is found that a χ^2 distribution results in a bad fit to the histogram generated from pseudo experiments. Because we are interested in spots with very small local p-values, for the all-sky scan especially the right tail of the distribution is of interest. The tail of a χ^2 distribution is described by an exponential function. Therefore, an exponential function is fitted to the right tail of the TS distribution which follows this functional behaviour:

$$f(TS) = N \cdot \frac{1}{scale} \exp\left(-\frac{TS}{scale}\right) . \tag{F.1}$$

Note that *scale* is a free fit parameter. The normalization N is given by the fraction of pseudo experiments within the fit range. We define the right tail of the distribution as $TS > 5$.

In Fig. F.1 the fitted exponential function is shown as green solid line. The pull shown in the lower panel looks reasonable within the fit range. Note that only 50% of the pseudo experiments are used in the fitting procedure to allow for an independent sample to verify the goodness of fit.

In Fig. F.2 the fraction of pseudo experiments with $TS > 5$ are shown in the upper left panel. It can be seen that about 1% of all TS values are larger than 5. There is only a week dependence on the declination, except at the ends of the sample close to the pole and the horizon. The fitted scale parameters *scale* are shown with their uncertainties estimated by a profile-likelihood scan, in the upper right panel of Fig. F.2. The *scale* parameter is of the order of 1.8-1.9 and only changes quit slowly with declination.

To determine the goodness of fit, the actual fit is done only on 50% of all pseudo experiments. Thus we have an independent sample with the same statistics. To verify the goodness of fit a Kolmogorov-Smirnov-test [252, 253] is performed using the TS values from pseudo experiments and the best-fit exponential function within the fit range. The p-value resulting

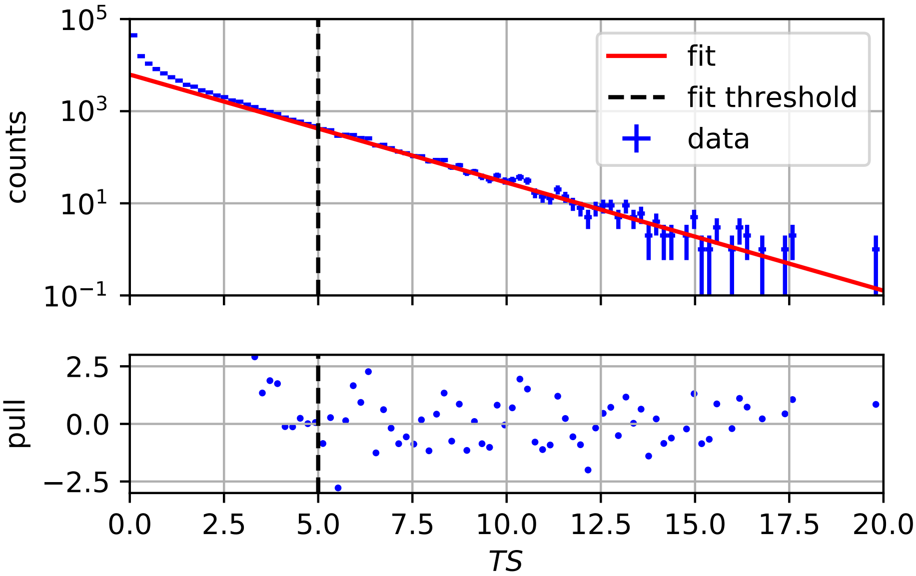

Figure F.1: Background TS distribution for a declination of 5.8°. The histogram of TS values from $5 \cdot 10^5$ pseudo experiments is shown as blue error bars. An exponential function is fitted to the right tail of the distribution with $TS > 5$ and is shown as red solid line. The threshold of $TS = 5$ is indicated by a dashed black line). The lower panel shows the pull of the fit and the histogram. Within the fit region the pull distribution looks reasonable.

from the Kolmogorov-Smirnov-test is shown in Fig. F.2 as a function of declination. The test is carried out two times. Once using the same data sample that was used for the fit and once on the independent data sample. A histogram of the KS-test p-values from the 135 fits is shown in the middle right panel of Fig. F.2. Note that if the sample is a representation of the PDF tested in a Kolmogorov-Smirnov test, we expect that the p-value is uniformly distributed between 0 and 1. However the distribution is slightly skewed to 1 in case that the KS-test is performed on the same data as used for the fit and is slightly skewed to 0 in case that the KS-test is performed on the independent data sample.

This can be understood as follows: The fitted exponential function is not the true PDF but the best-fit estimate of the true PDF, because one parameter is fitted. Thus the best fit estimate will be close but not exactly the correct PDF. In case we use the same data sample as used for the fit, the best-fit estimate will match slightly better than the true distribution, and thus the p-values are slightly skewed to 1, while in case of an independent data sample it is slightly skewed to 0.

This behaviour is tested using a toy Monte Carlo, where we generated 10^5 values following an exponential distribution with scale parameter of 2. 50% of the data are used to fit an exponential function with a free *scale* parameter and a KS-test is performed once on the same and once on the independent data sample. As we also know the true PDF, in addition, we do a KS-test using the true PDF. The histogram of KS-test p-values is shown in Fig. F.3. Note that the behaviour is the same as for our TS parametrization. The exact shape and skewness

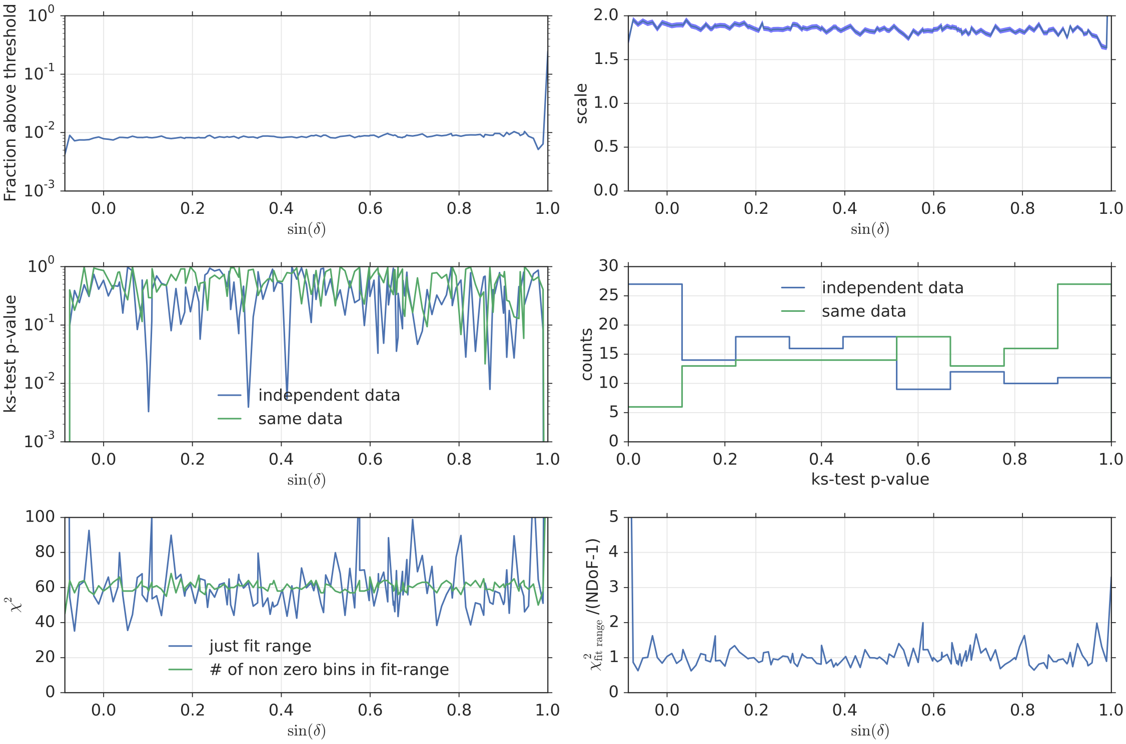

Figure F.2: Parameters and goodness of fit for the TS parametrization of different declinations. The upper left panel shows the fraction of pseudo experiments with $TS > 5$. The upper right panel shows the fitted *scale* parameter where uncertainties estimated from a profile likelihood scan are given as blue shaded band. The middle left panel gives the KS-test probability comparing the fitted distribution with the histogram in the fit region. This test is done on two subsets, once the data used in the fit and once data independent from the fit. The middle right panel is a histogram of all p-values shown in the middle left panel. The lower left panel shows the χ^2 and the number of non zero bins for the different fits and the right lower panel shows the χ^2 per number of degrees of freedom.

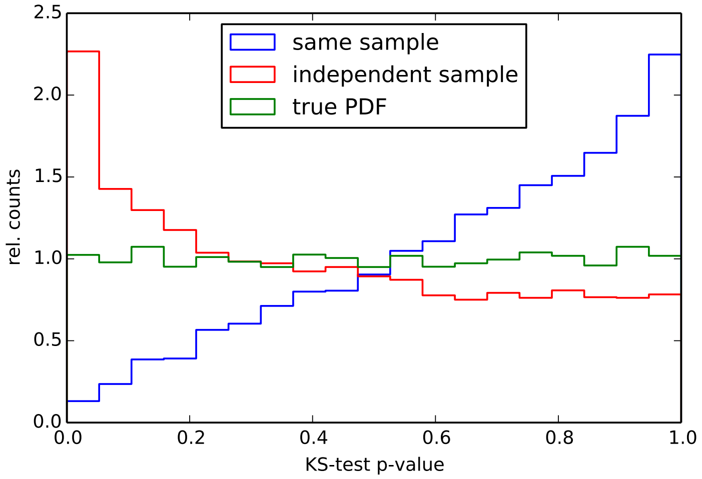

Figure F.3: P-value distribution of KS-test p-values from a toy Monte Carlo. The blue distribution shows the p-values obtained when using a fit function as PDF in the KS-test where the fit function is obtained from the same data. If independent data are used the p-value distribution follows the red histogram. The green distribution gives the p-values obtained if the true distribution is used in the KS-test.

depends on the underling function, the statistics and the number of fit parameters.

In addition to the test for goodness of fit using a Kolmogorov-Smirnov-test, also the χ^2 is calculated in the fit region. The χ^2 and the number of non zero bins are shown in Fig. F.2 in the lower left panel. The χ^2 per degrees of freedom is shown in the lower right panel. It is very close to one and thus indicates a good fit for all declinations.

The fitted exponential is used for $TS > 5$ to extrapolate to very small p-values. The p-values for $TS < 5$ are calculated from trials directly. Note that p-values calculated from trials directly are not very important for the all-sky scan, because due to the large number of trials only locations with local p-values of 10^{-5} and below are important for the hottest spot. Also in the hot spot population analysis (HPA) discussed in Sec. 9.2 only p-values smaller than 10^{-2} are considered.

In Fig. F.4 the local p-value as a function of TS value is shown for a declination of 17.8° declination as an example. The region where the p-value is calculated from trial directly is shown in blue while the region where the p-value is calculated based on the exponential fit is shown in green. Note that due to the choice of normalization of the exponential function we get a continuous distribution.

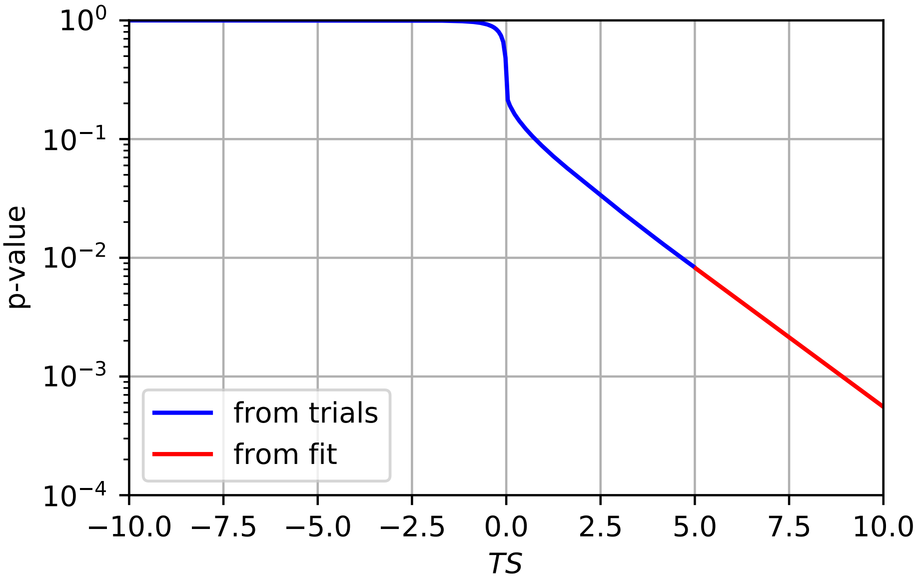

Figure F.4: Local p-value as a function of test statistic value TS for a declination of 5.8°. The region where the p-value is calculated from trials directly is shown in blue while the region where the exponential function is used is shown in red.

Appendix G

Sources in Source List Catalog

In this appendix we list all sources that are tested within the source catalog, tested in Sec. 8.2. For each source we give a short summary of their type, properties and why they are tested to be sources of an astrophysical neutrino flux. In addition we give the test statistic distribution for each source, similar to Fig. 8.6 in Sec. 8.2.1 at the end of this appendix. In this appendix sources are sorted in alphabetic order.

G.1 Description of Sources

1ES 0229+200 is a high-frequency peaked blazar (HBL) at a distance of $z = 0.1396$, that was discovered by H.E.S.S. in 2006 [272]. The X-ray spectrum is very hard and no cut-off is observed up to 100 keV in X-ray, thus 1ES 0229+200 is belongs to the class of extreme blazars. For extreme blazars 1ES 0229+200 has an unusual hard spectrum with a spectral index of ~ 2.5 which extends up to 10 TeV [272, 326]. The test statistic distribution for the declination of 1ES 0229+200 is shown in Fig. G.1.

1ES 1959+650 is a high-frequency peaked blazar (HBL) at a distance of $z = 0.048$ and thus a nearby TeV blazar [272]. It was discovered by Telescope Array in 1999 [272] and was the third BL Lac object for which TeV gamma emission was detected. The flux of 1ES 1959+650 is variable with an average flux of 0.18 crab which reaches during flaring states 0.62 crab and flares on the timescale of several month down to several hundred seconds. In 2004 1ES 1959+650 exhibits an *orphan* gamma-ray flare [272]. Since 2015, 1ES 1959+650 is exhibiting enhanced X-ray activity [327]. The test statistic distribution for the declination of 1ES 1959+650 is shown in Fig. G.2.

1ES 2344+514 is a high-frequency peaked blazar (HBL) at a distance of $z = 0.044$ and thus a nearby TeV blazar [272]. It was discovered by Whipple in 1995 [328]. The gamma-ray flux of 1ES 2344+514 is variable and no steady baseline of very-high-energy gamma-ray emission could be observed, leading to the conclusion that the variable TeV gamma-ray flux origins from a compact region most probably within the jet [272]. The spectrum between 0.8 TeV and 12.6 TeV has a spectral index of ~ -2.5 [328]. The test statistic distribution for the declination of 1ES 2344+514 is shown in Fig. G.3.

3C454.3 is a flat spectrum radio quasar (FSRQ) at a distance of $z = 0.859001 \pm 0.000170$ [273] and is the brightest gamma-ray blazar in the sky [284] and with a maximum absolute magnitude of -31.4 the most luminous object ever observed. It also shows strong flares in radio and visible wavelengths and had a bright flare in June 2014 with an apparent magnitude of 13.4 [285]. The test statistic distribution for the declination of 3C454.3 is shown in Fig. G.4.

3C66A is an intermediate-frequency peaked blazar (IBL) at a distance of $z = 0.34$ [272]. It was discovered by Crimea in 1998 [272]. The flux of 3C 66A is variable on the timescale of days and an optical outburst was observed in 2007. The spectrum in VHE gamma-rays has a soft photon index of 4.1 [329]. The test statistic distribution for the declination of 3C66A is shown in Fig. G.5.

3C 123.0 is a radio galaxy at a distance of $z = 0.2177$. The radio galaxy shows two hot spots on either side of the active nucleus, however the radio structure is peculiar as the lobes take the form of diffuse twisted plumes [330]. For the measured redshift, the radio luminosity is unusually high with $\sim 6\,Jy$ at 5 GHz in the eastern double hotspot, which is the second brightest hotspot complex known [330]. The test statistic distribution for the declination of 3C 123.0 is shown in Fig. G.6.

3C 273 is a flat spectrum radio quasar (FSRQ) and the first ever identified quasar. It has a distance of z=0.158 [331] and is the optical brightest quasar observed. With an absolute magnitude of -26.7 it is one of the most luminous quasars known [332]. 3C 273 was the first extra-galactic source detected in gamma-rays by COS-B observations in 1976. The test statistic distribution for the declination of 3C 273 is shown in Fig. G.7.

4C 38.41 is an optically violent variable flat spectrum radio quasar (FSRQ) at a redshift of $z = 1.813970 \pm 0.000155$ [273, 280]. The gamma-rays flux varies significantly on a day timescale. that had a big optical outburst in 2011 which was also detected in X-ray and in the UV band by Swift and in gamma-rays by Fermi [282, 283]. The test statistic distribution for the declination of 4C 38.41 is shown in Fig. G.8.

BL Lacertae (BL Lac) is an intermediate-frequency peaked blazar (IBL) at a distance of $z = 0.069$ [272]. It was first discovered in 1929 but wrongly assigned to be a variable star. In 1968 it was identified as a bright, variable radio source [333]. Due to its early discovery it is the namesake of the class of AGNs known as *BL Lacertae objects*. Due to its variability the apparent magnitude ranges from 14 to 17. It was discovered in TeV gamma-rays by Crimea in 2001 [272]. The test statistic distribution for the declination of BL Lacertae is shown in Fig. G.9.

Cassiopeia A (Cas A) is a supernova remnant (SNR) at a distance of 3.4 kpc and thus within the Milki Way [272]. It is the brightest extra-solar radio source in the sky at frequencies >1 GHz. Gamma ray emission from Cas A was discovered by HEGRA in 2001 [272]. The gamma-ray peak position deviates from the nominal position of the SNR. The energy spectrum was derived up to 10 TeV and exhibits a spectral index of $\sim$ 2.2 [272]. The test statistic distribution for the declination of Cas A is shown in Fig. G.10.

Crab Nebula is a pulsar wind nebula (PWN) at a distance of 2 kpc. It is the first astronomical object identified with a historical supernova explosion in 1054. The Crab Nebula is the brightest persistent source in the sky. The gamma-ray spectrum extends up to 10 TeV. In 2019 the Tibet ASγ collaboration claimed the first detection of gamma-rays with energies of 100 TeV [334]. The test statistic distribution for the declination of Crab Nebula is shown in Fig. G.11.

Cygnus A (Cyg A) is the closest ultra-luminous radio galaxy [286] with a redshift of $z = 0.056075 \pm 0.000067$ [273] and thus one of the strongest radio sources in the sky. Note that it has not been detected in gamma-rays so far [287]. The lobe of the extended radio jets have a distance of about 0.05° and thus appears point-like for IceCube. The test statistic distribution for the declination of Cyg A is shown in Fig. G.12.

Cyg OB2 is a star cluster of massive stars of the spectral class O and B at a distance of about 1400 pc. It hosts some of the most massive and most luminous stars known. Cygnous OB2 is hidden behind a massive dust cloud and thus obscures the view from Earth. Several surveys in the radio to X-ray wavelength have scanned the region to learn about the processes of star formation. The test statistic distribution for the declination of Cyg OB2 is shown in Fig. G.13.

Cyg X-1 is a galactic X-ray source at a distance of 1900 pc. Its one of the strongest X-ray sources seen from Earth. Cyg X-1 has been observed as a point-like radio source [273]. The spectrum is consistent with synchrotron emission by non-thermal electrons. Cyg X-1 and the supergiant variable star HDE 226868 build a high-mass X-ray binary system with a orbit distance of 0.2 AU [273]. The variability in the X-ray is on the scale of ms. The test statistic distribution for the declination of Cyg X-1 is shown in Fig. G.14.

Cyg X-3 is a high-mass X-ray binary (HMXB) and considered to be a microquasar at a distance of 7.4 kpc. The opening angle of the jet is 14° [86]. Cyg X-3 is also a weak gamma-rays source [335] for which gamma-ray flares can be observed. The test statistic distribution for the declination of Cyg X-3 is shown in Fig. G.15.

Geminga is a pulsar wind nebula (PWN) and forms a TeV halo at a distance of 0.25 kpc [272]. Gaminga has been first discovered in gamma-rays by Milagro in 2009 [272] where it was the first example of an unidentified gamma-ray source. The PWN has an extension of 2.6°. The spectrum extends above 35 TeV. The test statistic distribution for the declination of Geminga is shown in Fig. G.16.

HESS J0632+057 is a high mass x-ray binary (HMXB) at a distance of 1.4 kpc [272]. It is the only binary that has been detected in TeV energies but not at GeV energies, however a GeV counterpart was proposed recently [336]. In gamma-rays the binary has been first detected by

H.E.S.S. in 2007 [272]. The test statistic distribution for the declination of HESS J0632+057 is shown in Fig. G.17.

H 1426+428 is a high-frequency peaked blazar (HBL) at a distance of $z = 0.129$ [272]. It was first detected in gamma-rays by Whipple in 2002 [272]. The flux of H1426+428 is variable. At its detection in 2002, it was the most distant source detected in TeV gamma-rays [337]. The test statistic distribution for the declination of H 1426+428 is shown in Fig. G.18.

IC 443 is a supernova remnant (SNR) at a distance of 1.5 kpc [272]. The SNR has an extension of 0.16° and was first detected in TeV gamma-rays by MAGIC in 2007. It is one of the first sources for which a characteristic poin-decay signature was observed in the energy spectrum [43]. The test statistic distribution for the declination of IC 443 is shown in Fig. G.19.

LS I +61 303 is a binary system containing a compact object. It is a microquasar with periodic bursts at a distance of 2 kpc [272] and first discovered in TeV gamma-rays by MAGIC in 2006. The period is about 26.5 days [338]. At each orbit one radio outburst occurs whose amplitude is modulated with a long-term period of more than 4 yr [338]. The test statistic distribution for the declination of LS I +61 303 is shown in Fig. G.20.

M82 is a starburst galaxy at a distance of 3900 kpc [272] and thus the closest starburst galaxy to Earth. M82 is on average about five times and in the center about 100 times more luminous than the Milky Way. The starburst activity may be triggered by interaction with the neighboring galaxy M81. The test statistic distribution for the declination of M82 is shown in Fig. G.21.

M87 is a Fanaroff-Riley I supergiant galaxy at a distance of $z = 0.0044$ [272]. Its one of the most massive galaxies in the observable universe and exhibits a jet of energetic plasma. M87 is one of the brightest radio sources in the sky. It was first discovered in TeV gamma-rays by HEGRA in 2003 [272]. The energy spectrum has an spectral index varying with time between 2.2 and 2.9 [272]. The test statistic distribution for the declination of M87 is shown in Fig. G.22.

MGRO J1908+06 is a galactic extended TeV gamma-ray emission region with a standard deviation of $\sigma_{\mathrm{src}} = 0.44° \pm 0.02°$ [272, 281]. It can be attributed to the pulsar PSR J1907+0602 at a distance of 3.2 kpc or the supernova remnant G40.5-0.5 at a distance of 3.4 kpc. It is one of few sources that have been detected in gamma-rays above 56 TeV by HAWC [288] and has been proposed to be a detectable neutrino source, e.g. in [289]. The test statistic distribution for the declination of MGRO J1908+06 is shown in Fig. G.23.

MGRO J2019+37 is a pulsar wind nebula (PWN) at a distance 1-2 kpc[272, 339]. The gamma-ray emission region has an extension of 0.75° [272]. MGRO J2019+37 was discovered in TeV gamma-rays by Milagro in 2007. Its flux at 20 TeV is similar to the flux of Crab [339].

The spectrum is best fitted by a power law with spectral index of ~ 2.0 and a cut off at 29 TeV [272]. The test statistic distribution for the declination of MGRO J2019+37 is shown in Fig. G.24.

Markarian 421 (Mrk 421) is a high-frequency peaked blazar (HBL) at a distance of $z = 0.031$ [272] and thus one of the closest blazars to Earth and one of the brightest quasar in the sky. Markarian 421 was discovered in TeV gamma-rays by Whipple in 1992. Its flux is highly variable and changes by up to a factor of 24 [272]. The energy spectrum has a spectral index of 2.2 and shows evidence for an exponential cut off [272]. The test statistic distribution for the declination of Markarian 421 is shown in Fig. G.25.

Markarian 501 (Mrk 501) is a high-frequency peaked blazar (HBL) at a distance of $z = 0.034$ [272] and thus one of the closest blazars to Earth and the brightest quasar in the sky. Markarian 501 was discovered in TeV gamma-rays by Whipple in 1996. The flux if Markarian 501 is variable. The energy spectrum in quiescent state follows a power law with spectral index of ~ 2.7 [272]. The test statistic distribution for the declination of Markarian 501 is shown in Fig. G.26.

NGC 1275 is a Fanaroff-Riley I galaxy at a distance of $z = 0.017559$ [272] and corresponds to the radio galaxy Perseus A at the center of the Perseus cluster of galaxies. NGC 1275 was discovered in TeV gamma-rays by MAGIC in 2010 during a period of increased high gamma-ray activity. The spectrum has a spectral index of ~ 4. The test statistic distribution for the declination of NGC 1275 is shown in Fig. G.27.

PKS 0235+164 is a blazar at a distance of $z = 0.94$ [340]. PKS 0235+164 shows a violent variability with amplitudes larger than 1 mag. It exhibits radio burst regularly with a periodicity of ~ 5.7 yr [340]. PKS 0235+164 was observed in gamma-rays e.g. by EGRET with a power law flux with spectral index 1.85 [341]. The test statistic distribution for the declination of PKS 0235+164 is shown in Fig. G.28.

PKS 0528+134 is a blazar at a distance of $z = 2.07$ [273]. It is one of the most luminous active galactic nuclei with a high flux from radio, through infrared and has been measured in gamma-rays e.g. by EGRET [342]. The flux shows high variability with intensity variations of a factor of 20. The spectrum follows a power law with differential photon spectral index between 1.5 and 2.7 [342]. The test statistic distribution for the declination of PKS 0528+134 is shown in Fig. G.29.

PKS 1502+106 is a flat spectrum radio quasar (FSRQ) at a distance of $z = 1.8385$ [273]. It shows significant variability in the x-ray and gamma-ray bands. In 2008 Fermi measured a rapid and strong gamma-ray outburst followed by a variable flux in the following month [276]. The test statistic distribution for the declination of PKS 1502+106 is shown in Fig. G.30.

S5 0716+71 is an intermediate-frequency peaked blazar (IBL) at a distance of $z = 0.31$ [272]. It was first discovered in TeV gamma-rays by MAGIC in 2008. It is one of the most active blazars showing a variable flux with two high states in January and February 2015. The spectrum follows a power law with a spectral index of ~ 3.45 [272]. The test statistic distribution for the declination of S5 0716+71 is shown in Fig. G.31.

SS 433 is a steady galactic microquasar and a binary system at a distance of 5.5 kpc [272]. The gamma-ray emission is localised in two different regions corresponding to the lobes of SS 433 and was discovered in TeV gamma-rays by HAWC [292]. It is the only microquasar with a confirmed proton component in the jet by observation of the Doppler-shifted H_α-line [86]. It's distance is about 3kpc, the velocity within the jets is about 0.3c and the opening angle is about 79°. It is surrounded by a diffuse nebula W50 [86]. The test statistic distribution for the declination of SS 433 is shown in Fig. G.32.

TYCHO is a supernova remnant (SNR) shell at a distance of about 3.5 kpc [272]. The remnant corresponds to a supernova observed in 1572. It has been discovered in TeV gamma-rays by VERITAS in 2010. The spectrum follows a power law with spectral index of 1.95 [272]. The test statistic distribution for the declination of TYCHO is shown in Fig. G.33.

W Comae is an intermediate-frequency peaked blazar (IBL) at a distance of $z = 0.102$ [272]. It was first discovered in TeV gamma-rays by VERITAS in 2008. The blazar shows a spectrum following a power law with spectral index of 3.81 and time variability [272]. The test statistic distribution for the declination of W Comae is shown in Fig. G.34.

G.2 Background Test Statistic Distributions for Sources in the Source Catalog

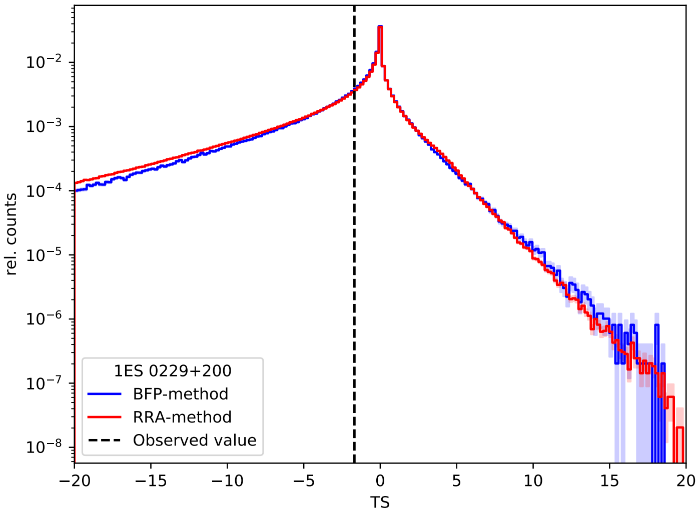

Figure G.1: Background test statistic (TS) distribution for 1ES 0229+200. The blue histogram uses the best-fit parametrization (BFP) method to generate background pseudo experiments, while the red histogram is based on the randomized right ascension (RRA) method (see Sec. 7.1). Statistical uncertainties due to limited statistics are indicated by the blue and red shaded regions. The observed test statistic value is indicated by a black vertical line.

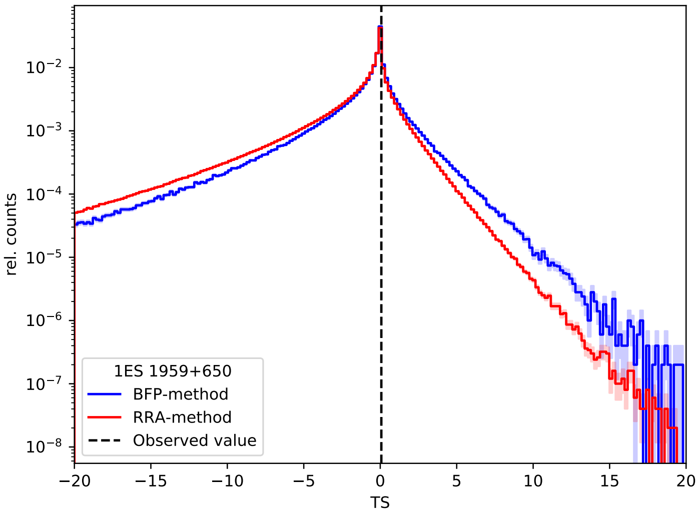

Figure G.2: Same as Fig. G.1 but for 1ES 1959+650.

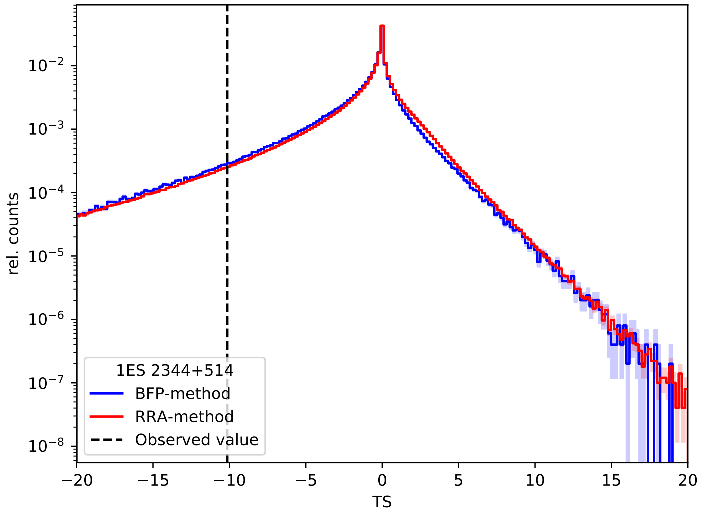

Figure G.3: Same as Fig. G.1 but for 1ES 2344+514.

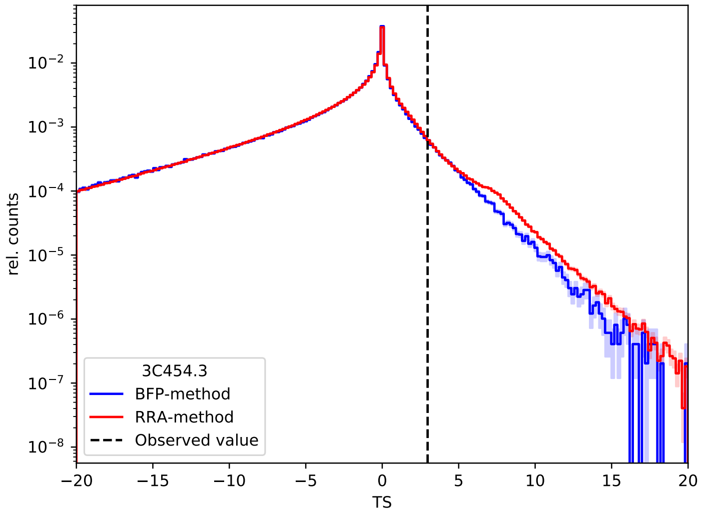

Figure G.4: Same as Fig. G.1 but for 3C454.3.

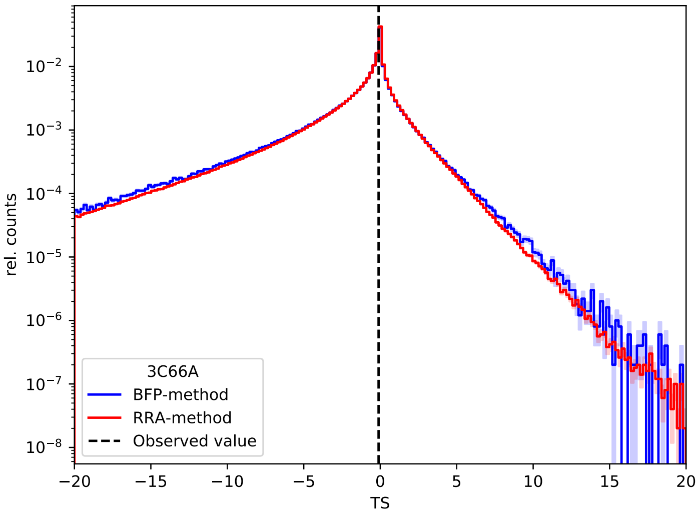

Figure G.5: Same as Fig. G.1 but for 3C66A.

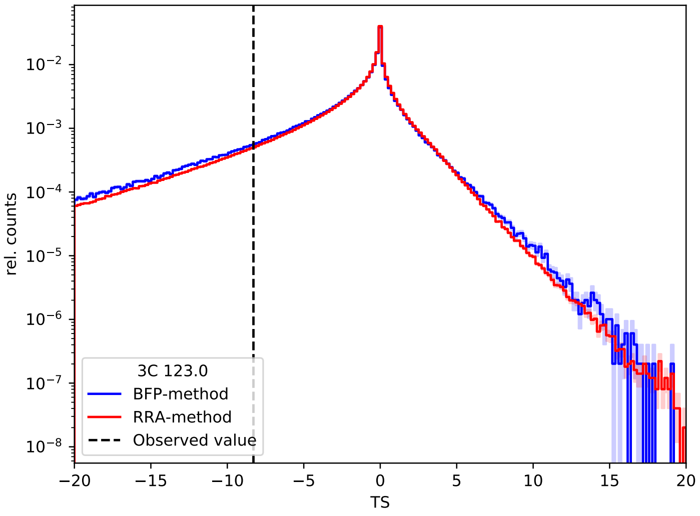

Figure G.6: Same as Fig. G.1 but for 3C 123.0.

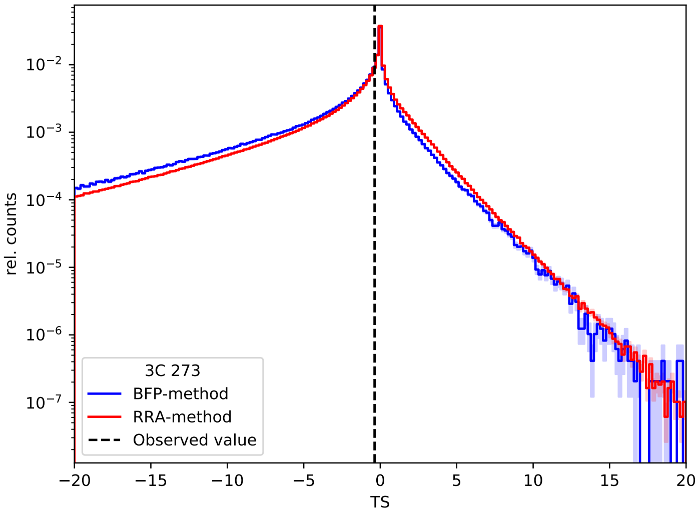

Figure G.7: Same as Fig. G.1 but for 3C 273.

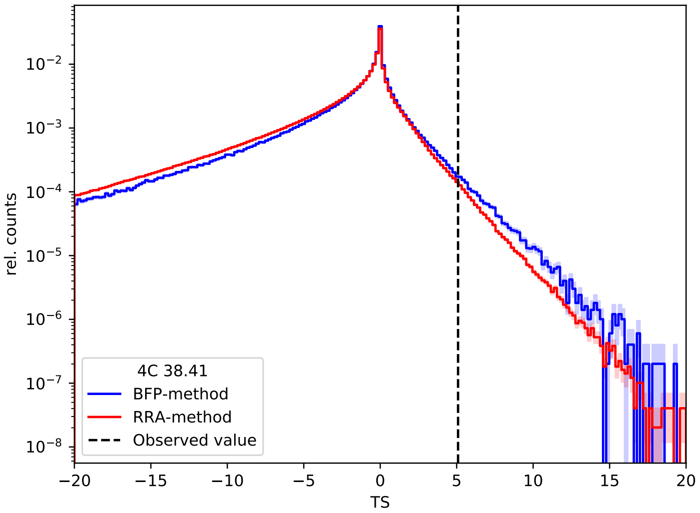

Figure G.8: Same as Fig. G.1 but for 4C 38.41.

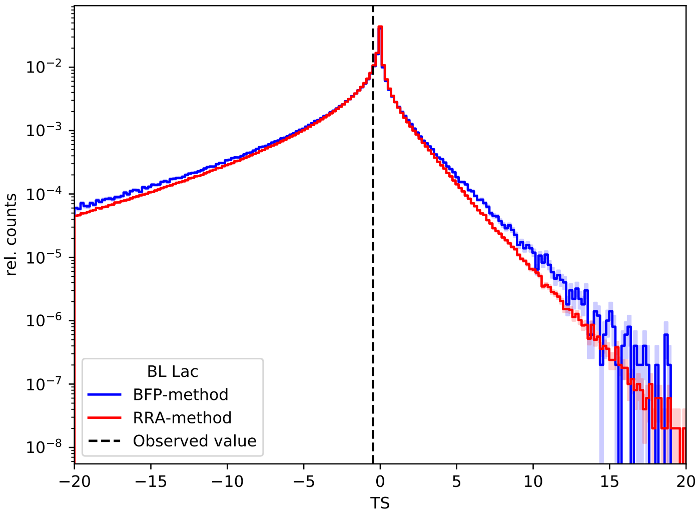

Figure G.9: Same as Fig. G.1 but for BL Lac.

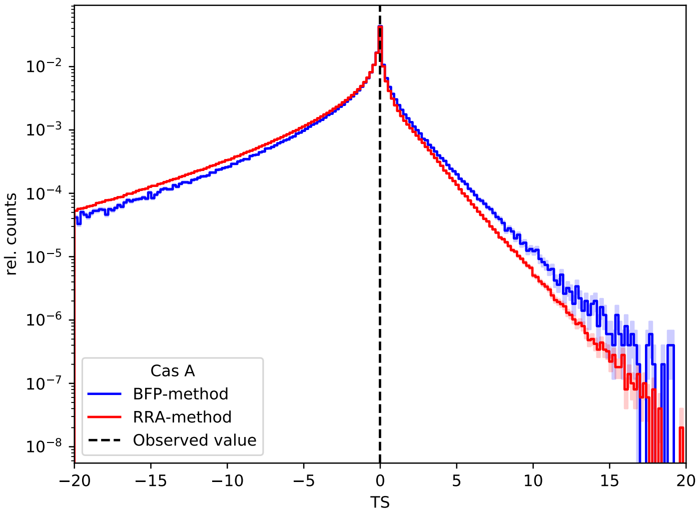

Figure G.10: Same as Fig. G.1 but for Cas A.

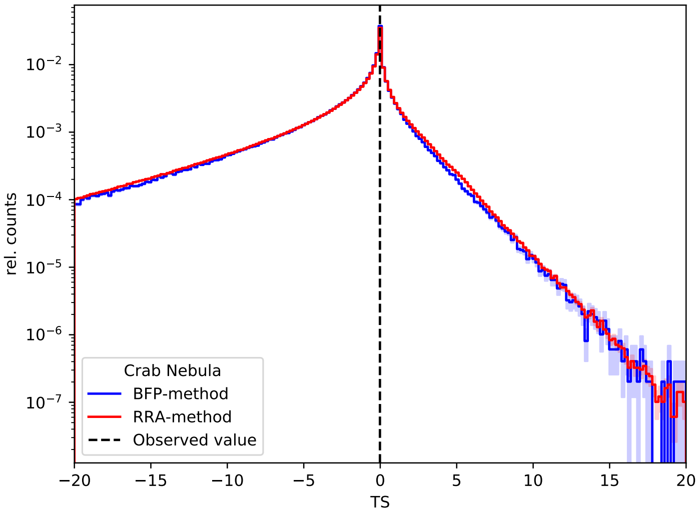

Figure G.11: Same as Fig. G.1 but for Crab Nebula.

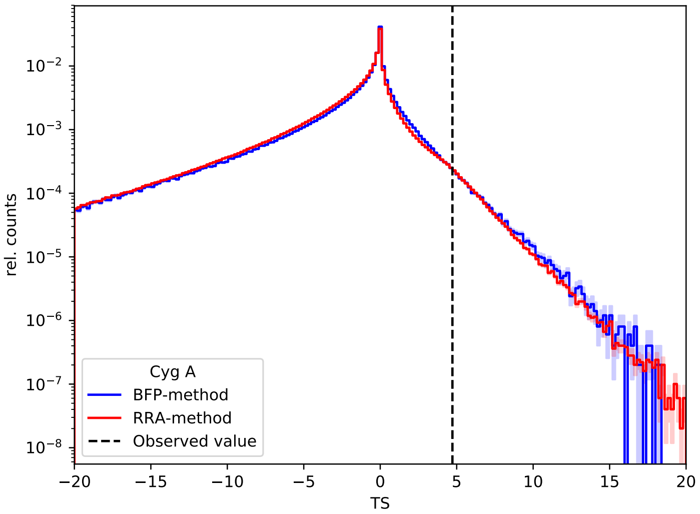

Figure G.12: Same as Fig. G.1 but for Cyg A.

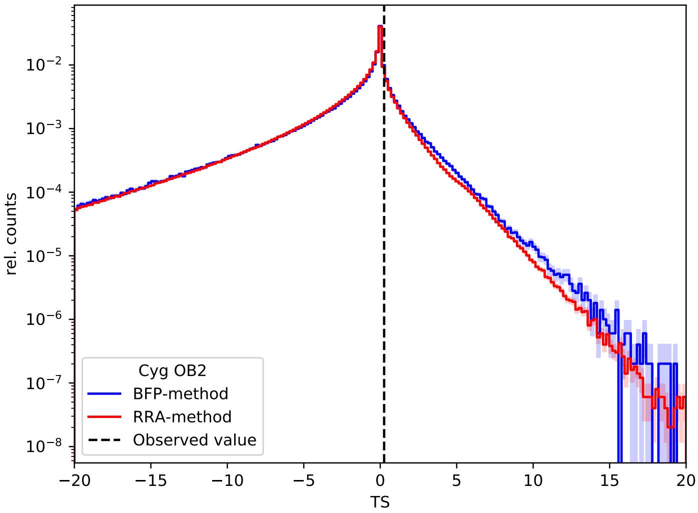

Figure G.13: Same as Fig. G.1 but for Cyg OB2.

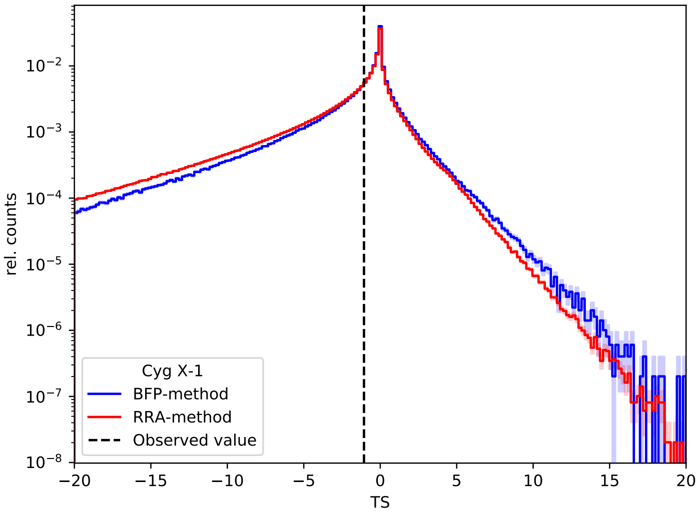

Figure G.14: Same as Fig. G.1 but for Cyg X-1.

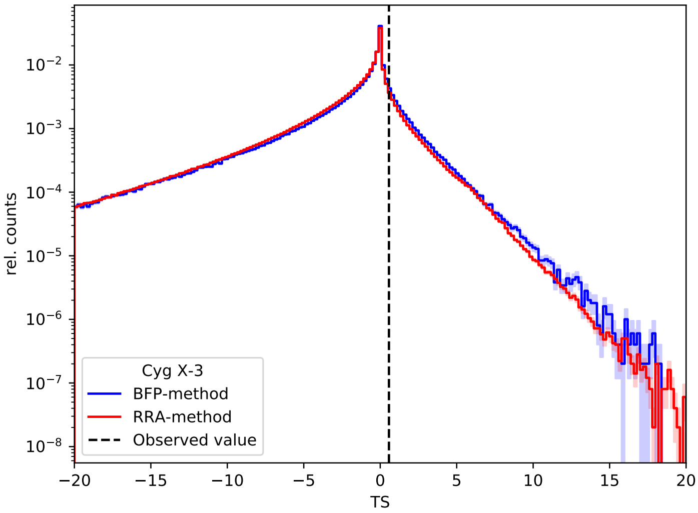

Figure G.15: Same as Fig. G.1 but for Cyg X-3.

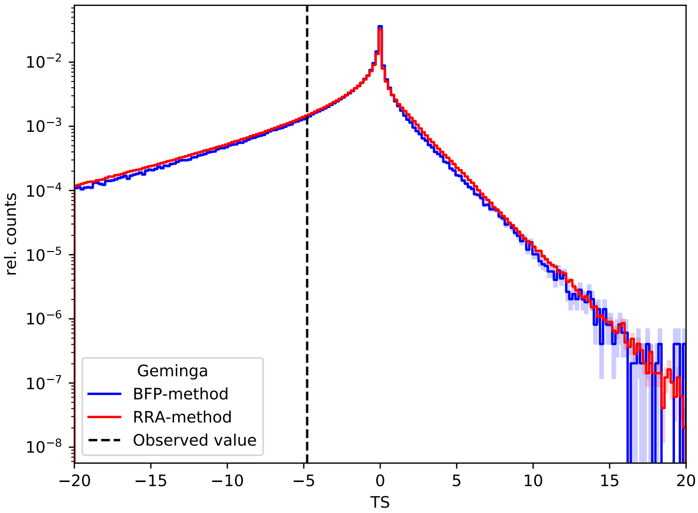

Figure G.16: Same as Fig. G.1 but for Geminga.

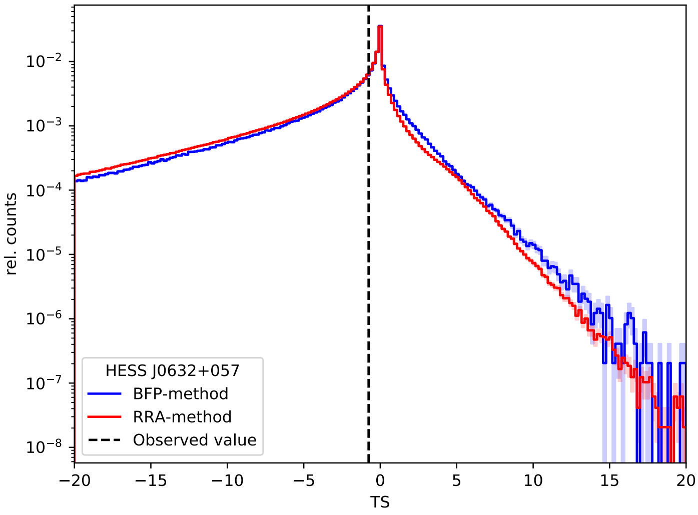

Figure G.17: Same as Fig. G.1 but for HESS J0632+057.

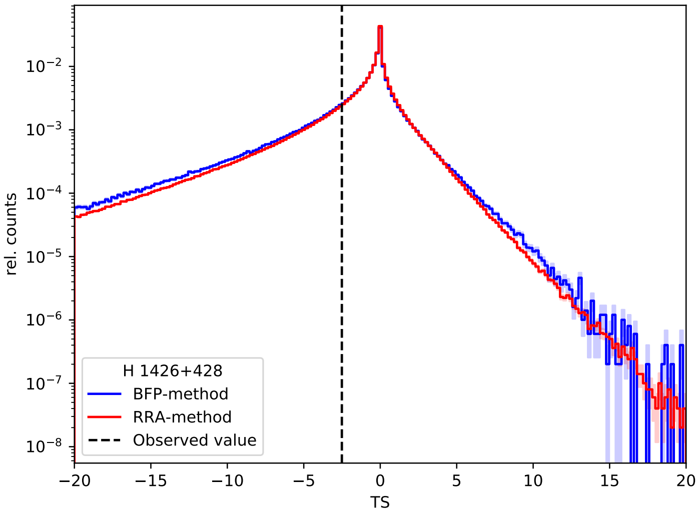

Figure G.18: Same as Fig. G.1 but for H 1426+428.

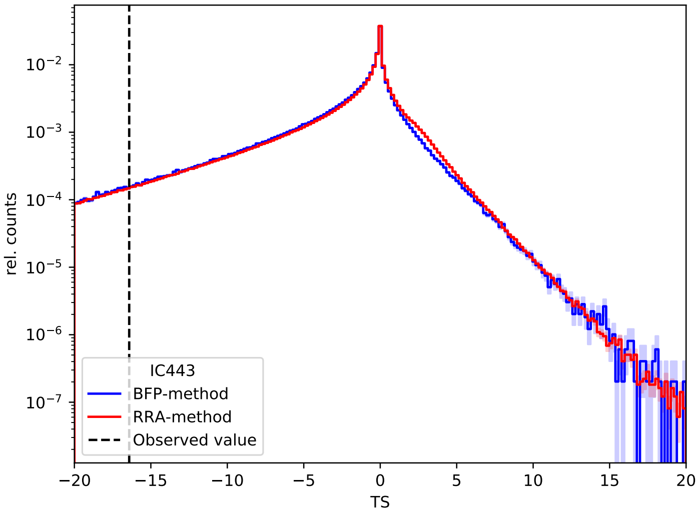

Figure G.19: Same as Fig. G.1 but for IC443.

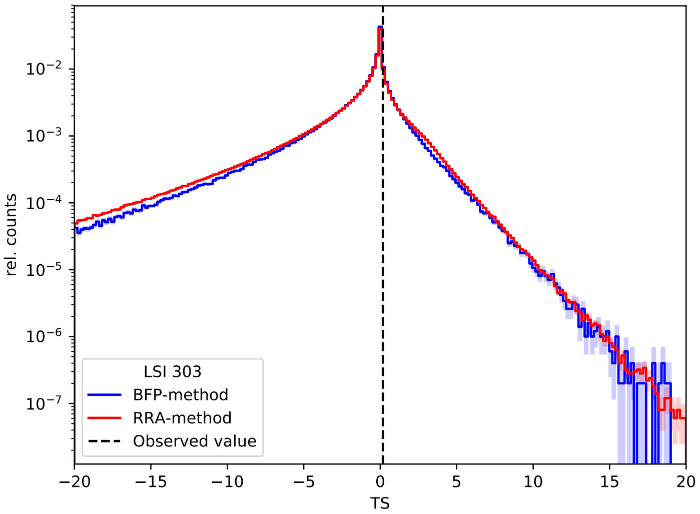

Figure G.20: Same as Fig. G.1 but for LSI 303.

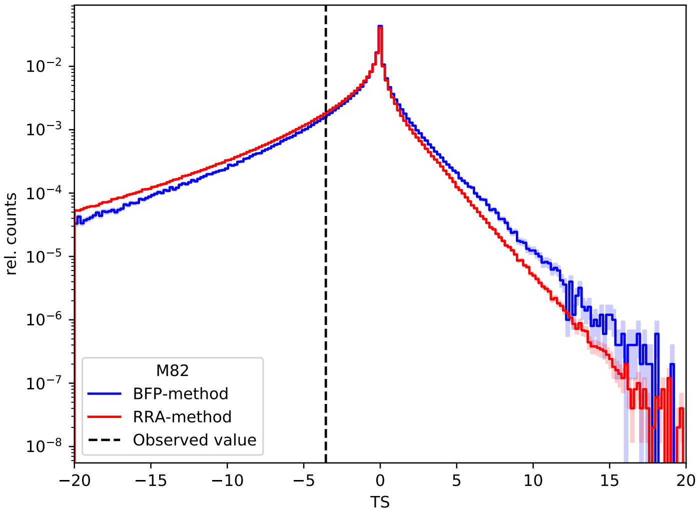

Figure G.21: Same as Fig. G.1 but for M82.

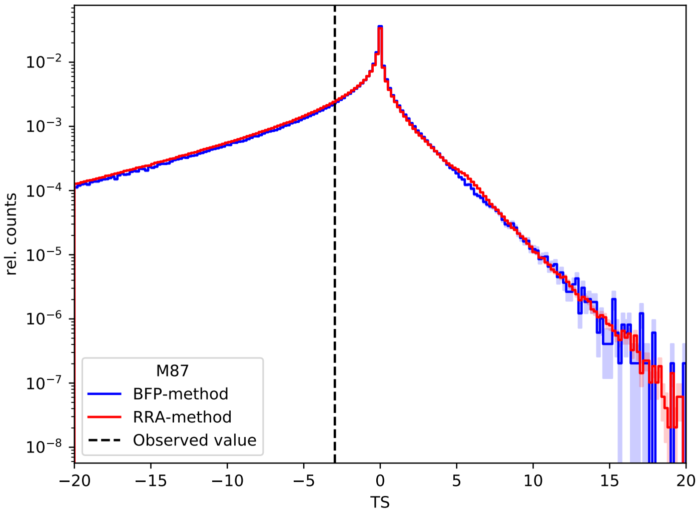

Figure G.22: Same as Fig. G.1 but for M87.

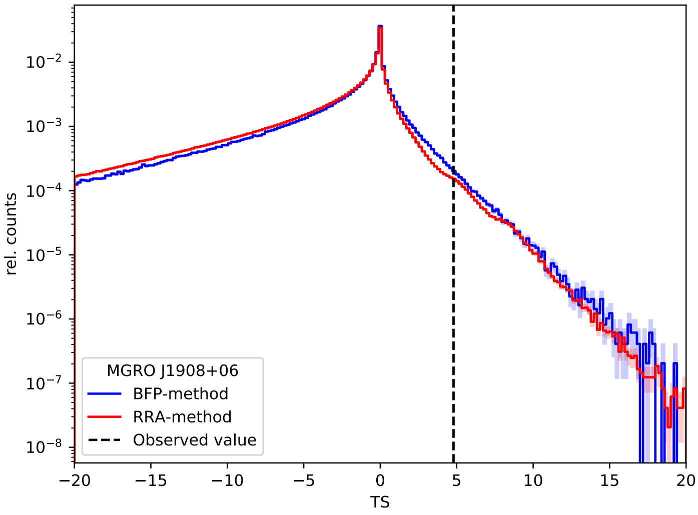

Figure G.23: Same as Fig. G.1 but for MGRO J1908+06.

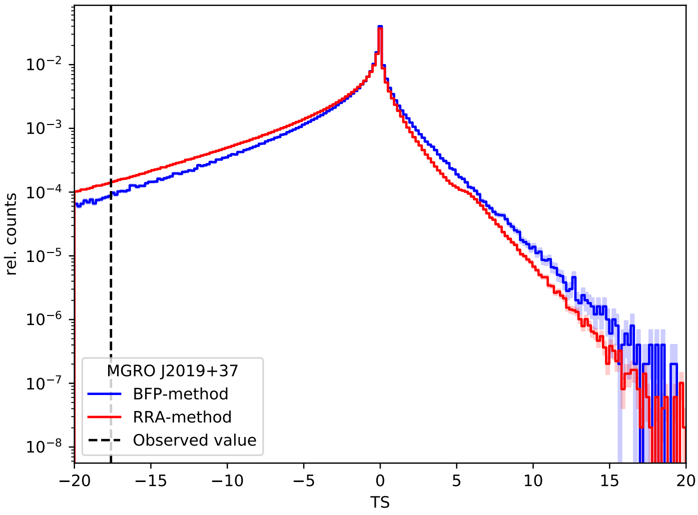

Figure G.24: Same as Fig. G.1 but for MGRO J2019+37.

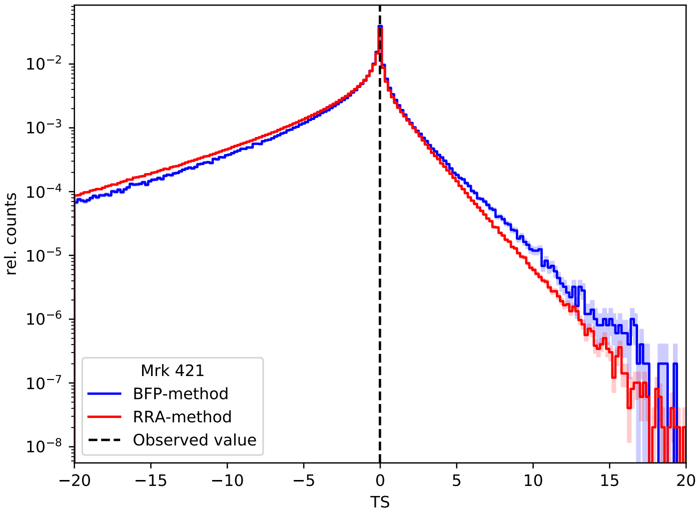

Figure G.25: Same as Fig. G.1 but for Mrk 421.

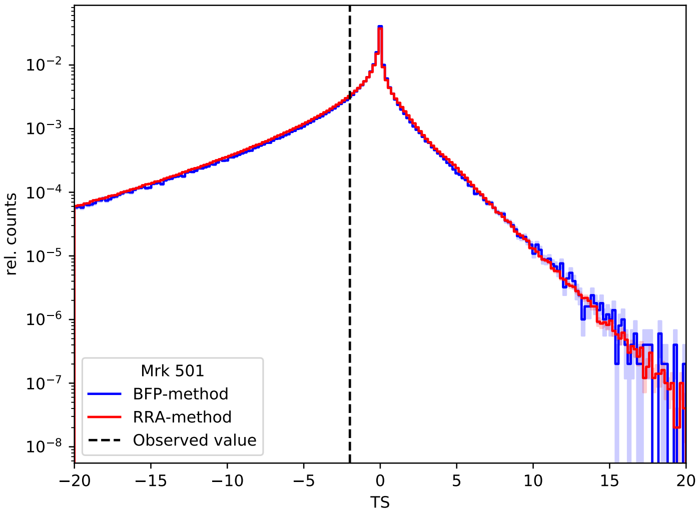

Figure G.26: Same as Fig. G.1 but for Mrk 501.

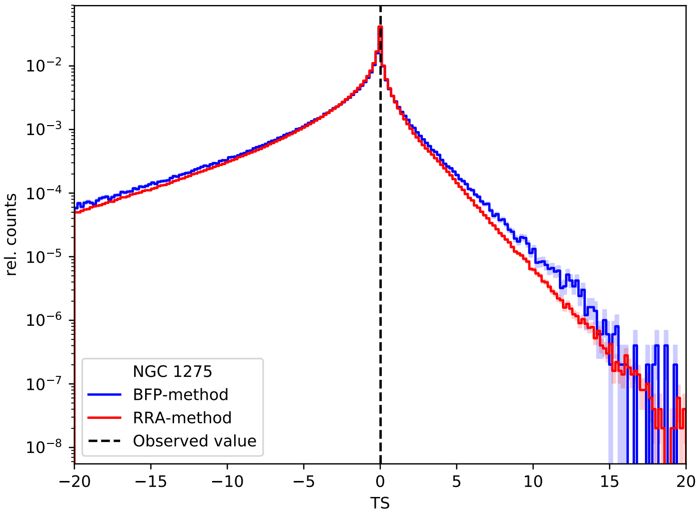

Figure G.27: Same as Fig. G.1 but for NGC 1275.

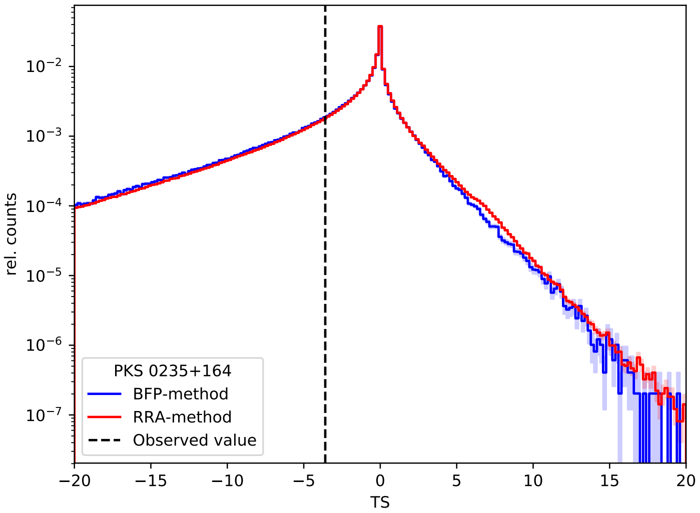

Figure G.28: Same as Fig. G.1 but for PKS 0235+164.

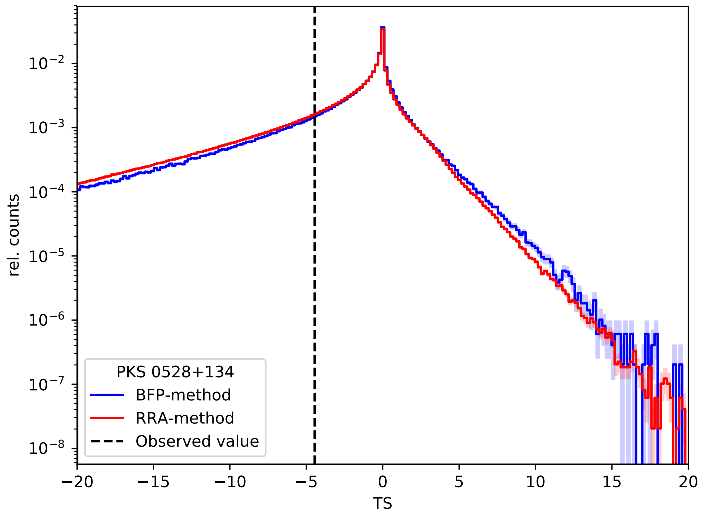

Figure G.29: Same as Fig. G.1 but for PKS 0528+134.

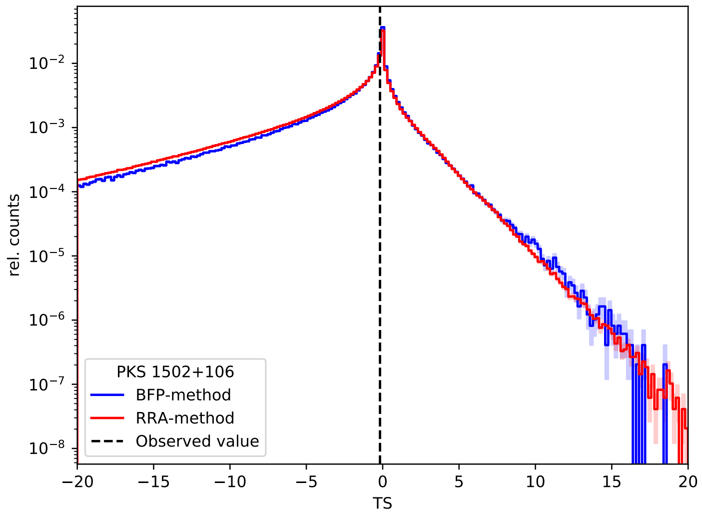

Figure G.30: Same as Fig. G.1 but for PKS 1502+106.

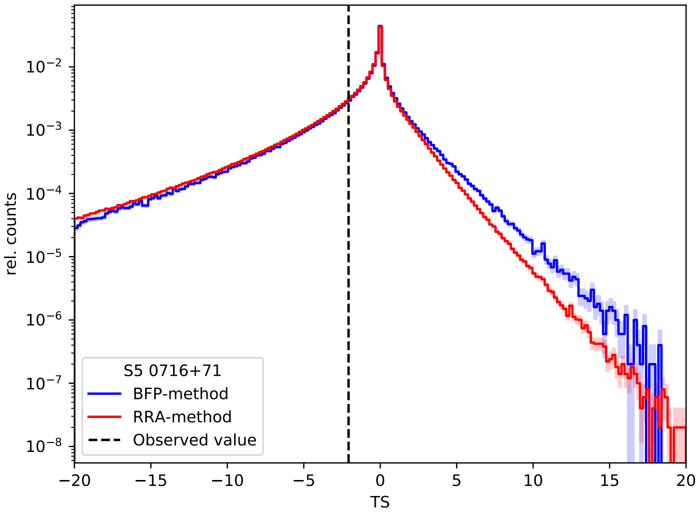

Figure G.31: Same as Fig. G.1 but for S5 0716+71.

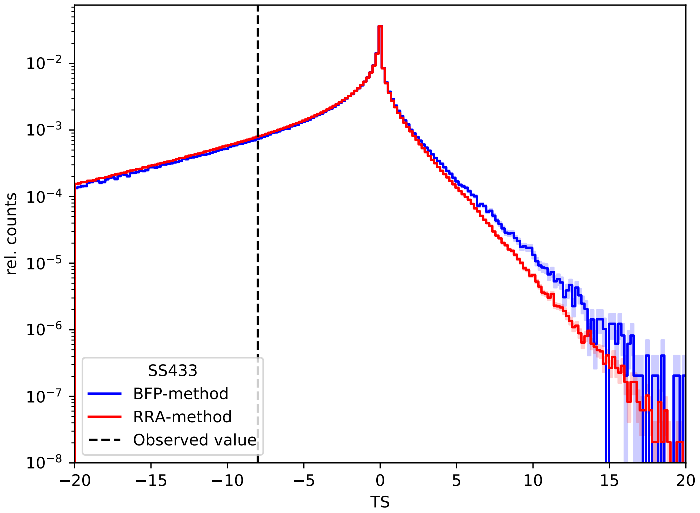

Figure G.32: Same as Fig. G.1 but for SS433.

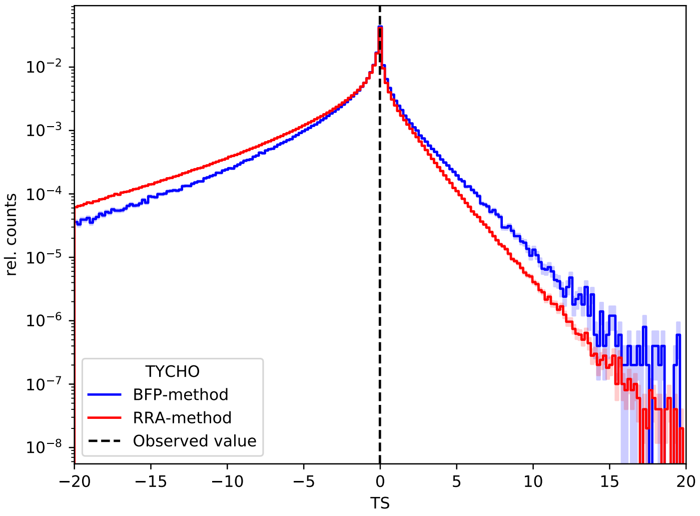

Figure G.33: Same as Fig. G.1 but for TYCHO.

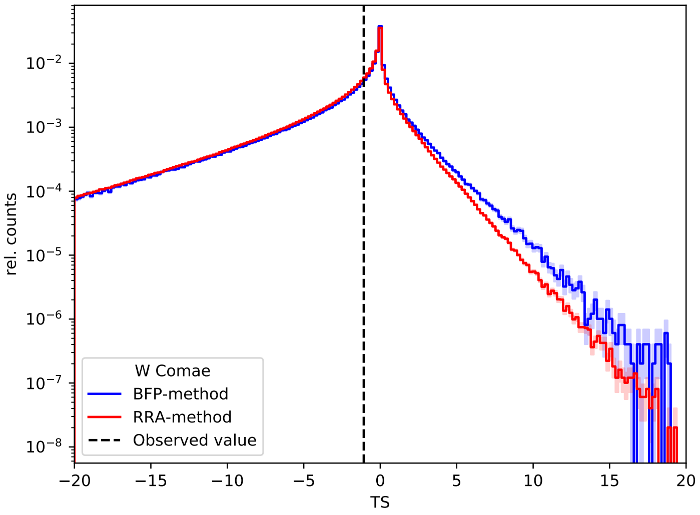

Figure G.34: Same as Fig. G.1 but for W Comae.

Bibliography

[1] IceCube Collaboration, "Physicus," `https://gallery.icecube.wisc.edu/internal/v/GraphicRe/promo/Particle+Physics/physicus.pdf.html` (accessed: Jan 17, 2018).

[2] A. Domínguez, J. D. Finke, F. Prada, J. R. Primack, F. S. Kitaura, B. Siana, and D. Paneque, "Detection of the cosmic γ-ray horizon from multiwavelength observations of blazars," The Astrophysical Journal **770**, 77 (2013), arXiv:1305.2162.

[3] M. G. Aartsen *et al.* (IceCube Collaboration), "Evidence for High-Energy Extraterrestrial Neutrinos at the IceCube Detector," Science **342**, 1242856 (2013), arXiv:1311.5238.

[4] M. G. Aartsen *et al.* (IceCube Collaboration), "Evidence for Astrophysical Muon Neutrinos from the Northern Sky with IceCube," Physical Review Letters **115**, 081102 (2015), arXiv:1507.04005.

[5] M. G. Aartsen *et al.* (IceCube Collaboration), "Observation and Characterization of a Cosmic Muon Neutrino Flux from the Northern Hemisphere using six years of IceCube data," The Astrophysical Journal **833**, 3 (2016), arXiv:1607.08006.

[6] C. Haack and C. Wiebusch on behalf of the IceCube Collaborations, "A Measurement of the Diffuse Astrophysical Muon Neutrino Flux Using Eight Years of IceCube Data," in *Proceedings, 35th International Cosmic Ray Conference — PoS(ICRC2017)*, Vol. 301 (2017) p. 1005.

[7] M. G. Aartsen *et al.* (IceCube Collaboration), "Search for Prompt Neutrino Emission from Gamma-Ray Bursts with IceCube," The Astrophysical Journal **805**, L5 (2015), arXiv:1412.6510.

[8] M. G. Aartsen *et al.* (IceCube Collaboration), "Searches for Time-dependent Neutrino Sources with IceCube Data from 2008 to 2012," The Astrophysical Journal **807**, 46 (2015), arXiv:1503.00598.

[9] S. Adrián-Martínez *et al.* (ANTARES Collaboration and IceCube Collaboration), "The First Combined Search for Neutrino Point-sources in the Southern Hemisphere with the ANTARES and IceCube Neutrino Telescopes," The Astrophysical Journal **823**, 65 (2016), arXiv:1511.02149.

[10] M. G. Aartsen *et al.* (IceCube Collaboration), "Lowering IceCubes Energy Threshold for Point Source Searches in the Southern Sky," The Astrophysical Journal **824**, L28 (2016), arXiv:1605.00163.

[11] M. G. Aartsen *et al.*, “The Contribution of Fermi-2LAC Blazars to Diffuse TeV-PeV Neutrino Flux,” The Astrophysical Journal **835**, 45 (2017), arXiv:1611.03874.

[12] M. G. Aartsen *et al.* (IceCube Collaboration), “Very high-energy gamma-ray follow-up program using neutrino triggers from IceCube,” Journal of Instrumentation **11**, P11009 (2016), arXiv:1610.01814.

[13] M. G. Aartsen *et al.* (IceCube Collaboration), “All-sky Search for Time-integrated Neutrino Emission from Astrophysical Sources with 7 yr of IceCube Data,” The Astrophysical Journal **835**, 151 (2017), arXiv:1609.04981.

[14] M. G. Aartsen *et al.* (IceCube Collaboration), “Extending the Search for Muon Neutrinos Coincident with Gamma-Ray Bursts in IceCube Data,” The Astrophysical Journal **843**, 112 (2017), arXiv:1702.06868.

[15] M. G. Aartsen *et al.* (IceCube Collaboration), “Multiwavelength follow-up of a rare IceCube neutrino multiplet,” Astronomy & Astrophysics **607**, A115 (2017), arXiv:1702.06131.

[16] A. Albert *et al.* (ANTARES Collaboration, IceCube Collaboration, LIGO Scientific Collaboration and Virgo Collaboration), “Search for High-Energy Neutrinos from Gravitational Wave Event GW151226 and Candidate LVT151012 with ANTARES and IceCube,” Physical Review D **96**, 022005 (2017), arXiv:1703.06298.

[17] M. G. Aartsen *et al.* (IceCube Collaboration), “Search for Astrophysical Sources of Neutrinos Using Cascade Events in IceCube,” The Astrophysical Journal **846**, 136 (2017), arXiv:1705.02383.

[18] M. G. Aartsen *et al.* (IceCube Collaboration), “Constraints on Galactic Neutrino Emission with Seven Years of IceCube Data,” The Astrophysical Journal **849**, 67 (2017), arXiv:1707.03416.

[19] The IceCube Collaboration, Fermi-LAT, MAGIC, AGILE, ASAS-SN, HAWC, H.E.S.S., INTEGRAL, Kanata, Kiso, Kapteyn, Liverpool Telescope, Subaru, Swift/NuSTAR, VERITAS, VLA/17B-403 teams, “Multimessenger observations of a flaring blazar coincident with high-energy neutrino IceCube-170922A,” Science **361**, eaat1378 (2018).

[20] M. G. Aartsen *et al.* (IceCube Collaboration), “Neutrino emission from the direction of the blazar TXS 0506+056 prior to the IceCube-170922A alert,” Science **361**, 147 (2018), arXiv:1807.08794.

[21] Z. Malkin, “The current best estimate of the Galactocentric distance of the Sun based on comparison of different statistical techniques,” (2012), arXiv:1202.6128.

[22] I. D. Karachentsev, V. E. Karachentseva, W. K. Huchtmeier, and D. I. Makarov, “A Catalog of Neighboring Galaxies,” The Astronomical Journal **127**, 2031 (2004).

[23] B. Abbott *et al.* (LIGO Scientific Collaboration and Virgo Collaboration), "Observation of Gravitational Waves from a Binary Black Hole Merger," Physical Review Letters **116**, 061102 (2016), arXiv:1602.03837.

[24] T. K. Gaisser, *Cosmic Rays and Particle Physics* (Cambridge University Press, 1991).

[25] V. F. Hess, "Über Beobachtungen der durchdringenden Strahlung bei sieben Freiballonfahrten," Physikalische Zeitschrift **13**, 1084 (1912).

[26] J. Linsley, "Evidence for a Primary Cosmic-Ray Particle with Energy 10^{20} eV," Physical Review Letters **10**, 146 (1963).

[27] C. Patrignani *et al.* (Particle Data Group), "Review of Particle Physics," Chinese Physics C **40**, 100001 (2016), and update 2017.

[28] B. Peters, "Primary cosmic radiation and extensive air showers," Il Nuovo Cimento **22**, 800 (1961).

[29] A. M. Hillas, "The Origin of Ultra-High-Energy Cosmic Rays," Annual Review of Astronomy and Astrophysics **22**, 425 (1984).

[30] A. M. Hillas, "Cosmic Rays: Recent Progress and some Current Questions," (2006), arXiv:astro-ph/0607109.

[31] T. K. Gaisser, "Spectrum of cosmic-ray nucleons, kaon production, and the atmospheric muon charge ratio," Astroparticle Physics **35**, 801 (2012), arXiv:1111.6675.

[32] T. K. Gaisser, T. Stanev, and S. Tilav, "Cosmic ray energy spectrum from measurements of air showers," Frontiers of Physics **8**, 748 (2013), arXiv:1303.3565.

[33] V. Berezinsky, A. Z. Gazizov, and S. I. Grigorieva, "On astrophysical solution to ultrahigh energy cosmic rays," Physical Review D **74**, 043005 (2006), arXiv:hep-ph/0204357.

[34] K. Greisen, "End to the Cosmic-Ray Spectrum?" Physical Review Letters **16**, 748 (1966).

[35] G. T. Zatsepin and V. A. Kuz'min, "Upper Limit of the Spectrum of Cosmic Rays," JETP Letters **4**, 78 (1966).

[36] S. Lee, "Propagation of extragalactic high energy cosmic and γ rays," Physical Review D **58**, 043004 (1998).

[37] A. Aab *et al.* (Pierre Auger Collaboration), "Inferences on Mass Composition and Tests of Hadronic Interactions from 0.3 to 100 EeV Using the Water-Cherenkov Detectors of the Pierre Auger Observatory," Physical Review D **96**, 122003 (2017), arXiv:1710.07249.

[38] R. U. Abbasi *et al.* (Telescope Array Collaboration), "Mass Composition of Ultra-High-Energy Cosmic Rays with the Telescope Array Surface Detector Data," Physical Review D **99**, 022002 (2019), arXiv:1808.03680.

[39] M. Ahlers, “Multi-messenger aspects of cosmic neutrinos,” EPJ Web of Conferences **116**, 11001 (2016).

[40] M. Tanabashi *et al.* (Particle Data Group), “Review of Particle Physics,” Physical Review D **98**, 030001 (2018).

[41] R. Naeye and D. Thompson, “NASA - a timeline of gamma-ray astronomy,” `https://www.nasa.gov/mission_pages/GLAST/main/timeline.html` (accessed: Feb 22, 2018).

[42] NASA/DOE/Fermi-LAT Collaboration, “Fermi 5 year Skymap above 1GeV,” `https://fermi.gsfc.nasa.gov/ssc/Fermi_5_year.jpg` (accessed: Jan 31, 2018).

[43] M. Ackermann *et al.* (Fermi-LAT Collaboration), “Detection of the Characteristic Pion-Decay Signature in Supernova Remnants,” Science **339**, 807 (2013), arXiv:1302.3307.

[44] A. Giuliani *et al.*, “Neutral Pion Emission from Accelerated Protons in the Supernova Remnant W44,” The Astrophysical Journal **742**, L30 (2011), arXiv:1111.4868.

[45] M. Tavani *et al.*, “Direct Evidence for Hadronic Cosmic-Ray Acceleration in the Supernova Renmant IC 443,” The Astrophysical Journal **710**, L151 (2010), arXiv:1001.5150.

[46] S. Hümmer, M. Maltoni, W. Winter, and C. Yaguna, “Energy dependent neutrino flavor ratios from cosmic accelerators on the Hillas plot,” Astroparticle Physics **34**, 205 (2010), arXiv:1007.0006.

[47] Z. Maki, M. Nakagawa, and S. Sakata, “Remarks on the Unified Model of Elementary Particles,” Progress of Theoretical Physics **28**, 870 (1962).

[48] E. Majorana, “Teoria simmetrica dell’elettrone e del positrone,” Il Nuovo Cimento **14**, 171 (1937).

[49] NuFIT Collaboration, “NuFIT | NuFIT,” `http://www.nu-fit.org/` (accessed: May 11, 2018).

[50] I. Esteban, M. C. Gonzalez-Garcia, M. Maltoni, I. Martinez-Soler, and T. Schwetz, “Updated fit to three neutrino mixing: exploring the accelerator-reactor complementarity,” Journal of High Energy Physics **2017**, 87 (2017), arXiv:1611.01514.

[51] M. Bustamante, J. F. Beacom, and W. Winter, “Theoretically palatable flavor combinations of astrophysical neutrinos,” Physical Review Letters **115**, 161302 (2015), arXiv:1506.02645.

[52] R. Svoboda, L. Gordan, and NASA, “Astronomy Picture of the Day: Neutrinos in the Sun,” (1998), `https://apod.nasa.gov/apod/ap980605.html` (accessed Jul 25, 2019).

[53] B. T. Cleveland, T. Daily, J. Raymond Davis, J. R. Distel, K. Lande, C. K. Lee, P. S. Wildenhain, and J. Ullman, “Measurement of the Solar Electron Neutrino Flux with the Homestake Chlorine Detector,” The Astrophysical Journal **496**, 505 (1998).

[54] S. Fukuda *et al.* (Super-Kamiokande Collaboration), "The Super-Kamiokande detector," Nucl. Instrum. Methods Phys. Res. A **501**, 418 (2003).

[55] M. Aglietta *et al.*, "On the Event Observed in the Mont Blanc Underground Neutrino Observatory during the Occurrence of Supernova 1987 a," Europhysics Letters **3**, 1315 (1987).

[56] E. N. Alekseev, L. N. Alekseeva, V. I. Volchenko, and I. V. Krivosheina, "Possible detection of a neutrino signal on 23 February 1987 at the Baksan underground scintillation telescope of the Institute of Nuclear Research," JETP Letters **45**, 461 (1987).

[57] R. M. Bionta *et al.*, "Observation of a neutrino burst in coincidence with supernova 1987A in the Large Magellanic Cloud," Physical Review Letters **58**, 1494 (1987).

[58] K. Hirata *et al.*, "Observation of a neutrino burst from the supernova SN1987A," Physical Review Letters **58**, 1490 (1987).

[59] M. G. Aartsen *et al.* (IceCube Collaboration), "Observation of High-Energy Astrophysical Neutrinos in Three Years of IceCube Data," Physical Review Letters **113**, 101101 (2014), arXiv:1405.5303.

[60] N. Wandkowsky on behalf of the IceCube Collaborations, "Latest results on astrophysical neutrinos using high-energy events with contained vertices," in *Neutrino 2018 - XXVIII International Conference on Neutrino Physics and Astrophysics* (Heidelberg, 2018) `https://icecube.wisc.edu/~hese/index.html`.

[61] A. Kappes, J. Hinton, C. Stegmann, and F. A. Aharonian, "Potential Neutrino Signals from Galactic γ-Ray Sources," The Astrophysical Journal **656**, 870 (2007), arXiv:astro-ph/0607286.

[62] F. W. Stecker, C. Done, M. H. Salamon, and P. Sommers, "High-energy neutrinos from active galactic nuclei," Physical Review Letters **66**, 2697 (1991).

[63] A. Einstein, "Näherungsweise Integration der Feldgleichungen der Gravitation," Sitzungsberichte der Königlich Preussischen Akademie der Wissenschaften Berlin , 688 (1916).

[64] A. Einstein, "Über Gravitationswellen," Sitzungsberichte der Königlich Preussischen Akademie der Wissenschaften Berlin , 154 (1918).

[65] B. P. Abbott *et al.* (LIGO Scientific Collaboration and Virgo Collaboration), "GW170817: Observation of Gravitational Waves from a Binary Neutron Star Inspiral," Physical Review Letters **119**, 161101 (2017), arXiv:1710.05832.

[66] B. P. Abbott *et al.* (LIGO Scientific Collaboration, Virgo Collaboration, Fermi-GBM, INTEGRAL), "Gravitational Waves and Gamma-Rays from a Binary Neutron Star Merger: GW170817 and GRB 170817A," The Astrophysical Journal **848**, L13 (2017), arXiv:1710.05834.

[67] LIGO Scientific Collaboration, Virgo Collaboration, Fermi GBM, INTEGRAL, IceCube Collaboration, AstroSat Cadmium Zinc Telluride Imager Team, IPN Collaboration, The Insight-Hxmt Collaboration, ANTARES Collaboration, The Swift Collaboration, AGILE Team, The 1M2H Team, The Dark Energy Camera GW-EM Collaboration, the DES Collaboration, The DLT40 Collaboration, GRAWITA: GRAvitational Wave Inaf TeAm, The Fermi-LAT Collaboration, ATCA: Australia Telescope Compact Array, ASKAP: Australian SKA Pathfinder, Las Cumbres Observatory Group, OzGrav, DWF, AST3, CAASTRO Collaborations, The VINROUGE Collaboration, MASTER Collaboration, J-GEM, GROWTH, JAGWAR, Caltech-NRAO, TTU-NRAO, NuSTAR Collaborations, Pan-STARRS, The MAXI Team, TZAC Consortium, K. U. Collaboration, Nordic Optical Telescope, ePESSTO, GROND, Texas Tech University, SALT Group, TOROS: Transient Robotic Observatory of the South Collaboration, The BOOTES Collaboration, MWA: Murchison Widefield Array, The CALET Collaboration, IKI-GW Follow-up Collaboration, H.E.S.S. Collaboration, LOFAR Collaboration, LWA: Long Wavelength Array, HAWC Collaboration, The Pierre Auger Collaboration, ALMA Collaboration, Euro VLBI Team, Pi of the Sky Collaboration, The Chandra Team at McGill University, DFN: Desert Fireball Network, ATLAS, High Time Resolution Universe Survey, RIMAS, RATIR, and SKA South Africa/MeerKAT, “Multi-messenger Observations of a Binary Neutron Star Merger,” The Astrophysical Journal **848**, L12 (2017), arXiv:1710.05833.

[68] E. Fermi, “On the Origin of the Cosmic Radiation,” Physical Review **75**, 1169 (1949).

[69] E. M. de Gouveia Dal Pino and G. Kowal, in *Magnetic Fields in Diffuse Media*, Astrophysics and Space Science Library, edited by A. Lazarian, E. M. de Gouveia Dal Pino, and C. Melioli (Springer Berlin Heidelberg, Berlin, Heidelberg, 2015) pp. 373–398.

[70] F. M. Rieger and P. Duffy, “Shear Acceleration in Expanding Flows,” The Astrophysical Journal **833**, 34 (2016), arXiv:1611.04342.

[71] M. S. Longair, *High Energy Astrophysics*, thired ed. (Cambridge University Press, 2011).

[72] Y. Li, X. Sun, M. D. Ding, J. Qiu, and E. R. Priest, “Imaging Observations of Magnetic Reconnection in a Solar Eruptive Flare,” The Astrophysical Journal **835**, 190 (2017), arXiv:1612.09417.

[73] H. Tanabe *et al.* (MAST Team), “Recent Progress of Magnetic Reconnection Research in the MAST Spherical Tokamak,” Physics of Plasmas **24**, 056108 (2017).

[74] P. A. Sweet, “The Neutral Point Theory of Solar Flares,” in *Electromagnetic Phenomena in Cosmical Physics*, Vol. 6 (1958) p. 123.

[75] E. N. Parker, “Sweet’s mechanism for merging magnetic fields in conducting fluids,” Journal of Geophysical Research (1896-1977) **62**, 509 (1957).

[76] H. E. Petschek, “Magnetic Field Annihilation,” NASA Special Publication **50**, 425 (1964).

[77] T. G. Forbes and E. R. Priest, "A Comparison of Analytical and Numerical Models for Steadily Driven Magnetic Reconnection," Reviews of Geophysics **25**, 1583 (1987).

[78] K. Kotera and A. V. Olinto, "The Astrophysics of Ultrahigh-Energy Cosmic Rays," Annual Review of Astronomy and Astrophysics **49**, 119 (2011).

[79] E. Waxman, "High energy cosmic ray and neutrino astronomy," Astronomy at the Frontiers of Science **1**, 43 (2011), arXiv:1101.1155.

[80] M. Lemoine and E. Waxman, "Anisotropy vs chemical composition at ultra-high energies," Journal of Cosmology and Astroparticle Physics **2009**, 009 (2009), arXiv:0907.1354.

[81] V. N. Zirakashvili and V. S. Ptuskin, "Type IIn supernovae as sources of high energy astrophysical neutrinos," Astroparticle Physics **78**, 28 (2016), arXiv:1510.08387.

[82] D. Lai, "Physics of Neutron Star Kicks," Stellar Astrophysics **254**, 127 (2000), arXiv:astro-ph/9912522.

[83] E. van der Swaluw, T. P. Downes, and R. Keegan, "An evolutionary model for pulsar-driven supernova remnants - A hydrodynamical model," Astronomy & Astrophysics **420**, 937 (2004), arXiv:astro-ph/0311388.

[84] E. Amato, D. Guetta, and P. Blasi, "Signatures of high energy protons in pulsar winds," Astronomy & Astrophysics **402**, 827 (2003), arXiv:astro-ph/0302121.

[85] A. Levinson and E. Waxman, "Probing Microquasars with TeV Neutrinos," Physical Review Letters **87**, 171101 (2001).

[86] C. Distefano, D. Guetta, E. Waxman, and A. Levinson, "Neutrino flux predictions for known Galactic microquasars," The Astrophysical Journal **575**, 378 (2002), arXiv:astro-ph/0202200.

[87] A. Abramowski *et al.* (H.E.S.S. Collaboration), "Diffuse Galactic gamma-ray emission with H.E.S.S," Physical Review D **90**, 122007 (2014), arXiv:1411.7568.

[88] M. Ackermann *et al.* (Fermi-LAT Collaboration), "Fermi-LAT Observations of the Diffuse Gamma-Ray Emission: Implications for Cosmic Rays and the Interstellar Medium," The Astrophysical Journal **750**, 3 (2012), arXiv:1202.4039.

[89] D. Gaggero, D. Grasso, A. Marinelli, A. Urbano, and M. Valli, "The Gamma-Ray and Neutrino Sky: A Consistent Picture of Fermi-LAT, Milagro, and IceCube Results," The Astrophysical Journal **815**, L25 (2015), arXiv:1504.00227.

[90] N. Sherf, U. Keshet, and I. Gurwich, "IceCube Constraints on the Fermi Bubbles," The Astrophysical Journal **847**, 95 (2017), arXiv:1705.06665.

[91] P. A. R. Ade *et al.* (Planck Collaboration), "Planck 2015 results. XIII. Cosmological parameters," Astronomy & Astrophysics **594**, A13 (2016), arXiv:1502.01589.

[92] M. Cirelli, "Indirect Searches for Dark Matter: a status review," Pramana **79**, 1021 (2012), arXiv:1202.1454.

[93] A. Esmaili, A. Ibarra, and O. L. G. Peres, "Probing the stability of superheavy dark matter particles with high-energy neutrinos," Journal of Cosmology and Astroparticle Physics **2012**, 034 (2012), arXiv:1205.5281.

[94] E. Waxman and J. Bahcall, "High Energy Neutrinos from Astrophysical Sources: An Upper Bound," Physical Review D **59**, 023002 (1998), arXiv:hep-ph/9807282.

[95] P. Padovani *et al.*, "Active galactic nuclei: what's in a name?" The Astronomy and Astrophysics Review **25**, 2 (2017), arXiv:1707.07134.

[96] C. M. Urry and P. Padovani, "Unified Schemes for Radio-Loud Active Galactic Nuclei," Publications of the Astronomical Society of the Pacific **107**, 803 (1995), arXiv:astro-ph/9506063.

[97] K. Murase, "Active Galactic Nuclei as High-Energy Neutrino Sources," in *Neutrino Astronomy*, edited by T. Gaisser and A. Karle (2017) Chap. 2, pp. 15–31, arXiv:1511.01590.

[98] K. Murase, Y. Inoue, and C. D. Dermer, "Diffuse neutrino intensity from the inner jets of active galactic nuclei: Impacts of external photon fields and the blazar sequence," Physical Review D **90**, 023007 (2014), arXiv:1403.4089.

[99] K. Mannheim, T. Stanev, and P. L. Biermann, "Neutrinos from flat-spectrum radio quasars," Astronomy & Astrophysics **260**, L1 (1992).

[100] V. Beckmann and C. R. Shrader, "The AGN phenomenon: open issues," (2013), arXiv:1302.1397.

[101] L. Dai and K. Fang, "Can tidal disruption events produce the IceCube neutrinos?" Monthly Notices of the Royal Astronomical Society **469**, 1354 (2017), arXiv:1612.00011.

[102] C. Lunardini and W. Winter, "High Energy Neutrinos from the Tidal Disruption of Stars," Physical Review D **95**, 123001 (2017), arXiv:1612.03160.

[103] P. Mészáros, "Gamma Ray Bursts as Neutrino Sources," in *Neutrino Astronomy*, edited by T. Gaisser and A. Karle (2017) Chap. 1, pp. 1–14, arXiv:1511.01396.

[104] M. G. Aartsen *et al.* (IceCube Collaboration), "An All-Sky Search for Three Flavors of Neutrinos from Gamma-Ray Bursts with the IceCube Neutrino Observatory," The Astrophysical Journal **824**, 115 (2016), arXiv:1601.06484.

[105] A. Loeb and E. Waxman, "The cumulative background of high energy neutrinos from starburst galaxies," Journal of Cosmology and Astroparticle Physics **2006**, 003 (2006), arXiv:astro-ph/0601695.

[106] K. Bechtol, M. Ahlers, M. Di Mauro, M. Ajello, and J. Vandenbroucke, “Evidence against star-forming galaxies as the dominant source of IceCube neutrinos,” The Astrophysical Journal **836**, 47 (2017), arXiv:1511.00688.

[107] K. Kotera, D. Allard, K. Murase, J. Aoi, Y. Dubois, T. Pierog, and S. Nagataki, “Propagation of Ultrahigh Energy Nuclei in Clusters of Galaxies: Resulting Composition and Secondary Emissions,” The Astrophysical Journal **707**, 370 (2009), arXiv:0907.2433.

[108] K. Murase, S. Inoue, and S. Nagataki, “Cosmic Rays above the Second Knee from Clusters of Galaxies and Associated High-Energy Neutrino Emission,” The Astrophysical Journal **689**, L105 (2008), arXiv:0805.0104.

[109] R. Aloisio, D. Boncioli, A. di Matteo, A. F. Grillo, S. Petrera, and F. Salamida, “Cosmogenic neutrinos and ultra-high energy cosmic ray models,” Journal of Cosmology and Astroparticle Physics **2015**, 006 (2015), arXiv:1505.04020.

[110] M. G. Aartsen *et al.* (IceCube Collaboration), “Differential limit on the extremely-high-energy cosmic neutrino flux in the presence of astrophysical background from nine years of IceCube data,” Physical Review D **98**, 062003 (2018), arXiv:1807.01820.

[111] J. Braun, J. Dumm, F. D. Palma, C. Finley, A. Karle, and T. Montaruli, “Methods for point source analysis in high energy neutrino telescopes,” Astroparticle Physics **29**, 299 (2008), arXiv:0801.1604.

[112] M. G. Aartsen *et al.* (IceCube Collaboration), “Searches for Extended and Point-like Neutrino Sources with Four Years of IceCube Data,” The Astrophysical Journal **796**, 109 (2014), arXiv:1406.6757.

[113] M. G. Aartsen *et al.* (IceCube Collaboration), “Search for time-independent neutrino emission from astrophysical sources with 3 years of IceCube data,” The Astrophysical Journal **779**, 132 (2013), arXiv:1307.6669.

[114] R. Abbasi *et al.* (IceCube Collaboration), “Time-integrated Searches for Point-like Sources of Neutrinos with the 40-string IceCube Detector,” The Astrophysical Journal **732**, 18 (2011), arXiv:1012.2137.

[115] R. Abbasi *et al.* (IceCube Collaboration), “Searches for High-Energy Neutrino Emission in the Galaxy with the Combined IceCube-AMANDA Detector,” The Astrophysical Journal **763**, 33 (2013), arXiv:1210.3273.

[116] R. Abbasi *et al.* (IceCube Collaboration), “First Neutrino Point-Source Results From the 22-String IceCube Detector,” The Astrophysical Journal **701**, L47 (2009), arXiv:0905.2253.

[117] R. Abbasi *et al.* (IceCube Collaboration), “Extending the Search for Neutrino Point Sources with IceCube above the Horizon,” Physical Review Letters **103**, 221102 (2009), arXiv:0911.2338.

[118] R. Abbasi *et al.* (IceCube Collaboration), "Search for Point Sources of High Energy Neutrinos with Final Data from AMANDA-II," Physical Review D **79**, 062001 (2009), arXiv:0809.1646.

[119] S. Adrián-Martínez *et al.* (ANTARES Collaboration), "First Search for Point Sources of High Energy Cosmic Neutrinos with the ANTARES Neutrino Telescope," The Astrophysical Journal **743**, L14 (2011), arXiv:1108.0292.

[120] S. Adrián-Martínez *et al.* (ANTARES Collaboration), "Search for Cosmic Neutrino Point Sources with Four Years of Data from the ANTARES Telescope," The Astrophysical Journal **760**, 53 (2012), arXiv:1207.3105.

[121] S. Adrian-Martinez *et al.* (ANTARES Collaboration), "Searches for Point-like and extended neutrino sources close to the Galactic Centre using the ANTARES neutrino Telescope," The Astrophysical Journal **786**, L5 (2014), arXiv:1402.6182.

[122] A. Albert *et al.* (ANTARES Collaboration), "First All-Flavor Neutrino Pointlike Source Search with the ANTARES Neutrino Telescope," Physical Review D **96**, 082001 (2017), arXiv:1706.01857.

[123] M. G. Aartsen *et al.* (IceCube Collaboration), "Neutrinos below 100 TeV from the Southern Sky Employing Refined Veto Techniques to IceCube Data," (2019), submitted to Astroparticle Physics, arXiv:1902.05792.

[124] C. Kopper on behalf of the IceCube Collaborations, "Observation of Astrophysical Neutrinos in Six Years of IceCube Data," in *Proceedings of 35th International Cosmic Ray Conference — PoS(ICRC2017)*, Vol. 301 (2017) p. 981.

[125] M. G. Aartsen *et al.* (IceCube Collaboration), "A Search for Neutrino Emission from Fast Radio Bursts with Six Years of IceCube Data," The Astrophysical Journal **857**, 117 (2018), arXiv:1712.06277.

[126] R. Abbasi *et al.* (IceCube Collaboration), "Time-Dependent Searches for Point Sources of Neutrinos with the 40-String and 22-String Configurations of IceCube," The Astrophysical Journal **744**, 1 (2012), arXiv:1104.0075.

[127] M. G. Aartsen *et al.* (IceCube Collaboration), "Search for Transient Astrophysical Neutrino Emission with IceCube-DeepCore," The Astrophysical Journal **816**, 75 (2016), arXiv:1509.05029.

[128] M. G. Aartsen *et al.* (IceCube Collaboration), "Constraints on Minute-Scale Transient Astrophysical Neutrino Sources," Physical Review Letters **122**, 051102 (2019), arXiv:1807.11492.

[129] M. G. Aartsen *et al.* (IceCube Collaboration), "Searches for Small-Scale Anisotropies from Neutrino Point Sources with Three Years of IceCube Data," Astroparticle Physics **66**, 39 (2015), arXiv:1408.0634.

[130] T. Glauch and A. Turcati on behalf of the IceCube Collaboration, "Search for Weak Neutrino Point Sources Using Angular Auto-Correlation Analyses in IceCube," in *Proceedings of 35th International Cosmic Ray Conference — PoS(ICRC2017)*, Vol. 301 (2017) p. 1014.

[131] A. Albert *et al.* (ANTARES Collaboration and IceCube Collaboration), "Joint constraints on galactic diffuse neutrino emission from the ANTARES and IceCube neutrino telescopes," The Astrophysical Journal **868**, L20 (2018), arXiv:1808.03531.

[132] M. Huber and K. Krings on behalf of the IceCube Collaboration, "Results of IceCube Searches for Neutrinos from Blazars Using Seven Years of Through-Going Muon Data," in *Proceedings of 35th International Cosmic Ray Conference — PoS(ICRC2017)*, Vol. 301 (2018) p. 994.

[133] G. Maggi, K. D. de Vries, and N. van Eijndhoven on behalf of the IceCube Collaboration, "Investigation of Obscured Flat Spectrum Radio AGN with the IceCube Neutrino Observatory," in *Proceedings of 35th International Cosmic Ray Conference — PoS(ICRC2017)*, Vol. 301 (2018) p. 1000.

[134] M. G. Aartsen *et al.* (IceCube Collaboration), "Search for Correlations between the Arrival Directions of IceCube Neutrino Events and Ultrahigh-Energy Cosmic Rays Detected by the Pierre Auger Observatory and the Telescope Array," Journal of Cosmology and Astroparticle Physics **2016**, 037 (2016), arXiv:1511.09408.

[135] A. Albert *et al.* (ANTARES, IceCube, LIGO and Virgo Collaborations), "Search for Multi-Messenger Sources of Gravitational Waves and High-Energy Neutrinos with Advanced LIGO during Its First Observing Run, ANTARES and IceCube," The Astrophysical Journal **870**, 134 (2019), arXiv:1810.10693.

[136] A. Albert *et al.* (ANTARES, IceCube, Pierre Auger, LIGO Scientific, and Virgo Collaborations), "Search for High-Energy Neutrinos from Binary Neutron Star Merger GW170817 with ANTARES, IceCube, and the Pierre Auger Observatory," The Astrophysical Journal **850**, L35 (2017), arXiv:1710.05839.

[137] K. Meagher and C. Raab on behalf of the IceCube Collaboration, "Search for a Cumulative Neutrino Signal from Blazar Flares Using IceCube Data," in *Proceedings of 35th International Cosmic Ray Conference — PoS(ICRC2017)*, Vol. 301 (2018) p. 957.

[138] T. Kintscher, K. Krings, D. Dorner, W. Bhattacharyya, and M. Takahashi on behalf of the IceCube, FACT, MAGIC Collaborations, "IceCube Search for Neutrinos from 1ES 1959+650: Completing the Picture," in *Proceedings of 35th International Cosmic Ray Conference — PoS(ICRC2017)*, Vol. 301 (2018) p. 969.

[139] R. Abbasi *et al.* (IceCube Collaboration), "Neutrino Analysis of the September 2010 Crab Nebula Flare and Time-Integrated Constraints on Neutrino Emission from the Crab Using IceCube," The Astrophysical Journal **745**, 45 (2012), arXiv:1106.3484.

[140] S. Schoenen and L. Rädel, "ATel #7856: Detection of a Multi-PeV Neutrino-Induced Muon Event from the Northern Sky with IceCube," The Astronomers Telegram **#7856** (2015).

[141] M. G. Aartsen *et al.* (IceCube Collaboration), "The IceCube Realtime Alert System," Astroparticle Physics **92**, 30 (2017), arXiv:1612.06028.

[142] E. Blaufuss on behalf of the IceCube Collaboration, "Realtime Neutrino Alerts and Follow-up in IceCube," in *Proceedings of 35th International Cosmic Ray Conference — PoS(ICRC2017)*, Vol. 301 (2018) p. 982.

[143] S. Barthelmy, "GCN: The Gamma-Ray Coordinates Network," `https://gcn.gsfc.nasa.gov/` (accessed: May 31, 2019).

[144] M. W. E. Smith *et al.* (AMON), "The Astrophysical Multimessenger Observatory Network (AMON)," Astroparticle Physics **45**, 56 (2013), arXiv:1211.5602.

[145] K. Meagher on behalf of the IceCube Collaboration, "IceCube as a Neutrino Follow-up Observatory for Astronomical Transients," in *Proceedings of 35th International Cosmic Ray Conference — PoS(ICRC2017)*, Vol. 301 (2018) p. 1007.

[146] R. Rutledge, "The Astronomer's Telegram: A Web-Based Short-Notice Publication System for the Professional Astronomical Community," Publications of the Astronomical Society of the Pacific **110**, 754 (1998), arXiv:astro-ph/9802256.

[147] S. Weinberg, "A Model of Leptons," Physical Review Letters **19**, 1264 (1967).

[148] A. Cooper-Sarkar, P. Mertsch, and S. Sarkar, "The high energy neutrino cross-section in the Standard Model and its uncertainty," Journal of High Energy Physics **08**, 042 (2011), arXiv:1106.3723.

[149] J. A. Formaggio and G. P. Zeller, "From eV to EeV: Neutrino cross sections across energy scales," Reviews of Modern Physics **84**, 1307 (2012), arXiv:1305.7513.

[150] S. J. Schoenen, *Discovery and Characterization of a Diffuse Astrophysical Muon Neutrino Flux with the IceCube Neutrino Observatory*, Ph.D. thesis, RWTH Aachen University (2017).

[151] R. Gandhi, C. Quigg, M. Hall Reno, and I. Sarcevic, "Ultrahigh-Energy Neutrino Interactions," Astroparticle Physics **5**, 81 (1996), arXiv:hep-ph/9512364.

[152] S. L. Glashow, "Resonant Scattering of Antineutrinos," Physical Review **118**, 316 (1960).

[153] A. Gazizov and M. P. Kowalski, "ANIS: High energy neutrino generator for neutrino telescopes," Computer Physics Communications **172**, 203 (2005), arXiv:astro-ph/0406439.

[154] L. Rädel, *Measurement of High-Energy Muon Neutrinos with the IceCube Neutrino Observatory*, Ph.D. thesis, RWTH Aachen University (2017).

[155] E. Bugaev, T. Montaruli, Y. Shlepin, and I. Sokalski, “Propagation of tau neutrinos and tau leptons through the Earth and their detection in underwater/ice neutrino telescopes,” Astroparticle Physics **21**, 491 (2004), arXiv:hep-ph/0312295.

[156] J. G. Learned and K. Mannheim, “High-energy neutrino astrophysics,” Annual Review of Nuclear and Particle Science **50**, 679 (2000).

[157] A. Schukraft, *Search for a diffuse flux of extragalactic neutrinos with the IceCube Neutrino Observatory*, Ph.D. thesis, RWTH Aachen University (2013).

[158] D. E. Groom, N. V. Mokhov, and S. I. Striganov, “Muon Stopping Power and Range Tables 10 MeV–100 TeV,” Atomic Data and Nuclear Data Tables **78**, 183 (2001).

[159] H. Bethe, “Zur Theorie des Durchgangs schneller Korpuskularstrahlen durch Materie,” Annalen der Physik **397**, 325 (1930).

[160] F. Bloch, “Zur Bremsung Rasch Bewegter Teilchen Beim Durchgang Durch Materie,” Annalen der Physik **408**, 285 (1933).

[161] J. H. Koehne, K. Frantzen, M. Schmitz, T. Fuchs, W. Rhode, D. Chirkin, and J. Becker Tjus, “PROPOSAL: A tool for propagation of charged leptons,” Computer Physics Communications **184**, 2070 (2013).

[162] D. Groom, “Atomic Nuclear Properties - Ice,” `http://pdg.lbl.gov/2018/AtomicNuclearProperties/HTML/water_ice.html` (accessed: May 31, 2019).

[163] P. Lipari and T. Stanev, “Propagation of Multi-TeV Muons,” Physical Review D **44**, 3543 (1991).

[164] M. Dunsch, J. Soedingrekso, A. Sandrock, M. Meier, T. Menne, and W. Rhode, “Recent Improvements for the Lepton Propagator PROPOSAL,” Computer Physics Communications **242**, 132 (2019), arXiv:1809.07740.

[165] M. Leuermann, *Testing the neutrino mass ordering with IceCube DeepCore*, Ph.D. thesis, RWTH Aachen University (2018).

[166] M. Wallraff, *Design, Implementation and Test of a New Feature Extractor for the IceCube Neutrino Observatory*, Diploma thesis, RWTH Aachen University (2010).

[167] P. Hallen, *On the Measurement of High-Energy Tau Neutrinos with IceCube*, Master’s thesis, RWTH Aachen University (2013).

[168] L. Kuzmichev, “On the velocity of light signals in deep underwater neutrino experiments,” Nucl. Instrum. Methods Phys. Res. A **482**, 304 (2002), arXiv:hep-ex/0005036.

[169] P. Price and K. Woschnagg, “Role of group and phase velocity in high-energy neutrino observatories,” Astroparticle Physics **15**, 97 (2001), arXiv:hep-ex/0008001.

[170] I. Frank and I. Tamm, “Coherent Visible Radiation of Fast Electrons Passing Through Matter,” in *Selected Papers*, edited by I. E. Tamm, B. M. Bolotovskii, V. Y. Frenkel, and R. Peierls (Springer Berlin Heidelberg, Berlin, Heidelberg, 1991) pp. 29–35.

[171] L. Rädel, *Simulation Studies of the Cherenkov Light Yield from Relativistic Particles in High-Energy Neutrino Telescopes with Geant4*, Master’s thesis, RWTH Aachen University (2012).

[172] K. Abe *et al.* (Super-Kamiokande Collaboration), “Calibration of the Super-Kamiokande Detector,” Nucl. Instrum. Methods Phys. Res. A **737**, 253 (2014), arXiv:1307.0162.

[173] C. Spiering, “History of High-Energy Neutrino Astronomy,” (2019), arXiv:1903.11481.

[174] M. Ageron *et al.* (ANTARES Collaboration), “ANTARES: The first undersea neutrino telescope,” Nucl. Instrum. Methods Phys. Res. A **656**, 11 (2011), arXiv:1104.1607.

[175] M. Aartsen *et al.* (IceCube Collaboration), “The IceCube Neutrino Observatory: instrumentation and online systems,” Journal of Instrumentation **12**, P03012 (2017), arXiv:1612.05093.

[176] A. D. Avrorin *et al.* (Baikal-GVD Collaboration), “Baikal-GVD: Status and Prospects,” EPJ Web of Conferences **191**, 01006 (2018), arXiv:1808.10353.

[177] S. Adrián-Martínez *et al.* (KM3NeT Collaboration), “Letter of Intent for KM3NeT 2.0,” Journal of Physics G: Nuclear and Particle Physics **43**, 084001 (2016), arXiv:1601.07459.

[178] M. G. Aartsen *et al.* (IceCube-Gen2 Collaboration), “IceCube-Gen2: A Vision for the Future of Neutrino Astronomy in Antarctica,” (2014), arXiv:1412.5106.

[179] J. Alvarez-Muñiz, A. Romero-Wolf, and E. Zas, “Practical and Accurate Calculations of Askaryan Radiation,” Physical Review D **84**, 103003 (2011), arXiv:1106.6283.

[180] P. Allison *et al.*, “Design and Initial Performance of the Askaryan Radio Array Prototype EeV Neutrino Detector at the South Pole,” Astroparticle Physics **35**, 457 (2012), arXiv:1105.2854.

[181] S. W. Barwick *et al.*, “Design and Performance of the ARIANNA HRA-3 Neutrino Detector Systems,” IEEE Transactions on Nuclear Science **62**, 2202 (2015), arXiv:1410.7369.

[182] J. Vandenbroucke, *Acoustic Detection of Astrophysical Neutrinos in South Pole Ice*, Ph.D. thesis, University of California, Berkeley (2009), arXiv:1201.0072.

[183] J. A. Aguilar *et al.* (ANTARES collaboration), “AMADEUS - The Acoustic Neutrino Detection Test System of the ANTARES Deep-Sea Neutrino Telescope,” Nucl. Instrum. Methods Phys. Res. A **626-627**, 128 (2011), arXiv:1009.4179.

[184] P. Abreu *et al.* (Pierre Auger Collaboration), “Ultrahigh Energy Neutrinos at the Pierre Auger Observatory,” Advances in High Energy Physics **2013**, 708680 (2013), arXiv:1304.1630.

[185] P. Gorham *et al.* (ANITA Collaboration), "The Antarctic Impulsive Transient Antenna Ultra-High Energy Neutrino Detector Design, Performance, and Sensitivity for 2006-2007 Balloon Flight," Astroparticle Physics **32**, 10 (2009), arXiv:0812.1920.

[186] T. Gaisser, "Seasonal Variation of Atmospheric Neutrinos in IceCube," in *Proceedings, 33th International Cosmic Ray Conference (ICRC2013)* (2013) p. 0492.

[187] M. Honda, T. Kajita, K. Kasahara, S. Midorikawa, and T. Sanuki, "Calculation of Atmospheric Neutrino Flux Using the Interaction Model Calibrated with Atmospheric Muon Data," Physical Review D **75**, 043006 (2007), arXiv:astro-ph/0611418.

[188] T. K. Gaisser, "Spectrum of Cosmic-Ray Nucleons, Kaon Production, and the Atmospheric Muon Charge Ratio," Astroparticle Physics **35**, 801 (2012).

[189] J. I. Illana, P. Lipari, M. Masip, and D. Meloni, "Atmospheric muon and neutrino fluxes at very high energy," Astroparticle Physics **34**, 663 (2011), arXiv:1010.5084.

[190] A. Schukraft, C. Haack, C. Wiebusch, and A. Zilles, "Re-Weighting Atmospheric Neutrino Fluxes to Account for the Cosmic-Ray Knee with Neutrinoflux," (2013), IceCube Internal Report.

[191] R. Enberg, "Neutrinos from Charm Production in the Atmosphere," (2014), arXiv:1402.0880.

[192] A. Achterberg *et al.* (IceCube Collaboration), "First year performance of the IceCube neutrino telescope," Astroparticle Physics **26**, 155 (2006), arXiv:astro-ph/0604450.

[193] R. Abbasi *et al.* (IceCube Collaboration), "The Design and Performance of IceCube DeepCore," Astroparticle Physics **35**, 615 (2012), arXiv:1109.6096.

[194] R. Abbasi *et al.* (IceCube Collaboration), "IceTop: The surface component of IceCube," Nucl. Instrum. Methods Phys. Res. A **700**, 188 (2013), arXiv:1207.6326.

[195] P. B. Price, K. Woschnagg, and D. Chirkin, "Age vs Depth of Glacial Ice at South Pole," Geophysical Research Letters **27**, 2129 (2000).

[196] M. G. Aartsen *et al.* (IceCube Collaboration), "Measurement of South Pole ice transparency with the IceCube LED calibration system," Nucl. Instrum. Methods Phys. Res. A **711**, 73 (2013), arXiv:1301.5361.

[197] H. Craig, H. Shoji, and C. C. Langway, "Nonequilibrium Air Clathrate Hydrates in Antarctic Ice: A Paleopiezomdter for Polar Ice Caps," Proceedings of the National Academy of Sciences **90**, 11416 (1993).

[198] D. Chirkin on behalf of the IceCube Collaboration, "Evidence of optical anisotropy of the South Pole ice," in *Proceedings, 33th International Cosmic Ray Conference (ICRC2013)* (2013) p. 0580, arXiv:1309.7010.

[199] R. Abbasi *et al.* (IceCube Collaboration), "Calibration and Characterization of the IceCube Photomultiplier Tube," Nucl. Instrum. Methods Phys. Res. A **618**, 139 (2010), arXiv:1002.2442.

[200] R. Abbasi *et al.* (IceCube Collaboration), "The IceCube data acquisition system: Signal capture, digitization, and timestamping," Nucl. Instrum. Methods Phys. Res. A **601**, 294 (2009), arXiv:0810.4930.

[201] IceCube Collaboration, "Project Wavedeform — IceCube Software," `http://software.icecube.wisc.edu/documentation/inspect/wavedeform.html` (accessed: May 31, 2019), IceCube Internal Document.

[202] IceCube Collaboration, "SuperDST — IceCube Documentation," `http://software.icecube.wisc.edu/documentation/projects/dataclasses/superdst.html` (accessed: May 31, 2019), IceCube Internal Document.

[203] M. G. Aartsen *et al.* (IceCube Collaboration), "Improvement in fast particle track reconstruction with robust statistics," Nucl. Instrum. Methods Phys. Res. A **736**, 143 (2014), arXiv:1308.5501.

[204] J. Ahrens *et al.* (AMANDA Collaboration), "Muon track reconstruction and data selection techniques in AMANDA," Nucl. Instrum. Methods Phys. Res. A **524**, 169 (2004), arXiv:astro-ph/0407044.

[205] IceCube Collaboration, "Trigger Filter Transmission Board - IceCubeWiki," `https://wiki.icecube.wisc.edu/index.php/Trigger_Filter_Transmission_Board` (accessed: May 31, 2019), IceCube Internal Document.

[206] J. A. Aguilar, P. Berghaus, J. Dumm, and T. Montaruli, "IceCube Muon Filter for 2009 Pole Season," `https://docushare.icecube.wisc.edu/dsweb/Get/Document-48360/2009_TFT_MuonFilterv8.pdf` (accessed: Jul 25, 2019) (2009), IceCube Internal Document.

[207] P. M. Baker, J. A. Aguilar, J. Dumm, and T. Montaruli, "IceCube Muon Filter for 2010 Pole Season," `https://docushare.icecube.wisc.edu/dsweb/Get/Document-52529/2010_TFT_MuonFilterv1p1-1.pdf` (accessed: Jul 25, 2019) (2009), IceCube Internal Document.

[208] N. Kurahashi, "IceCube Muon Filter for 2011 Pole Season," `https://docushare.icecube.wisc.edu/dsweb/Get/Document-56581/MuonFilterProposal.pdf` (accessed: Jul 25, 2019) (2010), IceCube Internal Document.

[209] J. Auffenberg, "EHE Filter Proposal 2010/11," `https://docushare.icecube.wisc.edu/dsweb/Get/Document-56550/EHE_Filter_proposal.PDF` (accessed: Jul 25, 2019) (2010), IceCube Internal Document.

[210] T. Glusenkamp, "Muon Filter Proposal IC86-2012," `https://docushare.icecube.wisc.edu/dsweb/Get/Document-59906/MuonFilter2012_v3_with_addendum.pdf` (accessed: Jul 25, 2019) (2012), IceCube Internal Document.

[211] A. Ishihara, H. Wissing, and S. Yoshida, "Request for the EHE Filter," `https://docushare.icecube.wisc.edu/dsweb/Get/Document-59306/EHEFilter_proposal_2012.pdf` (accessed: Jul 25, 2019) (2012), IceCube Internal Document.

[212] P. Berghaus, "2013 Muon Filter/Offline L2 Proposal," `https://docushare.icecube.wisc.edu/dsweb/Get/Document-62960/filterprop_muon_13.pdf` (accessed: Jul 25, 2019) (2012), IceCube Internal Document.

[213] K. Mase, "Request for the EHE Filter (2013) (Ver. 4)," `https://docushare.icecube.wisc.edu/dsweb/Get/Document-62962/EHE_filter_2013.pdf` (accessed Jul 25, 2019) (2012), IceCube Internal Document.

[214] A. M. Dziewonski and D. L. Anderson, "Preliminary reference earth model," Phys. Earth Planet. Interiors **25**, 297 (1981).

[215] C. Andreopoulos *et al.*, "The GENIE Neutrino Monte Carlo Generator," Nucl. Instrum. Methods Phys. Res. A **614**, 87 (2010), arXiv:0905.2517.

[216] D. Heck, J. Knapp, J. Capdevielle, G. Schatz, and T. Thouw, *CORSIKA: A Monte Carlo Code to Simulate Extensive Air Showers*, Tech. Rep. FZKA 6019 (Forschungszentrum Karlsruhe Report, 1998).

[217] J. van Santen, *Neutrino Interactions in IceCube above 1 TeV: Constraints on Atmospheric Charmed-Meson Production and Investigation of the Astrophysical Neutrino Flux with 2 Years of IceCube Data Taken 2010–2012*, Ph.D. thesis, University of Wisconsin-Madison (2014).

[218] D. Chirkin and W. Rhode, *Propagating leptons through matter with Muon Monte Carlo (MMC)* (2004), arXiv:hep-ph/0407075.

[219] B. Voigt, *Sensitivity of the IceCube Detector for Ultra-High Energy Electron-Neutrino Events*, Ph.D. thesis, Humboldt-Universität zu Berlin (2008).

[220] L. D. Landau and I. Pomeranchuk, "Electron cascade process at very high-energies," Dokl. Akad. Nauk Ser. Fiz. **92**, 535 (1953).

[221] A. B. Migdal, "Bremsstrahlung and Pair Production in Condensed Media at High Energies," Physical Review **103**, 1811 (1956).

[222] L. Rädel and C. Wiebusch, "Calculation of the Cherenkov light yield from electromagnetic cascades in ice with Geant4," Astroparticle Physics **44**, 102 (2013), arXiv:1210.5140.

[223] L. Rädel and C. Wiebusch, "Calculation of the Cherenkov light yield from low energetic secondary particles accompanying high-energy muons in ice and water with Geant4 simulations," Astroparticle Physics **38**, 53 (2012), arXiv:1206.5530.

[224] D. Chirkin (IceCube Collaboration), "Photon tracking with GPUs in IceCube," Nucl. Instrum. Methods Phys. Res. A **725**, 141 (2013).

[225] C. Kopper, "CLSim," `https://github.com/claudiok/clsim` (accessed: Feb 17, 2015).

[226] J. Lundberg, P. Miocinovic, T. Burgess, J. Adams, S. Hundertmark, P. Desiati, K. Woschnagg, and P. Niessen, "Light tracking through ice and water — Scattering and absorption in heterogeneous media with Photonics," Nucl. Instrum. Methods Phys. Res. A **581**, 619 (2007), arXiv:astro-ph/0702108.

[227] N. Whitehorn, J. van Santen, and S. Lafebre, "Penalized splines for smooth representation of high-dimensional Monte Carlo datasets," Computer Physics Communications **184**, 2214 (2013), arXiv:1301.2184.

[228] T. R. De Young, "IceTray: a Software Framework for IceCube," in *Computing in High Energy Physics and Nuclear Physics 2004*, CERN-2005-002 (2005) p. 463.

[229] V. J. Stenger, "Track Fitting For Dumand II Octagon Array," (1990), DUMAND External Reports.

[230] K. Schatto, *Stacked searches for high-energy neutrinos from blazars with IceCube*, Ph.D. thesis, Johannes-Gutenberg-Universität, Mainz (2014).

[231] M. G. Aartsen *et al.* (IceCube Collaboration), "Energy reconstruction methods in the IceCube neutrino telescope," Journal of Instrumentation **9**, P03009 (2014), arXiv:1311.4767.

[232] D. Pandel, *Bestimmung von Wasser- und Detektorparametern und Rekonstruktion von Myonen bis 100 TeV mit dem Baikal Neutrinoteleskop NT-72*, Diploma thesis, Humboldt-Universität zu Berlin (1996).

[233] K. Schatto, "Spline-Reco - IceCubeWiki," `https://wiki.icecube.wisc.edu/index.php/Spline-reco` (2014), IceCube Internal Document.

[234] T. Neunhoffer, "Estimating the angular resolution of tracks in neutrino telescopes based on a likelihood analysis," Astroparticle Physics **25**, 220 (2006), arXiv:astro-ph/0403367.

[235] T. Neunhöffer, *Die Entwicklung eines neuen Verfahrens zur Suche nach kosmischen Neutrino-Punktquellen mit dem AMANDA-Neutrinoteleskop*, Ph.D. thesis, Johannes-Gutenberg-Universität, Mainz (2004).

[236] S. S. Wilks, "The Large-Sample Distribution of the Likelihood Ratio for Testing Composite Hypotheses," The Annals of Mathematical Statistics **9**, 60 (1938).

[237] M. G. Aartsen *et al.* (IceCube Collaboration), "Observation of the cosmic-ray shadow of the Moon with IceCube," Physical Review D **89**, 102004 (2014), arXiv:1305.6811.

[238] R. Reimann, *Untersuchungen Mit Graphik-Prozessoren (GPU) Zur Messung Der Abschattung Kosmischer Strahlung Durch Den Mond in IceCube*, Bachelor's Thesis, RWTH Aachen (2011).

[239] E. Vogel, *Noboloid - An Improved Likelihood Estimation for Angular Uncertainties of Muon Tracks in IceCube* , Master's thesis, RWTH Aachen University (2017).

[240] R. Abbasi *et al.* (IceCube Collaboration), "An improved method for measuring muon energy using the truncated mean of dE/dx," Nucl. Instrum. Methods Phys. Res. A **703**, 190 (2013), arXiv:1208.3430.

[241] L. Rädel and S. Schoenen, "Event Selection IC86-2011," `https://icecube.wisc.edu/~lraedel/html/multi_year_diffuse/event_selections/IC86-2011.html` (2012), IceCube Internal Website.

[242] J. I. Pütz, *Selektion eines hochreinen Myon-Neutrino-Datensatzes for die Suche kosmischer Neutrinoquellen mit IceCube*, Master's thesis, RWTH Aachen University, Germany (2014).

[243] M. C. R. Zoll, *A Search for Solar Dark Matter with the IceCube Neutrino Detector : Advances in Data Treatment and Analysis Technique*, Ph.D. thesis, Stockholm University (2016).

[244] J. Feintzeig, *Searches for Point-like Sources of Astrophysical Neutrinos with the IceCube Neutrino Observatory*, Ph.D. thesis, University of Wisconsin-Madison (2014).

[245] G. C. Hill, "Bayesian Event Reconstruction and Background Rejection in Neutrino Detectors," in *Proceedings of the 27th International Cosmic Ray Conference — PoS(ICRC2001)* (2001) p. 1279, arXiv:astro-ph/0106081.

[246] J. Ahrens *et al.* (AMANDA Collaboration), "Observation of High Energy Atmospheric Neutrinos with the Antarctic Muon and Neutrino Detector Array," Physical Review D **66**, 012005 (2002), arXiv:astro-ph/0205109.

[247] T. Hastie, S. Rosset, J. Zhu, and H. Zou, "Multi-Class AdaBoost," Statistics and Its Interface **2**, 349 (2009).

[248] L. Rädel and S. Schoenen, "Event Selection IC86-2012/13/14," `https://icecube.wisc.edu/~lraedel/html/multi_year_diffuse/event_selections/IC86-2012_2013.html#ic86-2012-13-14-goodrun-criterion` (2014), IceCube Internal Website.

[249] J. R. Hoerandel, "On the knee in the energy spectrum of cosmic rays," Astroparticle Physics **19**, 193 (2003), arXiv:astro-ph/0210453.

[250] R. Enberg, M. H. Reno, and I. Sarcevic, "Prompt neutrino fluxes from atmospheric charm," Physical Review D **78**, 043005 (2008), arXiv:0806.0418.

[251] D. Chirkin, “Likelihood description for comparing data with simulation of limited statistics,” (2013), arXiv:1304.0735.

[252] A. Kolmogorov, “Sulla Determinazione Empirica Di Una Lgge Di Distribuzione,” Inst. Ital. Attuari, Giorn. **4**, 83 (1933).

[253] N. V. Smirnov, “On the Estimation of the Discrepancy between Empirical Curves of Distribution for Two Independent Samples,” Moscow University Mathematics Bulletin **2**, 3 (1939).

[254] C. Zhu, R. H. Byrd, P. Lu, and J. Nocedal, “Algorithm 778: L-BFGS-B: Fortran Subroutines for Large-Scale Bound-Constrained Optimization,” ACM Transactions on Mathematical Software **23**, 550 (1997).

[255] E. Jones, T. Oliphant, P. Peterson, *et al.*, “SciPy: Open source scientific tools for Python,” (2001–), (accessed: Jun 04, 2019).

[256] The IceCube Collaboration, “IceCube SVN - Skylab,” `http://code.icecube.wisc.edu/svn/sandbox/skylab/`, IceCube Internal Document.

[257] R. J. Barlow, *Statistics: A Guide to the Use of Statistical Methods in the Physical Sciences* (John Wiley & Sons, 1998) pp. 81–90.

[258] S. Coenders, *High-energy cosmic ray accelerators: searches with IceCube neutrinos - Probing seven years of IceCube muon data for time-integrated emission of point-like neutrino sources*, Ph.D. thesis, Technische Universität München (2016).

[259] R. Reimann, “PS analysis of multi-year diffuse up-going muon sample - Update,” `https://docushare.icecube.wisc.edu/dsweb/Get/Document-79058/Reimann_PS_analysis_of_Diffuse_Sample.pdf` (accessed Jul 25, 2019) (2017), IceCube Point-Source Working Group Call, Jan 09, 2017.

[260] J. Neyman, “Outline of a Theory of Statistical Estimation Based on the Classical Theory of Probability,” Phil. Trans. R. Soc. A **236**, 333 (1937).

[261] L. B. Bezrukov and E. V. Bugaev, “Nucleon shadowing effects in photonuclear interactions,” Sov. J. Nucl. Phys. **33**, 1195 (1981).

[262] E. V. Bugaev and Y. V. Shlepin, “Photonuclear interactions of super-high energy muons and tau-leptons,” in *Proceedings of the 12th International Symposium on Very High Energy Cosmic Ray Interactions - (Nuclear Physics B)*, Vol. 122 (2003) pp. 341–344.

[263] E. V. Bugaev and Y. V. Shlepin, “Photonuclear interaction of high energy muons and tau leptons,” Physical Review D **67**, 034027 (2003), arXiv:hep-ph/0203096.

[264] H. Abramowicz, E. M. Levin, A. Levy, and U. Maor, “A parametrization of $\sigma_T(\gamma^* p)$ above the resonance region for $Q^2 \leq 0$,” Physics Letters B **269**, 465 (1991).

[265] H. Abramowicz and A. Levy, *The ALLM parameterization of* $\sigma_{tot}(\gamma^* p)$ *- an update*, Tech. Rep. DESY-97-251 (DESY, 1997) arXiv:hep-ph/9712415.

[266] K. M. Górski, E. Hivon, A. J. Banday, B. D. Wandelt, F. K. Hansen, M. Reinecke, and M. Bartelmann, "HEALPix: A Framework for High-Resolution Discretization and Fast Analysis of Data Distributed on the Sphere," The Astrophysical Journal **622**, 759 (2005), arXiv:astro-ph/0409513.

[267] F. Acero *et al.* (Fermi-LAT Collaboration), "Fermi Large Area Telescope Third Source Catalog," The Astrophysical Journal Supplement Series **218**, 23 (2015), arXiv:1501.02003.

[268] M. Ajello *et al.* (Fermi-LAT Collaboration), "3FHL: The Third Catalog of Hard Fermi-LAT Sources," The Astrophysical Journal Supplement Series **232**, 18 (2017), arXiv:1702.00664.

[269] J. Braun, "2005 AMANDA Point Source Analysis," `http://icecube.wisc.edu/~jbraun/2005_point_source/results.html` (accessed: April 15, 2017).

[270] J. Braun, "2000-2006 AMANDA Point Source Analysis," `http://icecube.wisc.edu/~jbraun/combined_point_source/unblinding.html` (accessed April 15, 2017).

[271] T. Montaruli, "IC9 Point Source List," `https://wiki.icecube.wisc.edu/index.php/IC9PointSourceList` (accessed April 15, 2017), IceCube Internal Document.

[272] S. P. Wakely and D. Horan, "TeVCat: An online catalog for Very High Energy Gamma-Ray Astronomy," International Cosmic Ray Conference **3**, 1341 (2008), `tevcat.uchicago.edu`.

[273] M. Wenger *et al.*, "The SIMBAD astronomical database - The CDS reference database for astronomical objects," Astronomy & Astrophysics Supplement Series **143**, 9 (2000), arXiv:astro-ph/0002110.

[274] K. I. I. Koljonen and T. J. Maccarone, "Gemini/GNIRS infrared spectroscopy of the Wolf-Rayet stellar wind in Cygnus X-3," Monthly Notices of the Royal Astronomical Society **472**, 2181 (2017), arXiv:1708.04050.

[275] N. J. Wright, J. E. Drew, and M. Mohr-Smith, "The Massive Star Population of Cygnus OB2," Monthly Notices of the Royal Astronomical Society **449**, 741 (2015), arXiv:1502.05718.

[276] V. Karamanavis, L. Fuhrmann, T. P. Krichbaum, E. Angelakis, J. Hodgson, I. Nestoras, I. Myserlis, J. A. Zensus, A. Sievers, and S. Ciprini, "PKS 1502+106: A high-redshift Fermi blazar at extreme angular resolution. Structural dynamics with VLBI imaging up to 86 GHz," Astronomy & Astrophysics **586**, A60 (2016), arXiv:1511.01085.

[277] A. Accomazzi *et al.*, "The sao/nasa astrophysics data system," `http://adsabs.harvard.edu/` (accessed: May 31, 2019).

[278] F. Aharonian *et al.* (H.E.S.S. Collaboration), "Fast Variability of Tera-Electron Volt γ Rays from the Radio Galaxy M87," Science **314**, 1424 (2006).

[279] H. Frommert, "The Interactive NGC Catalog Online," `http://spider.seds.org/ngc/ngc.html` (accessed: Jun. 15, 2019).

[280] C. M. Raiteri *et al.*, "Variability of the blazar 4C 38.41 (B3 1633+382) from GHz frequencies to GeV energies," Astronomy & Astrophysics **545**, A48 (2012), arXiv:1207.3979.

[281] E. Aliu *et al.* (VERITAS Collaboration), "Investigating the TeV Morphology of MGRO J1908+06 with VERITAS," The Astrophysical Journal **787**, 166 (2014), arXiv:1404.7185.

[282] C. M. Raiteri, "ATel #3483: Optical outburst of 4C 38.41 (1633+382) observed by the GASP," The Astronomers Telegram **#3483** (2011).

[283] A. Szostek, "ATel #3333: Fermi LAT detection of a GeV flare from quasar 4C +38.41," The Astronomers Telegram **#3333** (2011).

[284] S. Vercellone *et al.*, "The brightest gamma-ray flaring blazar in the sky: AGILE and multi-wavelength observations of 3C 454.3 during November 2010," The Astrophysical Journal **736**, L38 (2011), arXiv:1106.5162.

[285] S. Kafka, "Observations from the AAVSO International Database," `https://www.aavso.org` (accessed Jul 25, 2019) (2018).

[286] C. Carilli and P. Barthel, "Cygnus A," The Astronomy and Astrophysics Review **7**, 1 (1996).

[287] V. Beckmann and H. Walter, "Cygnus A and the unified model," in *40th COSPAR Scientific Assembly*, COSPAR Meeting, Vol. 40 (2014).

[288] I. Taboada (HAWC Collaboration), "HAWC Skymap above 56 TeV," (2018), privat communication, HAWC public plots.

[289] F. Halzen, A. Kheirandish, and V. Niro, "Prospects for Detecting Galactic Sources of Cosmic Neutrinos with IceCube: An Update," Astroparticle Physics **86**, 46 (2017), arXiv:1609.03072.

[290] Aharonian, F. *et al.* (H.E.S.S. Collaboration), "Detection of very high energy radiation from HESS J1908+063 confirms the Milagro unidentified source MGRO J1908+06," Astronomy & Astrophysics **499**, 723 (2009), arXiv:0904.3409.

[291] B. Bartoli *et al.* (Argo-YBJ Collaboration), "Observation of the TeV Gamma-Ray Source MGRO J1908+06 with ARGO-YBJ," The Astrophysical Journal **760**, 110 (2012), arXiv:1207.6280.

[292] A. U. Abeysekara *et al.* (HAWC Collaboration), "Very-High-Energy Particle Acceleration Powered by the Jets of the Microquasar SS 433," Nature **562**, 82 (2018), arXiv:1810.01892.

[293] C. Kopper and E. Blaufuss, "IceCube-170922A - IceCube observation of a high-energy neutrino candidate event," (2017), GRB Coordinates Network, Circular Service, No. 21916, #1.

[294] D. J. Thompson, "ATel #10791: Fermi-LAT detection of increased gamma-ray activity of TXS 0506+056, located inside the IceCube-170922A error region." The Astronomers Telegram **#10791** (2017).

[295] S. Paiano, R. Falomo, A. Treves, and R. Scarpa, "The Redshift of the BL Lac Object TXS 0506+056," The Astrophysical Journal **854**, L32 (2018), arXiv:1802.01939.

[296] M. Ackermann *et al.* (Fermi-LAT Collaboration), "The Second Catalog of Active Galactic Nuclei Detected by the Fermi Large Area Telescope," The Astrophysical Journal **743**, 171 (2011), arXiv:1108.1420.

[297] C. Rosset, "Healpy.Pixelfunc.Get_all_neighbours — Healpy 1.5Dev Documentation," `https://healpy.readthedocs.io/en/1.5.0/generated/healpy.pixelfunc.get_all_neighbours.html` (accessed: May 31, 2019).

[298] R. Reimann and S. Coenders, "Resolved discrepancy in Hotspot Population Analysis," `https://docushare.icecube.wisc.edu/dsweb/Get/Document-80292/Reimann_PS_analysis_of_Diffuse_Sample.pdf` (accessed Jul 25, 2019) (2017), IceCube Point-Source Working Group Call, Jun 05, 2017.

[299] J. Aleksić *et al.* (MAGIC Collaboration), "Measurement of the Crab Nebula Spectrum over Three Decades in Energy with the MAGIC Telescopes," Journal of High Energy Astrophysics **5-6**, 30 (2015), arXiv:1406.6892.

[300] F. Aharonian *et al.* (H.E.S.S. Collaboration), "Observations of the Crab Nebula with HESS," Astronomy & Astrophysics **457**, 899 (2006), arXiv:astro-ph/0607333.

[301] A. Reimer, "Photon-Neutrino Flux Correlations from Hadronic Models of AGN?" in *Proceedings of the 34th International Cosmic Ray Conference — PoS(ICRC2015)*, Vol. 236 (2015) p. 1123.

[302] M. Petropoulou, S. Dimitrakoudis, P. Padovani, A. Mastichiadis, and E. Resconi, "Photohadronic Origin of γ-Ray BL Lac Emission: Implications for IceCube Neutrinos," Monthly Notices of the Royal Astronomical Society **448**, 2412 (2015), arXiv:1501.07115.

[303] M. Mandelartz and J. Becker Tjus, "Prediction of the Diffuse Neutrino Flux from Cosmic Ray Interactions near Supernova Remnants," Astroparticle Physics **65**, 80 (2015), arXiv:1301.2437.

[304] A. Mücke, R. Engel, J. P. Rachen, R. J. Protheroe, and T. Stanev, "Monte-Carlo Simulations of Photohadronic Processes in Astrophysics," Computer Physics Communications **124**, 290 (2000), arXiv:astro-ph/9903478.

[305] D. W. Hogg, "Distance Measures in Cosmology," (1999), arXiv:astro-ph/9905116.

[306] K. Murase and E. Waxman, "Constraining High-Energy Cosmic Neutrino Sources: Implications and Prospects," Physical Review D **94** (2016), 10.1103/PhysRevD.94.103006, arXiv:1607.01601.

[307] K. Emig, C. Lunardini, and R. Windhorst, "Do High Energy Astrophysical Neutrinos Trace Star Formation?" Journal of Cosmology and Astroparticle Physics **2015**, 029 (2015), arXiv:1507.05711.

[308] A. M. Hopkins and J. F. Beacom, "On the Normalization of the Cosmic Star Formation History," The Astrophysical Journal **651**, 142 (2006), arXiv:astro-ph/0601463.

[309] H. Yuksel, M. D. Kistler, J. F. Beacom, and A. M. Hopkins, "Revealing the High-Redshift Star Formation Rate with Gamma-Ray Bursts," The Astrophysical Journal **683**, L5 (2008), arXiv:0804.4008.

[310] L.-G. Strolger, T. Dahlen, S. A. Rodney, O. Graur, A. G. Riess, C. McCully, S. Ravindranath, B. Mobasher, and A. K. Shahady, "The Rate of Core Collapse Supernovae to Redshift 2.5 From The CANDELS and CLASH Supernova Surveys," The Astrophysical Journal **813**, 93 (2015), arXiv:1509.06574.

[311] P. Madau and M. Dickinson, "Cosmic Star Formation History," Annual Review of Astronomy and Astrophysics **52**, 415 (2014), arXiv:1403.0007.

[312] P. Mertsch, M. Rameez, and I. Tamborra, "Detection Prospects for High Energy Neutrino Sources from the Anisotropic Matter Distribution in the Local Universe," Journal of Cosmology and Astroparticle Physics **2017**, 011 (2017), arXiv:1612.07311.

[313] I. Taboada, C. F. Tung, and J. Wood for the HAWC Collaboration, "Constrains on the Extragalactic Origin of IceCube's Neutrinos Using HAWC," in *Proceedings of 35th International Cosmic Ray Conference — PoS(ICRC2017)*, Vol. 301 (2018) p. 663, arXiv:1801.09545.

[314] C. F. Tung, I. Taboada, M. Ahlers, G. Japaridze, and K. Satalecka, *Document for First Extragalactic Simulation Of Neutrinos and Gamma-Rays*, Tech. Rep. (IceCube Internal Report, 2017).

[315] M. Ahlers and F. Halzen, "Opening a New Window onto the Universe with IceCube," Progress in Particle and Nuclear Physics **102**, 73 (2018), arXiv:1805.11112.

[316] M. Ahlers and F. Halzen, "Pinpointing Extragalactic Neutrino Sources in Light of Recent IceCube Observations," Physical Review D **90**, 043005 (2014), arXiv:1406.2160.

[317] C. Gruppioni *et al.*, "The Herschel PEP/HerMES Luminosity Function. I: Probing the Evolution of PACS Selected Galaxies to Z$\sim$4," Monthly Notices of the Royal Astronomical Society **432**, 23 (2013), arXiv:1302.5209.

[318] M. Ackermann *et al.* (Fermi-LAT Collaboration), "GeV Observations of Star-Forming Galaxies with *Fermi* LAT," The Astrophysical Journal **755**, 164 (2012), arXiv:1206.1346.

[319] F. Zandanel, I. Tamborra, S. Gabici, and S. Ando, “High-Energy Gamma-Ray and Neutrino Backgrounds from Clusters of Galaxies and Radio Constraints,” Astronomy & Astrophysics **578**, A32 (2015), arXiv:1410.8697.

[320] M. Ajello *et al.*, “The Luminosity Function of Fermi-Detected Flat-Spectrum Radio Quasars,” The Astrophysical Journal **751**, 108 (2012), arXiv:1110.3787.

[321] M. Ajello *et al.*, “The Cosmic Evolution of Fermi BL Lacertae Objects,” The Astrophysical Journal **780**, 73 (2013), arXiv:1310.0006.

[322] Y. Inoue, “Contribution of the Gamma-Ray Loud Radio Galaxies Core Emissions to the Cosmic MeV and GeV Gamma-Ray Background Radiation,” The Astrophysical Journal **733**, 66 (2011), arXiv:1103.3946.

[323] S. S. Kimura, K. Murase, and K. Toma, “Neutrino and Cosmic-Ray Emission and Cumulative Background from Radiatively Inefficient Accretion Flows in Low-Luminosity Active Galactic Nuclei,” The Astrophysical Journal **806**, 159 (2015), arXiv:1411.3588.

[324] L. C. Ho, “Nuclear Activity in Nearby Galaxies,” Annual Review of Astronomy and Astrophysics **46**, 475 (2008), arXiv:0803.2268.

[325] M. Aartsen *et al.* (IceCube-Gen2 Collaboration), “Letter of Intent: The Precision IceCube Next Generation Upgrade (PINGU),” (2017), arXiv:1401.2046v2.

[326] S. Kaufmann, S. J. Wagner, O. Tibolla, and M. Hauser, “1ES 0229+200: An Extreme Blazar with a Very High Minimum Lorentz Factor,” Astronomy & Astrophysics **534**, A130 (2011), arXiv:1109.3628.

[327] B. Kapanadze, D. Dorner, P. Romano, S. Vercellone, and L. Tabagari, “The TeV Blazar 1ES 1959+650 - a Short Review,” in *Proceedings of XII Multifrequency Behaviour of High Energy Cosmic Sources Workshop — PoS(MULTIF2017)* (Sissa Medialab, Palermo, Italy, 2018) p. 033.

[328] M. Schroedter *et al.*, “A Very High Energy Gamma-Ray Spectrum of 1ES 2344+514,” The Astrophysical Journal **634**, 947 (2005).

[329] V. A. Acciari *et al.* (VERITAS Collaboration), “VERITAS Observations of a Very High Energy Gamma-Ray Flare from the Blazar 3C 66A,” The Astrophysical Journal **693**, L104 (2009), arXiv:0901.4527.

[330] M. J. Hardcastle, M. Birkinshaw, and D. M. Worrall, “A Chandra Detection of the Radio Hotspot of 3C123,” Monthly Notices of the Royal Astronomical Society **323**, L17 (2001), arXiv:astro-ph/0101240.

[331] M. Schmidt, “3 C 273 : A Star-Like Object with Large Red-Shift,” Nature **197**, 1040 (1963).

[332] J. L. Greenstein and M. Schmidt, “The Quasi-Stellar Radio Sources 3C 48 and 3C 273.” The Astrophysical Journal **140**, 1 (1964).

[333] J. L. Schmitt, “BL Lac Identified as a Radio Source,” Nature **218**, 663 (1968).

[334] M. Amenomori *et al.* (Tibet ASγ Collaboration), “First Detection of Photons with Energy Beyond 100 TeV from an Astrophysical Source,” (2019), submitted to the Physical Review Letters, arXiv:1906.05521.

[335] M. Tavani *et al.*, “Extreme Particle Acceleration in the Microquasar Cygnus X-3,” Nature **462**, 620 (2009).

[336] J. Li, D. F. Torres, K.-S. Cheng, E. d. O. Wilhelmi, P. Kretschmar, X. Hou, and J. Takata, “GeV Detection of HESS J0632+057,” The Astrophysical Journal **846**, 169 (2017), arXiv:1707.04280.

[337] F. Aharonian *et al.* (HEGRA Collaboration), “TeV Gamma Rays from the Blazar H 1426+428 and the Diffuse Extragalactic Background Radiation,” Astronomy & Astrophysics **384**, L23 (2002), arXiv:astro-ph/0202072.

[338] M. Massi and G. Torricelli-Ciamponi, “Origin of the long-term modulation of radio emission of LS I +61 303,” Astronomy & Astrophysics **585**, A123 (2016), arXiv:1511.05621.

[339] C. Hou, S. Chen, Q. Yuan, Z. Cao, H. He, and X. Sheng, “Multi-Wavelength Study of the MGRO J2019+37,” Chinese Physics C **38**, 085001 (2014), arXiv:1403.6338.

[340] M. Sasada *et al.*, “Prominent Polarized Flares of the Blazars AO 0235+164 and PKS 1510-089,” Journal of Physics: Conference Series **355**, 012023 (2012), arXiv:1102.1856.

[341] S. D. Hunter *et al.*, “Detection of High Energy Gamma-Rays from Bl-Lacertae PKS:0235+164 by the EGRET Telescope on the Compton Observatory,” Astronomy & Astrophysics **272**, 59 (1993).

[342] M. Boettcher and W. Collmar, “Spectral Variability in PKS 0528+134 at Gamma-Ray Energies,” Astronomy & Astrophysics **329**, L57 (1998), arXiv:astro-ph/9711032.

Eidesstattliche Erklärung

Ich, René Reimann,
erklärt hiermit, dass diese Dissertation und die darin dargelegten Inhalte die eigenen sind und selbstständig, als Ergebnis der eigenen originären Forschung, generiert wurden.
Hiermit erkläre ich an Eides statt

1. Diese Arbeit wurde vollständig oder größtenteils in der Phase als Doktorand dieser Fakultät und Universität angefertigt;
2. Sofern irgendein Bestandteil dieser Dissertation zuvor für einen akademischen Abschluss oder eine andere Qualifikation an dieser oder einer anderen Institution verwendet wurde, wurde dies klar angezeigt;
3. Wenn immer andere eigene- oder Veröffentlichungen Dritter herangezogen wurden, wurden diese klar benannt;
4. Wenn aus anderen eigenen- oder Veröffentlichungen Dritter zitiert wurde, wurde stets die Quelle hierfür angegeben. Diese Dissertation ist vollständig meine eigene Arbeit, mit der Ausnahme solcher Zitate;
5. Alle wesentlichen Quellen von Unterstützung wurden benannt;
6. Wenn immer ein Teil dieser Dissertation auf der Zusammenarbeit mit anderen basiert, wurde von mir klar gekennzeichnet, was von anderen und was von mir selbst erarbeitet wurde;
7. Ein Teil oder Teile dieser Arbeit wurden zuvor veröffentlicht und zwar in:
    - M. G. Aartsen *et al.* [IceCube Collaboration] "Search for steady point-like sources in the astrophysical muon neutrino flux with 8 years of IceCube data" Eur. Phys. J. C **79** (2019) 3, 234

Aachen, den 26. November 2019

Acknowledgements

You have reached the end of this thesis and you had a long way through it. Also my way to finish this thesis was long and it would not have been possible without the help and support of many people.

First of all I want to thank the IceCube collaboration and the neutrino sources group, which accompanied me the over the last years. I would like to thank for all the advises and feedback, even if I did not like to here the criticism in the first place. I think that all the questions and remarks helped me to improve my understanding of the analysis and thus lead to a better analysis.

A special thanks goes to the IceCube Aachen group especially to Leif, Sebastian, Christian, Lisa, Jöran and Martin Leuermann how I always could bother with question. All the discussion we had about data samples, diffuse fits, different aspects of searches for point sources were very helpful.

I would like to thank Prof. Christopher Wiebusch for giving me the opportunity to work on such an interesting topic and betting two bottles of champagne on the success of my thesis - sorry that you lost. I acknowledge all his advises regarding my analysis, but also to give us the opportunity to look over the edge of the plate and to involve us in several aspects of academic live. Also I would like to thank Philipp Mertsch, not only for being my second referee, but how helped me out as I got stuck with the interpretation of the results from the population analysis.

A big thanks goes to all my office mates from the Kinderzimmer, especially Martin Leuermann for all the lively discussions we had at our frequent coffee breaks.

In the final step of my thesis I would like to thank Martin Leuermann, Martin Rongen, Lisa, Christian, Jöran, Jakob, Marit and Sandra for providing a lot of feedback and corrections to the text of this thesis.

Finally I would like to thank my parents, my wife Sandra and the rest of my family for all the support in all the past years. You supported me all my way through my study and gave me the chance to do what I found interesting. Especially Sandra had a lot of patience with me when I spend more time at work than at home. I do not have words to acknowledge her support. You are a support that I do not want to miss.

Thank you!